NATIONAL TECHNICAL UNIVERSITY OF ATHENS
SCHOOL OF NAVAL ARCHITECTURE AND MARINE ENGINEERING
DIVISION OF SHIP AND MARINE HYDRODYNAMICS

Hydroelastic analysis of slender bodies in waves by means of strip theory

---

Diploma Thesis

June 2017

Author : P.N. Kalogris

Supervisor : K.A. Belibassakis, Associate Professor, NTUA

Commitee : G.K. Politis, Professor, NTUA

G.J. Grigoropoulos, Professor, NTUA

Acknowledgements

The present Diploma Thesis is completing a five-year period of post-graduate studies at the School of Naval Architecture and Marine Engineering of National Technical University of Athens. Thus, I grab the chance to express my sincere gratitude to a number of people whose contribution was valuable for the accomplishment of this work and of my studies.

First of all, I would like to thank my supervisor and mentor Associate Professor K. Belibassakis for his guidance and support during the preparation of this thesis. His profound and wide knowledge in the field of marine hydrodynamics provided me with the required background to surpass the difficulties encountered in this study. Moreover, he gave me inspiration and encouragement during that educational journey.

Furthermore, I would like to thank for all his support and useful advices Mr. Yannis Georgiou, Naval Architect and Marine Engineer at Ship and Marine Hydrodynamics Laboratory, as he has significantly contributed in the completion of this thesis.

Last but not least, I would like to thank my family and my friends as if it hadn't be for their help, support and understanding it would be very difficult to finish my studies.

Contents

Abstract

Hydroelastic analysis represents a theory for calculating the responses of marine structures in a more accurate and realistic fashion since it integrates aspects of deformable body mechanics, namely elasticity theory, into classical ship and marine hydrodynamics. In that connection, it provides a powerful tool for the derivation of a unified, coupled system of responses, since the investigation of the hydrodynamic behavior of ships and other ocean structures is taking into account their mechanical/structural properties and in return a richer framework of analysis for strength aspects is provided to ocean engineers. One of the main aspects of this thesis is the assessment of the heave induced elastic deformations for an ocean going ship cruising at steady mean forward speed in heading (or following) seas. Symmetrical distortions (i.e. vertical bending) are triggered in specific frequencies called natural frequencies. Every structure can be modeled for an, up to some degree, elastic behavior and the associated flexibility is related to its structural characteristics. The latter define the natural frequencies of the structure. The eigenfrequencies of a marine structure may be met within the range of (encounter) frequencies on which the energy of a sea state is distributed, by means of wave energy spectrum. This may lead to critical conditions from the local and global strength point of view. In this work, we take advantage of the benefits of previously existed analytical theories in order to produce (linear) hydroelastic models applied to elongated (long and slender), monohull marine structures. First, the Euler – Bernoulli and Timoshenko beam models are used as main analytical tools for the “in vacuo’’, or “dry hull” analysis. Then by means of strip theory we employ a 2D potential flow theory in order to calculate the hydrodynamic and hydrostatic ship properties. Finally, the produced structure principal modes are imposed to the rigid ship motions producing the full set of equations which describe the ship responses to excitations due to harmonic waves.

Introduction

Hydroelasticity is a discipline, within marine and ocean engineering science, which it integrates aspects of deformable body mechanics, namely elasticity theory, into classical ship and marine hydrodynamics, thus introducing elasticity into fluid-structure interaction. Subsequently, wave loads and responses calculations for an ocean going vessel becomes more realistic. More specifically, since the action of the pressure field on the ship hull dynamically deforms the structure, the developed distortions modify the nearby flow field. Therefore, ocean going vessels, and marine structures exhibit properties, which must be determined through a combined/mixed modeling and design, i.e. using analytical and numerical tools stemming from both hydrodynamics/fluid mechanics and elasticity theory/mechanics of deformable bodies. Over the past years, hydroelasticity has proven to be of paramount importance for the design of a variety of marine structures, especially in the case of novel types, such as large vessels and VLFS, operating in the open seas.

Concerning the water environment, the most common cause of the marine structure loads are the surface gravity waves. Among the latter, the wind waves are the result of the turbulent wind flow field acting over and on the sea water free surface. The geometrical characteristics of the wind waves vary according to their height and length due to the excitation of the turbulent air flow, the related energy transfer to the sea water and the duration of the subsequent sea state. In addition, modeling of wave propagation must be enhanced when different bathymetry bottoms and transient regions coexist, and solid bodies are present acting as obstacles modifying the flow field characteristics due to refraction/diffraction phenomena.

Bodies floating or moving/travelling in a realistic sea water environment operate encountering sea waves, that is, under hydrodynamic loads/forces, which are the cause of body motions. Given the wide range of marine applications, several criteria have been developed in view to protecting and securing the operational capabilities and the safety of a ship starting from the early stages of its design. More specifically, ocean going vessels are designed taking into account several crucial factors, such as thrust efficiency, service speed attainment (both in calm and rough seas), seakeeping and maneuverability, cargo capacity, and hull structural strength, aiming to provide a sound design from different points of view, i.e., economic efficiency, ship's and crew/passengers safety and environmental protection. Especially, hull strength calculations focus on the determination of global and local wave induced loads on hull structural elements. During initial design stages, global stress analysis treats the ship as a hull girder operating under the effect of wave induced bending moments. Further examination may focus on the endurance of the structure by means of local analysis and/or the determination of the ship stiffness. Finally, an important criterion in the power performance of the ship is the added resistance in waves caused by the motion of the ship in rough seas. Many tools have been created over the years and are still in the process of further development and enhancement, leading to the current-state-of-the-art for the design of the ships taking hydroelastic phenomena into account. Amid others, Strip Theory, and Boundary Element Method, which lie in the core of the present thesis, as well as Computational Fluid Dynamics, and Finite Element Analysis, all contributing in the task of hydroelastic analysis.

Evolution of the Hydroelasticity theory

The term “hydroelasticity” was first introduced in the technical terminology by Heller and Abramson in 1959 pinpointing in this way a theory equivalent to aeroelasticity, i.e., the combined action of air induced loads together with structural responses, for application in the analysis of marine structures. It was not until 1974 when the enlightening work of Bishop and Price embodied a full hydroelastic analysis together with applications to specific type of ships, see, Hirdaris, Temarel (2009) and Wu, Cui (2009). Bishop, Price (1974) presented a new theory prying the distortions of beamlike hulls under the influence of both regular and irregular sea waves, emphasizing mainly in the symmetric distortions (vertical bending) while the antisymmetric ones (coupling of vertical, horizontal and twisting) were in a more premature stage, for adequate tools did not existed by that time. In this early stage, the tools for attacking the hydroelasticity problem were confined within the limits of 2D linear potential flow and linear structural criteria. In that connection, the calculation of principal modes for the structure using “dry hull” (or “in vacuo”) analysis adopts formulations for modeling the monohull vessels as elastic deformable beams by means of Timoshenko beam model (Timoshenko Beam Theory - TBT) together with finite difference analysis. Another method for predicting the influence of the surrounding fluid on a structure was the coupled, fluid – structure, system known as “wet mode” analysis. The calculation of the fluid actions on the hull and thus the estimation of the hydrodynamic ship properties are treated by means of Strip Theory. Basic assumptions for applying strip theory techniques are: (i) the fluid is inviscid, (ii) incompressible, and (iii) homogeneous together with adequate (iv) boundary conditions. Hence, generalized forces, added masses and damping coefficients can be calculated using the strip formulation and this, in turn, reduces the complex 3D problem to an adequate number of simplified 2D problems alongships. Numerically accurate results were produced for ship properties of lower modes given several local cross section forms, exploiting the existing methods for the calculation of added mass and damping coefficients, see, e.g., the seminal work by Lewis (1989) and other authors as referred in Bishop, Price (1979).

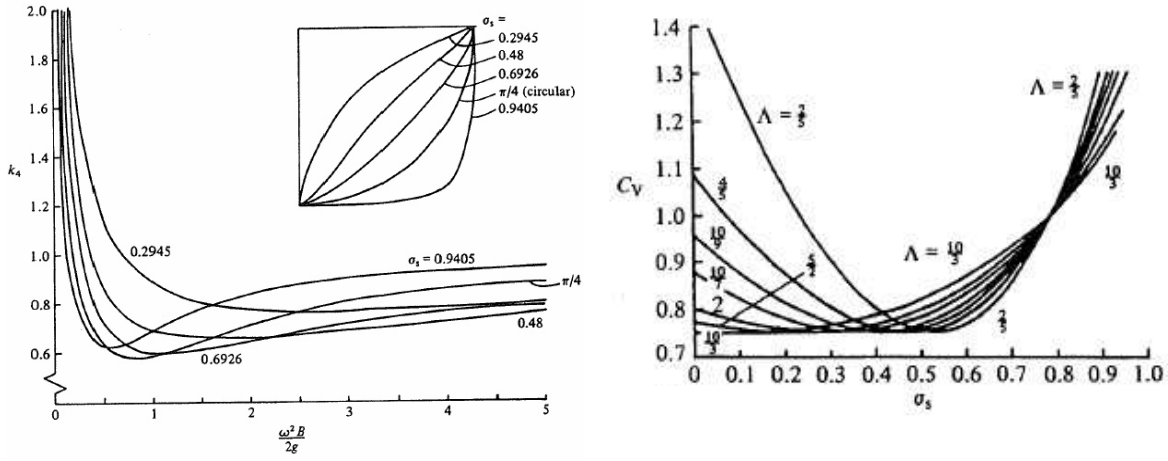

Fig. 01 Lewis forms (left) were employed to modify non – dimensionalized added mass in the vertical plane (right), from Lewis (1989).

The incorporation of the dry hull analysis to the ship rigid responses resulted in a unified model to treat hydroelastic problems reduced in 2D. This model has been applied on a plethora of slender beamlike hulls, e.g. container ship, bulk carrier, naval

vessel travelling with different service speeds under the effect of sea waves of various headings. Later methods included full – scale measurements concerning the aforementioned commercial ships in order to test the validity of the developed models, see, Bishop et al. (1983), Bishop et al. (1985), Bishop et al. (1991). A demonstration of the unified solution for the two – dimensional problem is illustrated in the following figure.

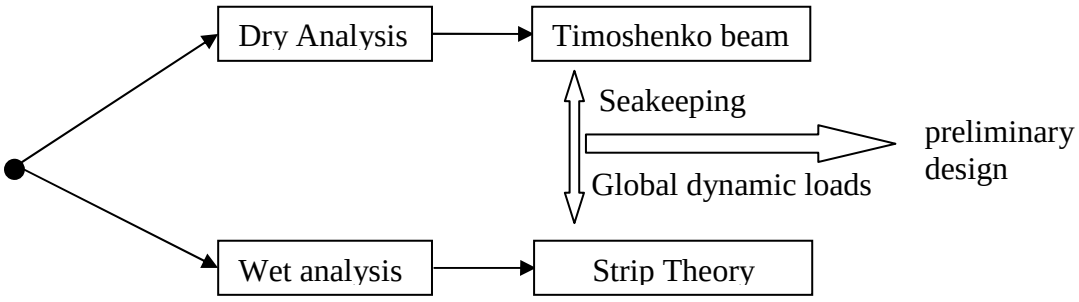

Fig. 02 2D hydroelasticity theory

It was not until 1980s when the application of the aforementioned basic principles by Bishop, Price was related to the development of a general and compact 3D theory for treat the problem of hydroelastic responses. The non – beamlike flexible marine structures were analyzed within the framework of linearity, see Bishop et al. (1986), Wu (1984), Price, Wu (1985). More specifically, exploitation of linearized boundary conditions on the mean free surface, on the mean hull surface and radiation conditions at infinity provided prerequisites for the derivation of a unique solution for the velocity potential of the flow field. In addition, structural linearities accounted for the assessment of the structural deformations on given/desired planes. Furthermore, based on the potential flow analysis simplifications, as adopted by Bishop, Price, were employed permitting the treatment of the fluid domain as of infinite depth, homogeneous, and inviscid with irrotational fluid motion. The abovementioned elements were embodied in a more advanced potential flow method, where panels of pulsating sources distribution placed over the vessel's mean hull set the basis for the application of Boundary Element Method (BEM) technique. Additionally, benefits of the Finite Element modeling (including Timoshenko and plate theories) were exploited for the determination of the principal modes in the case of the 3D structural modes. For such a purpose, the boundary condition problem was treated on the basis of several existed theories, see, e.g., Wu, Price (1985) and Timman, Newman (1962) for the "special" case of symmetric bodies. The advances in hydroelastic theory, permitting for a more realistic and efficient modeling of the related phenomena on marine structures, have contributed to the analysis method entitled "fluid – flexible structure interaction" and have paved the way to the development of design software appropriate to handle such problems. Over the last decades, investigations on different type of applications have been achieved using linear 3D modeling regarding commercial ships, such as large containers, bulks, and multihull ships. For instance, Price et al. (2002) have analyzed the dynamic behavior of a slender monohull vessel in oblique seas, and Hermundstad et al (1999) have examined the hydroelastic phenomena on a high speed catamaran; see, also, Hirdaris et al. (2003), Hirdaris et al (2006), Basaran et al. (2008).

Recent progress in the Hydroelastic models

Together with the development of more complex hydroelastic models, during the design stage, marine structures grew in sizes. Typical example is the introduction of the so called Very Large Floating Structures (VLFS). The VLF structures during their operational life in the sea environment are characterized by large motions, introducing non – linear phenomena to spring responses due to the influence of the instantaneous wetted surface. These applications can preserve linear structural characteristics, while nonlinear eigenvalue formulations are required for calculating the modes involved in the responses. In both frameworks of 2D or 3D analysis, specific techniques should be applied to confront this additional complexity. Therefore, quadratic elements embedded in strip theory and formulations for second order generalized hydrodynamic forces have been considered, see, e.g., the works by Jensen, Dogliani (1996) and Wu et al. (1997). The development of models for such large structures is facing efficiency problems. However, solutions applied in the VLFS modeling have already reported via the works of Wang et al. (1997) and Price, Wu (1989). The former have introduced two techniques. The first technique involves the use of a specific criterion in order to eliminate the influence of the pulsating source type Green function and its derivatives to achieve better convergence. The second technique introduces the implementation of iterative sparse solvers for the linear system of equations on the 3D theory. Other applications, extending the enhancements above, have incorporated fluid viscous damping effects while producing time domain simulations for slamming phenomena of large marine structures operating in irregular head and oblique seas, see, e.g., Aksu (1993). Later trends in the hydroelastic modeling of marine structures have introduced structural non – linearities for a floating plate using a generalized time dependent non – linear exciting force, see, Chen et al. (2003) and Chen et al. (2006). In conclusion, over the last two decades great progress has been achieved in the modeling of marine structures permitting the prediction of responses for a variety of applications, and therefore, we refer to Senjanovic et al. (2009) for the importance of developing accurate 3D models in some modern design applications.

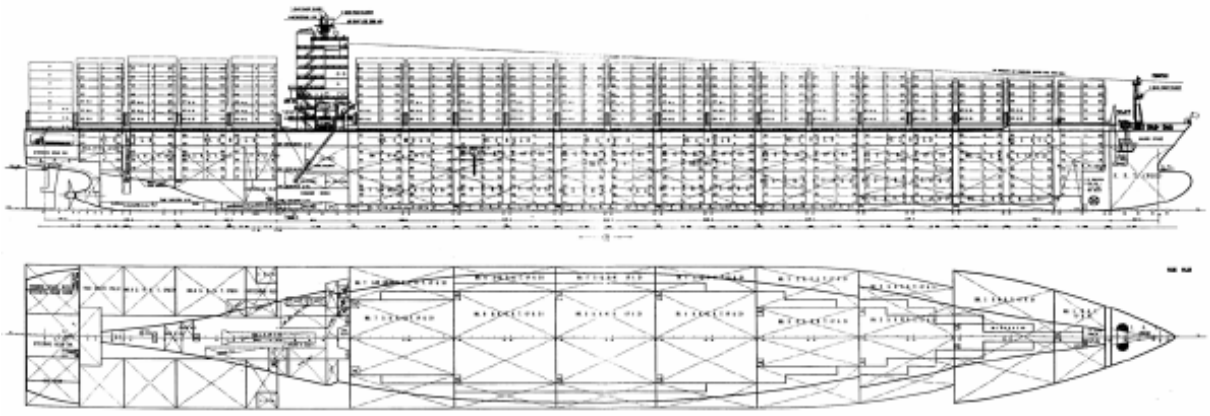

Fig. 03 7800 TEU Container Ship, L_{OA}=334 [m], B=42.8 [m], T=14.5 [m], Δ_{FLD}=135336 [t], from Senjanovic et al. (2010)

(a)

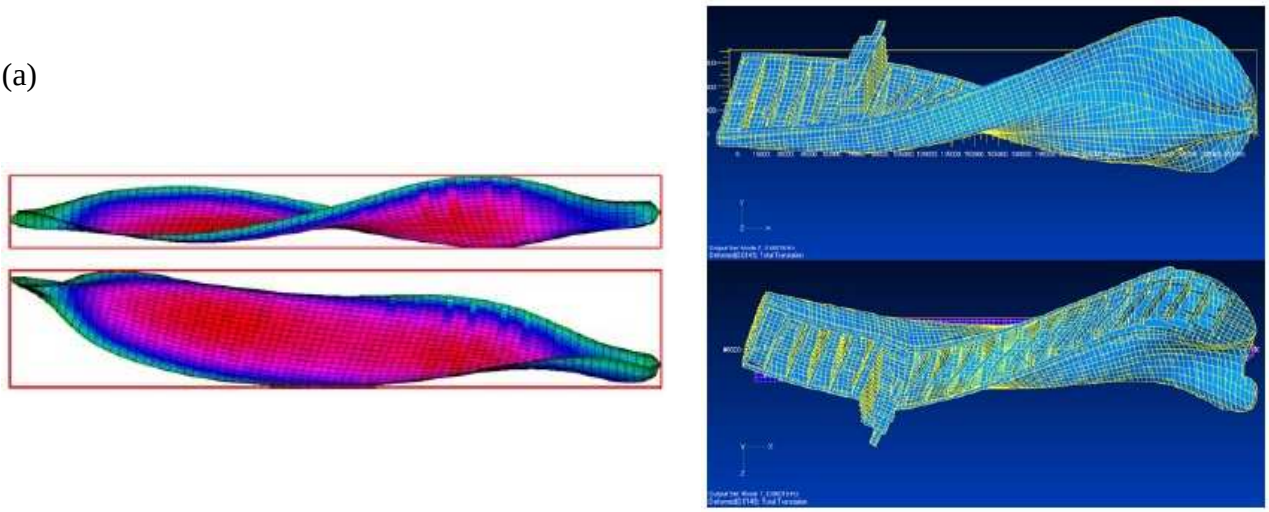

Fig. 04 Determination of natural modes, given the lightweight condition displacement Δ=33693 [t], by means of (a) 1D Finite element analysis (b) 3D Finite element analysis, from Senjanovic et al. (2010)

Dry natural frequencies, light weight, ω_i [rad/s].

Mode no.	Vert.		Horiz. + tors.		Mode no.
	1D	3D	1D	3D	
1	7.35	7.33	4.17	4.15	1(H0 + T1)
2	15.00	14.95	7.34	7.40	2(H1 + T2)
3	24.04	22.99	12.22	12.09	3(H2 + T3)
4	35.08	34.21	15.02	16.22	4(H3 + T4)

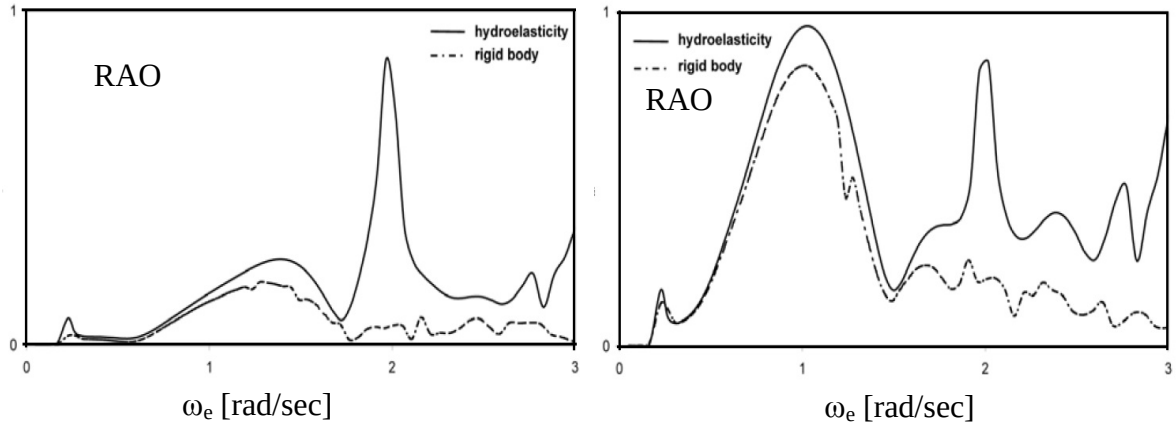

Fig. 05 Transfer functions of torsional (left) and horizontal bending (right) moment, β=120^o , U=25 [kn] , x= 155, 75 m from AP, from Senjanovic et al. (2010)

Other marine structures for specific applications such as pipelines conveying fluids, floating airplane runways, floating bridges and multihulls, e.g., trimarans, are some of the most popular designing trends calling for three – dimensional (3D) techniques.

Fig. 06 VLFS: Mega – Float at Tokyo bay

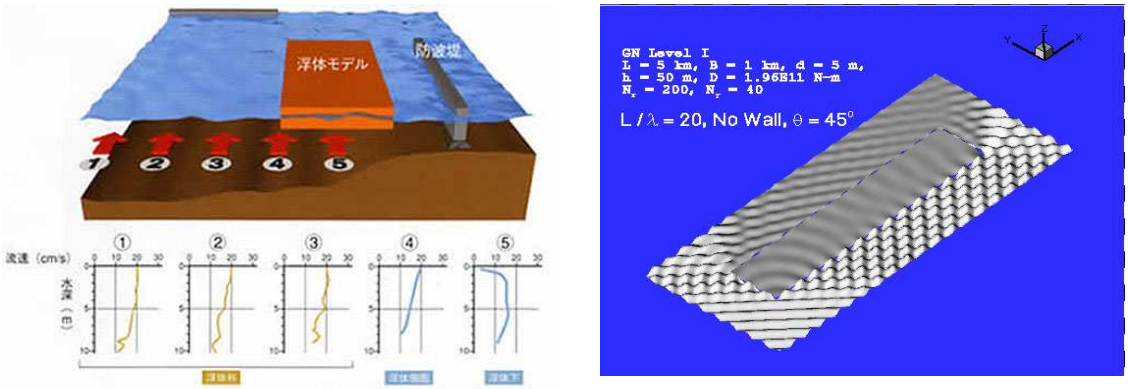

Fig. 07 (a) Velocity flow domain of the current, effects of transient bottom (left)
(b)Elastic responses of the Mega – Float structure at wave excitation (right)
(see, e.g., Wang & Wang 2015).

Given the demand for larger scale of different type of ships, which grow in numbers, models with higher requirements are on the rise. Regarding the advances in the hydroelastic theory, the last 30 years, significant enhancements provide us with new means to treat either the 2D or the 3D problem. Calculations concerning symmetric (vertical bending), antisymmetric (coupled horizontal bending and twisting), and unsymmetric (coupled vertical and horizontal bending and twisting) distortions together with the prediction of the responses due to slamming excitation are just some of the problems tackled by the developed 2D models. The associated non – linear phenomena involved in large motions of the large marine structures have been successfully treated by contemporary 3D modeling by means of Finite Element Method (FEM) and Computational Fluid Dynamics (CFD) techniques.

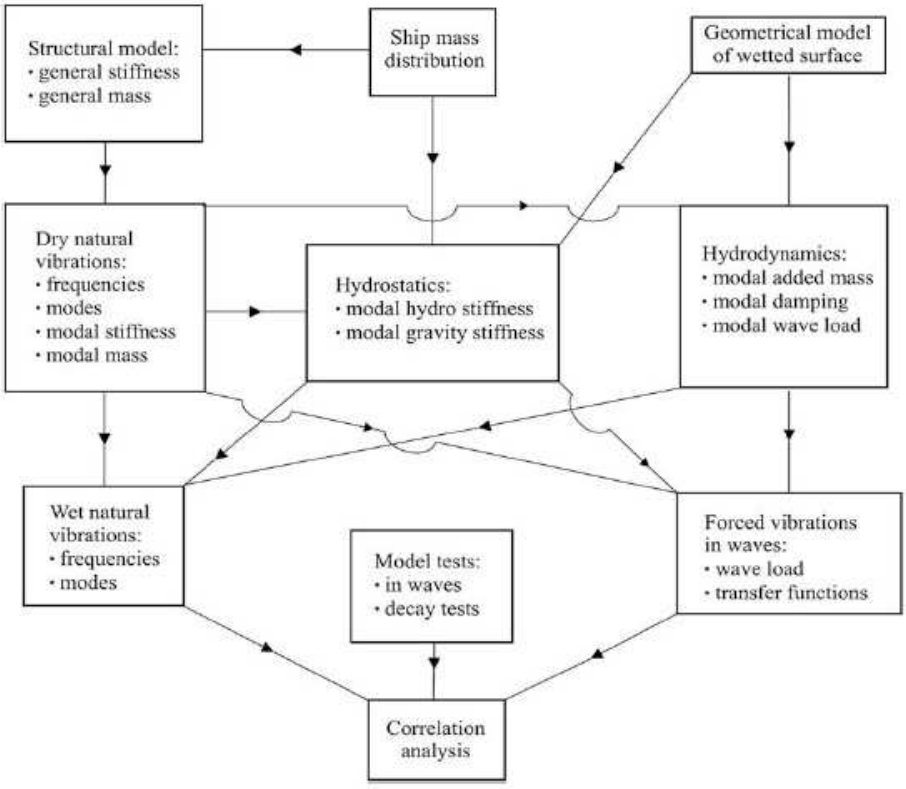

Fig. 08 Illustration of modern hydroelastic analysis, from Senjanovic et al. (2008)

In previous years, the conduction of tests for the elastic model of the S175 container ship has been included in the work by Chen et al. (1999); see, also, Watanabe et al. (1989). More recently, Remy et al. (2006) have conducted tests for a flexible barge based on the work of Malenica et al. (2003) and on the theoretical model of Ledoux et al. (2004). The barge model has been constructed by twelve rigid pontoons connected via a steel rod, and the conducted tests have focused on the investigation of the structural behavior under vertical bending as well as under horizontal bending and torsion for heading regular and irregular waves. The results obtained by these test have been compared with a solution of the coupled wave load- ship vibrations system, which has been obtained by the use of 1D Finite Element Method analysis for the determination of the dry modes together with a 3D potential flow theory. The comparison between the test and the theoretical solution has shown good agreement between measured and simulated barge responses. However, in a retest by Malenica et al. (2007) of the latter experiment, the elastic models have been proved to be accurate enough in order to produce a unified hydroelastic prediction of the behavior of long and slender marine structures for which the amplitude ratio of the elastic and rigid modes is a bit lower. In addition, other tests have been conducted concerning the prediction of responses of two frigates as presented by Bishop et al. (1983) and Aksu et al. (1991). Last, Oka et al. (2007) and Oka et al. (2008) reported series of tests conducted on a backbone elastic model of a high speed vessel (taking also into consideration whipping vibrations) as well as for a large container carrier.

Present work

In the context of the present thesis we examine the hydroelastic responses of, long and slender, monohull marine structures in waves considering the action of vertical bending moments, which produce symmetric distortions. The calculation of the natural frequencies and the corresponding principal modes of the structure is initially based on examining the free edged thin beam, which is a common/standard approach for ships, by using "dry hull" analysis. We employ the Euler – Bernoulli and Timoshenko beam models in Chapters 1 and 2, respectively, see, e.g., Graff (1975) to calculate the structural responses of the beam by means of 1D Finite Difference formulations. The former model provides us with results concerning beams under pure bending, while the latter one incorporates the effects of shear deformations in the vertical plane (coupled system). In addition, we compare the results of the Euler – Bernoulli and Timoshenko models and we evaluate the accuracy of the two theories based on comparisons of numerical and analytical results. To better understand the use of the two models, the structural responses of different beam models are tested for specific examples, i.e., for different geometrical characteristics and types of end conditions. Results are presented in Chapters 1 and 2 concerning Euler-Bernoulli and Timoshenko beam models, respectively. Detailed comparisons are included in Appendix A.

Subsequently, in Chapter 3 the rigid responses of an elongated (long and slender) marine structure travelling in deep water with steady mean forward speed U in head or following incident waves are calculated by means of strip theory in the context of the potential flow. Head seas are considered most important from point the point of view of the severity of wave induced loads affecting the overall performance of the ship. The assessment of the ship hydrodynamic properties (added mass and damping coefficients, and generalized hydrodynamic forces) are calculated by the celebrated STF strip theory model (Salvensen et al 1970) using systematic sectional results that are obtained by means of Boundary Element Method (BEM). In this method the wet surface of the ship is divided into a number of strips (transverse sections of local characteristics) and then a 2D, linearized, potential flow analysis is applied to the local hydrodynamic problem for each strip. Potential flow analysis is used in conjunction with linearized boundary conditions obtained on the basis of assumptions concerning small wave amplitudes, small perturbation of the flow due to the ship forward motion and also small oscillatory ship motions. The present BEM applied to treat the sectional problems in deep water conditions is based on low order panels with continuous source-sink distribution, in conjunction with an absorbing layer technique to treat radiation conditions at appropriate distances of adequate wave lengths away of each body strip/section. Details concerning the method are presented in Appendix B. Then, the calculated sectional results of various quantities, including added mass, damping, Froude - Krylov and diffraction forces are integrated alongships to obtain the 3D hydrodynamic coefficients and exciting forces and moments. Using the latter results the system of dynamic equations is solved and the ship's responses are derived.

In the Chapter 4 the above model is extended to treat the problem of hydroelastic responses of a beamlike elongated marine structure and derive information concerning the elastic responses associated with flexural vertical vibrations in waves. In particular, a strip hydroelastic model is developed by exploiting the hull girder vertical dry modes and by using the additional elastic forces beyond those related to

inertia, damping and hydrostatic terms of a linear oscillator. Results are obtained for a particular floating structure (elastic barge) in waves and compared against measured data from model tests presented by Remy et al. 2006, Malenica et al. 2003. The hull form under investigation has specific geometry, mass and flexural rigidity distribution and the experiment concerns a flexible barge with transverse plane symmetry designed to permit hydroelastic phenomena at zero speed.

Finally, conclusions and proposals for future work and further extensions are presented and discussed.

Chapter 1

The Euler-Bernoulli Beam Model

1.1 Introduction to the Euler – Bernoulli model

We start the present work by studying the linear model presented by the Euler-Bernoulli (EB) beam and its full mechanics. We assume the steady state problem with respect to a harmonic forcing; thus, we consider the harmonic character of the solution corresponding to any permissible given frequency.

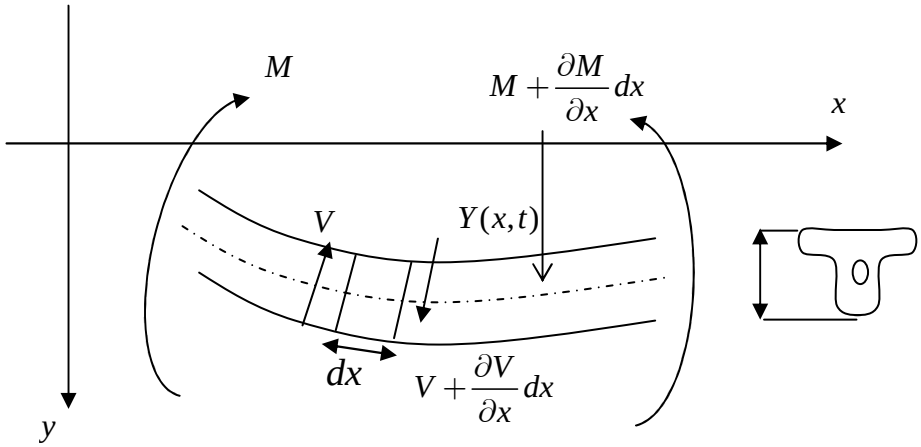

Fig. 1. Thin beam undergoing transverse oscillations [$y(x,t)$]

The governing equation describing the motion of a thin beam forced by bending moment, $M(x)$, in the context of Euler-Bernoulli theory, is given by the following equation see, .e.g., Graff (1975, Ch.3),

$$D(x)\frac{\partial^4 y(x,t)}{\partial x^4}+m(x)\frac{\partial^2 y(x,t)}{\partial t^2}=q(x,t), \qquad (1)$$

where $D(x)=EI(x)$ is the modulus of rigidity of the beam, E *is* the Young modulus of the material, and $I(x)$ is the moment of inertia of the cross section of the beam at each longitudinal position x; see Fig.1. Also, $m(x)$ is the linear mass density of the beam. For uniformly compact beams, it holds $m(x)=\rho_{\mathrm{E}}A(x)$, where ρ_{E} is the constant density of the material, and $A(x)$ is the area of the cross section of the beam at each longitudinal position x. The term $q(x,t)$ denotes the distribution of imposed forces, and the term $M(x)$ denotes the longitudinal bending moment.

Thin beam theory provides a methodology which, in its range of applicability, allows the analysis of structures in a simplified yet efficient way. Its basic characteristics are (**i**) linear mass density and linear bending stiffness, (**ii**) shear deformation is considered to be zero during pure bending. Consequently, (**iii**) the cross section areas remain always planar and the neutral axis passes through the centroid of the cross section area of the beam. Also, the motion of the beam lies on the $xy-$plane only, while cross section areas are considered to be symmetric Finally, within the confines of linear elastic behavior, (**iv**) we assume transverse deformations and slopes to be small.

The shear force, as provided by integrating the elastic line equation, is

$$V(x) = \frac{dM(x)}{dx} \ . \tag{2}$$

Focusing on the steady state linear problem we can examine free harmonic oscillations of the thin beam. Therefore, we eliminate the time dependence using complex amplitude technique. Hence, the representation of the flexural deflection can be written as follows

$$y(x,t) = \mathrm{Re}\left(\overset{\circ}{y}(x) e^{-j\omega t} \right) , \tag{3}$$

where the over-circle denotes the complex amplitude of the corresponding quantity, $\mathrm{Re}(\cdot)$ denotes the real part of the complex quantity, and $j = \sqrt{-1}$ is the imaginary unit.

Consequently, equation (1) takes the following form

. $$D(x)\frac{\partial^4 \overset{\circ}{y}(x)}{\partial x^4} + m(x)\omega^2 \overset{\circ}{y}(x) = \overset{\circ}{q}(x) \ . \tag{4}$$

To find the natural modes of the thin beam we must consider the corresponding homogeneous version of (4), which is:

$$D(x)\frac{\partial^4 \overset{\circ}{y}(x)}{\partial x^4} + m(x)\omega^2 \overset{\circ}{y}(x) = 0 \ . \tag{5}$$

The calculation of the eigenvalues (eigenfrequencies) and the corresponding eigenfunctions (mode shapes) of the model expressed by Eqn. (5) imposes the consideration of adequate boundary conditions Eqn. (5) can be solved using different boundary conditions, which in turn correspond to different practical problems. Thus, the mathematical formulas for the free-free, pinned-pinned and clamped–clamped type of boundary conditions are investigated in this present work, expressed by the following equations

Free – Free Boundary Conditions

Concerning the free type of edges, the bending moment and shear force are zero, $M = 0$ and $V = 0$ respectively, at the ends of the beam, i.e.:

$$\partial^2_{,x} y(x=0) = \partial^3_{,x} y(x=0) = 0 \ , \tag{6a}$$

$$\partial^2_{,x} y(x=L) = \partial^3_{,x} y(x=L) = 0 \ . \tag{6b}$$

Clamped – clamped Boundary Conditions

The boundary condition at the ends of the beam meet the necessities of $Y = 0$ and $Y' = 0$, which are expressed as follows

$$y(x = 0) = \frac{dy(x = 0)}{dx} = 0 \ , \tag{7a}$$

$$y(x = L) = \frac{dy(x = L)}{dx} = 0 \ . \tag{7b}$$

Pinned – pinned Boundary Conditions

The end conditions in this last case, are $Y = 0$ and $M = 0$. More specifically

$$y(x = 0) = \frac{d^2 y(x = 0)}{dx^2} = 0 \ , \tag{8a}$$

$$y(x = L) = \frac{d^2 y(x = L)}{dx^2} = 0 \ . \tag{8b}$$

The boundary conditions (6)-(8) are also presented in the following table

Type of edge	*position*	*slope*	*Moment*	*Shear Force*
Free			$y'' = 0$	$y''' = 0$
Clamped	$y = 0$	$y' = 0$		
Pinned	$y = 0$		$y'' = 0$	

Table 1. Boundary Conditions for model (5)

In the section that follows, a numerical method based on finite differences (FDM) is developed and is applied to the solution of the above eigenvalue problems for a general Euler-Bernoulli beam and all combinations of boundary conditions; see Table 1. The code implementation of the method has been built using Matlab®. The numerical results are compared with the analytical solution in the cases of a homogeneous and inhomogeneous beam (square cross section) and rod (circular cross section) (which is listed in Appendix A) for validation purposes.

1.2 Analytical modeling of the Euler - Bernoulli beam

The general homogeneous solution of the equation (1.1.5) is (Graff 1975 , Ch.3)

$$Y(x;t) = C_1 \cos(\beta \mathrm{x}) + C_2 \cosh(\beta \mathrm{x}) + C_3 \sin(\beta \mathrm{x}) + C_4 \sinh(\beta \mathrm{x}) \ , \qquad (1)$$

where C_i, $i = 1,\ldots,4$, are constants representing the amplitude of the corresponding harmonic term and β is the wave number. In order to satisfy the given boundary conditions we form the first, the second and the third order derivative of $Y(x;t)$ as follows:

$$\partial_{,x} Y(x;t) = -C_1 \beta \sin(\beta \mathrm{x}) + \mathrm{C}_2 \, \beta \sinh(\beta \mathrm{x}) + \mathrm{C}_3 \, \beta \cos(\beta \mathrm{x}) + \mathrm{C}_4 \, \beta \cosh(\beta \mathrm{x}) \ , \qquad (2)$$

$$\partial^2_{,x} Y(x;t) = -C_1 \beta^2 \cos(\beta \mathrm{x}) + \mathrm{C}_2 \, \beta^2 \cosh(\beta \mathrm{x}) - \mathrm{C}_3 \, \beta^2 \sin(\beta \mathrm{x}) + \mathrm{C}_4 \, \beta^2 \sinh(\beta \mathrm{x}) \ , \qquad (3)$$

$$\partial^3_{,x} Y(x;t) = C_1 \beta^3 \sin(\beta \mathrm{x}) + \mathrm{C}_2 \, \beta^3 \sinh(\beta \mathrm{x}) - \mathrm{C}_3 \, \beta^3 \cos(\beta \mathrm{x}) + \mathrm{C}_4 \, \beta^3 \cosh(\beta \mathrm{x}) \ . \qquad (4)$$

Free – Free Boundary Conditions

Using the boundary conditions (3, 4) , in eq. (1) we obtain the analytical expressions for free edges of the beam, i.e.,

$$\partial^2_{,x} Y(x = 0;t) = -C_1 \beta^2 \cos(0) + \mathrm{C}_2 \, \beta^2 \cosh(0) - \mathrm{C}_3 \, \beta^2 \sin(0) + \mathrm{C}_4 \, \beta^2 \sinh(0) = 0 \, , \qquad (5)$$

$$\partial^3_{,x} Y(x = 0;t) = C_1 \beta^3 \sin(0) + \mathrm{C}_2 \, \beta^3 \sinh(0) - \mathrm{C}_3 \, \beta^3 \cos(0) + \mathrm{C}_4 \, \beta^3 \cosh(0) = 0 \ , \qquad (6)$$

$$\partial^2_{,x} Y(x = L;t) = -C_1 \beta^2 \cos(\beta L) + \mathrm{C}_2 \, \beta^2 \cosh(\beta L) - \mathrm{C}_3 \, \beta^2 \sin(\beta L) + \mathrm{C}_4 \, \beta^2 \sinh(\beta L) = 0 \, , \qquad (7)$$

$$\partial^3_{,x} Y(x = L;t) = C_1 \beta^3 \sin(\beta L) + \mathrm{C}_2 \, \beta^3 \sinh(\beta L) - \mathrm{C}_3 \, \beta^3 \cos(\beta L) + \mathrm{C}_4 \, \beta^3 \cosh(\beta L) = 0 \, , \qquad (8)$$

or equivalently, in matrix formulation,

$$\underbrace{\begin{pmatrix} -\beta^2 & \beta^2 & 0 & 0 \\ 0 & 0 & -\beta^3 & \beta^3 \\ -\beta^2 \cos(\beta L) & \beta^2 \cosh(\beta L) & -\beta^2 \sin(\beta L) & \beta^2 \sinh(\beta \mathrm{L}) \\ \beta^3 \sin(\beta \mathrm{L}) & \beta^3 \sinh(\beta \mathrm{L}) & -\beta^3 \cos(\beta \mathrm{L}) & \beta^3 \cosh(\beta \mathrm{L}) \end{pmatrix}}_{\boldsymbol{A}} \cdot \underbrace{\begin{pmatrix} C1 \\ C2 \\ C3 \\ C4 \end{pmatrix}}_{\boldsymbol{B}} = 0 \ .$$

The characteristic polynomial associated with matrix $\boldsymbol{A}$ of the homogeneous system above is, see, e.g. Graff (1975, Ch.3), Georgiou (2008, Ch.10) :

$$p(\beta L) = 2\beta^{10}\left(\cos(\beta L)\cosh(\beta L) - 1\right) \ . \qquad (9)$$

The characteristic roots of (9), are found by solving the equation

$$p(\beta L)=0 \;\Leftrightarrow\; \cos(\beta L)\cosh(\beta L)=1 \tag{10}$$

For the calculation of the roots, a numerical method also known as ‘’Newton-Raphson’’ is used. The analytical expression of the eigenfrequencies is

$$\omega_n=\left[\frac{\beta_n L}{L}\right]^2\sqrt{\frac{E\,\mathrm{I}}{\rho \mathrm{A}}}\ , \qquad n=1,2,\ldots\ . \tag{11}$$

Next, we proceed with the specification of the coefficients $C_i \quad i=1,\ldots,4$, in (1). By virtue of (5)-(8), we obtain

$$C_1=C_2 \qquad \text{and} \qquad C_3=C_4\,.$$

Thus,

$$C_1\left[-\cos(\beta_n L)+\cosh(\beta_n L)\right]+C_3\left[\sinh(\beta_n L)-\sin(\beta_n L)\right]=0\ , \tag{12a}$$

$$C_1\left[\sin(\beta_n L)+\sinh(\beta_n L)\right]+C_3\left[\cosh(\beta_n L)-\cos(\beta_n L)\right]=0\ , \tag{12b},$$

the latter Eqns. (12a-b) being equivalent.

Using eqn. (12a) or (12b) we introduce coefficient, C_A, as follows

$$C_A=\frac{C_3}{C_1}=\frac{\cos(\beta_n L)-\cosh(\beta_n L)}{\sinh(\beta_n L)-\sin(\beta_n L)}=-\frac{\sin(\beta_n L)+\sinh(\beta_n L)}{\cosh(\beta_n L)-\cos(\beta_n L)}\ . \tag{13}$$

Hence, the eqn. (1) becomes

$$Y_n(x)=C_1\left[\cos(x)+\cosh(x)+C_A\left[\sin(x)+\sinh(x)\right]\right]\ , \tag{14}$$

where C_1 is an undetermined coefficient. Thus we consider the non-dimensional version of (14):

$$Y_n(x)=\cos(x)+\cosh(x)+C_A(\sin(x)+\sinh(x))\ , \tag{15}$$

It should be noted that the modes $Y_n(x)$ are orthogonal. The normalized form of (14) is given by:

$$\hat{Y}_n(x)=\frac{Y_n(x)}{\left\|Y_n(x)\right\|}\ , \tag{16}$$

where $\left\|Y_n(x)\right\|$ is the norm

$$\left\|Y_n(x)\right\|=\sqrt{\int_0^L\left\{Y_n(x)\right\}^2 dx}\ . \tag{17}$$

The integral, $\int_0^L \{Y_n(x)\}^2 dx$, in the developed program ''EBT.m'', is calculated through the trapezoidal rule.

Given the group $Y_n(x)$, $\{Y_n(x),\ n=1,2,3..\}$ in the domain $-L \le x \le L$, the inner product provides us with the following result

$$\langle Y_n, Y_m \rangle = \int_{-L}^{L} Y_n Y_m dx \ . \tag{18}$$

If the functions are orthogonal over the domain $[-L, L]$, it is shown that, see, e.g., Boyce & Diprima (Ch. 10),

$$\langle Y_n, Y_m \rangle = 0 \qquad n \neq m, \tag{19a}$$

$$\langle Y_n, Y_n \rangle = L. \qquad n = m. \tag{19b}$$

Using the Dirac function, δ_{nm}, over the beam's length $[0, L]$, we obtain the alternative orthogonality schema

$$\langle Y_n, Y_m \rangle = \delta_{nm} \begin{cases} 0, & n \neq m \\ 1, & n = m \end{cases} . \tag{19c}$$

Hence, the function $Y_n(x)$ are an orthogonal basis. Furthermore, every function $f(x)$, which is defined on $[0, L]$, can be represented by a basis of the domain as follows

$$f(x) = \sum_{n=1}^{\infty} f_n Y_n(x), \quad x \in [0, L] \ ,$$

where,

$$f_n = \langle f(x), Y_n(x) \rangle \tag{20}$$

To enhance the orthogonality property for singular functions we begin by presenting the Dirac delta function at the point x_0, through the formula

$$\delta(x - x_0) = \sum_{n=1}^{\infty} \delta_n Y_n(x). \tag{21a}$$

Let δ_n be the inner product at $x = x_0$

$$\delta_n = \int_0^L \delta(x - x_0) Y_n(x_0) dx,$$

where

$$Y_n(x_0)\int_0^L \delta(x-x_0)dx \;=\; Y_n(x_0)\,, \qquad x=x_0\;.$$

Thus, the general form is

$$\delta(x-x_0)=\sum_{n=1}^{\infty} Y_n(x_0)Y_n(x)\,. \tag{21b}$$

To expand the previous results for other singular functions $f(x)$, at $x=x_0$, the schema to be used is

$$\int_0^L f(x)\delta(x-x_0)dx\;. \tag{22}$$

Applying (21b), the eqn. (22) is now changed to

$$\int_0^L f(x)\sum_{n=1}^{\infty} Y_n(x_0)Y_n(x)dx=\sum_{n=1}^{\infty} Y_n(x_0)\big\langle f(x),Y_n(x)\big\rangle dx\,.$$

Finally, using eqn. (20), the latter provides with the following result

$$\sum_{n=1}^{\infty} f_n Y_n(x_0)dx= f(x_0)\,. \tag{23}$$

Solving the equivalent system of equations for the clamped-clamped and pinned-pinned type of edges, we take the corresponding coefficients and the non-dimensional motion equations

Pinned-Pinned Boundary Conditions

The frequency equation meeting the pinned type of edges, is

$$p(\beta L)=0 \;\Leftrightarrow \sin(\beta L)=0\ , \tag{24}$$

see, e.g. Graff (1975, Ch.3).

To determine the natural frequencies using the roots βL, is based on the analytic expression

$$\omega_n=\left[\frac{\beta_n L}{L}\right]^2\sqrt{\frac{E\,\mathrm{I}}{\rho \mathrm{A}}}\ . \qquad n=1,2,\dots\ . \tag{25}$$

The solution of the system associated with the boundary conditions (1.1.8a), (1.1.8b) provides us with the coefficients of eq. (1)

$$C_1=C_2=C_4=0\,.$$

The corresponding non-dimensional form of the equation (1), is proved to be

$$Y_n(x)=\sin(x)\ , \tag{26}$$

Clamped-Clamped Boundary Conditions

Finally, the homogeneous system associated with the clamped type of edges leads to the frequency equation

$$p(\beta L)=0 \;\Leftrightarrow \cos(\beta L)\cosh(\beta L)=1\ , \tag{27}$$

which is identical to the one obtained from the free type of edges, see, e.g. Graff (1975, Ch.3). Using the Newton - Raphson, numerical, method we obtain the characteristic roots βL, which in turn are used to define the frequencies based on equation:

$$\omega_n=\left[\frac{\beta_n L}{L}\right]^2\sqrt{\frac{E\,\mathrm{I}}{\rho \mathrm{A}}}\ , \qquad n=1,2,\dots\ . \tag{28}$$

The system formulated by the boundary conditions (1.1.7a)-(1.1.7b) specifies the coefficients of the motion eq. (1) as follows

$$C_1=-C_2$$

$$C_3=-C_4$$

$$C_1\left[\cos(\beta_n L)-\cosh(\beta_n L)\right]+C_3\left[\sin(\beta_n L)-\sinh(\beta_n L)\right]=0\,, \tag{29}$$

$$-C_1\left[\sin(\beta_n L)+\sinh(\beta_n L)\right]+C_3\left[\cos(\beta_n L)-\cosh(\beta_n L)\right]=0\,. \qquad (30)$$

We calculate the coefficient:

$$C_A=\frac{C_3}{C_1}=-\frac{\cos(\beta_n L)-\cosh(\beta_n L)}{\sin(\beta_n L)-\sinh(\beta_n L)}\ , \qquad (31)$$

and the corresponding motion eqn. (1) is :

$$Y_n(x)=\cos(x)-\cosh(x)+C_A(\sin(x)-\sinh(x))\,, \qquad (32)$$

The investigation of the divergence between the normal modes derived from the numerical and the analytical solution consists of severe importance and will be illustrated in Appendix A.

1.3 Euler - Bernoulli modeling using Finite Difference Method

For the appropriate implementation of the Finite Differences Method (FDM), the discretization of the problem is necessary, through a suitable grid definition. Hence, we consider a discretization of the beam into a number of N elements of equal length $\Delta x=\frac{L}{N}$, defined by a set of $N+1$ points. For the domain $[0,L]$, we define the nodal points $\left\{x_i, y_i=y(x_i), i=1,2,...,N+1\right\}$ as depicted in the following figure,

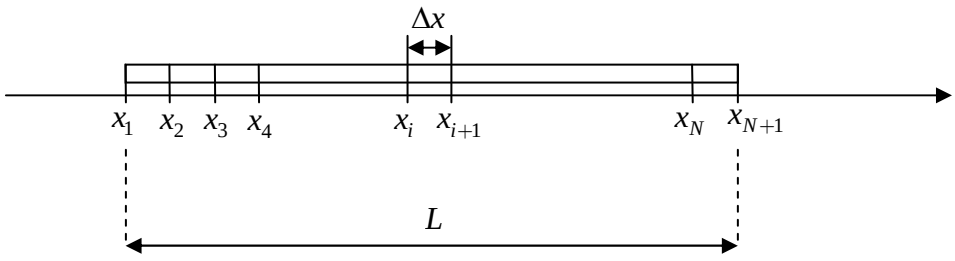

Fig. 1. Grid points

Thus, eqn. (1.1.5) is considered using its discrete analogue, which is presented by the linear form $A\boldsymbol{u}=F$, where matrix $A=[N\times N]$ is a banded one and its bandwidth depends on the order of the derivative. For a first order derivative a tridiagonal table is formed (see figure 2), in which all non-zero elements are placed in the main diagonal and in its two adjacent sub-diagonals:

$$A=\begin{pmatrix} a_{11} & a_{21} & & & 0 \\ a_{12} & \ddots & & & \\ & & & \ddots & \\ & & \ddots & & a_{N\,N+1} \\ 0 & \ddots & & a_{N+1\,N} & a_{N+1\,N+1} \end{pmatrix}$$

Fig. 2. Banded (tridiagonal) table

Thus, the higher the order derivative we approximate, the more banded the table becomes. Setting a smaller [(1)] step (Δx) we increase the size of the table A and in parallel we have a better description of the specific domain.

The discretization scheme for the Euler-Bernoulli equation is materialized by using second-order, central finite differences. Thus, first and second order derivatives of the deflection are approximated by the following formulas

$$y'(x_i) = \frac{y_{i+1} - y_{i-1}}{2\Delta x} + O(\Delta x)^2 \quad , \tag{1}$$

$$y''(x_i) = \frac{y_{i+1} - 2y_i + y_{i-1}}{\Delta x^2} + O(\Delta x)^2 \quad . \tag{2}$$

By virtue of the above equations, the calculation of the values at the nodes $x = x_1$ and $x = x_{N+1}$ needs a special treatment. An appropriate modification is used, based on the forward finite differences scheme at $x = x_1$ with a second order accuracy

$$y'(x_1 = 0) = \frac{-y_3 + 4y_2 - 3y_1}{2\Delta x} + O(\Delta x)^2 , \tag{3}$$

$$y''(x_1 = 0) = \frac{-y_4 + 4y_3 - 5y_2 + 2y_1}{\Delta x^2} + O(\Delta x)^2 , \tag{4}$$

$$y^{(3)}{}_{,x}(x_1 = 0) = \frac{-3y_5 + 14y_4 - 24y_3 + 18y_2 - 5y_1}{2\Delta x^3} + O(\Delta x)^2 , \tag{5}$$

and the backward finite differences scheme, at $x = x_{N+1}$

$$y'(x_{N+1} = L) = \frac{y_{N-1} - 4y_N + 3y_{N+1}}{2\Delta x} + O(\Delta x)^2 , \tag{6}$$

$$y''(x_{N+1} = L) = \frac{-y_{N-2} + 4y_{N-1} - 5y_N + 2y_{N+1}}{\Delta x^2} + O(\Delta x)^2 , \tag{7}$$

$$y^{(3)}{}_{,x}(x_{N+1} = L) = \frac{3y_{N-3} - 14y_{N-2} + 24y_{N-1} - 18y_N + 5y_{N+1}}{2\Delta x^3} + O(\Delta x)^2 \tag{8}$$

respectively.

[(1)] A smaller step (Δx) than the initially used, $\Delta x = L / N$, is achieved by increasing the number, N, of the elements.

At this point we grab the chance to investigate the method's consistency. Consistency of the numerical procedure is a property related to the discrepancy of the numerical solution against the exact one, see, Akrivis, Dougalis (1997). The term $O(\Delta x)^2$ in the above eqns. (1-8), constitutes the error of the numerical method and on the step, Δx used to discretize the domain.

More specifically, given a function $y(x) \in C^4[a,b]$, $x \in (a,b)$ and $\Delta x > 0 : x + \Delta x, x - \Delta x \in [a,b]$ we calculate the Taylor series of eqn. (1) as follows

$$u(x+\Delta x) = u(x) + \Delta x \frac{\partial u(x)}{\partial x}_i + \frac{\Delta x^2}{2}\frac{\partial^2 u(x)}{\partial x^2} + \frac{\Delta x^3}{6}\frac{\partial^3 u(x)}{\partial x^3} + \frac{\Delta x^4}{24}\frac{\partial^4 u(x_1)}{\partial x^3},$$

$$u(x-\Delta x) = u(x) - \Delta x \frac{\partial u(x)}{\partial x}_i + \frac{\Delta x^2}{2}\frac{\partial^2 u(x)}{\partial x^2} - \frac{\Delta x^3}{6}\frac{\partial^3 u(x)}{\partial x^3} + \frac{\Delta x^4}{24}\frac{\partial^4 u(x_2)}{\partial x^3},$$

where $x_1, x_2 \in (x - \Delta x, x + \Delta x)$. If we sum up the previous equations the approximation for the first and second order derivative becomes:

$$\left| \frac{u(x+\Delta x) - u(x-\Delta x)}{\Delta x} - u'(x_1) \right| \le \frac{\Delta x^2}{3} \max \left| u^{(3)}(x_3) \right|_{a \le x_3 \le b}$$

and

$$\left| \frac{u(x-\Delta x) - 2u(x) + u(x+\Delta x)}{\Delta x^2} - u''(x_1) \right| \le \frac{\Delta x^2}{12} \max \left| u^{(4)}(x_3) \right|_{a \le x_3 \le b},$$

respectively.

Let $C_1 = \max \left| u^{(3)}(x_3) \right|_{a \le x_3 \le b}$, $C_2 = \max \left| u^{(4)}(x_3) \right|_{a \le x_3 \le b}$, then the quantity on the right- hand side of each inequality is the maximum error of the approximation (finite difference method) , see also, Akrivis, Dougalis (1997, Ch.6). The first and the second order derivative in its discretized form is

$$\left| \frac{u_{i+1} - u_{i-1}}{\Delta x} - u_i' \right| \le C_1 \frac{\Delta x^2}{3}$$

$$\left| \frac{u_{i-1} - 2u_i + u_{i+1}}{\Delta x^2} - u_i'' \right| \le C_2 \frac{\Delta x^2}{12}.$$

Though, the convergence of the numerical solution (and the quality of the corresponding results) is strongly dependent on the elimination of the error factor. Hence, in the case of a dense partitioning, we assume that the error is too small and practically is negligible when $O(\Delta x)^2 \to 0$.

Since all the parameters have been defined, we proceed with the presentation of the modified version of the finite differences scheme that replaces the beam equation

(1.1.5). We consider a homogeneous beam version, where $D(x)=EI(x)=D=ct.$ is the constant modulus of rigidity of the beam. Also, $m(x)=m=ct.$ is the constant mass density of the beam. The number of the given equations to be solved is equal to the number of the nodes. The homogeneous equation (1.1.5) can be written as follows

First, we use the following notation

$$G(x) \;=\; D\frac{d^2y}{dx^2}\;, \tag{9}$$

$$\frac{d^2G(x)}{dx^2}+m\omega^2\,\mathring{y}(x)=0\;. \tag{10}$$

The finite difference scheme for (9) is written

$$\frac{d^2\,\mathrm{G}(x)}{dx^2}\approx\frac{G_{i+1}-2G_i+G_{i-1}}{dx^2}=\frac{Dy_{i+2}-4Dy_{i+1}+6Dy_i-4Dy_{i-1}+Dy_{i-2}}{dx^2}, \tag{11}$$

Also, the term

$$M\omega^2\;\mathbf{y}(x)\approx M\omega^2\;y_i\;. \tag{12}$$

Replacing the schemes (11, 12) into equation (1.5), its discrete version, becomes

$$\frac{1}{dx^2}\left[Dy_{i+2}-4Dy_{i+1}+(6D+M_i\omega^2)y_i\;-4Dy_{i-1}+Dy_{i-2}\right]=0\;. \tag{13}$$

1.4 Numerical code implementation

The solution of y can be expressed in matrix form and the dimensions of the matrices are defined by the number of the nodes as it is mentioned before. We set the table form of the problem and so the linear expression of the system is:

$$\sum_{j=1}^{N+1}A_{ij}y_j-\lambda y_j=0\,,\;\left\{\lambda_n=\omega_n^2,\;\mathbf{y}_n=y_i^{(n)},\quad n=1,2,3,.....\right\}, \tag{1}$$

The eigenfrequencies can be specified by solving the previous homogeneous system. Matrix A appearing in (1) is a banded (pentadiagonal) matrix, as mentioned in Ch.1.3.

Considering various types of boundary conditions, see Table 1 in Ch.1.1, and their analytical representation in Eqns. (1.3.1-1.3.8), we obtain the following cases for the construction of matrix A:

Clamped edges

$$A=\begin{pmatrix} 1 & 0 & 0 & \cdots & & \\ -1.5/dx & 2/dx & -0.5/dx & & 0 & \\ \ddots & & \ddots & & \ddots & \\ & & 0.5/dx & 2/dx & -1.5/dx & \\ 0 & & \cdots & 0 & 0 & 1 \end{pmatrix}$$

Free edges

$$A=\begin{pmatrix} 2/dx^2 & -5/dx^2 & 4/dx^2 & -1/dx^2 & 0 & \cdots & & & \\ -2.5/dx^3 & 9/dx^3 & -12/dx^3 & 7/dx^3 & -1.5/dx^3 & & & 0 & \\ & \ddots & & & \ddots & & & \ddots & \\ 0 & & & -1.5/dx^3 & -7/dx^3 & 12/dx^3 & -9/dx^3 & 2.5/dx^3 & \\ & & \cdots & 0 & -1/dx^2 & 4/dx^2 & -5/dx^2 & 2/dx^2 & \end{pmatrix}$$

Pinned edges

$$A=\begin{pmatrix} 1 & 0 & 0 & \cdots & & \\ 2/dx^2 & -5/dx^2 & 4/dx^2 & -1/dx^2 & 0 & \\ \ddots & & \ddots & & \ddots & \\ & & -1/dx^2 & 4/dx^2 & -5/dx^2 & 2/dx^2 \\ 0 & & \cdots & 0 & 0 & 1 \end{pmatrix}$$

All the remaining cells of table A are supplemented with the coefficients of eqn. (1.3.11). Now that the tables are set, we calculate the eigenfrequencies using a simple method. The first step is to set a big range of frequencies, ω , and search for the roots in it, using an iterative process. Replacing each value of the range into the equation $Ay-\omega^2 y$ we find all those frequencies that eliminate the equation. Those frequencies are called the 'natural frequencies' of the transverse oscillation of the homogeneous thin beam.

Both numerical and analytical solutions have been examined and are presented in the Appendix A. In the next chapter we examine the beam case using the Timoshenko model.

Chapter 2

The Timoshenko Beam Model

2.1 Introduction to the Timoshenko beam

So far, we have examined the simplified model of a thin beam based on the Euler Bernoulli Theory (EBT). An important and widely adopted enhance of EBT is referred as Timoshenko Beam Theory (TBT), in which a correction for the shear deformation is taken into account in parallel with the effects of the rotary-inertia. The basic assumptions govern TBT approach are: (i) Thin beam theory, (ii) linear mass distribution and linear bending stiffness, (iii) planar sections remain planar while bending, (iv) we assume transverse deformations and slopes to be small, and (v) the neutral axis no longer passes through the centroid of each section, thus shear deformation is observed. Shear deformation is caused by pure bending and not from additional kinematic condition, such as torsion. Obviously, assumptions (iii) and (iv) impose the departure from EBT. Additionally, both EBT and TBT examine planar deformations. Therefore, the motion of the beam lies on the $xy-\text{plane}$ only, while cross section areas are considered to be symmetric. Also, the basic differences of TBT as compared to EBT approach are: (**d1**) the neutral axis no longer passes through the centroid of each section, and thus shear deformation is observed, and (**d2**) rotary-inertia is no longer negligible. Finally, the forces acting on the beam are: the bending moment, M, the shear force, V, and the distribution of imposed forces, q.

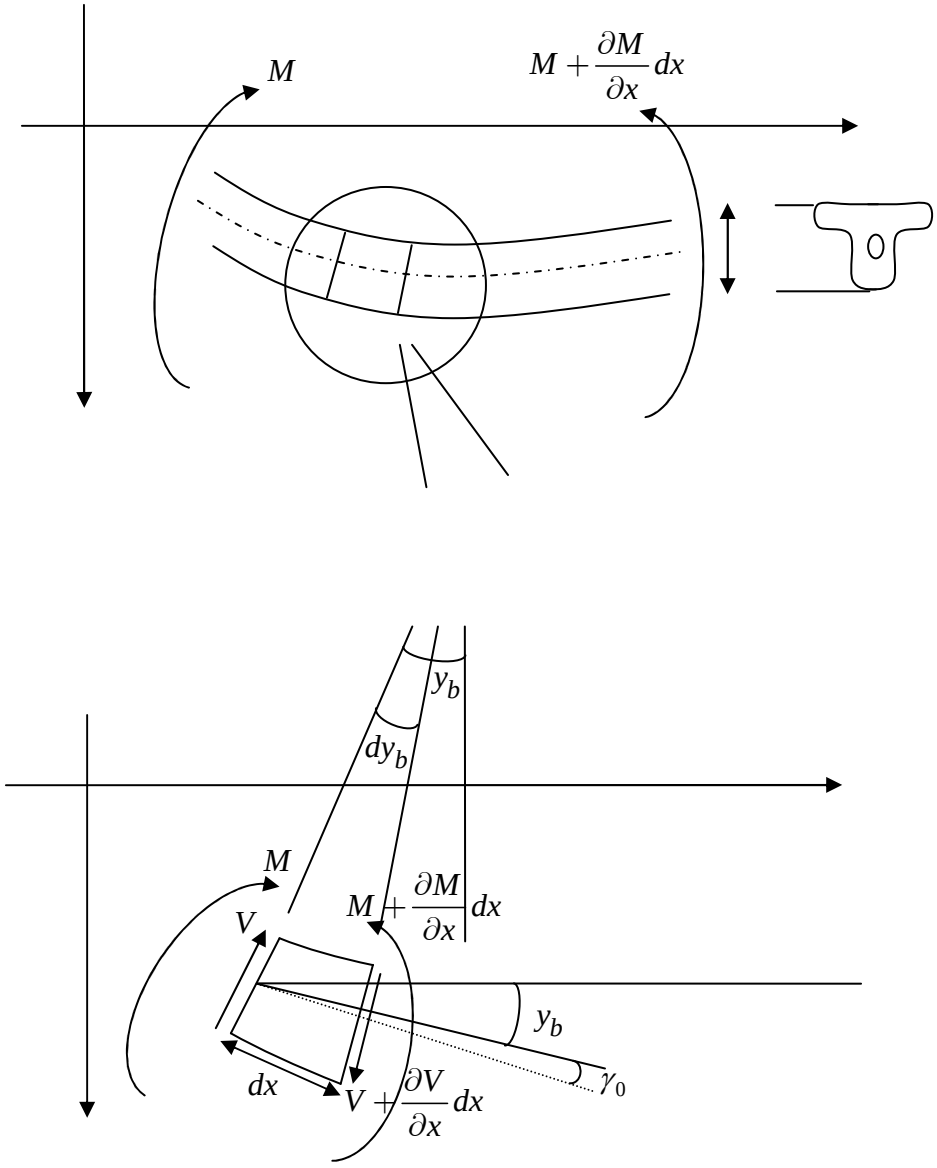

Fig. 1. Forces acting on the cross section area (Timoshenko model).

The deformations of the beam are now described by two equations with respect to both, bending and shear effects. The two, coupled governing equations, are

$$GA(x)K\left(\frac{\partial y(x,t)}{\partial x}-y_b\right)+D(x)\frac{\partial^2 y_b(x,t)}{\partial x^2}-\rho I(x)\frac{\partial^2 y_b(x,t)}{\partial t^2}=0\ , \tag{1}$$

$$GA(x)K\left(\frac{\partial y_b(x,t)}{\partial x}-\frac{\partial^2 y(x,t)}{\partial x^2}\right)+m(x)\frac{\partial^2 y(x,t)}{\partial t^2}=q(x,t)\ , \tag{2}$$

where $EI(x)$ is the modulus of rigidity of the beam, E *is* the Young modulus of the material, and $I(x)$ is the moment of inertia of the cross section of the beam at each longitudinal position x; see Fig.1. Shear modulus, G, has been also added to the equations, depicturing the shear deformation of the thin beam. Also, $m(x)$ is the linear mass density of the beam. For uniformly compact beams, it holds $m(x)=\rho_{\mathrm{E}}A(x)$, where ρ_{E} is the constant density of the material, and $A(x)$ is the area of the cross section of the beam at each longitudinal position x. The term $q(x,t)$ denotes, again, the distribution of forces which is zero in the homogeneous scenario.

Since, the cross sectional area is no longer perpendicular to the centroidal axis, we denote the displacement of the cross section by y_b and the displacement of the centroidal axis by y.Thus, the basic equation that describes the geometrical deformation of the axis, is

$$\frac{\partial y}{\partial x}=y_b+\gamma_0, \tag{3}$$

where, γ_0, is the shear strain at the centroidal axis area, see, e.g., Graff (1975), Samouilidis (2004) and $\partial y/\partial x$ determines the slope of the centroidal axis.

2.2 Dispersion relations

Assuming harmonic responses

$$y_b(x,t)=C_1\exp\left(j\left(\kappa x-\omega t\right)\right)\ , \tag{1}$$

and

$$y(x,t)=C_2\exp\left(j\left(\kappa x-\omega t\right)\right)\ , \tag{2}$$

We denote that the coefficient κ should be treated with extra caution as it consists of the wavenumber of the harmonic propagation, in contrast to the shape-dependent coefficient K of the beam. The harmonic response of the Timoshenko beam model can be specified by its phase velocity. For the calculation of the velocity we reduce the two equation motion system, (2.1.1, 2.2.2) into a single one by considering the homogeneous problem that is $q(x,t)=0$. Differentiating the eqn. (1) with respect to

x as times as needed in order to replace the term y_b into eqn. (2), see, e.g. Graff (1975, Ch.3.4) the following non-linear equation for the displacement, $y(x,t)$, is obtained:

$$\frac{EI}{\rho A}\frac{\partial y^4(x,t)}{\partial x^4}-\left(\frac{I}{A}+\frac{EI}{GKA}\right)\frac{\partial y^4(x,t)}{\partial x^2\partial t^2}+\frac{\partial y^2(x,t)}{\partial t^2}+\frac{\rho I}{GAK}\frac{\partial y^4(x,t)}{\partial t^4}=0\ . \tag{3}$$

Replacing eqn.(2) into eqn. (3), we get

$$\left[\frac{D}{\rho A}\kappa^4 i^4-\left(\frac{I}{A}+\frac{D}{GKA}\right)\kappa^2 j^2\omega^2 j^2+\omega^2 j^2+\frac{\rho I}{GAK}\omega^4 j^4\right]\exp\left(j\left(\kappa x-\omega t\right)\right)=0\,. \tag{4}$$

Recalling that $j=\sqrt{-1}$ and $D=EI$ we replace the phase velocity $c=\frac{\omega}{\kappa}$ and so the latter equation becomes

$$\frac{EI}{\rho A}-\left[\left(\frac{I}{A}+\frac{EI}{GKA}\right)+\frac{1}{\kappa^2}\right]c^2+\frac{\rho I}{GAK}c^4=0\,. \tag{5}$$

Let $c_0=\sqrt{\frac{E}{\rho}}$ be the factor to non-dimensionalize the velocity c. For the non – dimensionalized expression of the velocity, we use the bar symbol $\bar{c}=c/c_0$ and therefore we obtain

$$\frac{EI}{\rho A c_0^4}-\left[\left(\frac{I}{A}+\frac{EI}{GKA}\right)+\frac{1}{\kappa^2}\right]\frac{c^2}{c_0^4}+\frac{\rho I}{GAK}\frac{c^4}{c_0^4}=0\Rightarrow$$

$$\bar{c}^4-\left[\left(\frac{GK}{E}+1\right)+\frac{GAK}{IE\kappa^2}\right]\bar{c}^2+\frac{GK}{E}=0\ . \tag{6}$$

Let $x=\bar{c}^2$, $\beta=-\left[\left(\frac{GK}{E}+1\right)+\frac{GAK}{IE\kappa^2}\right]$, and $\gamma=\frac{GK}{E}$, the equation (6) may be expressed as a quadratic equation in its typical form, $x^2+\beta x+\gamma=0$. Calculating the discriminant of the problem, $\Delta=\beta^2-4\gamma$, only the positive roots are acceptable. Hence, the positive root we are interested in is

$$\bar{c}=\sqrt{x}=\sqrt{\frac{-\beta-\sqrt{\Delta}}{2}} \tag{7}$$

We also calculate the phase velocity of the Euler-Bernoulli model for comparison purposes with the Timoshenko beam model which involves beam shear deformations.

By the assumption of harmonic response, $y(x,t)=C\exp\left(j\left(\kappa x-\omega t\right)\right)$, the EBT motion equation (1.1.1) is reformulated as follows:

$$D\kappa^4 - m\omega^2 = 0 \Rightarrow \omega = \kappa^2\sqrt{\frac{D}{m}} \ .$$

The phase velocity $c = \dfrac{\omega}{\kappa}$ leads to the equation

$$c = \kappa\sqrt{\frac{D}{m}}\,, \tag{8}$$

which, by using $c_0 = \sqrt{E/\rho}$, takes the non-dimensional form

$$\bar{c} = \kappa\sqrt{\frac{D\rho}{mE}}\,. \tag{9}$$

The wavenumber to be used in the dispersion curves is also non-dimensionalized through the wavenumber $\kappa_0 = {}^{2\pi}\!/_{a}$, where a denotes the thickness of the thin beam (or the thickness radius of a thin rod). The following figures, to be presented, are the results of the implementation of the code "*Dispersion diagrams*". The shear coefficient K is defined based on analytical expressions, see, Hutchinson (2001).

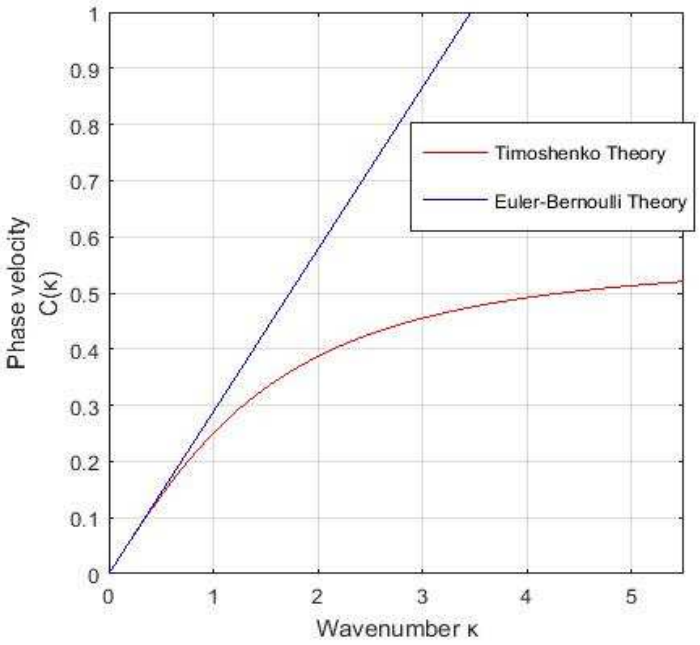

Fig. 2. Dispersion diagram for thin beam, $K = 0.8333$

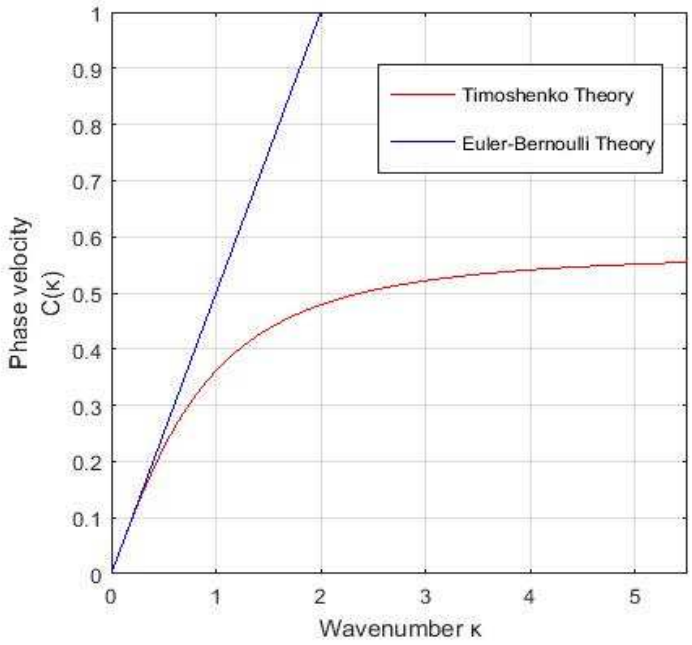

Fig. 3. Dispersion diagram for thin rod, $K = 0.8571$

2.2.1 Conclusions

$K = 0.8333\,(\text{rod}), K = 0.8571$ As expected, the dispersion curve predicted by the Euler-Bernoulli theory is a linear function, see, Fig.2, Fig.3, whereas the dispersion curve from the Timoshenko theory is a more complicated curve. In small wavenumbers κ the curve representing the phase velocity of the Euler – Bernoulli model coincides, in a short area, with the Timoshenko model one. In contrast to EBT, the TBT phase velocity converges to $C \approx 0.56$ (rod case) and $C \approx 0.54$ (beam case) when larger wavenumbers, κ approached. More specifically, let $\kappa \to \infty$ and then using eq. (2.6) we get

$$\overline{c}^4 - \left(\frac{GK}{E} + 1\right)\overline{c}^2 + \frac{GK}{E} = 0 \ ,$$

which in turn leads to a single root independent from wavenumber κ. With further investigation the slope of the EBT rod is greater than the one of the beam. Moreover, the curve referring to the rod for the TBT approaches faster its upper bound compared to the beam of the counterpart theory.

For the steady state linear problem, we eliminate the time dependence using complex amplitude technique. Hence, the representation of the flexural deflection for y_b and y, can be written as follows

$$y_b(x,t) = \mathrm{Re}\left(\overset{\circ}{y}_b(x)e^{-i\omega t}\right) , \tag{10}$$

$$y(x,t) = \mathrm{Re}\left(\overset{\circ}{y}(x)e^{-i\omega t}\right) , \tag{11}$$

Consequently, for the homogeneous problem, eqns. (1), (2) take the form

$$GA(x)K\left(\frac{\partial\, y(x)}{\partial x} - y_b\right) + D(x)\frac{\partial^2 y_b}{\partial x^2} - \rho I(x)\omega^2\, y_b = 0 \ , \tag{12}$$

$$GA(x)K\left(\frac{\partial y_b(x)}{\partial x} - \frac{\partial^2\, y(x)}{\partial x^2}\right) + m(x)\omega^2\, y(x) = 0 \ , \tag{13}$$

2.3 Timoshenko modeling using the Finite Difference Method

The domain $[0, L]$ is defined by the nodal points $\{x_i, y_i = y(x_i), i = 1, 2, ..., N+1\}$. Thus we consider a discretization of the beam into a number of N elements of equal length $\Delta x = \frac{L}{N}$, defined by a set of $N+1$ points. Considering the corresponding linear expressions of the systems (12), (13) are:

$$\sum_{j=1}^{N+1} A_{1ij} y_j - \lambda y_j = 0 \, , \ \left\{\lambda_n = \omega_n^2, \ \boldsymbol{y}_n = y_i^{(n)}, \quad n = 1, 2, 3, ...\right\}$$

, and

$$\sum_{j=1}^{N+1} A_{2ij} y_j - \lambda y_j = 0\,,\ \left\{\lambda_n = \omega_n^2,\ \boldsymbol{y}_n = y_i^{(n)},\quad n = 1,2,3,.....\right\}\,,$$

where $A_1 = [N \times 2N]$ and $A_2 = [N \times 2N]$ The grid definition of the domain determines the size of the tables A_1, A_2.The two tables will be merged into a larger matrix $A = 2[N+1]^2$ in which we will seek the eigenfrequencies ω.

For the solution, to be found, we must set the table form of the linear systems, which will be based on the FDM analysis. Using the schemes (1.3.1), (1.3.2) for the first and second order derivatives, we replace the equation (12) with its discrete analogue:

$$\frac{G_{i+1}A_{i+1}K_{i+1}}{2dx} y_{i+1} - \frac{G_{i-1}A_{i-1}K_{i-1}}{2dx} y_{i-1} - G_i A_i K_i y_{b_i} + \frac{D_{i+1}}{dx^2} y_{b_{i+1}}$$

$$- \frac{2D_i}{dx^2} y_{b_i} + \frac{D_{i-1}}{dx^2} y_{b_{i-1}} - \rho_i I_i \omega^2 y_{b_i} = 0 \qquad (1)$$

and the equation (13) becomes

$$\frac{G_{i+1}A_{i+1}K_{i+1}}{2dx} y_{b_{i+1}} - \frac{G_{i-1}A_{i-1}K_{i-1}}{2dx} y_{b_{i-1}} - \frac{G_{i+1}A_{i+1}K_{i+1}}{dx^2} y_{i+1}$$

$$+ \frac{2G_i A_i K_i}{dx^2} y_i - \frac{G_{i-1}A_{i-1}K_{i-1}}{dx^2} y_{i-1} - m_i \omega^2 y_i = 0 \qquad (2)$$

Setting-up the banded table A_1, its bandwidth depends on the order of the derivative of equation (1). It is consisted of second order derivative of the corresponding term y_b, in parallel with first order derivative of the corresponding term y Following this set-up, we obtain a tridiagonal table, $[N+1 \times N+1]$ in which all non-zero elements are placed in the main diagonal and in its two adjacent sub-diagonals, while in the rest table A_1,$[N \times 2N+1]$ all non-zero elements are placed in its two adjacent sub-diagonals, see fig. 1.

$$A_1 = \begin{pmatrix} a_{11} & a_{21} & & & 0 & a_{2,N+1} & & \\ a_{12} & \ddots & & 0 & a_{1,N+2} & \ddots & 0 & \\ & & \ddots & & & & \ddots & 0 \\ & & & \ddots & a_{N\,N+1} & & \ddots & a_{N,2N+1} \\ 0 & \ddots & & a_{N+1N} & a_{N+1N+1} & 0 & a_{N+1,2N} & 0 \end{pmatrix}$$

Fig. 1.

Table A_2 is consisted of first order derivative, of the displacement y_b, alonghead with second order derivative of the displacement y , see Fig. 2.

$$A_2 = \begin{pmatrix} a_{11} & a_{21} & & & 0 & & a_{1,N+2} & a_{2,N+3} & & & 0 \\ a_{12} & \ddots & & & & & a_{2,N+2} & \ddots & & & \\ & & 0 & & \ddots & & & & & \ddots & \\ & & & \ddots & & a_{N\,N+1} & & & & \ddots & a_{N,2N+1} \\ 0 & & \ddots & & a_{N+1N} & a_{N\,N} & & 0 & \ddots & a_{N+1,2N} & a_{N+1,2N+1} \end{pmatrix}$$

Fig. 2.

Array $A_1\,[N+1\times 2N+1]$, is the first to be placed in table A whereas it follows array $A_2\,[2N+1\times 2N+1]$.

The type of edges which are going to be tested are the ones that have been used in the (EBT) ,i.e. free-free, clamped-clamped and pinned-pinned boundary conditions. Thus, the mathematical formulas for the above type of boundary conditions should be recalculated considering the basic geometrical equation (2.1.3), for the (TBT). Based on the above assumption, that is, y_b consists of the displacement of the cross section area, we differentiate y_b, with respect to x, to calculate the slope of the cross section area. Its connection to the curvature is expressed by the equation, see, e.g. Graff (1975), Samouilidis (2004):

$$\frac{M}{EI} = -\frac{\partial y_b}{\partial x}\ , \tag{3}$$

The equation (3) ,is now changed into the equivalent form :

$$\frac{\partial^2 y}{\partial x^2} = \frac{\partial y_b}{\partial x}, \tag{4}$$

The expression of the shear force ,is:

$$V = GAK\gamma_0, \tag{5}$$

,where γ_0 replaced by the eqn. (3), provides us with the corresponding result:

$$V = GAK\left(\frac{\partial y}{\partial x} - y_b\right), \tag{6}$$

Setting the proper values for each case beam support, we obtain the following collection of :

Free – Free Boundary Conditions. In this case both bending moment and shear are zero at the ends of the beam. Using again the assumption that $\gamma_0 = 0$ at the ends of the clamped beam we obtain from Eq.(3)

$$\partial_{,x} y_b(x=0) = 0 \Rightarrow \partial^2_{,x} y(x=0) = 0 \ , \tag{7a}$$

$$\partial_{,x} y_b(x=L) = 0 \Rightarrow \partial^2_{,x} y(x=L) = 0 \ , \tag{7b}$$

and from Eq. (6)

$$\partial_{,x} y(x=0) - y_b(x=0) = 0 \ , \tag{8a}$$

$$\partial_{,x} y(x=L) - y_b(x=L) = 0 \ , \tag{8b}$$

respectively.

Pinned – pinned Boundary Conditions: The end conditions $Y = 0$ is straightforward in this case

$$y(x=0) = 0 \ , \tag{9a}$$

$$y(x=L) = 0 \ , \tag{9b}$$

The second condition necessitates zero bending moment at the ends of the beam M=0, which using Eq.(3) becomes

$$\partial_{,x} y_b(x=0) = 0 \Rightarrow \partial^2_{,x} y(x=0) = 0 \ , \tag{10a}$$

$$\partial_{,x} y_b(x=L) = 0 \Rightarrow \partial^2_{,x} y(x=L) = 0 \ . \tag{10b}$$

Clamped – clamped Boundary Conditions: The end conditions $Y = 0$ is straightforward

$$y(x=0) = 0 \ , \tag{11a}$$

$$y(x=L) = 0 \, . \tag{11b}$$

Furthermore, using the assumption that $\gamma_0 = 0$ at the ends of the clampted beam we obtain from Eq.(3) the corresponding boundary conditions

$$y_b(x=0) = 0 \ , \tag{12a}$$

$$y_b(x=L) = 0 \ , \tag{12b}$$

ensuring that also $Y' = 0$ at the ends of the beam.

As the basic geometrical parameters have been described, we use the forward and backward finite difference schemes (1.2.3-1.2.8) to discretize the above boundary conditions.

Considering various types of boundary conditions, as presented in Eqns. (7a)-(12b) we obtain the following matrices A :

Clamped- clamped

$$A=\left(\begin{array}{cccccccccc}
1 & 0 & \cdots & 0 & 0 & 0 & \cdots & 0 \\
0 & \ddots & & & 0 & \ddots & & \\
\vdots & & \ddots & & \vdots & & \ddots & \\
 & \ddots & \ddots & 0 & & \ddots & \ddots & 0 \\
0 & & \ddots & 0 & 0 & & \ddots & 0 \\
 & & 0 & 1 & & & 0 & 0 \\
\hline
0 & 0 & \cdots & 0 & 1 & 0 & \cdots & 0 \\
0 & \ddots & & & 0 & \ddots & & \\
\vdots & & \ddots & & \vdots & & \ddots & \\
 & \ddots & \ddots & 0 & & \ddots & \ddots & 0 \\
0 & & \ddots & 0 & 0 & & \ddots & 0 \\
 & & 0 & 0 & & & 0 & 1
\end{array}\right)$$

Free-Free

$$A=\left(\begin{array}{cccccccccc}
-1/dx & 1/dx & \cdots & 0 & 0 & 0 & \cdots & 0 \\
0 & \ddots & & & 0 & \ddots & & \\
\vdots & & \ddots & & \vdots & & \ddots & \\
 & \ddots & 0 & & & \ddots & \ddots & 0 \\
0 & \ddots & -1/dx & 1/dx & 0 & \ddots & 0 & 0 \\
\hline
-1 & 0 & & 0 & -1/dx & 1/dx & \cdots & 0 \\
0 & \ddots & & & 0 & \ddots & & \\
 & & \ddots & & \vdots & & \ddots & \\
 & \ddots & \ddots & 0 & & & \ddots & 0 \\
0 & \ddots & 0 & -1 & 0 & \ddots & -1/dx & 1/dx
\end{array}\right)$$

Pinned-pinned

$$A=\left(\begin{array}{cccccccccccc}
-1.5/dx & 2/dx & -0.5/dx & \cdots & 0 & 0 & 0 & 0 & \cdots & 0 \\
\vdots & & \ddots & & \vdots & & & \ddots & & \ddots \\
0 & & \cdots & 0 & 0.5/dx & -2/dx & 1.5/dx & 0 & \ddots & \cdots \; 0 \; 0 \; 0 \\
\hline
0 & 0 & 0 \; \cdots & 0 & & & 1 & 0 & 0 \; \cdots & 0 \\
\vdots & \ddots & & \vdots & & & & \ddots & & \ddots \\
0 & \cdots & & 0 & 0 & 0 & 0 & 0 & \ddots & \cdots \; 0 \; 0 \; 1
\end{array}\right)$$

We place the rest coefficients of Eqns. (1), (2) in all the non-zero cells.

2.4 Illustration of the modes for a beam cross sectional area (EBT, TBT)

In this chapter, we demonstrate the results derived from the developed numerical methods which are included in the program ‘’TBT.m’’ and ‘’’EBT.m’’. Regarding the Euler – Bernoulli model we depict the modes of a homogeneous and an inhomogeneous beam, see, Ch. (2.3.1), (2.3.3) respectively. It should be noted that we use the factor $\sqrt{2/L}$ to scale the modes in order to have a more distinct illustration of the modes and also in the homogeneous case we present the modes based on the analytical solution. Also we denote that beam represents a square sectional area while rod represents a circular sectional area. Furthermore, for comparison reasons we demonstrate the modes for a homogeneous and an inhomogeneous Timoshenko beam based, see, Ch. (2.3.2), (2.3.4). In all the previous cases we have used a set of M=100 points to discretize our domain. The main characteristics of the beam are: (i) Length: $L = 50\,[\mathrm{m}]$ [m], (ii) Young’s modulus: $E = 5\,10^6\,[\mathrm{Pa}]$, shear modulus $G = 80\,10^9\,[\mathrm{Pa}]$ (ii) Mass density: $\rho = 923\,[\mathrm{kg/m}^3]$, (iv) Thickness: $t = 1\,[\mathrm{m}]$, (v) Moment of inertia: $I = \pi t^3/12 = 0.0833\,[\mathrm{kg\,m}^2]$,(vi) Cross section area: $A = t^2 = 1\,[m^2]$ and (vii) Shear coefficient $K = 0.8333$. For a more detailed presentation of all the combinations concerning a circular and a square cross sectional area using both the Euler – Bernoulli and Timoshenko models, see Appendix A.

2.4.1 Euler – Bernoulli homogeneous beam

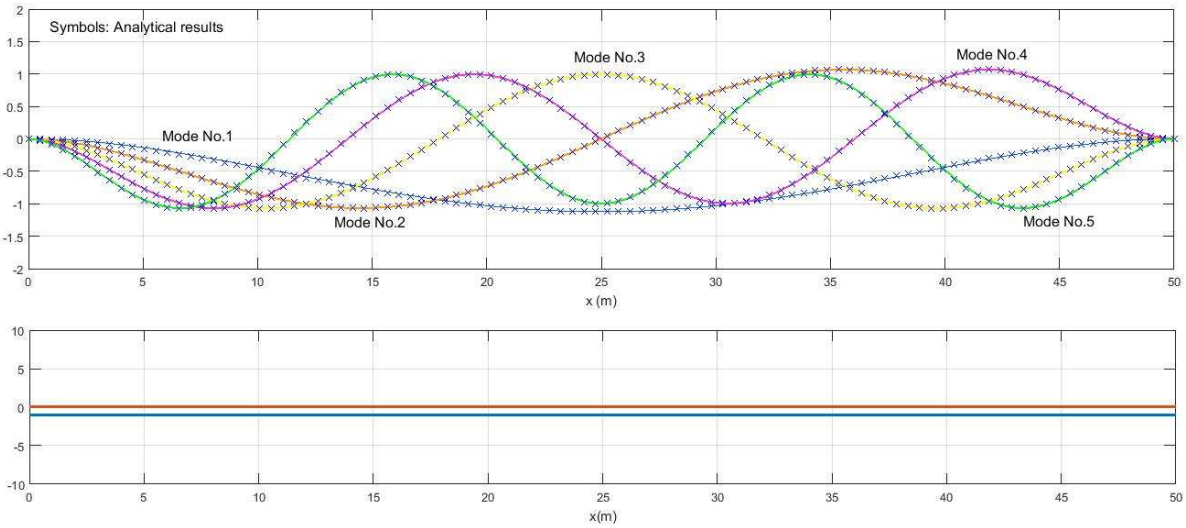

Fig. 1. Clamped edged homogeneous beam, factor $\sqrt{2/L}$ to scale the modes

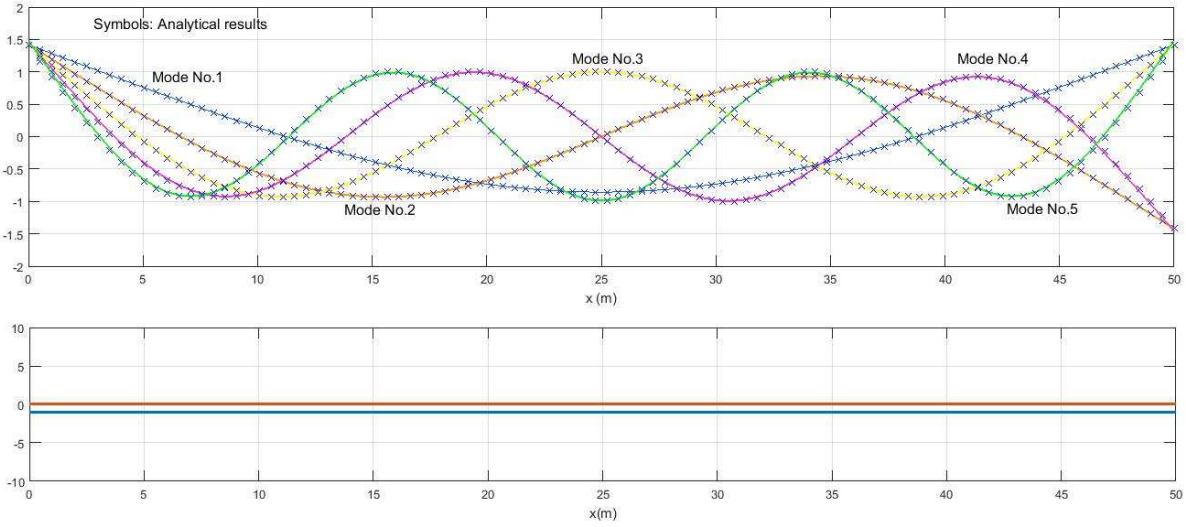

Fig. 2. Free edged homogeneous beam, factor $\sqrt{2/L}$ to scale the modes

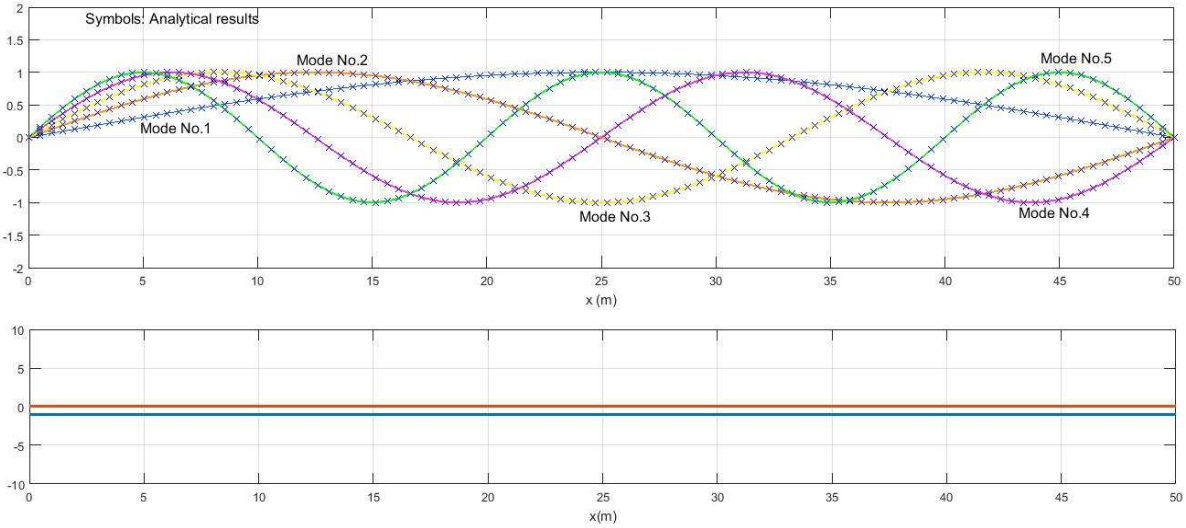

Fig. 3. Pinned edged homogeneous beam, factor $\sqrt{2/L}$ to scale the modes

2.4.2 Timoshenko homogeneous beam

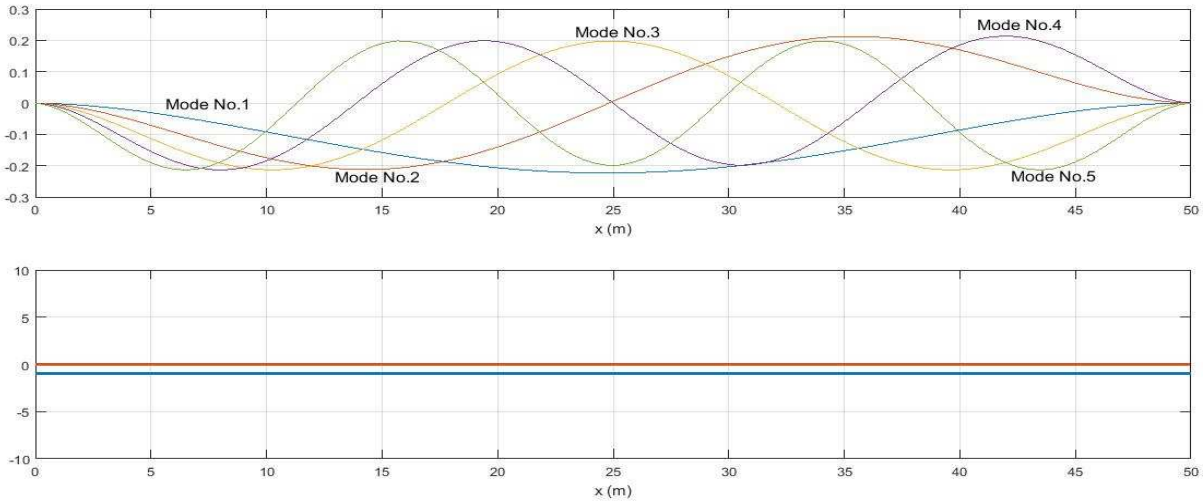

Fig. 1. Clamped edged homogeneous beam, M=100 points

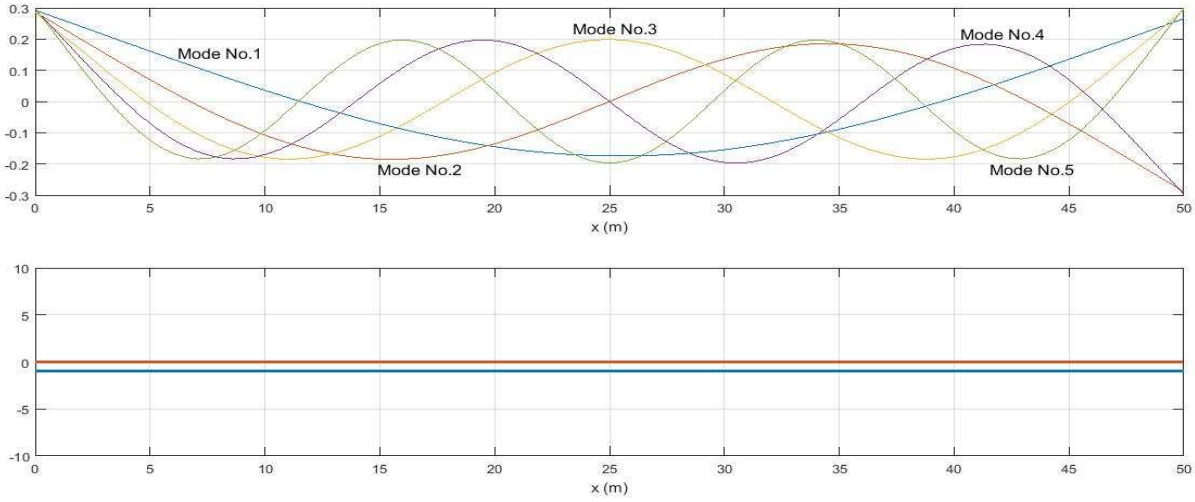

Fig. 2. Free edged homogeneous beam, M=100 points

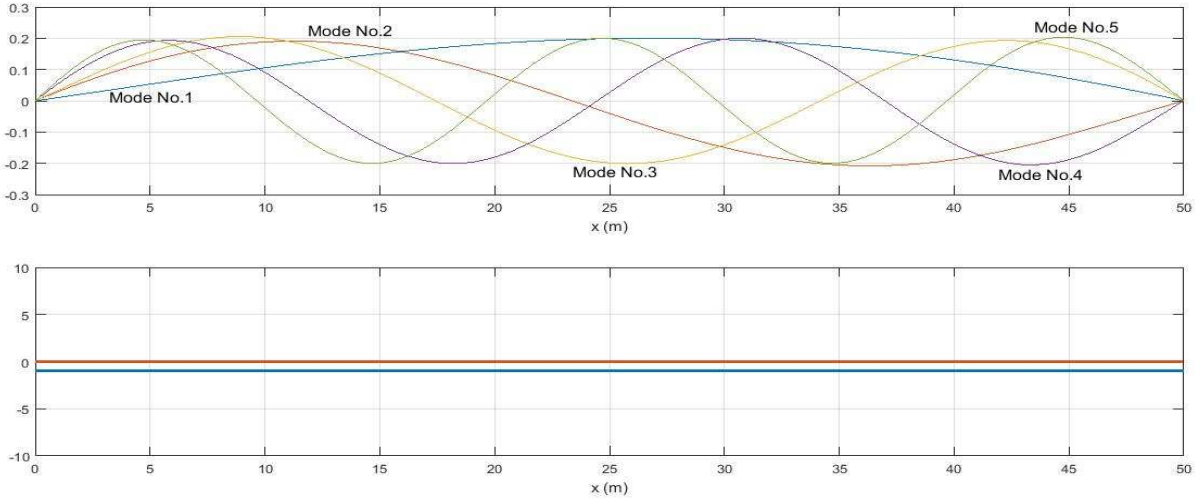

Fig. 3. Pinned edged homogeneous beam, M=100 points

2.4.3 Euler – Bernoulli inhomogeneous beam

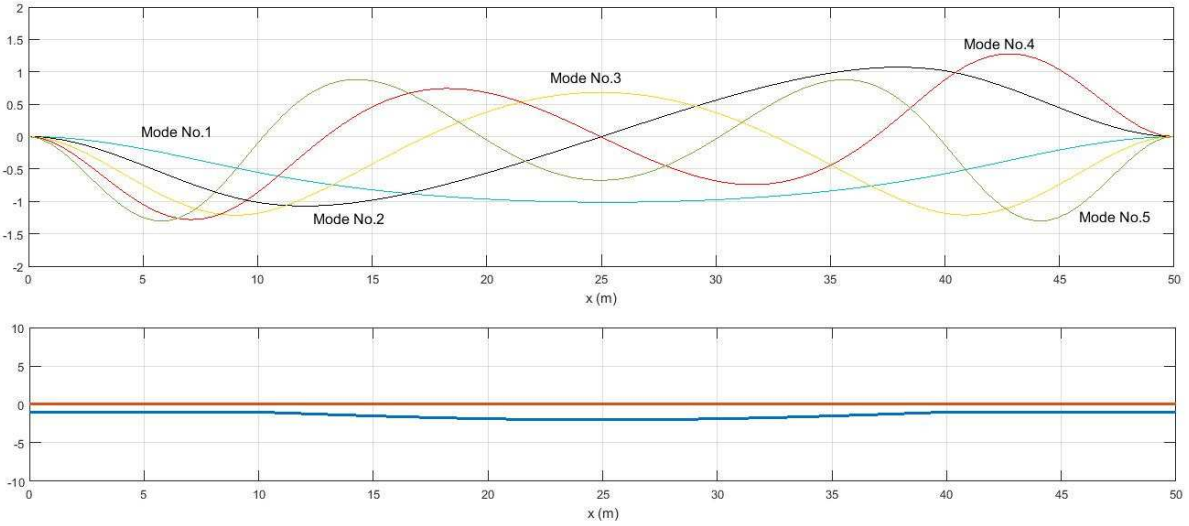

Fig. 1. Clamped edged homogeneous beam, $\sqrt{2/L}$ to scale the modes

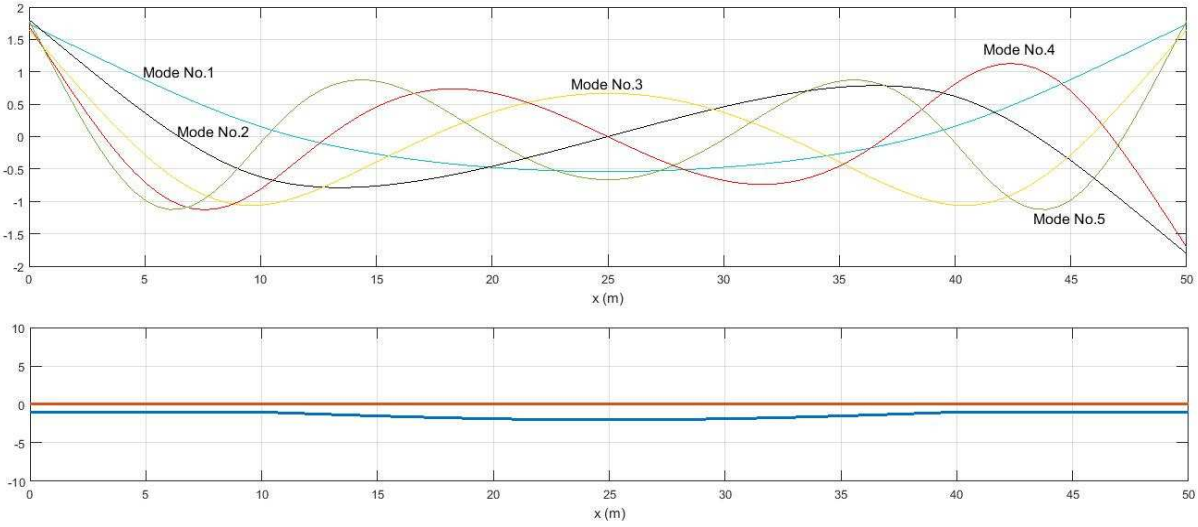

Fig. 2. Free edged homogeneous beam, $\sqrt{2/L}$ to scale the modes

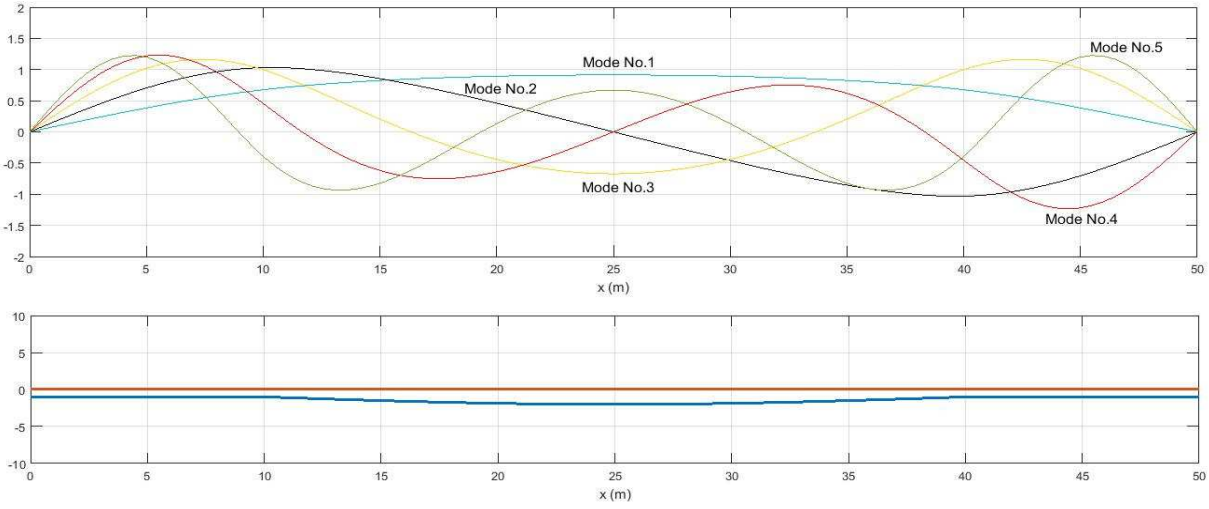

Fig. 3. Pinned edged homogeneous beam, $\sqrt{2/L}$ to scale the modes

2.4.4 Timoshenko inhomogeneous beam

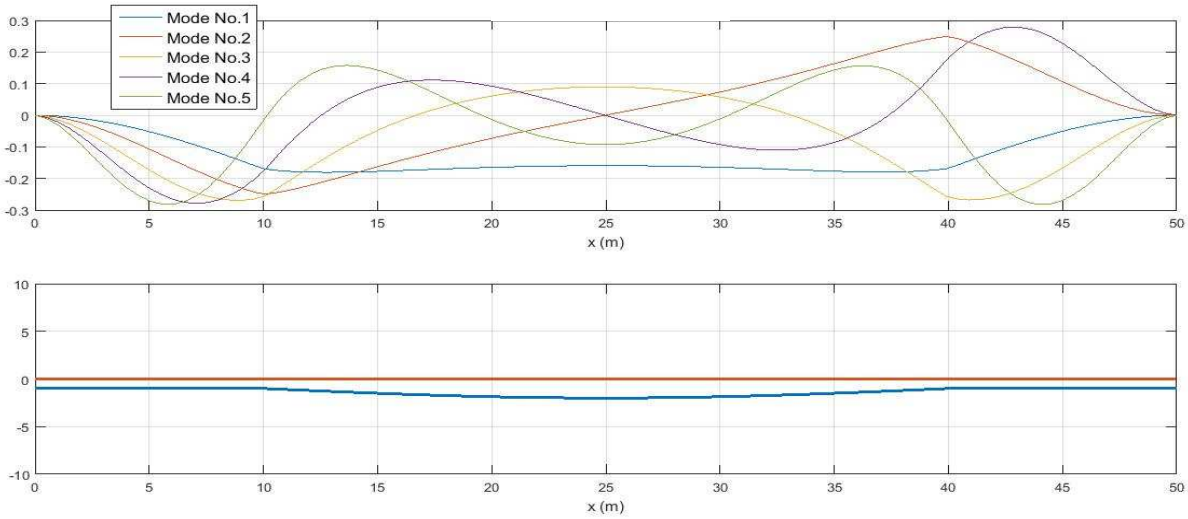

Fig. 1. Clamped edged homogeneous beam, M=100 points

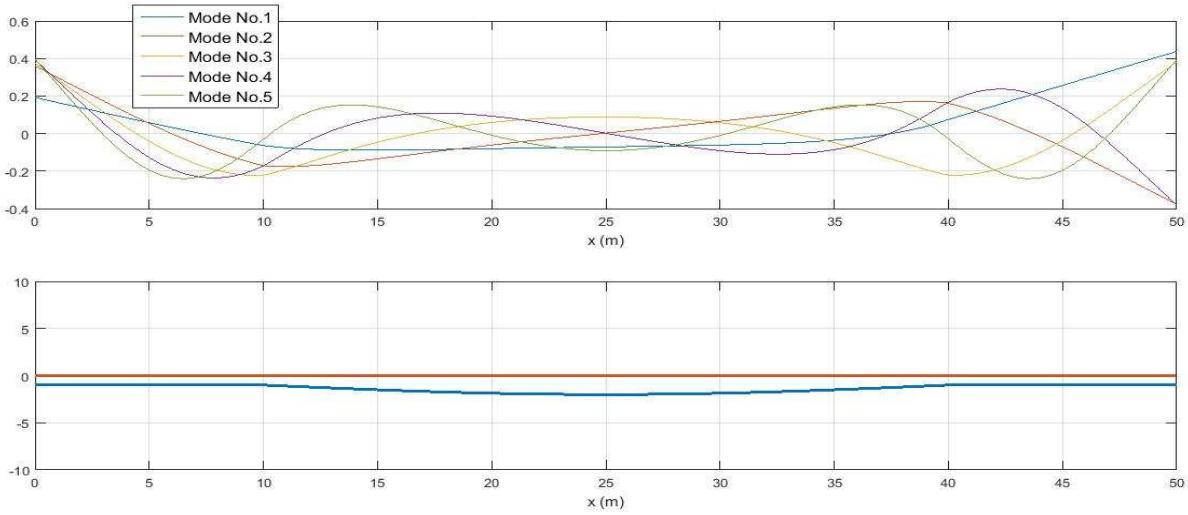

Fig. 2. Free edged homogeneous beam, M=100 points

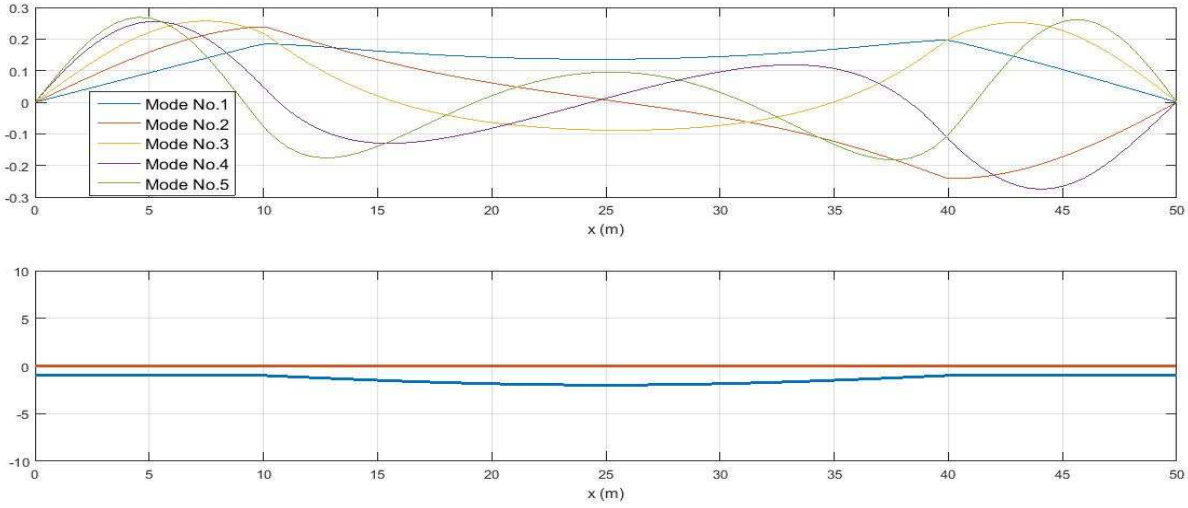

Fig. 3. Pinned edged homogeneous beam, M=100 points

Chapter 3

Ship Hydrodynamics

3.1 RIGID SHIP HYDRODYNAMICS

In the present chapter we review approximate methods for elongated bodies for treating the problem of ship (of length L, breadth B and draft T) responses in waves, considering first the structure, traveling at constant forward speed *U*, in deep water, to be rigid. Also the waves and the induced motions are considered small so that linear theory can be applied. The slenderness assumption for the body will permit strip theory approximations to be used. For simplicity only the case of head incident waves will be considered.

We begin by introducing a symmetric, x_1x_2-plane ship geometry and its motions analyzed on an orthogonal coordinate system, (x_1, x_2, x_3) see Fig.8. The axis system (x_1, x_2, x_3) is moving with the mean value of the ship's velocity and refers to a steady axis system (x_{1s}, x_{2s}, x_{3s}) . The steady coordinate system is placed on the free surface of the sea where the elevation of the water is zero. The $x_{1s}x_{2s}$-plane defines the horizontal plane and x_3-axis is opposite to the direction of the gravity and vertical to $x_{1s}x_{2s}$.

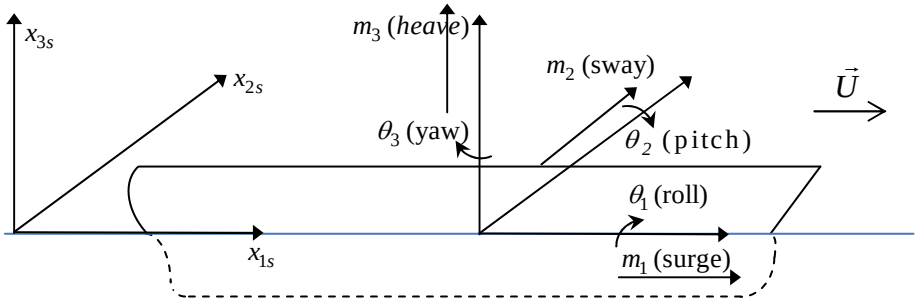

Fig. 1. Ship's motions

Let ξ_i, $i = 1,..,6$ describes the generalized motions of the ship, see, Table (1)

ξ_1	
ξ_2	
ξ_3	
$\xi_4 =$	θ_1
$\xi_5 =$	θ_2
$\xi_6 =$	θ_3

Table 1

Neglecting viscous effects we assume that the motion of the fluid is irrotational. Hence, we introduce the potential $\Phi(x_1, x_2, x_3; t)$ to formulate the body motions in the sea water. In order to solve the velocity potential of the waves a linearization scheme is followed.

The Doppler effects is associated with a frequency shift, which in ocean engineering terms is named after "encounter frequency", ω_e , and is represented in the steady moving reference system by

$$\omega_e = \omega_0 - U\kappa_0 \cos\beta \tag{1}$$

where $\kappa_0 = \omega_0^2 / g$ is the wavenumber and β is the wave incident angle (angle between the incident wave and the ship track). In the case of head seas (waves), $\beta = \pi$, relation (1) is simplified in $\omega_e = \omega_0 + U\kappa_0$ and from now on the expression ω_e will be presented as ω.

The linearized responses of the ship are obtained in the frequency domain $\xi_i(t) = \mathrm{Re}\left(\xi_i e^{j\omega t}\right)$ by the solution of the system of equations describing the dynamics

$$\sum_{i=1}^{6}\left(-\omega^2\left(M_{\ell i} + A_{\ell i}\right) + j\omega\left(UN_{\ell i} + B_{\ell i}\right) + C_{\ell i}\right)\xi_i = F_\ell \ , \tag{2}$$

where $F_\ell(t) = \mathrm{Re}\left(F_\ell e^{j\omega t}\right) = \mathrm{Re}\left(\left(F_{I\ell} + F_{D\ell}\right)e^{j\omega t}\right)$ are the Froude-Krylov generalized forces denoted by the incident, F_{Im} , and the diffraction, F_{Dm} , generalized forces. In the eqn. (2), the matrix M_{mi} is

$$M_{\ell i} = \begin{pmatrix} M & 0 & 0 & 0 & J_3 & -J_2 \\ 0 & M & 0 & -J_3 & 0 & J_1 \\ 0 & 0 & M & J_2 & -J_1 & 0 \\ 0 & -J_3 & J_2 & I_{11} & I_{12} & I_{13} \\ -J_3 & 0 & -J_1 & I_{21} & I_{22} & I_{23} \\ J_2 & -J_1 & 0 & I_{31} & I_{32} & I_{33} \end{pmatrix}., \tag{3}$$

where $M = \rho C_B LBT = \Delta / g$ is the mass of the ship (of displacement Δ) at draft T and C_B the block coefficient. Also $\boldsymbol{J} = \left(J_1, J_2, J_3\right) = \int_V r_B \rho \, dV$ is the polar moment of inertia, where, r_B , is the distance from the gravity center . Thus, $\boldsymbol{J} = M\boldsymbol{R}_G$, where $\boldsymbol{R}_G$ is the center of gravity. In the case of even keel ships $\boldsymbol{R}_G = \left(LCG, 0, VCG\right)$, with *LCG* denoting the long center and VGC the vertical center of gravity.

Furthermore, $I_{ii} = \int_V \rho \left(\sum_{m=1}^{3} r_m^2 - r_i^2 \right) dV$, $i = 1,2,3$ is the moment of inertia while $I_{\ell i} = \int_V \rho r_\ell r_i dV$, $\ell \neq i, i = 1,2,3$ is the rotary product.

The matrix $N_{\ell i} = \begin{pmatrix} 0 & 0 & 0 & 0 & 0 & 0 \\ 0 & 0 & 0 & 0 & 0 & M \\ 0 & 0 & 0 & 0 & -M & 0 \\ 0 & 0 & 0 & 0 & -J_2 & -J_3 \\ 0 & 0 & 0 & 0 & J_1 & 0 \\ 0 & 0 & 0 & 0 & 0 & J_1 \end{pmatrix}$. (4)

Also the, C_{mi} , stands for the hydrostatic forces

$$C_{\ell i} = \begin{pmatrix} 0 & 0 & 0 & 0 & 0 & 0 \\ 0 & 0 & 0 & 0 & 0 & 0 \\ 0 & 0 & C_{33} & C_{34} & C_{35} & 0 \\ 0 & 0 & C_{43} & C_{44} & C_{45} & 0 \\ 0 & 0 & C_{53} & C_{54} & C_{55} & 0 \\ 0 & 0 & 0 & 0 & 0 & 0 \end{pmatrix}. \quad (5)$$

The rest of the matrices such as A_{ji} is the added mass, and B_{ji} is the damping which dependent on the radiation potentials. Consequently, for head seas, $\beta = 180^\circ$, and using eqn. (1), we derive the following coupled-equations for the heave and the pitch motions of the ship,

$$\left(-\omega^2 (M + A_{33}) + j\omega B_{33} + C_{33}\right)\xi_3 + \left(-\omega^2 \left(A_{35} - J_1\right) + j\omega \left(B_{35} - MU\right) + C_{35}\right)\xi_5 = F_3 \ , \quad (6)$$

$$\left(-\omega^2 (M + A_{53}) + j\omega B_{53} + C_{53}\right)\xi_3 + \left(-\omega^2 \left(A_{55} + I_{22}\right) + j\omega \left(B_{55} + UJ_1\right) + C_{55}\right)\xi_5 = F_5 \ , \quad (7)$$

In the eqns. (6), (7) harmonic responses have been considered. In the above equations $C_{33} = \rho g A_{wl}$, where $A_{wl} = \int_{x_1} B(x_1)$ is waterline area, $C_{35} = C_{53} = A_{wl} LCF$ where *LCF* is the long center of flotation. Also, $C_{55} = gM\, GM_L = gM\left(KB + BM_L - KG\right)$, where *KB* is the vertical center of buoyancy, $BM_L = I_L / \nabla$, $I_L = I_{x_{11}} = A_{11}$ is the longitudinal metacentric radius, and *KG* is the vertical center of gravity (measured from the keel of the ship).

3.1.1 Flow potential linearization

Setting the linearization scheme, the velocity potential, $\Phi(x_1, x_2, x_3; t)$, and the elevation of the sea water, $\eta(x_1, x_2; t)$, are considered to be small. Due to small sea elevation, the boundary conditions, to be used, refer to the mean free surface of the sea, that is, $x_3 = 0$ instead of the exact position at $x_3 = \eta$. In addition ∂D_f , represents the free surface of the hull while, ∂D_B represents the wet surface of the hull. Summing the previous assumptions the linear boundary conditions, are

$$\Delta\Phi_{\mathrm{T}} = 0 \ , \tag{1}$$

$$\left(\frac{\partial}{\partial t} - U\frac{\partial}{\partial x_1}\right)^2 \Phi_{\mathrm{T}} + g\frac{\partial \Phi_{\mathrm{T}}}{\partial x_3} = 0, \quad \partial D_f \ \text{ at } \ x_3 = 0, \tag{2}$$

while the boundary condition for the wet surface is, see , e.g., Athanasoulis & Belibassakis (2012), Salvesen *et al* (1970)

$$\begin{aligned} \nabla\Phi_{\mathrm{T}}(\boldsymbol{r}\,;t)\cdot\boldsymbol{n} \;=\; & \boldsymbol{U}\cdot\boldsymbol{n} + \left[\boldsymbol{U} - \nabla\Phi_{\mathrm{T}}\right](\boldsymbol{n}\times\boldsymbol{\theta}) \\ & + \; \boldsymbol{u}\cdot\boldsymbol{n} \;+\; (\boldsymbol{\omega}\times\boldsymbol{r})\cdot\boldsymbol{n} - \left[\boldsymbol{\xi}\cdot\boldsymbol{n} + (\boldsymbol{\theta}\times\boldsymbol{r})\cdot\boldsymbol{n}\right] \end{aligned} \ , \ \boldsymbol{x}\in\partial D_B \tag{3}$$

In order to analyze the hydrodynamic responses of the ship we assume that: (i) the ship is treated as a long and slender body, that is, the length, L , is much greater compared to the other dimensions such as the beam, B , and the draft, T . Additionally, (ii) the water is considered deep, $h/\lambda > 0.5$ where, h is the depth of the sea and λ is the length of the wave. Finally, (iii) pitch is negligible as the ship is oscillating under the influence of incident sea waves.
According to the linearization scheme, the total velocity potential can be decomposed into a steady and an unsteady state potential, as follows

$$\Phi_T(x_1, x_2, x_3; t) = \Phi_s(x_1, x_2, x_3) + \mathrm{Re}\left(\overset{\circ}{\Phi}_u(x_1, x_2, x_3)e^{j\omega t}\right) x \in \mathbb{R} \ , \tag{4}$$

where $j = \sqrt{-1}$, $\Phi_s(x_1, x_2, x_3)$ is the steady potential and $\mathrm{Re}\left(\overset{\circ}{\Phi}_u(x_1, x_2, x_3)e^{j\omega t}\right)$ represents the real part of the unsteady potential, where $\overset{\circ}{\Phi}_u$ is the corresponding complex amplitude. For simplicity, from now on, the over-dot symbol of the complex amplitude will be omitted. Through Eq. (4) and by considering negligible contribution of the unsteady velocity potential, $\nabla\Phi_U$, the Eq. (3) changes to

$$\underline{\nabla\Phi_S\mathbf{n}} + \nabla\Phi_U\mathbf{n} = \underline{\mathbf{U}\cdot\mathbf{n}} + \left[\mathbf{U} - \nabla\Phi_S\right](\mathbf{n}\times\boldsymbol{\theta}) + \mathbf{u}\cdot\mathbf{n} + \boldsymbol{\omega}(\mathbf{r}\times\mathbf{n}) - \left[\boldsymbol{\xi}\cdot\mathbf{n} + \boldsymbol{\theta}(\mathbf{r}\times\mathbf{n})\right]\left(\frac{\partial^2\Phi_S}{\partial x_i\,\partial x_j}\right) \quad , \tag{5}$$

while the underlined terms refer to the time independent velocity potential and all the rest refer to the time dependent velocity potential. Hence, we obtain the following conditions

$$\nabla\Phi_S\mathbf{n} = \mathbf{U}\cdot\mathbf{n} \ , \tag{6}$$

$$\nabla\Phi_U\mathbf{n} = \left[\mathbf{U} - \nabla\Phi_S\right](\mathbf{n}\times\boldsymbol{\theta}) + \mathbf{u}\cdot\mathbf{n} + \boldsymbol{\omega}(\mathbf{r}\times\mathbf{n}) - \left[\boldsymbol{\xi}\cdot\mathbf{n} + \boldsymbol{\theta}(\mathbf{r}\times\mathbf{n})\right]\left(\frac{\partial^2\Phi_S}{\partial x_i\,\partial x_j}\right). \tag{7}$$

Analyzing the components of eqn. (7) which represents the vertical unsteady velocity potential, we get

- $\mathbf{u}\cdot\mathbf{n} + \boldsymbol{\omega}(\mathbf{r}\times\mathbf{n})$, the vertical component of the unsteady potential.
- $-\mathbf{U}(\mathbf{n}\times\boldsymbol{\theta})$, the effect of the steady velocity potential .
- $\nabla\Phi_S(\mathbf{n}\times\boldsymbol{\theta}) - \left[\boldsymbol{\xi}\cdot\mathbf{n} + \boldsymbol{\theta}(\mathbf{r}\times\mathbf{n})\right]\left(\frac{\partial^2\Phi_S}{\partial x_i\,\partial x_j}\right)$, the effect of the steady flow field in the unsteady disturbance field .

For long and slender hull geometry, the latter component representing the effect of the steady flow field on the unsteady disturbance field can be neglected because the velocity potential term $\nabla\Phi_S(\mathbf{n}\times\boldsymbol{\theta})$ is small. The final form of Eq. (7) is

$$\nabla\Phi_u\cdot\mathbf{n} = \mathbf{u}\cdot\mathbf{n} + \boldsymbol{\omega}(\mathbf{r}\times\mathbf{n}) - \mathbf{U}(\mathbf{n}\times\boldsymbol{\theta}) \ . \tag{8}$$

The expressions for the boundary conditions as described in Eqs. (1-3) , in terms of the steady and the unsteady potential, are

$$\nabla^2\Phi_S = 0 \ , \tag{9a}$$

$$\nabla^2\Phi_U = 0 \ , \tag{9b}$$

$$U^2\frac{\partial^2\Phi_S}{\partial x_1^2} + g\frac{\partial\Phi_S}{\partial x_3} = 0 \ , \qquad \partial D_f \ (\text{at } x_3 = 0) \tag{10a}$$

$$\left(\frac{\partial}{\partial t}-U\frac{\partial}{\partial x_1}\right)^2\Phi_U+g\frac{\partial\Phi_U}{\partial x_3}=0\ ,\qquad \partial D_f\ (\text{at } x_3=0) \tag{10b}$$

$$\nabla\Phi_S\cdot\mathbf{n}\ =\ \mathbf{U}\cdot\mathbf{n}\ ,\qquad \boldsymbol{x}\in\partial D_B \tag{11a}$$

$$\nabla\Phi_U\cdot\mathbf{n}\ =\ \mathbf{u}\cdot\mathbf{n}+\boldsymbol{\omega}\left(\mathbf{r}\times\mathbf{n}\right)+\boldsymbol{\theta}\left(\mathbf{n}\times\mathbf{U}\right)\ ,\qquad \mathbf{x}\in\partial D_B \tag{11b}$$

A boundary condition at infinity should be also taken into account, describing the vanishing potential Φ far away from the hull, $\sqrt{x_1^2+x_2^2}\to\infty$,

$$\Phi,\nabla\Phi\to 0\ ,\quad \sqrt{x_1^2+x_2^2}\to\infty \tag{12}$$

Furthermore, the time-dependent potential is linearly decomposed to three terms,

$$\Phi_u=\Phi_I+\Phi_D+\Phi_R\ , \tag{13}$$

where Φ_I is the incident wave potential, Φ_D is the diffraction wave potential and $\Phi_R=\sum_{i=1}^{6}j\omega\xi_i\Phi_i$, is the radiation potential caused from the i-motion of the ship, see , e.g., Athanasoulis, Belibassakis (2012). Using the relations $x_{01}=x_1+Ut$, $x_{02}=x_2$, $x_{03}=x_3$ and by the assumption of deep water the incident potential relation Φ_I , is

$$\Phi_I(\mathbf{x})\ =\ \frac{jgA}{\omega_0}\exp(k_0x_3)\exp\left[-\ jk_0\left(x_1\cos\beta+x_2\sin\beta\right)\right]\exp\left(j\omega t\right)\ , \tag{14}$$

The individual potentials Φ_I and Φ_D are part of the unsteady problem and represent the effect of the waves on a hull with zero velocity. Hence, the boundary conditions are satisfied as follows, see, e. g., Salvesen et al (1970) and also Athanasoulis, Belibassakis (2012).

$$\Delta\Phi_D=0\ , \tag{15}$$

$$\left(j\omega-U\frac{\partial}{\partial x_1}\right)^2\Phi_D+g\frac{\partial\Phi_D}{\partial x_3}=0\ ,\quad \partial D_f\ (\text{at } x_3=0)\ , \tag{16}$$

$$\frac{\partial}{\partial n}\left(\Phi_D+\Phi_I\right)=0\Rightarrow\ \frac{\partial\Phi_D}{\partial n}=-\frac{\partial\Phi_I}{\partial n}\ ,\quad \mathbf{x}\in\partial D_B\ , \tag{17}$$

while the boundary conditions for the radiation problem are

$$\nabla\Phi_j=0\ , \tag{18}$$

$$\left[\left(i\omega-U\frac{\partial}{\partial x_1}\right)^2+g\frac{\partial}{\partial x_3}\right]\Phi_j=0\ .\qquad \partial D_f\ (\text{at } x_3=0) \tag{19}$$

Also the conditions for the wet surface of the hull ($\boldsymbol{x} \in \partial D_B$)

$$\frac{\partial \Phi_i}{\partial n} = j\omega n_i, \quad i = 1,2,3,4 \ , \ \frac{\partial \Phi_i}{\partial n} = j\omega n_i, \quad i = 1,2,3,4, \tag{20a}$$

$$\frac{\partial \Phi_5}{\partial n} = j\omega n_5 + U n_3 \ , \tag{20b}$$

$$\frac{\partial \Phi_6}{\partial n} = j\omega n_6 - U n_2 \ , \tag{20c}$$

Let Φ_i^0 represent the radiation potential, which is considered independent from velocity U , and let Φ_i^U represent the counterpart term depending on velocity U . Also, m_i is the component of the velocity derivative, concerning the time-independent problem , due to the motion of the ship with steady velocity, U . It follows:

$$Um_i = -\sum_{k=1}^{3} n_k \frac{\partial w_i}{\partial x_i} \ , \qquad i = 1,2,3 \qquad \text{and} \qquad Um_i = -\sum_{k=1}^{3} n_k \frac{\partial (\mathbf{r} \times \mathbf{w})_i}{\partial x_i} \ , \qquad i = 4,5,6$$

where

$$w = (w_1, w_2, w_3) = \left(-U + \frac{\partial \Phi_S}{\partial x_1}, \frac{\partial \Phi_S}{\partial x_1}, \frac{\partial \Phi_S}{\partial x_1} \right) .$$

Calculating the previous formulas, we are provided with the following results , see , e.g. , Athanasoulis, Belibassakis (2012) , Ohkusu (1996)

$$m_i = 0 \ , \ i = 1,...,4 \ , \tag{21a}$$

and

$$m_5 = n_3 \ , \tag{21b}$$

$$m_6 = -n_2 \ , \tag{21c}$$

see, e.g., Athanasoulis, Belibassakis (2012, p.242), Salvesen et al, (1970, Appendix 1), we obtain

$$\frac{\partial \Phi_i^0}{\partial n} = j\omega n_i \ , \quad i = 1,...,6 \tag{22}$$

$$\frac{\partial \Phi_i^U}{\partial n} = j\omega m_i \ , \ i = 1,...,6 \tag{23}$$

Hence, we get

$$\Phi_i^U = 0 \ , \quad i = 1,...,4 \tag{24}$$

and

$$\Phi_5^U = \Phi_3^0 \ , \tag{25}$$

$$\Phi_6^U = -\Phi_2^0 \ , \tag{26}$$

$$\Phi_i^0 + \frac{U}{j\omega}\Phi_i^U = 0 \ , \quad i = 1,...,6 \tag{27}$$

In addition to the previous boundary conditions an appropriate condition at infinity , eqn. (12), should be considered.

3.1.2 Forces and moments

Since the viscous effects have been neglected, only pressure acting on the wet surface of the hull generating forces and moments given by the equations

$$F = \iint_{\partial D_B} p(\boldsymbol{x},t)\,\boldsymbol{n}\,dS_B \ , \tag{1}$$

$$M = \iint_{\partial D_B} p(\boldsymbol{x},t)\,\boldsymbol{r}\times\boldsymbol{n}\,dS_B \ , \tag{2}$$

By Bernoulli's equation, the dynamic pressure is given by

$$\frac{p}{\rho} = -\left[\left(j\omega - U\frac{\partial}{\partial x_1}\right)\Phi_T + \frac{1}{2}\left(\nabla\Phi_T\right)^2\right] \ , \tag{3}$$

In the linearized theory only the last term in the right-hand side is omitted as higher order quantity,

$$p(\boldsymbol{x},t) = -\rho\left(j\omega - U\frac{\partial}{\partial x_1}\right)\Phi_T \ , \tag{4}$$

and thus generalized dynamic forces are

$$F = -\rho\iint_{\partial D_B}\left(j\omega - U\frac{\partial}{\partial x_1}\right)\Phi(\boldsymbol{x})\,\boldsymbol{n}\,dS_B \ , \tag{5}$$

where $\boldsymbol{n} = \{n_\ell,\ \ell = 1,..,6\}$ is the generalized normal vector is defined by $n = n_1\,\boldsymbol{j}_1 + n_2\,\boldsymbol{j}_2 + n_3\,\boldsymbol{j}_3$ and by the cross product $\boldsymbol{r}\times\boldsymbol{n} = (n_4, n_5, n_6)$. The latter is analyzed as follows:

$$\boldsymbol{r}\times\boldsymbol{n}=\begin{vmatrix}\boldsymbol{j}_1 & \boldsymbol{j}_2 & \boldsymbol{j}_3\\ x_1 & x_2 & x_3\\ n_1 & n_2 & n_3\end{vmatrix}=(x_2n_3-x_3n_2)\boldsymbol{j}_1-(x_1n_3-x_3n_1)\boldsymbol{j}_2+(x_1n_2-x_2n_1)\boldsymbol{j}_3\ . \tag{6}$$

Hence,

$$n_4=x_2n_3-x_3n_2\,,\qquad n_5=-(x_1n_3-x_3n_1),\qquad n_6=x_1n_2-x_2n_1\ . \tag{7}$$

3.1.3 Hydrodynamic Coefficients

Using Eq.(1.2.5) in conjunction with the radiation potentials $\Phi_{i=1,2,..6}$ we obtain the hydrodynamic coefficients

$$\rho\omega^2\iint\limits_{\partial D_B} n_\ell\left(j\omega-U\frac{\partial}{\partial x_1}\right)\Phi_i\,dS_B=\rho\omega^2\iint\limits_{\partial D_B} n_\ell\left(j\omega-U\frac{\partial}{\partial x_1}\right)\left(\Phi_i^0+\frac{U}{j\omega}\Phi_i^U\right)dS_B\ ,$$
$$\ell,i=1,...,6 \tag{1}$$

where the integration refers to the mean position of the hull surface $\partial D_B=S_B$.

By Stokes theorem see, e.g., Salvesen (1970, Appendix 1), and by the assumption of a slender hull, the following equation is derived

$$\iint\limits_{\partial D_B} n_\ell U\frac{\partial\Phi_i^0}{\partial x_1}dS=U\iint\limits_{\partial D_B} m_\ell\Phi_i^0\,dS\ , \tag{2}$$

Firstly, considering the speed-independent scenario, the eqn. (1.2.5) expressing the hydrodynamic forces in terms of the hydrodynamic coefficients, changes to

$$F_{\ell i}=\Pi_{\ell i}^0=-\rho\iint\limits_{\partial D_B} j\omega\left(j\omega\Phi_i^0\right)n_\ell\,dS_B\Rightarrow\ ,$$

$$\frac{F_{\ell i}}{\omega^2}=\Pi_{\ell i}^0=\rho\iint\limits_{\partial D_B} n_\ell\Phi_i^0\,dS_B\quad , \tag{3}$$

where, $\Pi_{\ell i}^0$, is the hydrodynamic coefficient of the , $i=1,...,6$, radiation potential in the $\ell=1,...,6$ - motion, referring to the steady body, i.e. $U=0$.

Applying eqns. (1), (1.1.23) ,(3) to (1.2.5), we get

$$\frac{F_{\ell i}}{\omega^2}=\Pi_{\ell i}^0-\frac{U}{j\omega}\rho\iint\limits_{\partial D_B} m_\ell\Phi_i^0\,dS_B\quad ,\ \ell,i=1,...,4\ , \tag{4a}$$

and through (1.1.21b), (1.1.21c) ,respectively, we obtain

$$\frac{F_{\ell i}}{\omega^2}=\Pi_{\ell i}^0-\frac{U}{j\omega}\rho\Pi_{i3}^0\ ,\qquad \ell=5\ ,\quad i=1,...,4 \tag{4b}$$

and

$$\frac{F_{\ell i}}{\omega^2} = \Pi^0_{\ell i} + \frac{U}{j\omega}\rho\,\Pi^0_{i2}\ , \qquad \ell = 6\ , \qquad i = 1,...,4 \tag{4c}$$

Following the same method

$$\frac{F_{\ell i}}{\omega^2} = \Pi^0_{\ell i} - \frac{U}{j\omega}\rho \iint\limits_{\partial D_B} n_\ell \Phi^0_i\, dS_B\ , \qquad i = 5,6\ , \qquad \ell = 1,...,4$$

(5a)

and the corresponding terms

$$\frac{F_{\ell i}}{\omega^2} = \Pi^0_{\ell i} - \frac{U}{j\omega}\rho\,\Pi^0_{3\ell}\ , \qquad i = 5\ , \qquad \ell = 1,...,4 \tag{5b}$$

and

$$\frac{F_{\ell i}}{\omega^2} = \Pi^0_{\ell i} + \frac{U}{j\omega}\rho\,\Pi^0_{2\ell}\ , \qquad i = 6\ , \qquad \ell = 1,...,4\ . \tag{5c}$$

Finally,

$$\frac{F_{\ell i}}{\omega^2} = \Pi^0_{\ell i} + \frac{U^2}{\omega^2}\rho \iint\limits_{\partial D_B} m_\ell \Phi^0_i\, dS_B \quad , \qquad \ell = i = 5,6\,, \tag{6a}$$

and the corresponding terms which are derived from eqn.(13a)

$$\frac{F_{\ell i}}{\omega^2} = \Pi^0_{\ell i} + \frac{U^2}{\omega^2}\rho\,\Pi^0_{33}\ , \qquad \ell = i = 5\ , \tag{6b}$$

and

$$\frac{F_{\ell i}}{\omega^2} = \Pi^0_{\ell i} + \frac{U^2}{\omega^2}\rho\,\Pi^0_{22}\ , \qquad \ell = i = 6\ . \tag{6c}$$

3.2 Strip theory approximations

The strip theory approximation is derived by using specific assumptions concerning the geometrical characteristics of the hull, i.e. the beam and the draft of the ship are much smaller than the length, which results in a long and slender hull shape. It follows that, close to the hull, the derivative in the x_1 -direction is much smaller than the other directions $\frac{\partial}{\partial x_1} \ll \frac{\partial}{\partial x_2}, \frac{\partial y}{\partial x_3}$. Thus, differentials with respect to x_1 are omitted. In addition, for the components of the normal vector on the wetted hull it holds

$$n_1 \ll n_2, n_3\ . \tag{1}$$

Furthermore, introducing the two dimensional geometry of each vertical section, see e.g. Fig.1, the components of the generalized three dimensional normal vector $n_\ell(x_1, x_2, x_3)$, $\ell = 2,..,6$ are approximated by the corresponding two dimensional ones $N_\ell(x_2, x_3; x_1)$ on each section over the length of the hull, parametrically dependent on the section shape (through the longitudinal position x_1), as follows

$$n_\ell(x_1, x_2, x_3) \approx N_\ell(x_2, x_3; x_1) \ , \quad \ell = 2,3,4 \tag{2}$$

$$n_5(x_1, x_2, x_3) \approx -x_1 N_3(x_2, x_3; x_1) \ , \tag{3}$$

$$n_6(x_1, x_2, x_3) \approx x_1 N_2(x_2, x_3; x_1) \ , \tag{4}$$

where

$$N_4(x_2, x_3; x_1) = x_3 N_2(x_2, x_3; x_1) - x_2 N_3(x_2, x_3; x_1) \ . \tag{5}$$

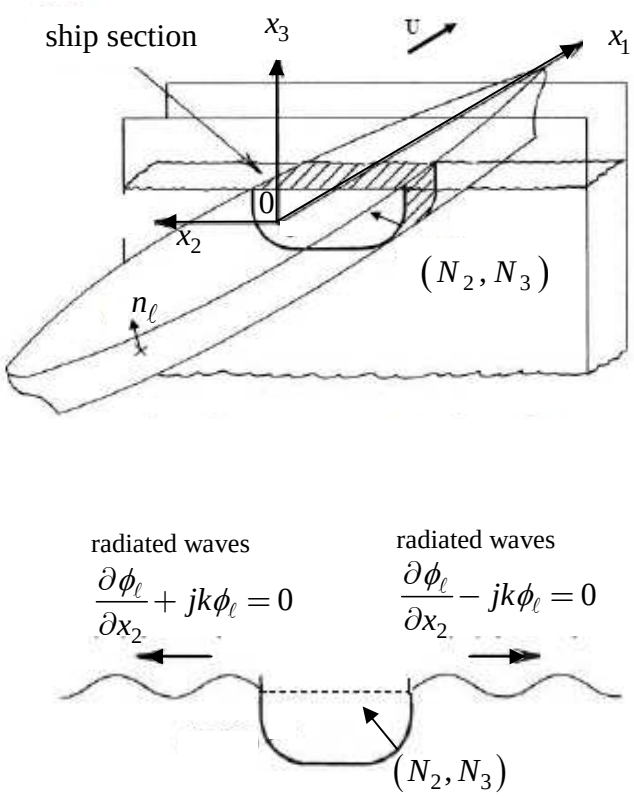

Fig. 1. Strip theory 2D model

Also, the tree-dimensional radiation potentials $\Phi_i^0(x_1, x_2, x_3)$, for $i = 2,3,4$ are approximated by the two-dimensional ones $\phi_i(x_2, x_3; x_1)$, as follows

$$\Phi_i^0(x_1,x_2,x_3)=\phi_i(x_2,x_3;x_1)\ ,\ i=2,3,4 \tag{6a}$$

and for $i=5,6$ by

$$\Phi_5^0(x_1,x_2,x_3)=-x_1\phi_3(x_2,x_3;x_1)\ , \tag{6b}$$

$$\Phi_6^0(x_1,x_2,x_3)=x_1\phi_2(x_2,x_3;x_1)\ . \tag{6c}$$

The two dimensional potentials $\phi_i(x_2,x_3;x_1)$, $i=5,6$ are obtained as solutions of the Laplace equation on the vertical plane x_2x_3 for each ship – section at each x_1 position. The latter satisfies the following boundary condition

$$\frac{\partial^2\phi_i}{\partial x_2^2}+\frac{\partial^2\phi_i}{\partial x_3^2}=0\ ,\quad i=2,3,4\ , \tag{7}$$

the free surface boundary condition

$$-\omega^2\phi_i+g\frac{\partial\phi_i}{\partial x_3}=0\ ,\quad i=2,3,4\ ,\text{on}\ x_3=0\ , \tag{8}$$

boundary condition on the wet surface of each section

$$\frac{\partial\phi_i}{\partial N}=N_i\ ,\quad i=2,3,4\ ,\text{on}\ \partial D_B(x_1)\ , \tag{9}$$

and finally the condition at infinity expressing the fact that the waves are outgoing at infinity , see, Fig.1 .

$$\frac{\partial\phi_i}{\partial x_2}\pm\frac{j\omega^2}{g}\phi_i=0\ , \tag{10}$$

Clearly the 2D potentials $x_3=0$ represent wave fields produced by the horizontal $(i=2)$, vertical $(i=3)$ and rotational oscillation of the x_2x_3 transverse ship oscillation of each section.

For the solution of the above problems in the present work a Boundary Element Method is developed and systematically applied, for all $i=2,3,4$ and all ship sections, which are described in more details in Appendix B, where also numerical results are systematically presented and compare with measured data for validation.

Based on the strip theory approximations and on eqns. (1.3.3)-(1.3.6), the hydrodynamic coefficients are obtained by the following integral

$$\Pi_{\ell i}^0=\rho\int_L\int_{C(x_1)}N_\ell\phi_i^0\,ds\,dx_1=\int_L\varpi_{i\ell}(x_1)\,dx_1\ ,\ \ell,i=2,3,4\ , \tag{11a}$$

where

$$\varpi_{i\ell}(x_1) = \int_{C(x_1)} N_\ell \phi_i^0 ds \quad , \quad \ell, i = 2,3,4 . \tag{11b}$$

The above matrix $\varpi_{i\,\ell}(x_1)$ is the two dimensional hydrodynamic coefficients, for each section at the point x_1 see, e.g. G. Athanasoulis, K. Belibassakis (lectures, 2012).

The rest of the hydrodynamic coefficients can be formulated through eqn. (11b) as follows

$$\Pi_{25}^0 = \int_L \varpi_{52} dx_1 \ , \tag{12a}$$

and by Eq. (6b)

$$\Pi_{25}^0 = -x_1 \int_L \varpi_{22} dx_1 \ . \tag{12b}$$

Equivalently,

$$\Pi_{55}^0 = \int_L x_1^{\,2} \varpi_{33} dx_1 \ . \tag{13}$$

In addition,

$$\varpi_{i\ell}(x_1) = a_{i\ell}(x_1) + \frac{b_{i\ell}(x_1)}{j\omega} \ , \quad \ell, i = 2,3,4 , \tag{14}$$

where $a_{i\ell}$, $b_{i\ell}$ depicture the added mass and the damping coefficients, respectively. Based on Green's second the added mass and damping matrices are symmetric,

$$a_{i\ell} = a_{\ell i} \text{ and } b_{i\ell} = b_{\ell i} \ . \tag{15}$$

Moreover, the component N_3 is symmetric while N_2 and N_4 are anti-symmetric, and therefore, the potential ϕ_3 is symmetric and ϕ_2 , ϕ_4 are anti-symmetric. It follows:

$$a_{32} = a_{34} = 0 \ , \ b_{32} = b_{34} = 0 \ , \tag{16}$$

Hydrodynamic Forces

According to strip theory, the three dimensional generalized forces on the surface of the hull due to incident wave potential (Froude-Krylov forces) and the diffraction forces are also calculated by corresponding integration along the length of the hull.

3.2.1 Froude-Krylov force

$$F_{I\ell} = \iint_{\partial D_B} -\rho \left(j\omega_0 - U \frac{\partial}{\partial x_1} \right) \Phi_I(\boldsymbol{x})\, n_\ell \, dS_B \ , \tag{1}$$

where

$$\Phi_I(\boldsymbol{x}) = \frac{jgA}{\omega_0} \frac{\cosh[\kappa_0(x_3+h)]}{\cosh \kappa_0(h)} e^{-j\kappa_0(x_1\cos\beta + x_2 \sin\beta)} \ , \tag{2a}$$

denotes the incident potential for finite water depth (h), while the incident potential equation for deep water is

$$\Phi_I(\boldsymbol{x}) = \frac{jgA}{\omega_0} e^{(\kappa_0 x_3)} e^{-j\kappa_0(x_1\cos\beta + x_2 \sin\beta)} \ , \tag{2b}$$

where A stands for the amplitude of the incident wave, see, G. Athanasoulis, K. Belibassakis (2012), Salvesen (1970, Appendix 1). Eqn. (1), can be written

$$F_{I\ell} = -j\rho\omega_0 \int_L \left[\int_{C_{(x_1)}} \Phi_I n_\ell ds \right] dx_1 \ . \tag{3a}$$

Using (2.2)-(2.5), we obtain

$$F_{I\ell} = -j\omega_0\rho \int_L \left[\int_{C_{(x_1)}} \Phi_I N_\ell ds \right] dx_1 \ , \ \ \ell = 2,3,4 \ , \tag{3b}$$

and

$$F_{I5} = j\omega_0\rho \int_L x_1 \left[\int_{C_{(x_1)}} \Phi_I N_3 ds \right] dx_1 \ , \quad \text{and} \quad F_{I6} = -j\omega_0\rho \int_L x_1 \left[\int_{C_{(x_1)}} \Phi_I N_2 ds \right] dx_1 \ ,$$

(3c,d) for $\ell = 5$ and $\ell = 6$, respectively.

3.2.2 Diffraction force

The general expression depicturing the force produced by the deflection potential is

$$F_{D\ell} = \iint_{\partial D_B} -\rho \left(j\omega - U \frac{\partial}{\partial x_1} \right) \Phi_D n_\ell \, dS_B \ . \tag{1}$$

The analytical schema for the diffraction potential Φ_D remains undefined. Having presented the equation (1.3.2) for the radiation problem we use the Stoke's theorem, and then we apply the conditions (1.1.18), (1.1.19) in conjunction with the free surface boundary condition (1.1.20). Then the formula (1) becomes

$$F_{Di} = \rho j\omega \iint\limits_{\partial D_B} \left(\frac{\partial \Phi_i^0}{\partial n} - \frac{U}{j\omega} \frac{\partial \Phi_i^U}{\partial n} \right) \Phi_I \, dS_B \ . \tag{2}$$

The application of Gauss's second theorem on the pairs of functions, $\left(\Phi_i^0, \Phi_I\right)$ and $\left(\Phi_i^U, \Phi_I\right)$, which both satisfy the Laplace field equation and the free surface boundary condition, see, e.g. G. Athanasoulis, K. Belibassakis, (2012), provides us with

$$\iint\limits_{\partial D_B} \frac{\partial \Phi_i^0}{\partial n} \Phi_I dS_B = \iint\limits_{\partial D_B} \frac{\partial \Phi_I}{\partial n} \Phi_i^0 dS_B \ , \tag{3}$$

$$\iint\limits_{\partial D_B} \frac{\partial \Phi_i^U}{\partial n} \Phi_I dS_B = \iint\limits_{\partial D_B} \frac{\partial \Phi_I}{\partial n} \Phi_i^U dS_B \ . \tag{4}$$

Hence, Eqn. (3) is now

$$F_{Di} = \rho j\omega \iint\limits_{\partial D_B} \left(\Phi_i^0 - \frac{U}{j\omega} \Phi_i^U \right) \frac{\partial \Phi_I}{\partial n} dS_B \ . \tag{5a}$$

Additionally , using $\Phi_i^U = 0$, $i = 2,3,4$ in (5a), we get

$$F_{Di} = \rho j\omega \iint\limits_{\partial D_B} \Phi_i^0 \frac{\partial \Phi_I}{\partial n} dS_B \ , \quad i = 2,3,4 \ , \tag{5b}$$

and from $\Phi_5^U = \Phi_3^0$, $\Phi_6^U = -\Phi_2^0$ it becomes

$$F_{D5} = \rho j\omega \left[\iint\limits_{\partial D_B} \Phi_5^0 \frac{\partial \Phi_I}{\partial n} dS_B - \iint\limits_{\partial D_B} \frac{U}{j\omega} \Phi_3^0 \frac{\partial \Phi_I}{\partial n} dS_B \right] , \tag{6a}$$

$$F_{D6} = \rho j\omega \left[\iint\limits_{\partial D_B} \Phi_6^0 \frac{\partial \Phi_I}{\partial n} dS_B + \iint\limits_{\partial D_B} \frac{U}{j\omega} \Phi_2^U \frac{\partial \Phi_I}{\partial n} dS_B \right] , \tag{6b}$$

The derivative of Φ_I with respect to the components of the normal vector $\boldsymbol{n}$ (consider slender body assumptions for the x_1 direction), i.e.

$$\frac{\partial \Phi_I}{\partial n} = jA\omega_0 \left(n_3 - jn_2 \sin\beta\right) e^{\kappa_0 x_3} \, e^{-j\kappa_0 (x_1 \cos\beta + x_2 \sin\beta)} \tag{7}$$

shows that the expressions (5b) and (6a,b), take the equivalent forms

$$F_{Di} = \rho j\omega A \int_L \omega_0 \, e^{-j\kappa_0 x_1 \cos\beta} \left[\int_{C(x_1)} (jN_3 + N_2 \sin\beta) e^{\kappa_0 x_3} e^{-j\kappa_0 x_2 \sin\beta} \Phi_i^0 ds \right] dx_1 \ ,$$

$$i = 2,3,4 \qquad (8a)$$

where $\Phi_i^0 = \varphi_i$, $i = 1,2,3$, see eq. (6a) , and so, F_{Di}, becomes

$$F_{Di} = \rho j\omega A \int_L \omega_0 \, e^{-j\kappa_0 x_1 \cos\beta} \left[\int_{C(x_1)} (jN_3 + N_2 \sin\beta) e^{\kappa_0 x_3} e^{-j\kappa_0 x_2 \sin\beta} \varphi_i ds \right] dx_1 \ .$$

$$i = 2,3,4 \qquad (8b)$$

Let, h_i , be the expression

$$h_i(x_1) = \int_{C(x_1)} (jN_3 + N_2 \sin\beta) e^{\kappa_0 x_3} e^{-j\kappa_0 x_2 \sin\beta} \phi_i ds \ , \qquad i = 2,3,4 \qquad (9)$$

referring to the two-dimensional problem of the section at x_1 , of the hull, where the radiation potential is given through eqn. (2.6a).

Furthermore, by (2.6b) and (2.6c)

$$F_{D5} = -j\omega\rho A \int_L \left(x_1 + \frac{U}{j\omega} \right) h_3(x_1) \, dx_1 \ , \qquad i = 5, \qquad (10a)$$

where $h_3(x_1) = \int_{C(x_1)} (jN_3 + N_2 \sin\beta) \, e^{\kappa_0 x_3} \, e^{-j\kappa_0 x_2 \sin\beta} \phi_3 \, ds$

and

$$F_{D6} = j\omega\rho A \int_L \left(x_1 + \frac{U}{j\omega} \right) h_2(x_1) \, dx_1 \ , \qquad i = 6 \ , \qquad (10b)$$

respectively, where $h_2(x_1) = \int_{C(x_1)} (jN_3 + N_2 \sin\beta) \, e^{\kappa_0 x_3} \, e^{-j\kappa_0 x_2 \sin\beta} \phi_2 \, ds$.

3.3 Numerical results

An experiment conducted in the BGO-First Basin, Toulon, France with regards to a flexible barge of specific characteristics is presented by Senjanovic, Malenica, Tomasevic (2007). The barge, as described in their work, consists of 12 pontoons attached to each other through a steel rod which is placed above the deck level in such a way that the gravity center is lower than the deformation center, see, Fig.10. Though, the shape of the front pontoon is different from the others. In the context of this experiment the determination of the hydrodynamic ship properties employs a 3D hydrodynamic model which exploits linear (3D) flow potential analysis. However, concerning the used hydrostatic model (Malenica et al. 2007), it actually calculates the modal forces as the work of static and dynamic forces on the rigid body and so modal restoring forces include large displacements contrasting to the developed method of this thesis. From our viewpoint, we treat the hydrodynamic responses of the barge by means of Strip theory and a low order panel (BEM) within a 2D potential flow analysis. The illustration of the barge geometry is derived through the program barge.m, see, Fig. 1. In this section we will compare the hydrodynamic ship properties, obtained by the developed model of this thesis (cresolg.m), with the ones derived from the Toulon experiment, see also, Tomasevic (2007) and Senjanovic, Grubisic (1991).

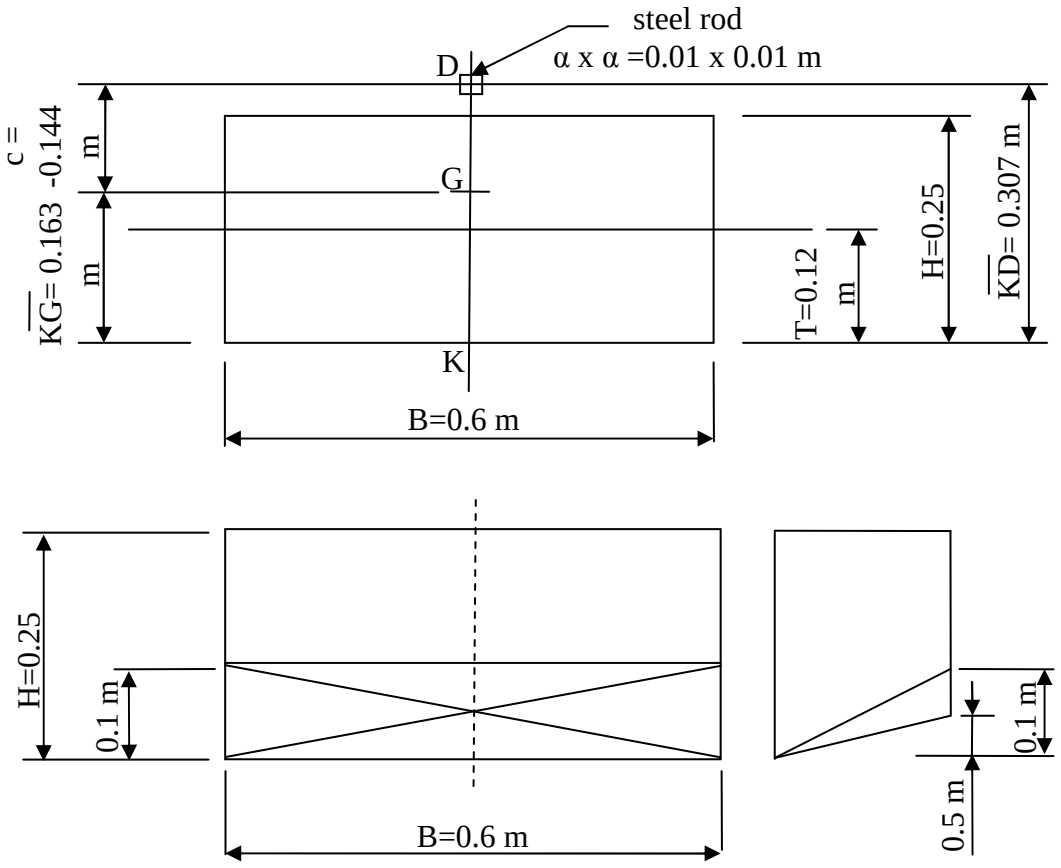

Fig. 1. Barge's cross section

The main characteristics of the barge are:

- Young's modulus of rod : $E = 2.1\ 10^{11}\ \left[\mathrm{N/m^2}\right]$
- Moment of inertia of rod cross section : $I_y = I_z = \dfrac{\alpha^4}{12} = 8.33\ 10^{-10}\ \left[\mathrm{m^4}\right]$
- Bending stiffness of rod : $EI = 175\ \left[\mathrm{N\,m^2}\right]$
- Pontoon length : $l = 0.19\ \left[\mathrm{m}\right]$
- Barge length (pontoons + clearances) : $L = 2.445\ \left[\mathrm{m}\right]$
- Total mass (pontoons and equipment) : $M = 171.77\ \left[\mathrm{kg}\right]$
- Distributed mass : $m = M/L = 70.253\ \left[\mathrm{kg/m}\right]$
- $i_x = 0.225\ \left[\mathrm{m}\right]$
- $J = mi_x^2 = 3.556\ \left[\mathrm{kg\,m}\right]$.

For a more detailed description of the barges main characteristic see, Remy et al (2006) and also Malenica et al (2003).

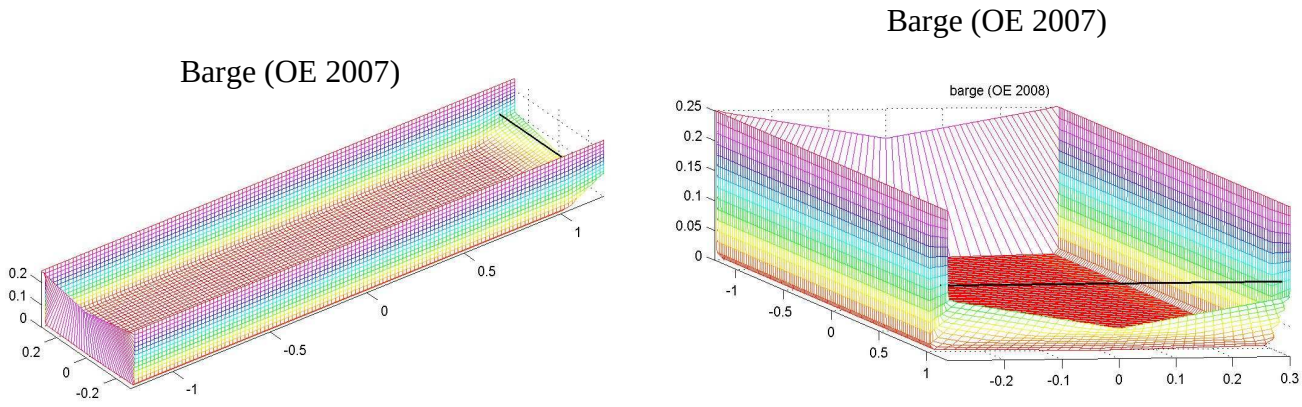

Fig. 2. 3D modeling of the barge (OE 2008)

Calculation of the hydrostatic and hydrodynamic coefficients of the prismatic barge

By means of BEM analysis we calculate the radiation potential given a cross section area with geometrical characteristics $B/T=6$, see Appendix B. Then, we determine the 2D hydrodynamic coefficients $a_{\ell,i}, b_{\ell,i}$ and demonstrating the results Fig. 1.

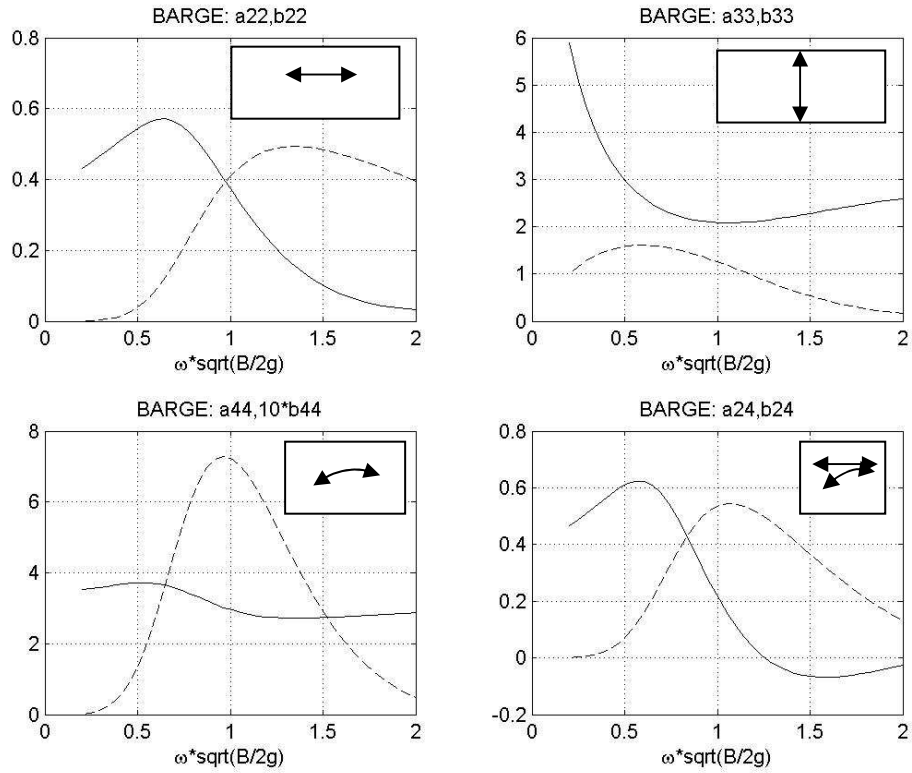

Fig. 1. Numerical hydrodynamic coefficients for $B/T=6$.

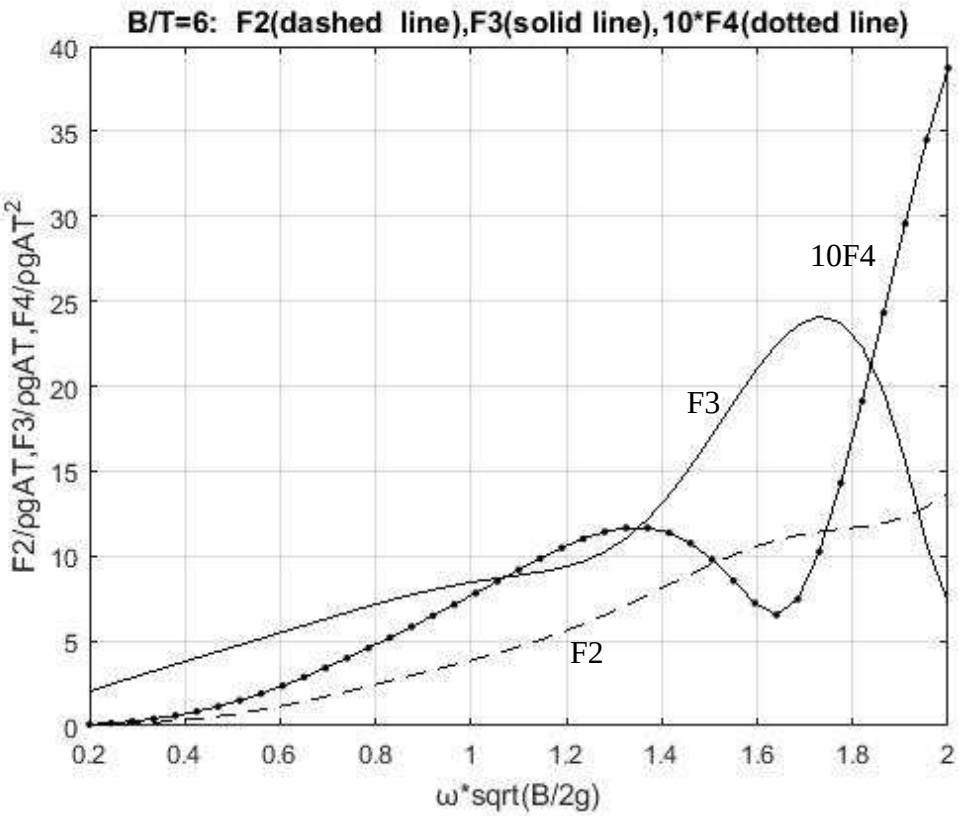

Fig. 2. Numerical hydrodynamic forces F_2 , F_3 ,$10F_4$ for $B/T = 6$

Finally, the strip theory analysis is used to calculate the forces acting on the hull of the barge. We illustrate the results in Fig.2

The produced results present quite good agreement based on the results obtained from the research of Senjanovic et al. (2009, Fig. 9). In particular, the Response Amplitude Operator (RAO) of the barge in heaving motion for wave period domain $T \le 5s$, is presented in Fig. 3. The results shown in this figure concern nondimensional heave amplitude ξ_3 with respect to the wave height $A = \frac{H}{2}$. We investigate the calculated RAOs under different incidence wave angles for the case of the barge with zero Froude number.

We observe that for high period values the response of the barge, ξ_3, is approximately equal to the wave height A, i.e. $RAO = 1$, while moving to higher wave angles the peak of the RAO is transferred to lower period values. The response of the barge is highly increased as we move to higher angles of attack, e.g., 90°. On the other hand, we regard the wave angle of 60° to be the most proper case to represent the coupling between the rigid and the flexural modes concerning vertical vibrations, in order to compare the developed method with experimental measurements obtained from Senjanovic et al (2009, Fig. 12) , via digitization.

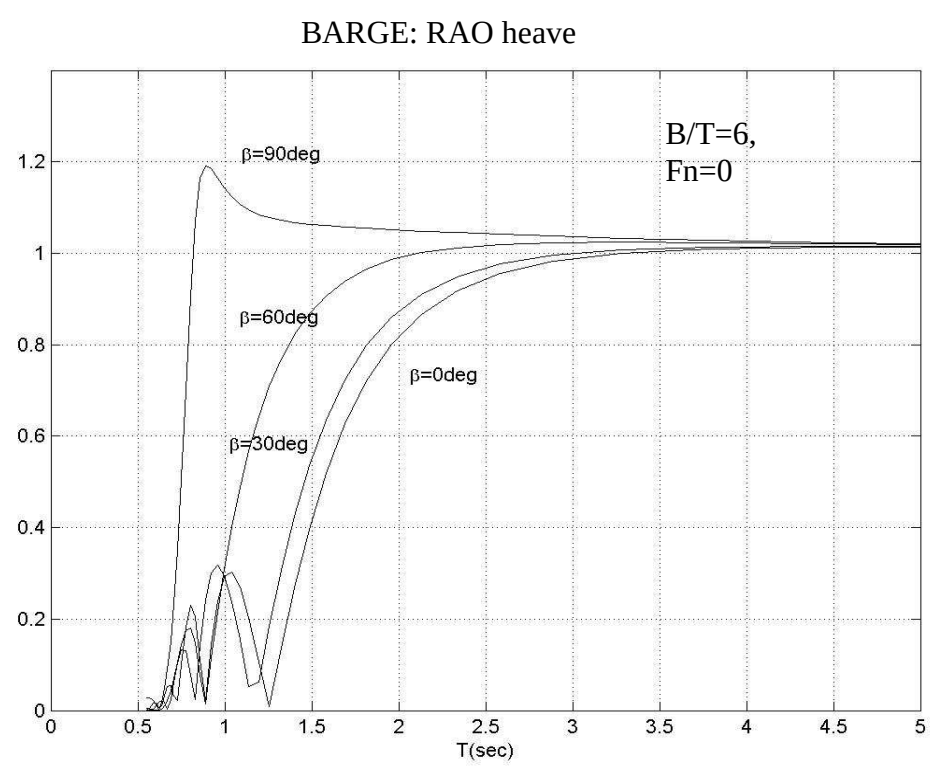

Fig. 3. Response Amplitude Operator (RAO) for heading angles (0, 30, 60, 90)

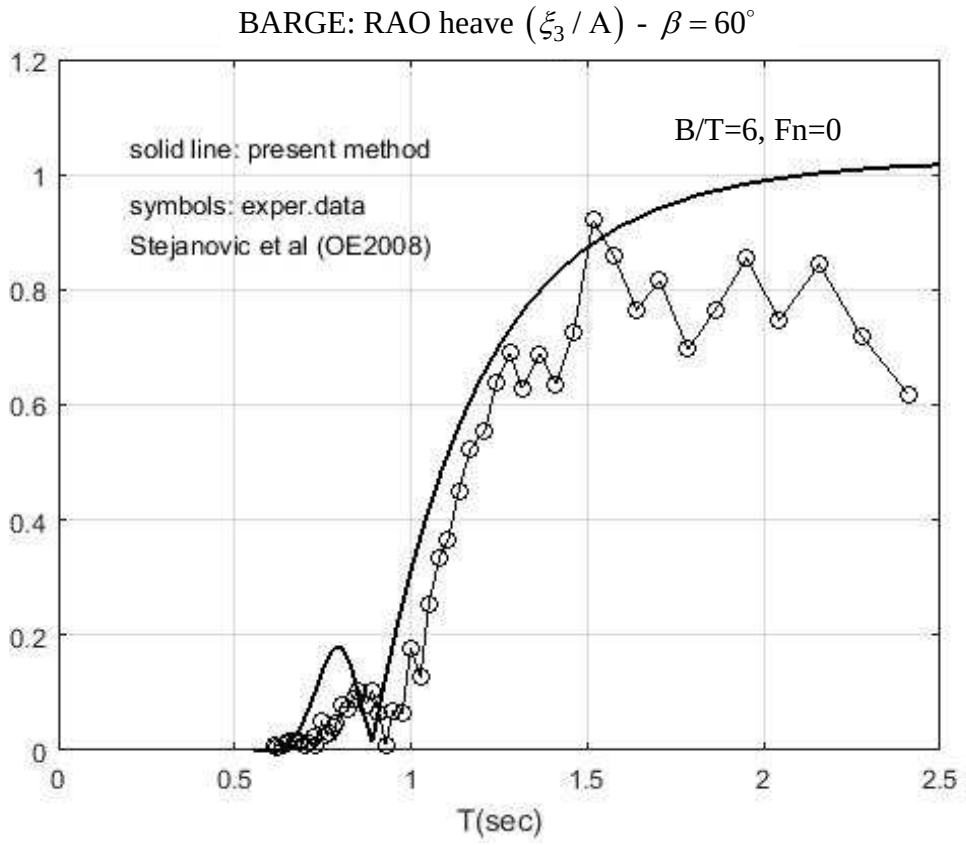

Fig. 4. Numerical method vs. experimental measurements, for angle 60°

The experimental measurements included in Fig. 4 are obtained through digitization from experimental results presented in Senjanovic et al. (2009, Fig. 12). It is obvious that the most significant discrepancies spotted between the experimental points and the numerical method, occur in the area of the peak of the response, $\xi_3/A \approx 0.19$. Also because of the resonance of the vertical oscillations in the area where unit convergence of the RAO is occurred, we observe a small dispersion of the measured points that slightly differs from the convergence of the numerical results.

Chapter 4

Hydroelasticity effects

4.1 Hydroelasticity of ships

In the previous chapters we have presented results concerning the determination of the dry vibrations of a beam, analyzed in the context of Euler Bernoulli (Chap.1) and Timoshenko (Chap.2) theory. The numerical solution has been obtained by discretizing and solving the corresponding equations by means of FDM. Subsequently, in Chap.3 the standard strip theory by Salvensen et al (1970) is described and applied to the calculation the hydrodynamic responses of a ship of slender hull form. In this part, for a specific hull geometry and mass distribution of a ship or floating structure (e.g. an elongated barge), an approximate hydroelastic model is presented, facilitating the treatment of vertical deformations of the hull girder. This is succeeded by expanding the deflection into dry modes, and then calculating the elastic responses by coupling with ship hydrodynamics in the framework of strip theory. For simplicity in this work only head (and/or following) harmonic waves will be considered resulting into motions and deflections considered only on the vertical plane. However, it should be remarked that the problem of head incident waves constitutes one of the most severe case (from the point of view of wave loads and responses) and thus, also a characteristic case to examine concerning the studied structure.

First, by treating the ship or the floating structure as a girder of specific mass and flexural rigidity distributions, the natural frequencies and normal modes are calculated by using the specific beam model. In the examples presented in this chapter the Euler – Bernoulli model is used. From the solution of problem concerning the rigid motions of the ship under the action of sea waves, using the strip theory model, the corresponding longitudinal distributions of added mass and damping coefficients, as well as the sectional Froude - Krylov and diffractions forces are calculated. Then, by incorporating into the model the additional distributed elastic forces, the hydroelastic responses will be estimated.

To begin with, we recall Eqs. (3.1.4) describing the rigid motions of the ship or elongated floating body on the vertical plane:

$$\left(-\omega^2(M+A_{33})+i\omega B_{33}+C_{33}\right)\xi_3+\left(-\omega^2\left(A_{35}-J_1\right)+j\omega\left(B_{35}-MU\right)+C_{35}\right)\xi_5=F_3\,, \quad (1a)$$

where

$$F_3=X_{03}+X_{d3}\ , \quad (1b)$$

are the Froude-Krylov and diffraction vertical forces due to head incident waves on the ship's hull. These forces are defined by the following x_1-integrals

$$X_{03}=\int_{x_1} f(x_1)dx_1, \quad X_{d3}=\int_{x_1} h(x_1)dx_1\ . \quad (2)$$

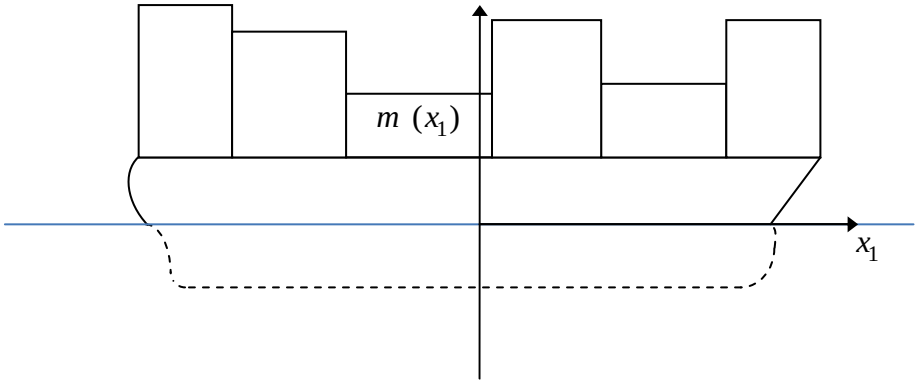

Fig. 1. Ship's mass distribution

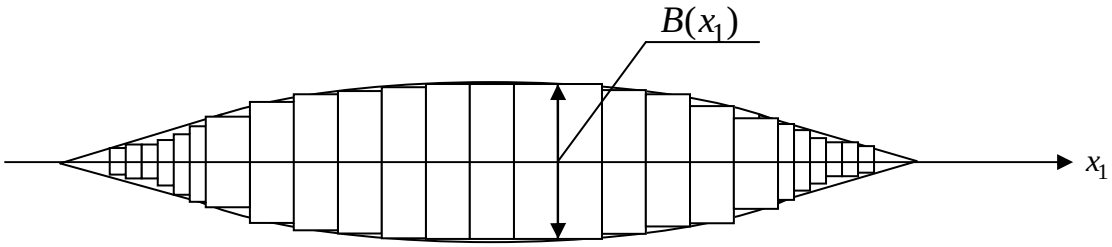

Fig. 2. Discretized sections and waterline

In Eq.(1a) M is the total mass, $M = \int_{x_1} m(x_1)dx_1$, where $m(x_1)$ denotes an equivalent mass distribution along the length of the ship, derived from the analysis of ship weights; see Fig.1. Also, we recall here that $C_{33} = \rho g A_{wl}$, where $A_{wl} = \int_{x_1} B(x_1)dx_1$ is waterline area, $C_{35} = C_{53} = -\rho g A_{wl} LCF = -\rho g \int_{x_1} x_1 B(x_1)dx_1$, where LCF is the longitudinal center of flotation; see Fig.2. Moreover, $\boldsymbol{J} = M\boldsymbol{R}_G$, where $\boldsymbol{R}_G$ is the center of gravity, and in the case of even keel ships , with LCG denoting the long center and VGC the vertical center of gravity. By using the above definitions in Eq.(1), the latter takes the following form

$$\left\{-\omega^2\left(\int_{x_1} m(x_1)dx_1+\int_{x_1} a_{33}(x_1;\omega)dx_1\right)+j\omega\int_{x_1} b_{33}(x_1;\omega)dx_1+\rho g\int_{x_1} B(x_1)dx_1\right\}\xi_3+$$

$$+\left(-\omega^2\left(-\int_{x_1} x_1 a_{35}(x_1;\omega)dx_1-LCG\int_{x_1} m(x_1)dx_1\right)+j\omega\left(-\int_{x_1} x_1 b_{35}(x_1;\omega)dx_1-U\int_{x_1} m(x_1)dx_1\right)\right)\xi_5+$$

$$-\left(\rho g\int_{x_1} x_1 B(x_1)dx_1\right)\xi_5=\int_{x_1} f(x_1)dx_1+\int_{x_1} h(x_1)dx_1=X_{03}+X_{d3}\ , \qquad (3)$$

where the hydrodynamic coefficients have been also expressed following the strip-theory approximation as longitudinal integrals of the hydrodynamic coefficients of the transverse sections of the hull in vertical oscillations

$$A_{33}(\omega)=\int_{x_1} a_{33}(x_1;\omega)dx_1\ , \qquad B_{33}(\omega)=\int_{x_1} b_{33}(x_1;\omega)dx_1\ , \qquad (4a)$$

$$A_{35}(\omega)=-\int_{x_1} x_1 a_{33}(x_1;\omega)dx_1\ , \qquad B_{35}(\omega)=-\int_{x_1} x_1 b_{33}(x_1;\omega)dx_1\ . \qquad (4b)$$

4.2 Hydroelastic responses

Let now $\Xi_3(x_1;\omega)$ denote the additional vertical oscillation at the same frequency (encounter frequency) due to the elastic responses of the ship or elongated floating structure in head or following waves $\left(\beta=180^o \text{ or } 0^o\right)$. The above hydroelastic deflection are calculated by the vertical deflection of the ship hull girder treated as an elastic Euler-Bernoulli beam, with longitudinal mass distribution $m(x_1)$ and equivalent rigidity (stiffness parameter) $D(x_1)$.

In practical applications the stiffness parameter of the structure (modeled as a floating beam) is calculated using the equation: $D(x_1)=E\,I(x_1)$, where E is the Young's modulus of the material of the structure, e.g. $E=210\cdot 10^9 GPa$ in the case of steel structure. Also, $I(x_1)$ represents the hull girder moment of inertia of the section at $x_1=const$, over the whole length of the structure. Obviously in the case of more complex or composite structures the calculation of an equivalent flexural deflection coefficient $D(x_1)$ has to be based on an appropriate analysis of the structure into its elements. Usually, such an analysis is performed only for the mid-ship section considering that the highest bending stresses occur in the middle of the ship hull. For the purposes of the present study such an analysis is needed for a number of ship sections except of the mid-section.

In order to calculate the moment of inertia of all the supporting members of a section, data are taken from the structural design of the ship, and the moment is calculated with respect to the neutral axis (of the section). The latter, is determined through the

weighted sum of all supporting members (plates, stiffeners, etc.) expressed by the relation: $(N.A.)=\left(\sum_{n=1}^{M} I_s \times a_s\right)\left(\sum_{n=1}^{M} a_s\right)^{-1}$, where a_s and I_s denote the surface and the moment of inertia of each stiffener, respectively. Following the same procedure we calculate the moment of inertia of a number of representative sections from the stem to the bow of the ship or marine structure.

To proceed, we consider that the total vertical response of the ship beam in waves is obtained as a superposition of the rigid motion on the vertical plane and the elastic deflection , as follows

$$\Xi_3(x_1;\omega)=\xi_3(\omega)+\Xi(x_1;\omega)\ , \tag{1}$$

where ξ_3 stands for the heaving motion and $\Xi(x_1)$ denotes the flexural deformation of the ship treated as a beam. Then, by considering the additional elastic forces of each beam section expressed by the term $\left(D(x_1)\Xi_{,xx}\right)_{,xx}$ in the Euler-Bernoulli beam model, and using Eq. (1.1) the latter equation takes the following form:

$$\left\{-\omega^2\left(\int_{x_1} m(x_1)dx_1+\int_{x_1} a_{33}(x_1;\omega)dx_1\right)+j\omega\int_{x_1} b_{33}(x_1;\omega)dx_1+\rho g\int_{x_1} B(x_1)dx_1\right\}(\xi_3+\Xi(x_1))+$$

$$+\left(-\omega^2\left(-\int_{x_1} x_1 a_{33}(x_1;\omega)dx_1-LCG\int_{x_1} m(x_1)dx_1\right)+j\omega\left(-\int_{x_1} x_1 b_{33}(x_1;\omega)dx_1-U\int_{x_1} m(x_1)dx_1\right)\right)\xi_5+$$

$$-\left(\rho g\int_{x_1} x_1 B(x_1)dx_1\right)\xi_5=\int_{x_1} f(x_1)dx_1+\int_{x_1} h(x_1)dx_1-\int_{x_1}\left(D(x_1)\Xi_{,xx}\right)_{,xx}dx_1\ . \tag{2}$$

By subtracting by parts Eq.(3) of the last section (expressing the rigid heave responses) from the above equation, we obtain the following equation modeling the hydroelastic vertical deformation $\Xi(x_1;\omega)$ of the hull girder in waves:

$$\int_{x_1}\left(D(x_1)\Xi(x_1)_{,xx}\right)_{,xx}dx_1-\omega^2\left(\int_{x_1} m(x_1)dx_1+\int_{x_1} a_{33}(x_1;\omega)dx_1\right)\Xi(x_1)+$$

$$+j\omega\left(\int_{x_1} b_{33}(x_1;\omega)dx_1-U\int_{x_1} m(x_1)dx_1+\rho g\int_{x_1} B(x_1)dx_1\right)\Xi(x_1)+$$

$$=\int_{x_1} f(x_1)dx_1+\int_{x_1} h(x_1)dx_1-\left(X_{03}+X_{d3}\right)\ . \tag{3}$$

From the above equation it is seen that the vertical hydroelastic responses of the hull girder in head (or following) harmonic waves can be approximately calculated by the Euler-Benoulli beam model forced by the distribution of the Froude-Krylov and diffraction forces of the wetted surface of the hull. In order to illustrate this point, let

x_1^C denote point of application of the Froude-Krylov and diffraction forces $X_{03} + X_{d3}$, while $f(x_1) + h(x_1)$ represents the distribution of the same forces over the length of the ship hull. Using a Dirac function to represent the application point x_1^C, we obtain

$$\int_{x_1} \delta(x_1 - x_1^C)\left(X_{03} + X_{d3}\right) dx_1 = X_{03} + X_{d3} \ , \tag{4}$$

and thus, Eq. (3) takes the form

$$\left(D(x_1)\Xi(x_1)_{,xx}\right)_{,xx} + \left(-\omega^2\left(m(x_1) + a_{33}(x_1;\omega)\right) + j\omega\left(b_{33}(x_1;\omega) - Um(x_1)\right) + \rho g B(x_1)\right)\Xi(x_1) =$$

$$= f(x_1) + h(x_1) - \delta(x_1 - x_1^C)\left(X_{03} + X_{d3}\right) \ . \tag{5}$$

We recall the completeness property of the beam eigenmodes $\Xi_n(x_1)$, $n = 1, 2, 3...$, which forms an orthonormal basis along the length of the ship or marine structure, defined in the case of Euler Bernoulli model considered in this chapter in the interval $-L/2(\text{stern}) < x_1 < L/2(\text{bow})$. These eigenfunctions are found as a solution of the following problem

$$\left(D(x_1)\Xi_n(x_1)_{,xx}\right)_{,xx} + \omega_n^2 m(x_1)\Xi_n(x_1) = 0 \ , \qquad n = 1, 2, 3..., \tag{6a}$$

in conjunction with the free-end conditions at the stern and bow of the ship

$$\frac{d\Xi_n(x_1 = \pm L/2)}{dx_1^2} = \frac{d\Xi_n(x_1 = \pm L/2)}{dx_1^3} = 0 \ , \qquad n = 1, 2, 3..., \tag{6b}$$

where $\omega_n, n = 1, 2, 3...,$ are the corresponding eigenfrequencies. We now express the solution $\Xi(x_1)$ of the above hydroelastic equation (Eq.5) into the modes $\Xi_n(x_1)$ as follows

$$\Xi(x_1) = \sum_{n=1}^{M} \xi_n \Xi_n(x_1) \ , \tag{7}$$

where ξ_n are the unknown hydroelastic mode amplitudes. Due to the completeness and orthogonality property of the basis $\Xi_n(x_1)$, $n = 1, 2, 3...,$ it can be also used to express the Dirac function in the following form

$$\delta(x_1 - x_1^C) = \sum_{n=1}^{M} \Xi_n(x_1)\Xi_n(x_1^C) \ . \tag{8}$$

We use the same property to express the distributions of Froude-Krylov and diffraction forces on the hull girder

$$f(x_1) = \sum_{n=1}^{M} f_n \Xi_n(x_1), \text{ where } f_n = \int_{x_1} f(x_1)\Xi_n(x_1)dx_1 \ , \tag{9a}$$

and

$$h(x_1) = \sum_{n=1}^{M} h_n \, \Xi_n(x_1), \quad \text{where } h_n = \int_{x_1} h(x_1)\Xi_n(x_1)dx_1 \ . \tag{9b}$$

Using Eq. (7) and the solution concerning the eigenvalue problem of the Euler – Bernoulli beam we have

$$\left(D(x_1)\Xi(x_1)_{,xx}\right)_{,xx} = \sum_{n=1}^{M} \xi_n \left(D(x_1)\Xi_n(x_1)_{,xx}\right)_{,xx} = -m(x_1)\sum_{n=1}^{M} \omega_n^2 \Xi_n(x_1) \ . \tag{8}$$

Replacing the representation of the solution given by Eq. (8) into Eq.(5), and using Eq.(8), the equation concerning the hydroelastic responses takes the following form

$$\sum_{n=1}^{M} \xi_n \Xi_n(x_1)\left\{-m(x_1)\omega_n^2 - \omega^2\left(m(x_1) + a_{33}(x_1;\omega)\right) + j\omega\left(b_{33}(x_1;\omega) - Um(x_1)\right) + \rho g B(x_1)\right\} =$$

$$= \sum_{n=1}^{M}\left(f_n + h_n - \left(X_{03} + X_{d3}\right)\Xi_n(x_1^C)\right)\Xi_n(x_1) \ . \tag{9}$$

Denoting the term in the brackets in the left-hand side of the above equation as

$$G_n(x_1;\omega) = -m(x_1)\omega_n^2 - \omega^2\left(m(x_1) + a_{33}(x_1;\omega)\right) + j\omega\left(b_{33}(x_1;\omega) - Um(x_1)\right) + \rho g B(x_1) \tag{10}$$

Eq. (9) is put in the form

$$\sum_{n=1}^{M} \xi_n G_n(x_1;\omega)\Xi_n(x_1) = \sum_{n=1}^{M}\left(f_n + h_n - \left(X_{03} + X_{d3}\right)\Xi_n(x_1^C)\right)\Xi_n(x_1) \ . \tag{11}$$

We now exploit the completeness of the set $\Xi_m(x_1)$, $m = 1, 2, ...,$ and project the above equation on the latter basis. Consequently, by following a Galerkin procedure, we obtain

$$\sum_{n=1}^{M} \xi_n \left\langle G_n(x_1;\omega)\Xi_n(x_1), \Xi_m(x_1)\right\rangle = \sum_{n=1}^{M}\left\{\left(f_n + h_n\right) - \left(X_{03} + X_{d3}\right)\Xi_n(x_1^C)\right\}\left\langle \Xi_n(x_1), \Xi_m(x_1)\right\rangle, \tag{12}$$

where $\left\langle f, g \right\rangle = \int_{x_1} f(x_1), g(x_1)dx_1$ denotes the L_2-inner product in the x_1-interval, and $\left\langle \Xi_n, \Xi_m \right\rangle = \delta_{nm}$, the Kronecker's delta. Subsequently, by defining the coefficient matrix in the left-hand side of Eq.(12)

$$A_{mn} = \left\langle G_n(x_1;\omega)\Xi_n(x_1), \Xi_m(x_1)\right\rangle, \tag{13a}$$

and the right-hand side vector as follows

$$H_m = f_m(x_1) + h_m(x_1) - \left(X_{03} + X_{d3}\right)\Xi_m(x_1^C) \ , \tag{13b}$$

and thus the hydroelastic amplitudes $\xi_n(\omega)$ are found as the solution of the following linear algebraic system

$$\sum_{n=1}^{M} A_{mn}(\omega)\xi_n = H_m(\omega),\ m=1,2,...M\ . \tag{14}$$

The corresponding hydroelastic complex RAO at each frequency ω is obtained as

$$RAO_{\Xi}(x_1;\omega) = \frac{\Xi(x_1;\omega)}{\mathrm{A}} = \frac{\sum_{n=1}^{M}\xi_n(\omega)\Xi_n(x_1)}{\mathrm{A}}\ , \tag{15a}$$

where $A=H/2$ is the wave amplitude. In addition the RAO associated with the hydroelastic amplitudes

$$RAO_n(\omega) = |\xi_n|/A\ , \tag{15b}$$

are sometimes used for illustrating the responses.

In the case of a ship or marine structure with constant sections, i.e.

$$m(x_1) = const\ ,\ B(x_1) = const\ ,\ a_{33}, b_{33}(x_1) = const\ ,$$

the coefficient matrix $A_{mn}(\omega)$ contains only its diagonal elements and the following expression is obtained the modal amplitudes $\xi_n(\omega)$

$$\xi_n(\omega) = \frac{f_n + h_n - (X_{03} + X_{d3})\Xi_n(x_1^C)}{-m(\omega_n^2 + \omega^2) - \omega^2 a_{33} + j\omega(b_{33} - Um) + \rho g B},\ n=1,2,....M.\ , \tag{16}$$

at a wave frequency ω .

4.3 Hydroelastic analysis of a barge in waves

At this point, we recall the previously mentioned experiment of the flexible barge, conducted in the BGO-First Basin, Toulon, see, Senjanovic et al. (2008). In this case, the structural response of the barge concerned both the vertical and the coupled horizontal – torsional system of, the global load induced, vibrations. The vertical distortions have been found analytically based on the Timoshenko, Young (1955) while the system of horizontal – torsional distortions has been calculated analytically by direct integration and Ritz method in addition to numerical calculations by means of 1D FEM analysis. It is worth mentioning that this barge is a special form of ship with zero velocity $U=0$ and specific geometrical characteristics see Fig.1 and Ch. 3.3. The design of the barge permits the development of hydroelastic phenomena which are associated with the flexural deformations of the barge as it, approximately, follows the elevation of its water environment. For simplicity we set the origins of the coordinate system in the middle of the barge as seen in Fig. (1) To model the dry vibrations of the barge we treat the latter as an Euler – Bernoulli beam with free edges and then by means of FDM analysis we discretize the barge into 150 elements using the program EBT2.m.

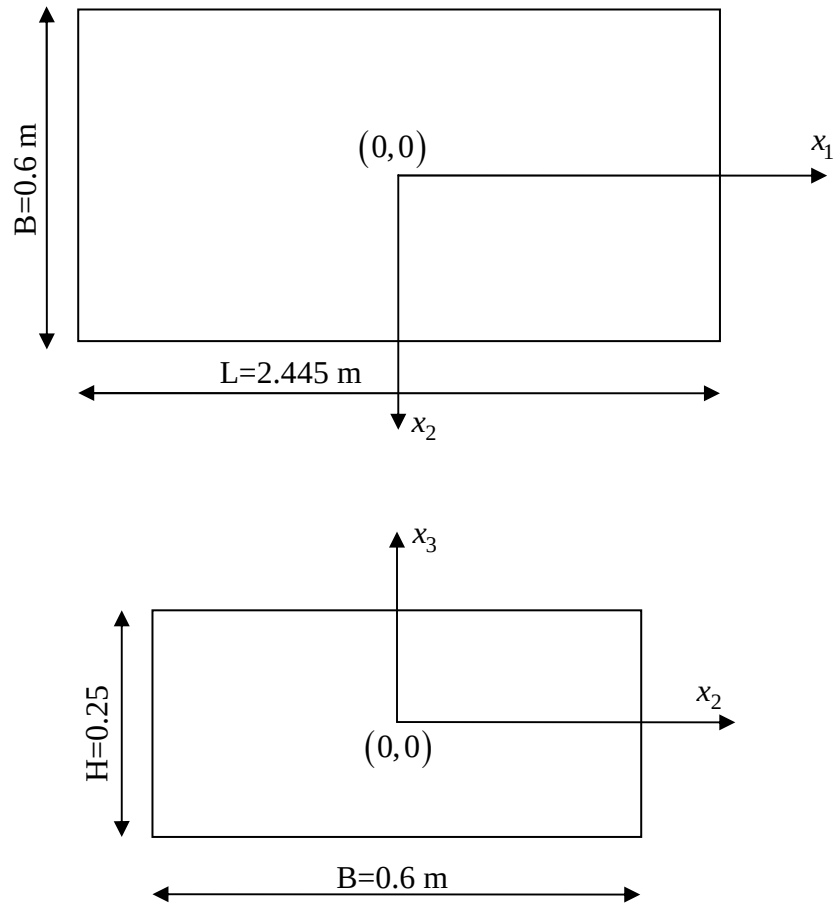

Fig. 3. Barge's geometrical characteristics

This specific type of ship, is associated with a set of geometrical and hydrostatic properties such as: (i) symmetry with respect to the transverse, x_2x_3-plane , see Fig. 1. (ii) The barge is even keel and therefore the VCB lies on the same vertical segment with VCG. (iii) Due to the barge's symmetry LCF and LCG are located at the origins of the coordinate system where $x_1 = 0$.

Given the above properties we get:

- $C_{35} = C_{53} = -\rho g \int_{x_1} x_1 B(x_1) dx_1 = 0$, due to ship's symmetry, see (i)

- $J_1 = M\ LCG = 0$, because of property (iii).

Also given the negligible velocity of the barge, $U = 0$ we reduce the Eq. (1.1.a) to

$$\left(-\omega^2(M + A_{33}) + i\omega B_{33} + C_{33}\right)\xi_3 + \left(-\omega^2\left(A_{35}\right) + j\omega\left(B_{35}\right)\right)\xi_5 = F_3 \ , \qquad (1)$$

which in turn is analyzed , based on the Eq. (2.5), as follows

$$\int_{x_1}\left(D(x_1)\Xi(x_1)_{,xx}\right)_{,xx}dx_1-\omega^2\left(\int_{x_1}m(x_1)dx_1+\int_{x_1}a_{33}(x_1;\omega)dx_1\right)\Xi(x_1)+$$

$$+j\omega\left(\int_{x_1}b_{33}(x_1;\omega)dx_1+\rho g\int_{x_1}B(x_1)dx_1\right)\Xi(x_1)=\int_{x_1}f(x_1)dx_1+\int_{x_1}h(x_1)dx_1-\left(X_{03}+X_{d3}\right)\ .$$

(2)

4.3.2 Flexural Responses

The Euler – Bernoulli beam modeled barge problem (eigenfrequencies and eigenmodes) is solved by the program ''EBT2.m'' and the results are depicted in Table 1. For the analytical determination of the eigenfrequencies eq. (11) in Ch. 1.2 , see also, Timoshenko , Young (1995).

Mode	Analytic Method Frequencies	Numerical Method Frequencies
1	5.7291	5.9249
2	16.1276	16.3192
3	31.7252	32.009
4	53.042	52.9193

Table 1 Natural frequencies $\left[\text{rad/s}\right]$

The results (numerical and analytical) are in a good agreement. The flexural modes of the barge dry vibrations are depicted in Fig. 1 and in addition we demonstrate the deformation of the wet surface for the first three natural frequencies, see, Fig. 2 (a) , (b) .

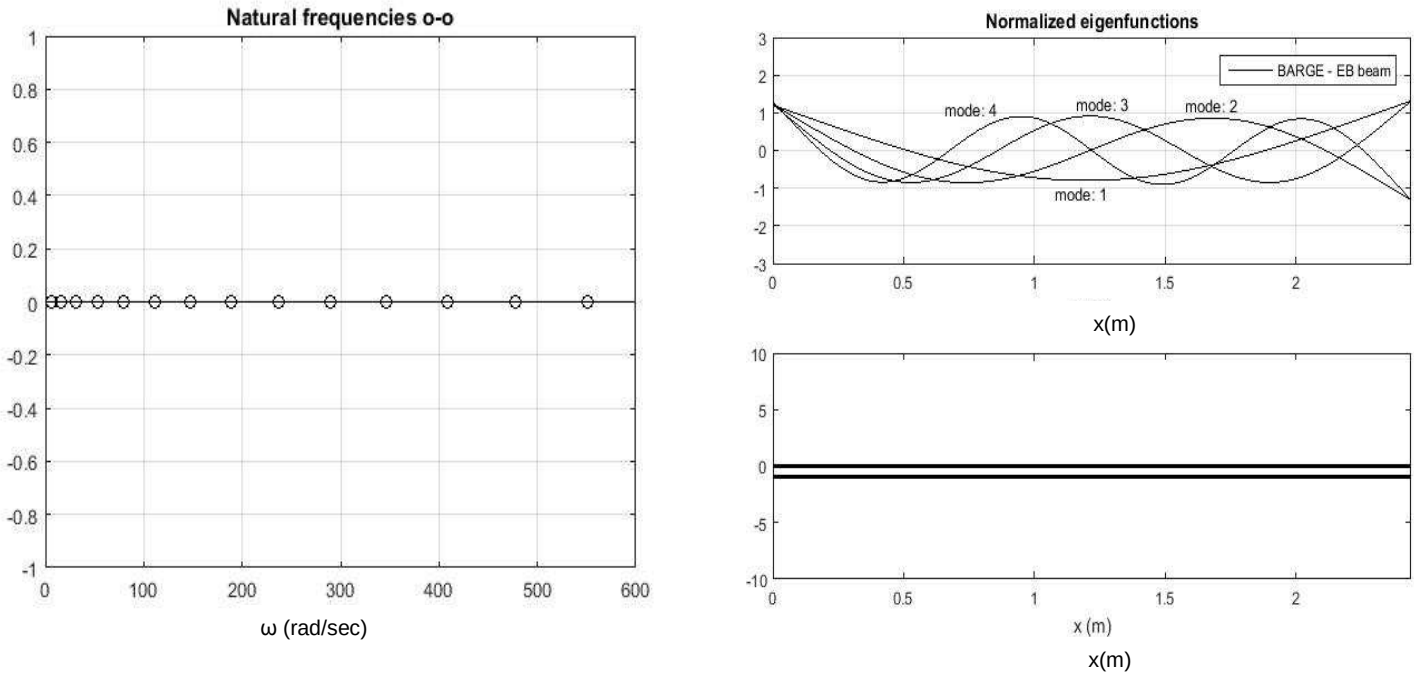

Fig. 4. Natural frequencies (left), normal modes (right)

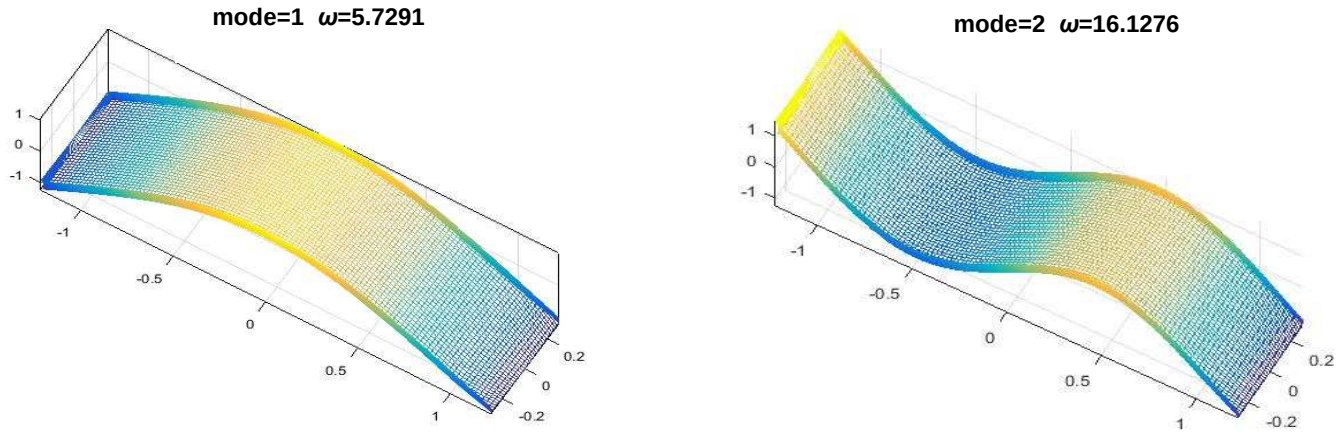

Fig. 5. (a) Barge surface at the first (left) and second (right) natural modes

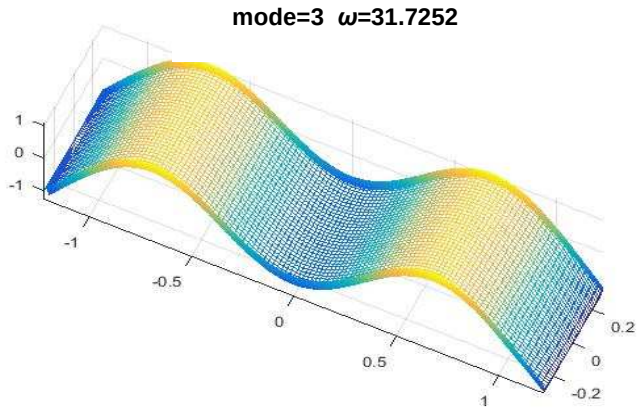

Fig. 5. (b) Barge surface at the third natural mode

4.3.4 Hydroelasticity of the barge

The determination of the dry modes in addition to the determination of the hydrodynamic coefficients (four rigid body motions included, see, Ch.3.2.3) provide us with all the proper parameters that are needed so as to define the barge's response in different heading wave angles. The flexible design of the barge allows its distortion according to the elevation of the waves, see, Fig.1.

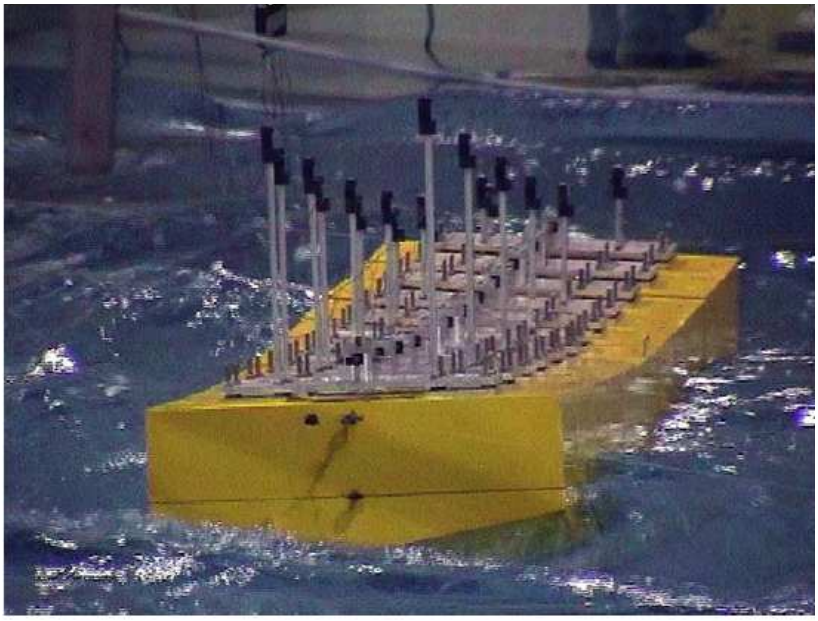

Fig. 6. Barge flexibility during test experiments , from Malenica et al. (2008)

As described in Ch. 4.2 the hydroelastic response in its discretized form is

$$\sum_{n=1}^{M} \xi_n G_n(x_1;\omega)\Xi_n(x_1) = \sum_{n=1}^{M} \left(f_n + h_n - \left(X_{03} + X_{d3}\right)\Xi_n(x_1^c)\right)\Xi_n(x_1) \ , \qquad (1)$$

where

$$G_n(x_1;\omega) = -m(x_1)\omega_n^2 - \omega^2\left(m(x_1) + a_{33}(x_1;\omega)\right) + j\omega b_{33}(x_1;\omega) + \rho g B(x_1) \ . \quad (2)$$

and ω_n , $n = 1, 2, ...,$ are the eigenfrequencies of the barge modeled as a beam, see, Table1 in chapter 4.3.2.

The final solution of the ξ_n amplitudes require the solution of the linear algebraic system

$$\sum_{n=1}^{M} \xi_n \left\langle G_n(x_1;\omega)\Xi_n(x_1), \Xi_m(x_1)\right\rangle = \sum_{n=1}^{M} \left\{ \left(f_n + h_n\right) - \left(X_{03} + X_{d3}\right)\Xi_n(x_1^c)\right\}\left\langle \Xi_n(x_1), \Xi_m(x_1)\right\rangle \ . \quad (3)$$

Because of the barge geometry, see, Fig. 3.1.1, we obtain the properties $m(x_1) = const$, $B(x_1) = const$, $a_{33}, b_{33}(x_1) = const$ and so the coefficient matrix $A_{mn}(\omega)$, which stands for the left- hand side of Eq. (3), is a diagonal matrix.

Therefore, the modal amplitudes of its hydroelastic response are given be their reduced form

$$\xi_n(\omega) = \frac{f_n + h_n - (X_{03} + X_{d3})\Xi_n(x_1^C)}{-m(\omega_n^2 + \omega^2) - \omega^2 a_{33} + j\omega(b_{33} - Um) + \rho g B}, \; n = 1,2,....M. \; , (4)$$

In the following figures we present the modal amplitude, ξ_3 of the heave related motion and the elastic responses too. In the following figure the second mode is related to heave motion while the rest modes, starting from mode No.4, concern the elastic response of the barge. The structural behavior of the hull is determined for heading waves with angle 120° using a variety of single length waves that are $\lambda/L = (0.51, 1.01, 1.48, 2.06)$.

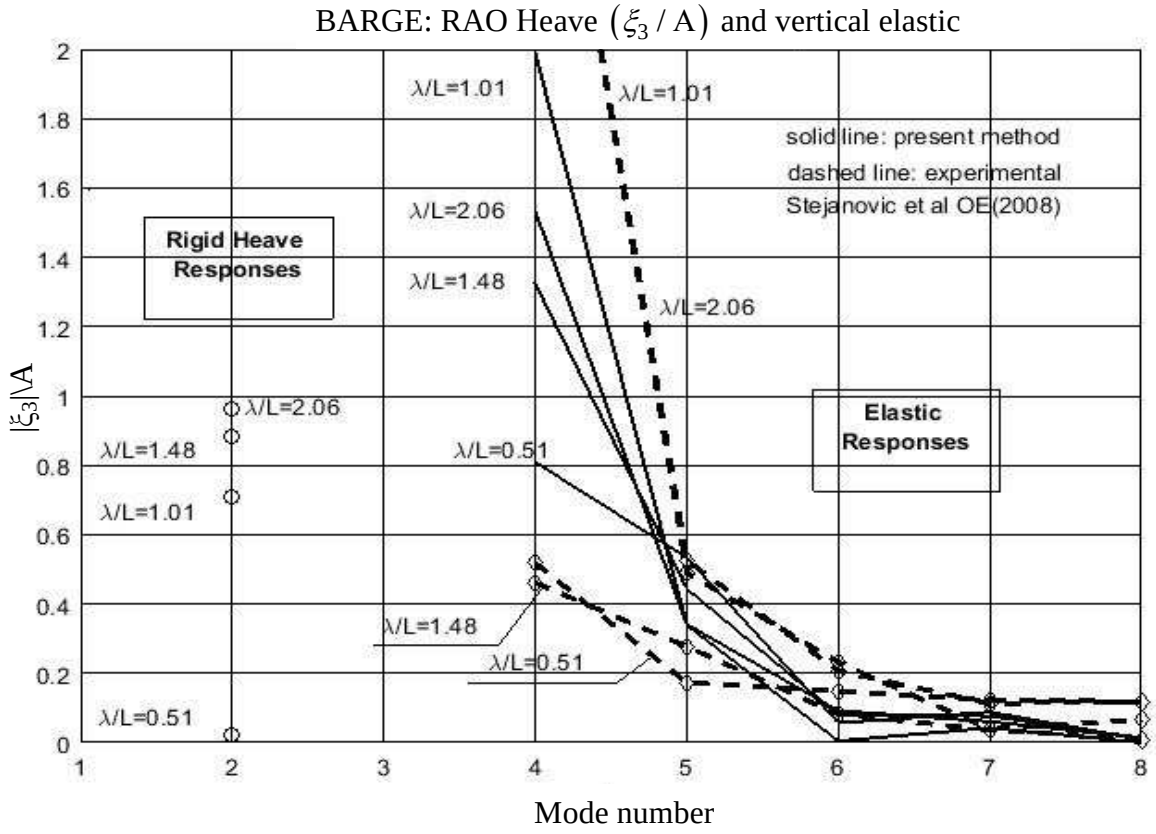

Fig. 7. Modal amplitude, heading angle 120°. Elastic modes start from mode number 4.

Conclusions - suggestions for future work

In the present thesis, we use the Euler – Bernoulli (EBT) and the Timoshenko beam (TBT) models to calculate the "dry modes" of a ship or a marine structure. Numerical calculations are based on second order Finite Difference Method for the solution of the eigenvalue problems, for pinned, fixed and free ends of an elastic beam, which models the marine structure. We implement the aforementioned models for both the case of a rectangular cross section area, i.e., a beam, and of a circular section area, i.e., a rod, and for selected end conditions, such as (i) free - free, (ii) clamped – clamped, and (iii) pinned – pinned. The dispersion relations of the two models are studied in the case of homogeneous beams illustrating significant differences, and showing that the elastic disturbances (waves of vertical beam deflections) disperse faster in EBT than TBT model. Concerning TBT formulation, the elastic wave phase velocity converges to a single value which is higher in the case of a rod ($C \approx 0.56$) than in the case of the beam ($C \approx 0.54$). Subsequently, the above models are applied to specific examples, and numerical results are compared to existing analytical ones, concerning the determination of the natural frequencies and of the principal modes of the structure. Convergence tests are conducted in order to estimate the validity of the developed numerical methods. It turns out that the obtained results are very accurate and the rate of convergence is very fast.

Next, the standard STF (strip theory) model is used for the prediction of the rigid ship or elongated marine structure responses in head or following waves. To this aim, we use a 2D potential flow model implemented by means of Boundary Element formulations regarding sections with different local geometrical particulars, i.e., for various beam to draft ratios, B/T. The calculations predict very well the ship properties of interest, i.e., added mass and damping coefficients, and generalized forces, as compared with experimental results by Vughts (1968). Significant, though expected, discrepancies from the experimental values are observed in the case of roll motion, since roll hydrodynamics are dominated by viscous effects, which are not taken into account in the present ideal flow model.

Finally, in this work, a model is developed to calculate the hydroelastic responses of beamlike marine structures by combining strip theory and beam elastic models. Results and comparisons are presented concerning the hydroelastic response of a flexible barge in waves, for which experimental data are available by using model tests, see, e.g., Malenica et al. (2008). In general, present results regarding heave motion and corresponding elastic responses for various incident waves are in a good agreement with experimental data, showing that the developed model can produce accurate results. Additional studies concerning the hydroelastic analysis of ships, such as tankers or bulk carriers, could also be conducted in order to further test and validate the present model. Future work should focus on appropriate extensions of the present model in order to take into account more consistently 3D hydrodynamic and elastic structural phenomena.

References

Akrivis G.D, Dougalis B.A., 1997, *Numerical methods for differential equations*.

Aksu, S., Price, W. G., Temarel, P. 1991 A comparison of two-dimensional and three-dimensional hydroelasticity theories including the effect of slamming. Proc. IMechE, Part C: J.Mechanical Engineering Science, 205(C1), pp.3–15. DOI: 10.1243/PIME_PROC_1991_205_084_02

Aksu, S., 1993 Steady state and transient responses of flexible ship structures travelling in irregular sea – way, PhD thesis, University of Southampton

Athanasoulis, G.A, Belibassakis, K.A., 2012, Ship Dynamics – Lecture Notes, School of NA&ME, NTUA

Basaran, I., Belik, O., Temarel, P., 2008, Dynamic behavior of a container ship using two- and threedimensional hydroelasticity analyses. In Proceedings of the 27th OMAE, paper 57401

Belibassakis, K.A., Athanassoulis, G.A., Gerostathis, Th., 2001, A coupled-mode system for the refraction-diffraction of linear waves over steep three dimensional topography, Applied Ocean Research, Vol. 23, pp. 319-336.

Belibassakis, K.A., Athanassoulis, G.A., A coupled-mode system with application to nonlinear water waves propagating in finite water depth and in variable bathymetry regions, Coastal Engineering Vol. 58, pp.337-350 2011

Beer G., Smith I., Duenser, C. 2008 The Boundary Element Method with Programming, Springer

Berenger J.P. 1994 A perfectly matched layer for the absorption of electromagnetic waves. J. Comput. Phys. , pp 114 - 185

Bishop R.E.D, Price W.G. 1979 Hydroelasticity of ships, Cambridge University Press

Bishop, R. E. D., Price, W. G., and Wu, Y. 1986 A general linear hydroelasticity theory of floating structures moving in a seaway. Phil. Trans. R. Soc. Lond., A316, pp. 375–426

Bishop, R. E. D., Clarke, J. D., and Price, W. G. 1983 Comparison of full scale and predicted responses of two frigates in a severe weather trial. Trans. R. Instn Nav. Architects, 125, pp. 153–166

Bishop, R. E. D., Price, W. G., and Temarel, P. 1985 A hypothesis concerning the disastrous failure of the ONOMICHI-MARU, Trans. R. Instn Nav. Architects, 127, pp. 169–186

Bishop, R. E. D., Price, W. G., and Temarel, P., 1991, A theory on the loss of the MV Derbyshire, Trans. R. Instn Nav. Architects, 133, pp. 389–453

Boyce W.E, Diprima, R.C., 1997, Elementary Differential Equations and Boundary Value Problems, Department of Mathematical Sciences, Rensselaer Polytechnic Institute, John Wiley & Sons Inc.

Chen, X. J., Wu, Y. S., Cui, W. C., and Jensen, J. J., 2006, Review of hydroelasticity theories for global response of marine structures. Ocean Engng, 33, pp. 439–457

Chen, X. J., Jensen, J. J., Cui, W. C., and Fu, S. X., 2003, Hydroelasticity of a floating plate in multidirectional waves. Ocean Engng, 30(15), 1997–2017

Chen, R. S., Du, S. X., Wu, Y. S., Lin, J. R., Hu, J. J., and Yue, Y. L. 1999 Experiment on extreme wave loads of a flexible ship model of the S175 container ship, China Ship Scientific Research Center report

Collino F., Monk P.B., 1998, Optimizing the perfectly matched layer. Comput. Meth. Appl. Mech. Engng. pp. 27 - 533

Filippas E., Belibassakis K.A., 2014, Hydrodynamic analysis of flapping-foil thrusters operating beneath the free surface and in waves, Engineering Analysis with Boundary Elements, Vol.41, pp. 47-59

Frank, W., 1967, Oscillation of Cylinders in or Below the Free Surface of Deep Fluids, Report No. 2375, DTRC, Bethesda, Md.

Georgiou J., 2008, *Fundamentals of Dynamics and Linear Vibrations of Structures*, Lecture Notes, School of NA&ME, NTUA

Graff K. F., 1975, *Wave motion in elastic solids*, Dover

Gunter, N.M, 1967 Potential Theory and its Application to Basic Problems of Mathemtical Physics, Fr. Ungar Publ.

Heller, S. R., Abramson, H. N., 1959, Hydroelasticity – a new naval science. J. Am. Soc. Nav. Engrs, 71, pp. 205–209

Hermundstad, O. A., Aarsnes, J. V., and Moan, T. 1999 Linear hydroelastic analysis of high speed catamarans and monohulls. J. Ship Res. 43(1), pp. 48–63

Hirdaris S.E., Temarel P., 2009, Hydroelasticity of ships : Recent advances and future trends, IMechE Vo.223 Part M

Hirdaris, S. E., Price, W. G., and Temarel, P. 2003 Two and three-dimensional hydroelastic analysis of a bulker in waves. Mar. Structs, 16, pp. 627–658

Hutchinson J.R., 2001, Shear Coefficients for Timoshenko Beam Theory, J. Appl. Mech.;68(1):87-92.

Inglis, C. E., 1929, Natural frequencies and modes o fvibration in beams of non-uniform mass and section. Trans. R. Instn Nav. Architects, 72, pp. 145–166

Jensen, J. J., Dogliani, M., 1996, Wave-induced ship hull vibrations in stochastic seaways. Mar. Structs, 9(3), pp. 353–387

Kress R., 1989, Linear integral equations, Springer.

Lewis Ed., 1989, Principles of Naval Architecture, Motion in waves, Vol.III, SNAME

Malenica S., Molin B., Remy F., Senjanovic I. 2003, Hydroelastic response of a barge to impulsive and non-impulsive wave load, Proc. Hydroelasticity in Marine Technology, Oxford, UK, pp. 107–115

Novozilov , V. V. 1964 Thin Shell Theory. P. Noordhoff Ltd. , Groningen, The Netherlands

Ohkusu M. 1996, *Hydrodynamics of ships in wave,* Chapter 2 in Advances in Marine Hydrodynamics Computational Mechanics Publications.

Oka, M., Ogawa, Y., Tozawa, S., and Oka, S. 2007 A study for the assessment of design loads of a high speed vessel taking into account of the whipping vibration. Proc. International Conference on Violent flows, Fukuoka, Japan

Oka, M., Ogawa, Y., Oka, S., and Tozawa, S. 2008 The experimental study on wave loads acting on a large container carrier. Proc. Japan Society of Naval Architects and Ocean Engineers, vol. 6, pp. 31–43

Price, W. G., Salas Inzunza, M., and Temarel, P. 2002 The dynamic behaviour of a mono-hull in oblique waves using two- and three-dimensional fluid structure interaction models. Trans. R. Instn Nav. Architects, 144, pp. 1–26

Price, W. G., Wu, Y. S. 1989 The influence of non – linear fluid forces in the time domain responses of flexible SWATH ships excited by a seaway. Proc. Eight OMAE, Vol. 2, pp. 125 – 135

Price, W. G. and Wu, Y. S. 1985 Hydroelasticity of marine structures. Proc. Sixteenth International Congress of Theoretical and Applied Mechanics (IUTAM), Lyngby, Denmark: Sectional Lecture, S-10

Remy F., Molin B., Ledoux A. 2006, Experimental and numerical study of the wave response of a flexible barge, Proc. Hydroelasticity in Marine Technology, Wuxi, China, pp. 256-264.

Salmouilidis M., 2004, *Ship Vibrations,* Lecture notes School NA&ME.

Salvesen N, Tuck E.O, Faltisen O. 1970, Ship Motions and Sea Loads, Transactions SNAME, pp. 250-277.

Sclavounos, P., Borgen, 2004 H. Seakeeping analysis of a high-speed monohull with a motion control bow hydrofoil. J. Ship Res. 48 (2), 77.

Senjanovic I., Malenica S., Tomasevic S. 2008, Investigation of ship Hydroelasticity, Ocean Engineering 35, pp. 523–535.

Senjanovic I., Grubisic R. 1991 Coupled horizontal and torsional vibration of a ship hull with large hatch openings. Computers & Structures 4 (2)1, pp. 213 - 226

Senjanovic, I., Malenica, S. and Tomasevic S. 2009 Hydroelasticity of large ships Marine Structure 22 pp. 287 – 314

Shixiao F, Torgeir M. , Weicheng C. and Xujun C. 2007 Hydroelastic analysis of flexible floating interconnected structures Ocean Engineering 34 , pp. 1516 – 1531

Timoshenko, S. , Young, D. H. 1955 Vibration Problems in Engineering. D. Van Nostrand

Timman, R. and Newman, J. N. 1962 The coupled damping coefficients of symmetric ships. J. Ship Res. 5, pp.34–55

Tomasevic S. 2007 Hydroelastic model of dynamic response of Container ships in waves, Ph.D Thesis, FSB, Zagreb

Turkel E. Yefet A. 1998 Absorbing PML. boundary layers for wave-like equations. Appl Numer Meth

Ursell, F. 1949 On the heaving motion of a circular cylinder on the surface of a fluid.m Q. J. Mechanics and Applied Mathematics, 2, pp. 218 - 231

Vughts J. 1968 The hydrodynamic coefficients for swaying, heaving, and rolling cylinders in a free surface, T.H. Delft, Report No.194.

Watanabe, I., Ueno, M., and Swada, H. 1989 Effects of bow flare shape to wave impact pressure. J. Soc. Nav. Architects of Japan, pp. 259–266

Wang, S. Q., Ertekin, R. C. and Riggs, H. R. 1997 Computationally efficient techniques in the hydroelasticity analysis of very large floating structures, Computers Structs 62 (4), pp. 603 – 610

Wang C.M., Wang B.T., 2015, Large Floating Structures: Technological Advances, Springer.

Wu, Y. S. 1984 Hydroelasticity of floating bodies, PhD Thesis, Brunel University

Wu, Y. S., Maeda, H., and Kinoshita, T. 1997 The second order hydrodynamic actions on a flexible body. J. Inst. Ind. Sci., Univ. Tokyo, 49(4), pp. 8–19

Appendix A

Presentation of the comparative results for the EBT and TBT

In this present Appendix, we display the results of the implementation of the developed program ‘’EBT’’ for an Euler Bernoulli beam and for a Timoshenko beam. We will demonstrate the natural frequencies and the natural functions for both the thin rod and the thin beam case. The implementations will concern the free, clamped and pinned vibration cases.

Euler – Bernoulli model

Results concerning a homogeneous rod

The main characteristics of the rod are: (i) Length: $L = 50\,[\mathrm{m}]$ [m], (ii) Young's modulus: $E = 210\,10^9\,[\mathrm{Pa}]$, (ii) Mass density: $\rho = 7825\,[\mathrm{kg/m^3}]$, (iv) Thickness: $t = 1\,[\mathrm{m}]$, (v) Moment of inertia: $I = \pi t^4 / 4 = 0.7854\,[\mathrm{kg\,m^2}]$, (vi) Cross section area: $A = \pi t^2 = 3.1416\,[m^2]$. The results are illustrated in the following pages.

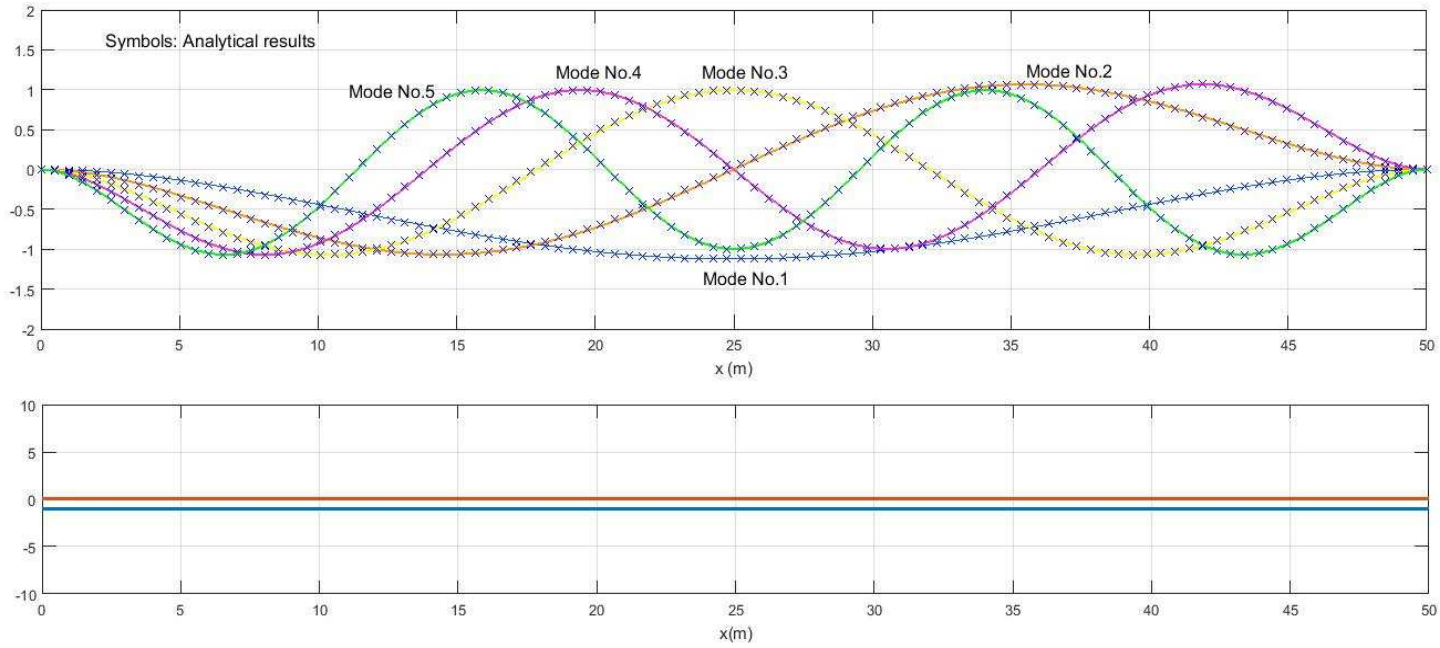

Fig. A. 1. Normalized eigenfunctions for homogeneous clamped rod, M=100 points, factor $\sqrt{\frac{2}{L}}$ to scale the modes

Mode	Analytic Method Frequencies	Numerical Method Frequencies (M=100)	Error (%)
1	23.144	23.155	0.050
2	63.797	63.836	0.062
3	125.067	125.148	0.065
4	206.742	206.837	0.046
5	308.837	308.866	0.009
6	431.351	431.158	0.045
7	574.284	573.629	0.114

Table A. 1 Natural frequencies, $[\text{rad/sec}]$, for clamped rod

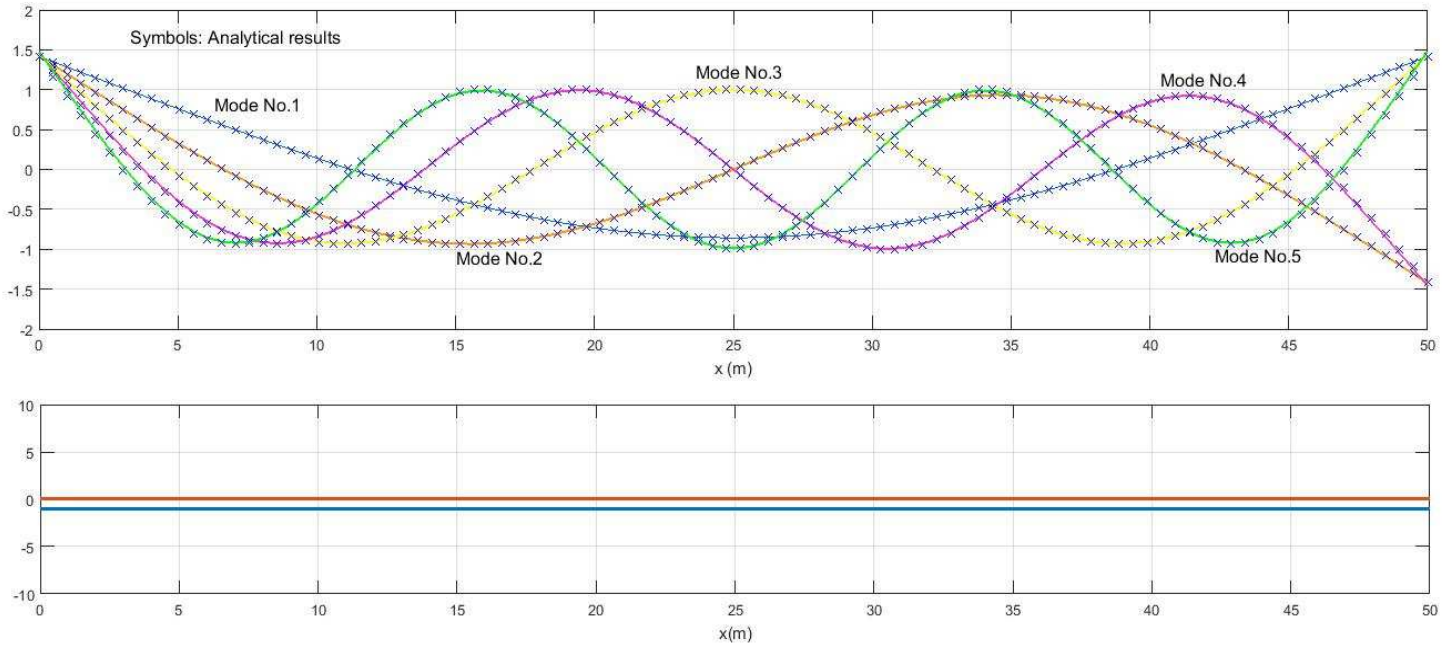

Fig. A. 2. Normalized eigenfunctions for homogeneous free rod, M=100 points, factor $\sqrt{\frac{2}{L}}$ to scale the modes

Mode	**Analytic Method Frequencies**	**Numerical Method Frequencies (M=100)**	**Error (%)**
1	23.144	23.176	0.139
2	63.797	63.956	0.249
3	125.067	125.486	0.335
4	206.742	207.595	0.413
5	308.837	310.305	0.475
6	431.352	433.620	0.526
7	574.285	577.504	0.561

Table A. 2 Natural frequencies, $[\text{rad/sec}]$, for free rod

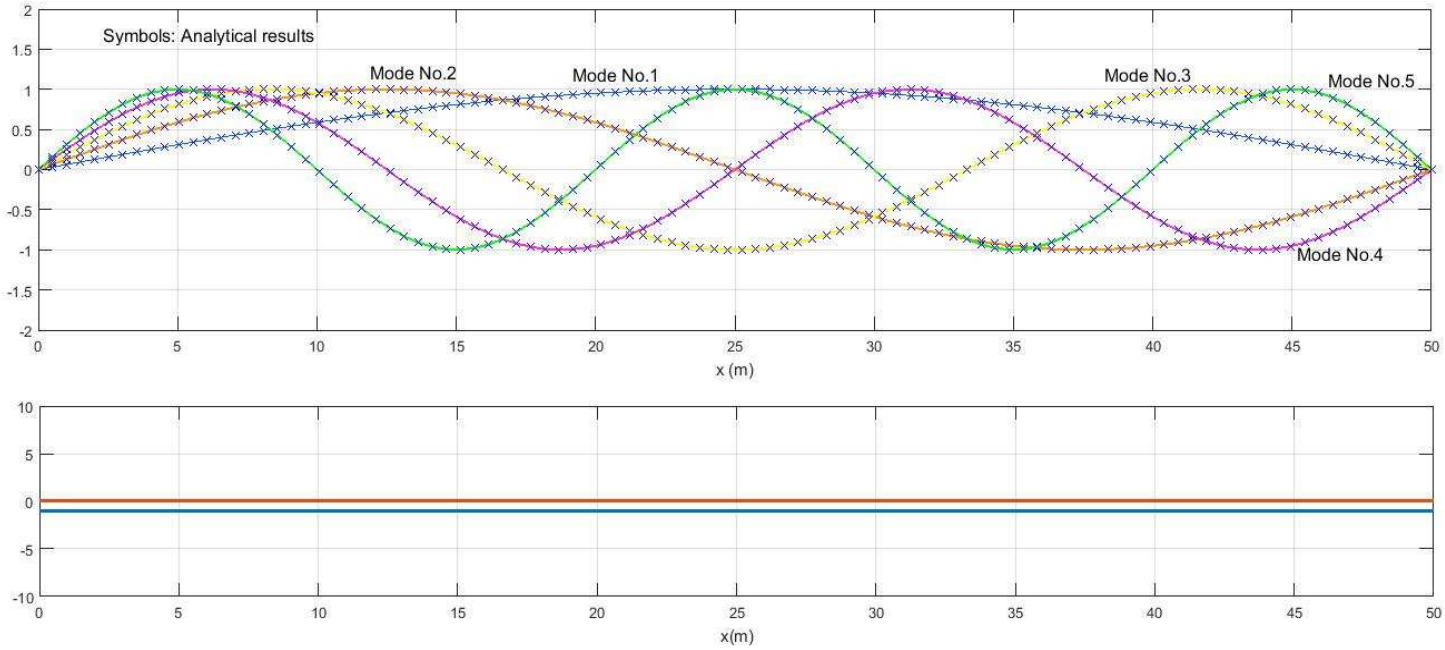

Fig. A. 3. Normalized eigenfunctions for homogeneous pinned rod, M=100 points, factor $\sqrt{\frac{2}{L}}$ to scale the modes

Mode	**Analytic Method Frequencies**	**Numerical Method Frequencies (M=100)**	**Error (%)**
1	10.210	10.206	0.033
2	40.838	40.826	0.030
3	91.886	91.833	0.057
4	163.352	163.185	0.102
5	255.238	254.826	0.161
6	367.542	366.693	0.231
7	500.266	498.698	0.313

Table A. 3 Natural frequencies, $[\text{rad/sec}]$, for pinned rod

Concerning the differences spotted on the previous numerical results, they are compatible with the approximation based on second order finite differences.

Regarding the modes, the number of the peaks (positive or negative ones) is increased accordingly with the number (index) of the mode. For instance, the first mode is represented by a single peak in the middle of the rod whereas in the second mode we get two peaks, in the third mode we get three peaks and so goes for the rest of the modes. It should be noted that the zero frequency is excluded as it represents a rigid body motion. Moreover, the convergence between the numerical (solid line) and the analytical solution (symbols) increases by using a higher number of grid points. More specifically, we illustrate the convergence of the developed numerical method. The results are depicted in the following figures

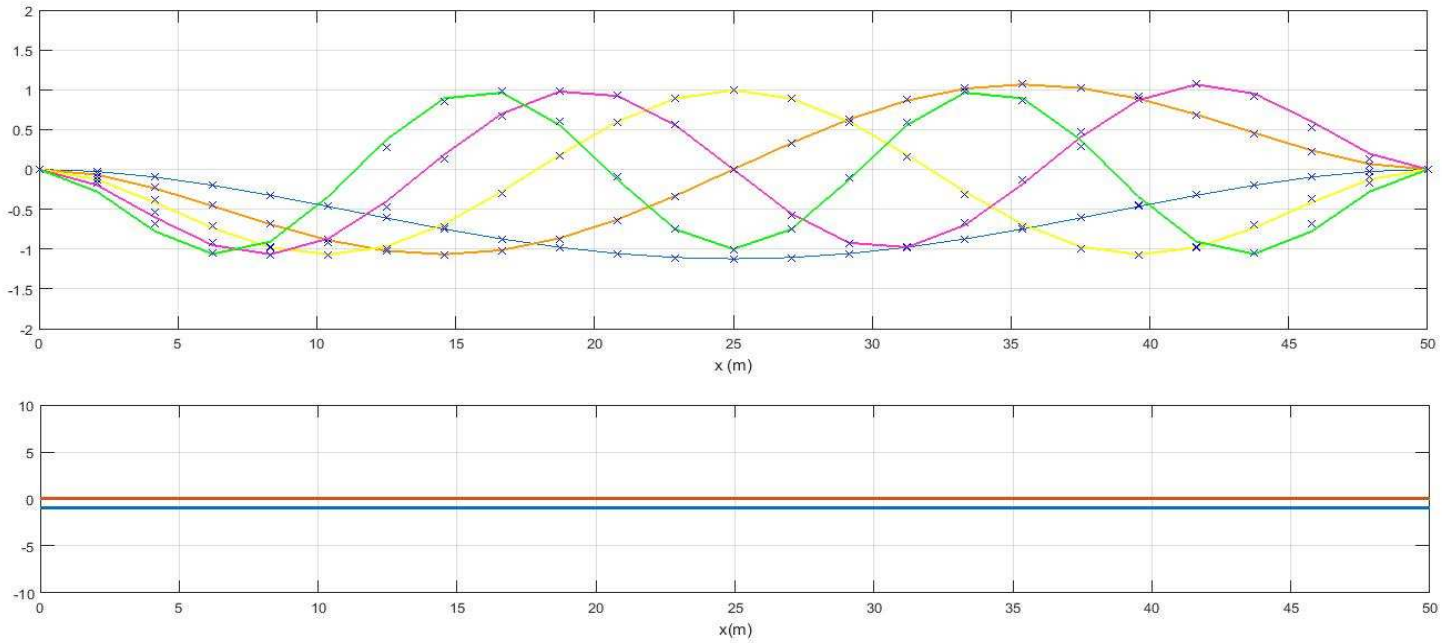

Fig. A. 4. Convergence numerical to analytical for a clamped edged homogeneous rod, M=25 points, factor $\sqrt{\frac{2}{L}}$ to scale the modes

Mode	Analytic Method Frequencies	Numerical Method Frequencies (M=25)	Error (%)
1	23.144	23.353	0.902
2	63.797	64.532	1.153
3	125.067	126.410	1.074
4	206.742	208.125	0.669
5	308.837	308.591	0.080
6	431.352	426.281	1.176
7	574.285	559.236	2.620

Table A. 4 Convergence for natural frequencies

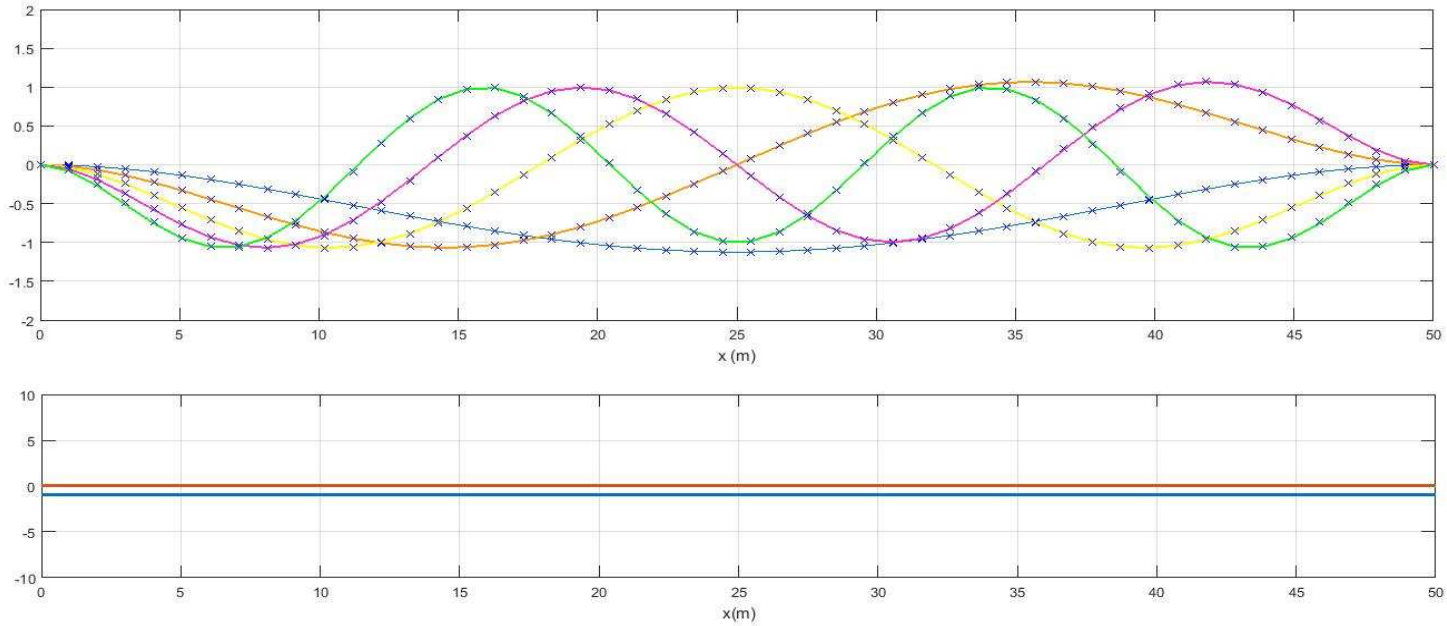

Fig. A. 5 Convergence numerical to analytical for a free edged homogeneous rod, M=50 points, factor $\sqrt{\frac{2}{L}}$ to scale the modes

Mode	**Analytic Method Frequencies**	**Numerical Method Frequencies (M=50)**	**Error (%)**
1	23.144	23.192	0.207
2	63.797	63.971	0.273
3	125.067	125.398	0.264
4	206.742	207.118	0.181
5	308.837	308.923	0.028
6	431.352	430.493	0.199
7	574.285	571.422	0.499

Table A. 5 Convergence for natural frequencies

Due to the small partitioning, the calculation speed is increased. However, increasing the knots on the beam the calculation speed is clearly decreasing.

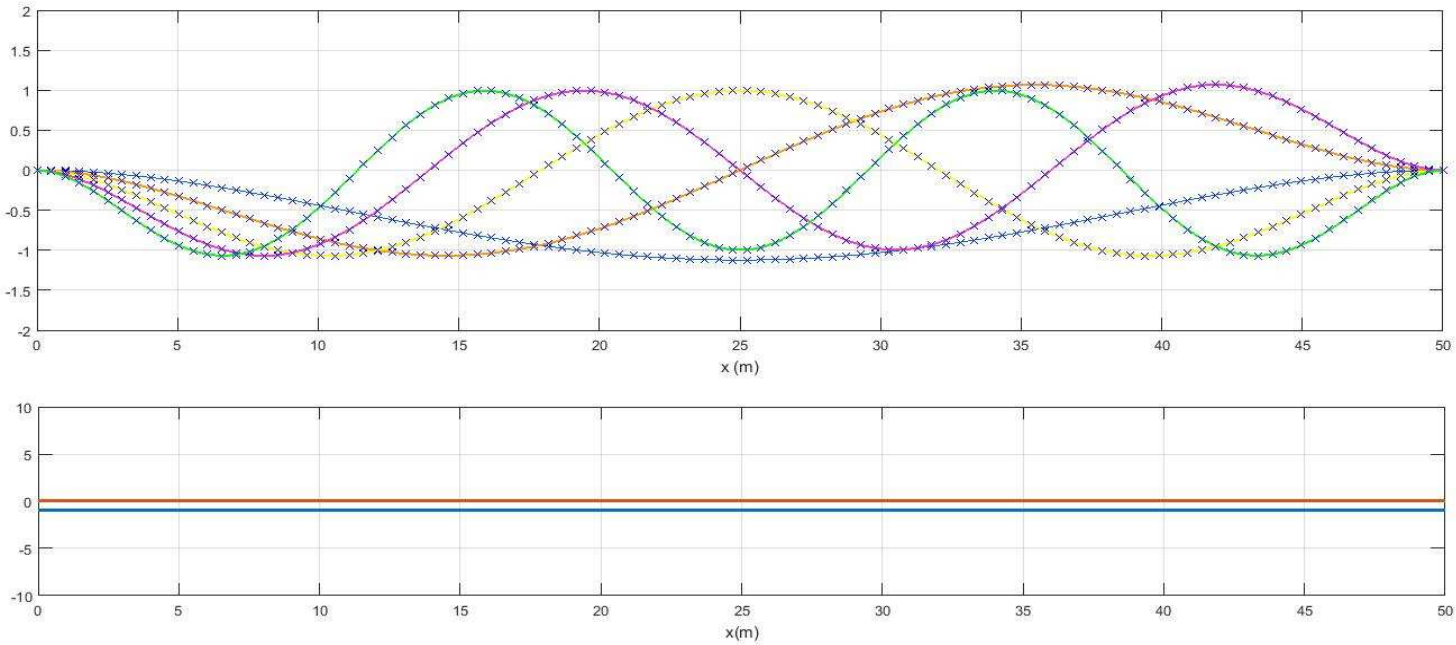

Fig. A.6 Convergence numerical to analytical for a free edged homogeneous rod, M=150 points, factor $\sqrt{\frac{2}{L}}$ to scale the modes

Mode	**Analytic Method Frequencies**	**Numerical Method Frequencies (M=150)**	**Error (%)**
1	23.144	23.144	0.000
2	63.797	63.797	0.000
3	125.067	125.067	0.000
4	206.742	206.742	0.000
5	308.837	308.837	0.000
6	431.351	431.351	0.000
7	574.285	574.284	0.001

Table A.6 Convergence for natural frequencies

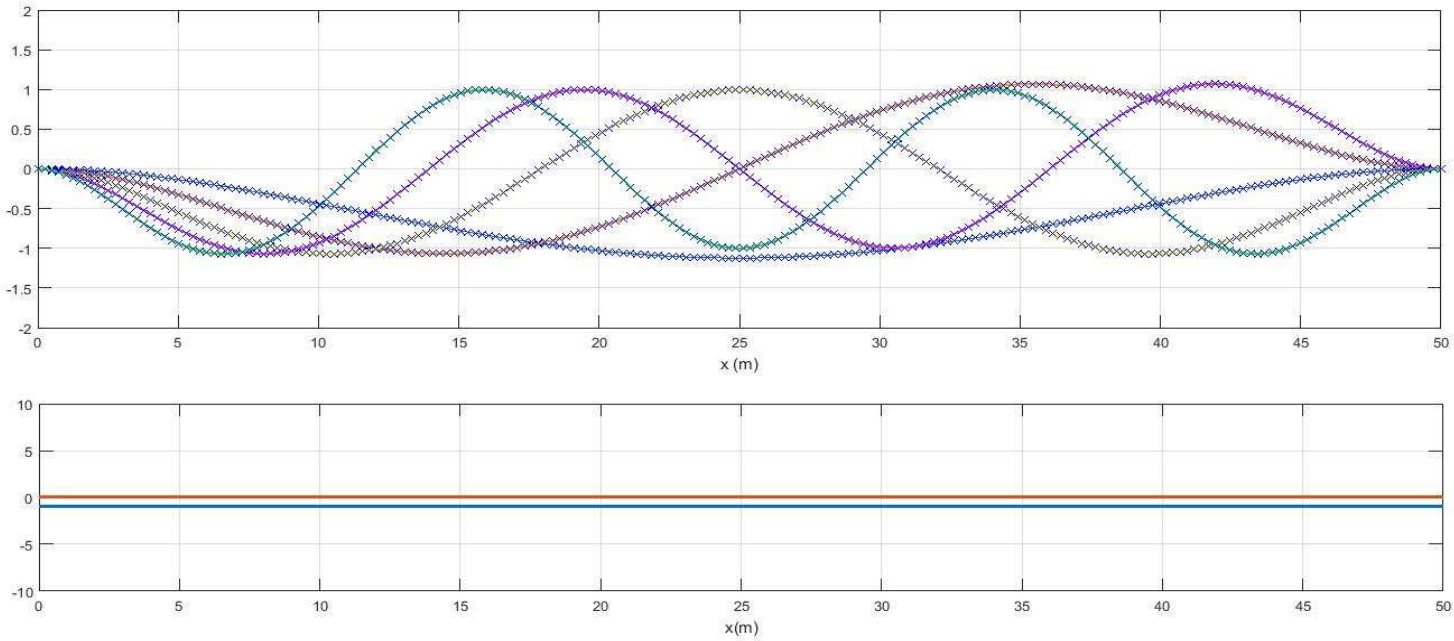

Fig. A.7. Convergence numerical to analytical for a free edged homogeneous rod, M=200 points, factor $\sqrt{\frac{2}{L}}$ to scale the modes

Mode	**Analytic Method Frequencies**	**Numerical Method Frequencies (M=200)**	**Error (%)**
1	23.144	23.145	0.005
2	63.797	63.805	0.013
3	125.067	125.086	0.015
4	206.742	206.764	0.011
5	308.837	308.840	0.001
6	431.351	431.309	0.010
7	574.284	574.107	0.031

Table A.7 Convergence for natural frequencies

Points / Mode	**25**	**50**	**100**	**150**	**200**	**Analytic Method**
1	23.353	23.192	23.155	23.144	23.145	23.144
2	64.532	63.971	63.836	63.797	63.805	63.797
3	126.410	125.398	125.148	125.067	125.086	125.067
4	208.125	207.118	206.837	206.742	206.764	206.742
5	308.591	308.923	308.866	308.837	308.840	308.837
6	426.281	430.493	431.158	431.351	431.309	431.352
7	559.236	571.422	573.629	574.284	574.107	574.284

Table A.8 Focusing results for the converge of the natural Frequencies

Apparently, investigating the lower frequencies the discrepancies of the results are very small. As we proceed to areas with higher frequencies the discrepancies between the results are more obvious, see, Table (8). In addition, increasing the number of the elements used over the rod the results converge to a single value. This latter comes in agreement with the used numerical theory according to which the higher we dense the grid the smaller declinations we get obtain.

Calculations for an inhomogeneous rod

In the following, we investigate the case of a inhomogeneous rod with varying thickness from $b=1$ [m], concerning the domain $x\leq 10$ and $x\geq 40$, to $b=2$ [m] in the domain , $10<x<40$, with its maximum thickness to be in the middle of the beam. The two cases (homo. and inhomogeneous) will be compared concerning both the normalized eigenfunctions and the normal frequencies. It is obvious that the analytical solution isn't feasible for cross sections with varying geometrical characteristics. Therefore, we demonstrate the results obtained from the numerical solution and only.

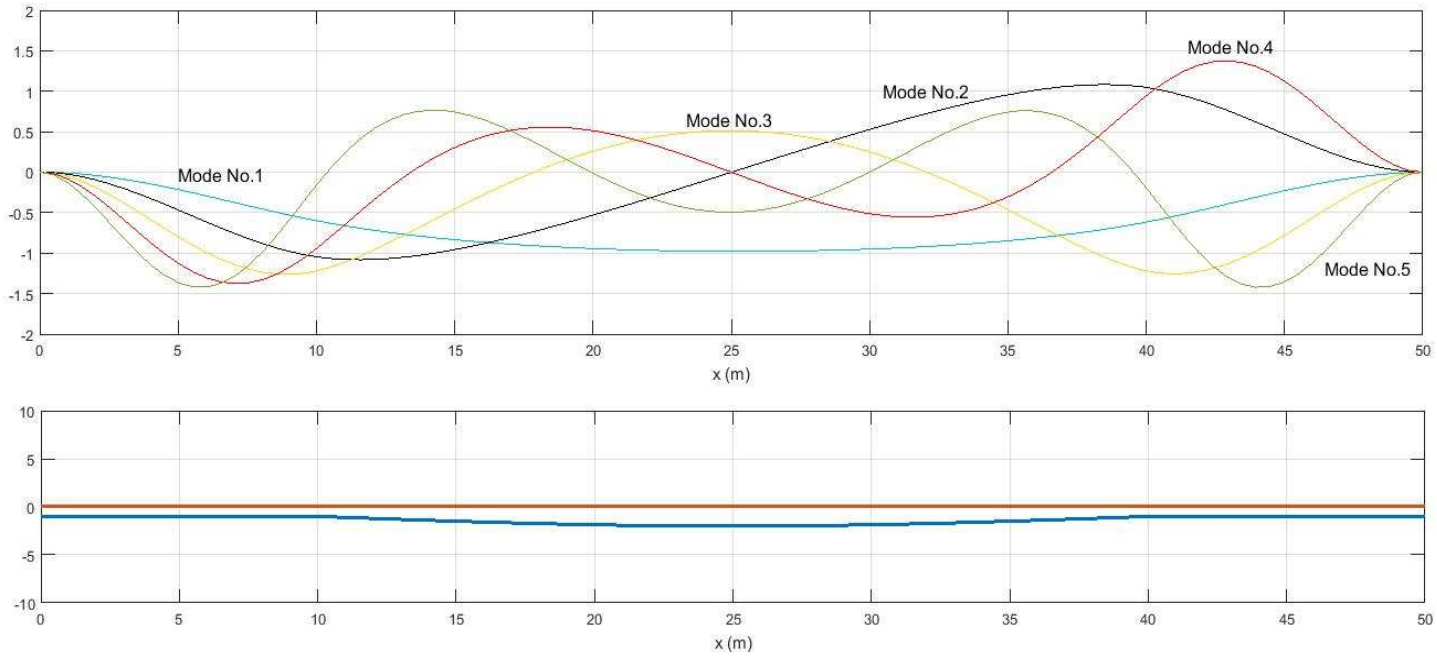

Fig. A.9 Normalized inhomogeneous clamped rod, M=100 points, factor $\sqrt{\frac{2}{L}}$ to scale the modes

Mode	Numerical Method Frequencies (M=100)
1	23.625
2	69.538
3	174.939
4	286.087
5	414.479
6	570.986
7	759.211

Table A. 9 Natural frequencies, $[\text{rad/sec}]$, for clamped rod

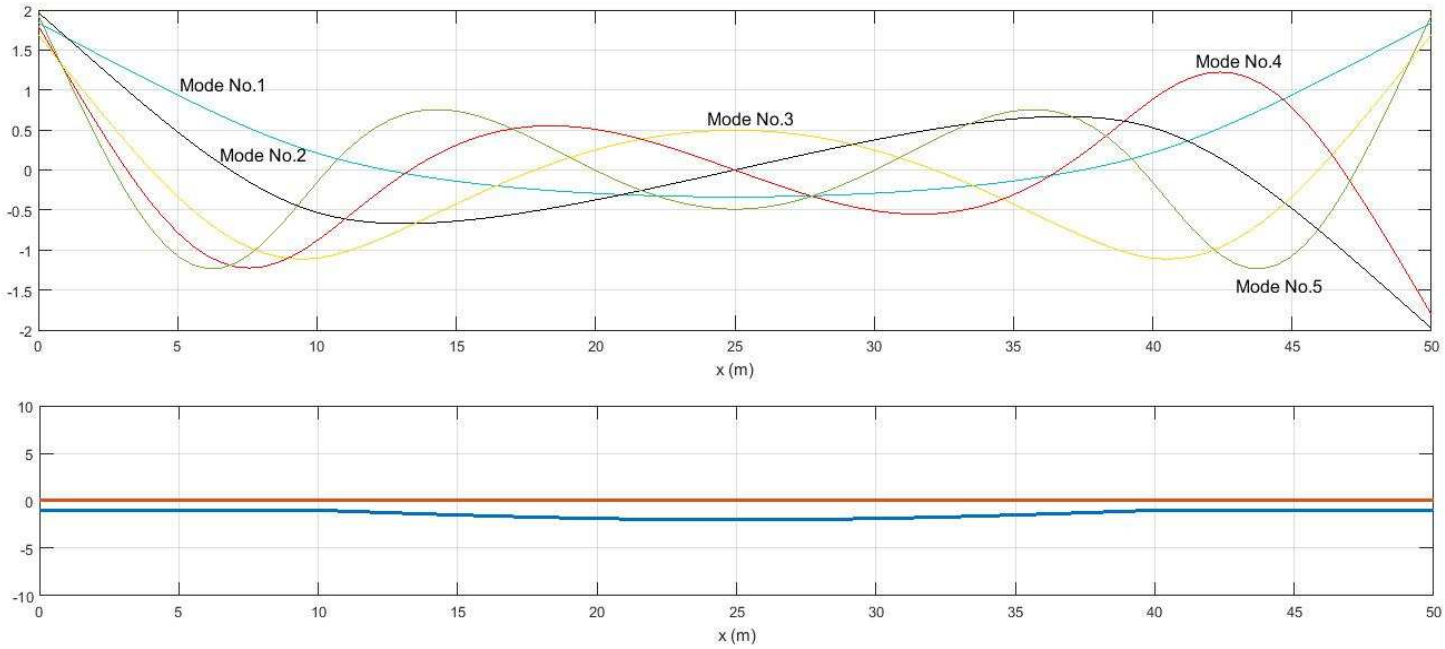

Fig. A.10 Normalized inhomogeneous free, M=100 points, factor $\sqrt{\frac{2}{L}}$ to scale the modes

Mode	**Numerical Method Frequencies (M=100)**
1	47.170
2	82.696
3	174.731
4	284.771
5	415.310
6	574.726
7	765.928

Table A.10 Natural frequencies, $[\text{rad/sec}]$, for free rod

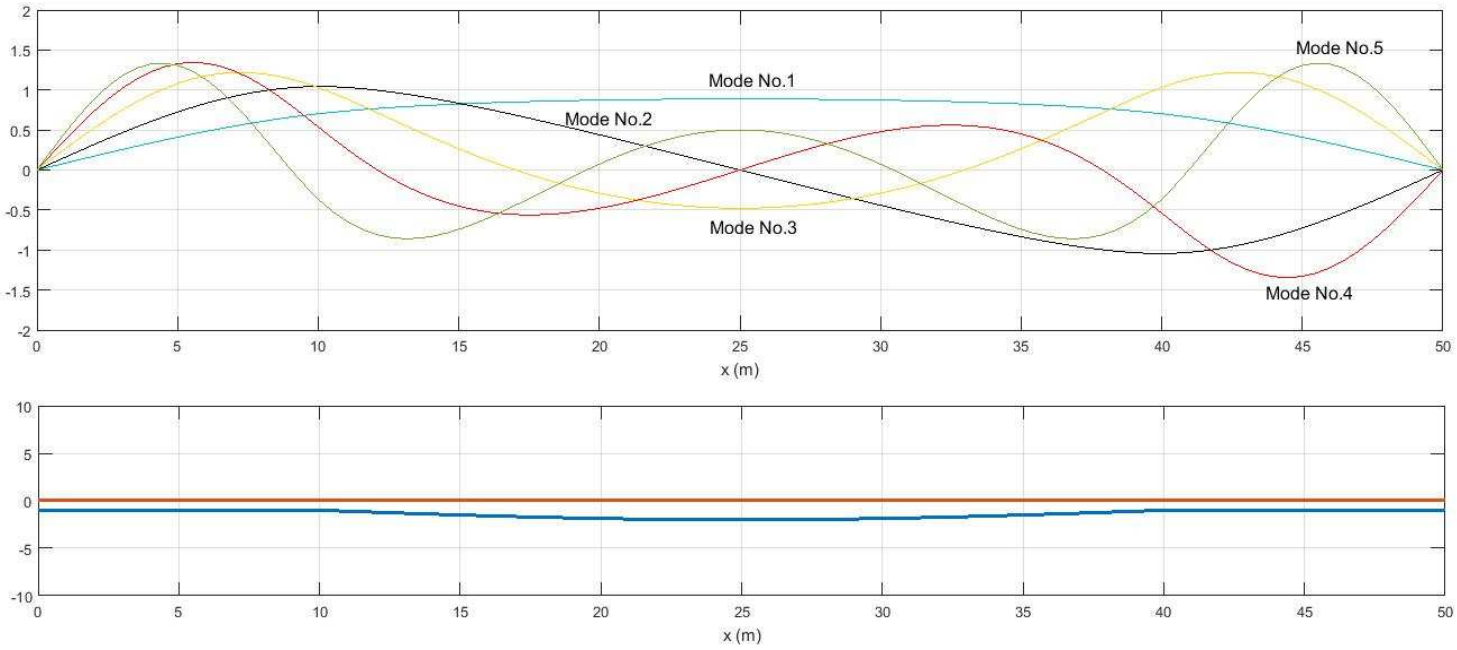

Fig. A.11 Normalized inhomogeneous pinned rod, M=100 points, factor $\sqrt{\frac{2}{L}}$ to scale the modes

Mode	Numerical Method Frequencies (M=100)
1	12.683
2	44.469
3	135.604
4	224.661
5	338.718
6	486.431
7	663.437

Table A.11 Natural frequencies, $\left[\text{rad/sec}\right]$, for pinned rod

Results for a homogeneous beam

The main characteristics of the rod are: (i) Length: $L = 50\,\left[\text{m}\right]$ [m], (ii) Young's modulus: $E = 5\,10^6\,\left[\text{Pa}\right]$, (ii) Mass density: $\rho = 923\,\left[\text{kg/m}^3\right]$, (iv) Thickness: $t = 1\,\left[\text{m}\right]$, (v) Moment of inertia: $I = \pi t^3/12 = 0.0833\,\left[\text{kg m}^2\right]$, Cross section area: $A = t^2 = 1\,\left[m^2\right]$

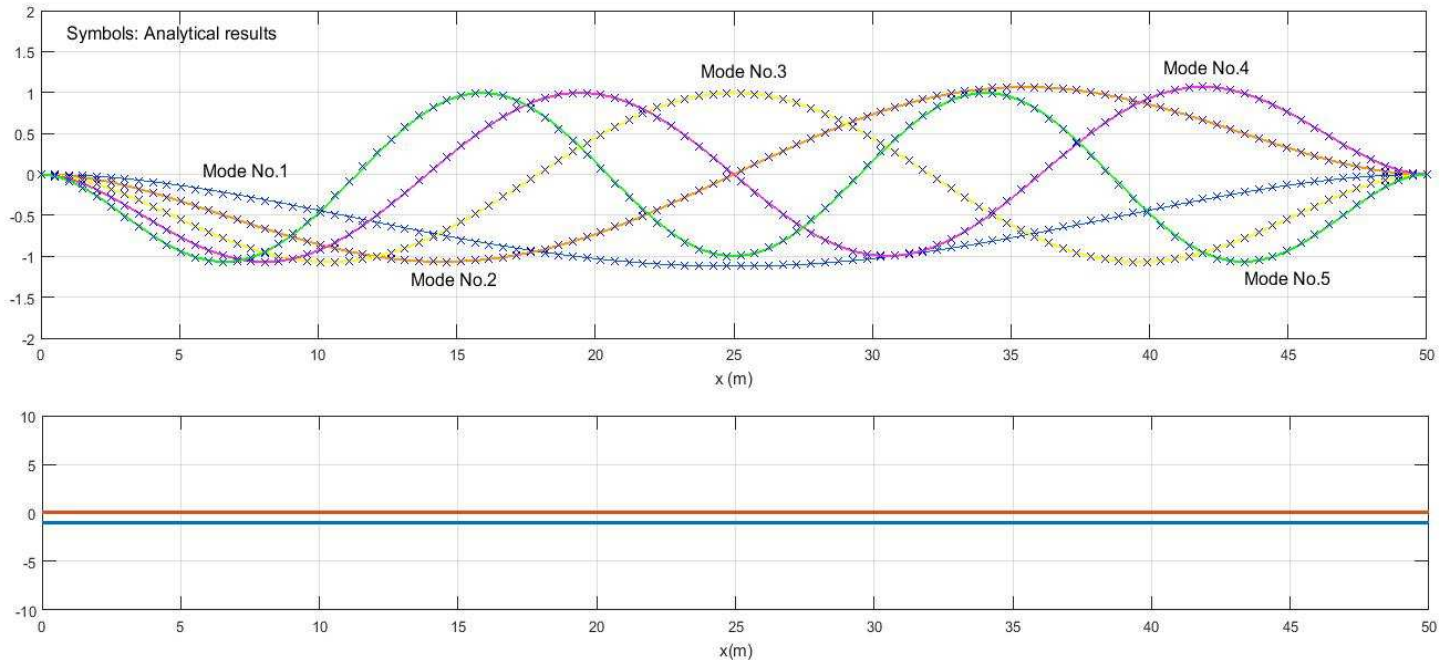

Fig. A.12 Normalized eigenfunctions for homogeneous clamped beam, M=100 points, factor $\sqrt{\frac{2}{L}}$ to scale the modes

Mode	**Analytic Method Frequencies**	**Numerical Method Frequencies (M=100)**	**Error (%)**
1	13.362	13.364	0.016
2	36.833	36.858	0.066
3	72.208	72.251	0.060
4	119.363	119.414	0.043
5	178.307	178.321	0.008
6	249.041	248.931	0.044
7	331.563	331.180	0.115

Table A.12 Natural frequencies, $[\text{rad/sec}]$, for clamped beam

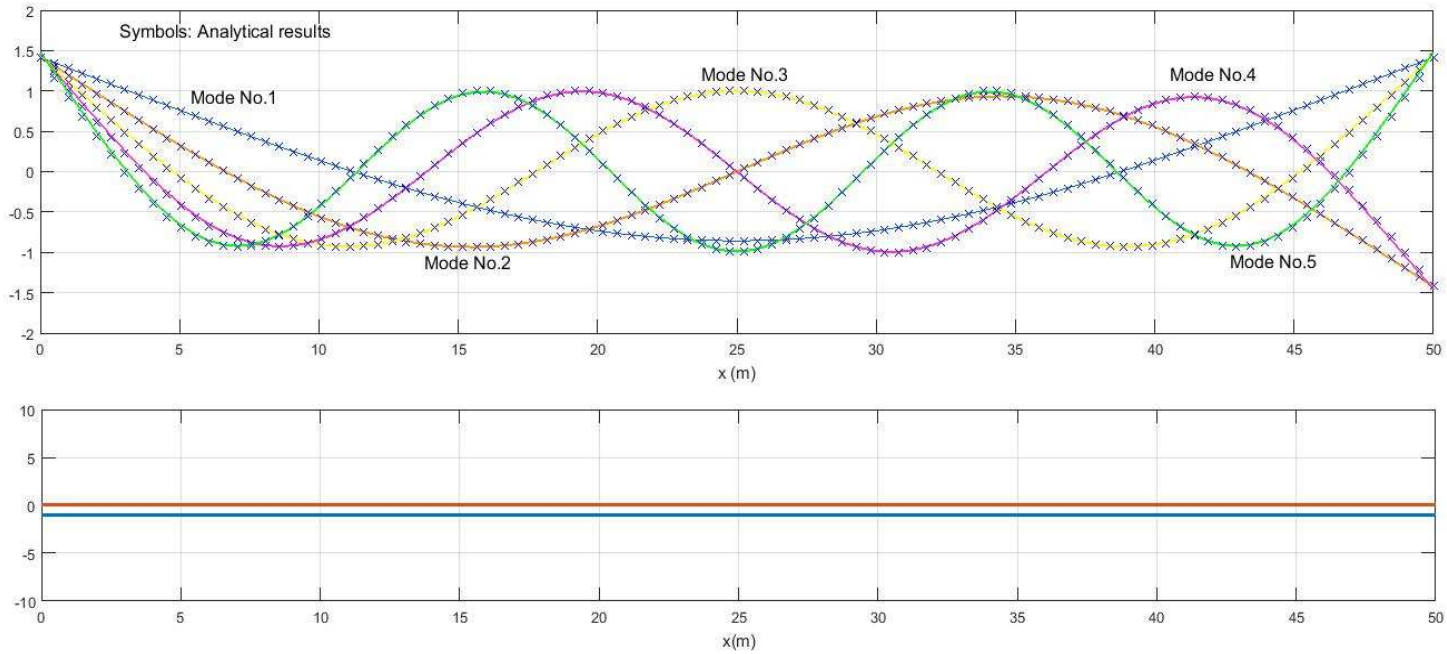

Fig. A.13 Normalized eigenfunctions for homogeneous free beam, M=100 points, factor $\sqrt{\frac{2}{L}}$ to scale the modes

Mode	**Analytic Method Frequencies**	**Numerical Method Frequencies (M=100)**	**Error (%)**
1	13.362	13.380	0.133
2	36.833	36.925	0.250
3	72.208	72.448	0.333
4	119.363	119.855	0.413
5	178.307	179.152	0.474
6	249.041	250.349	0.525
7	331.563	333.424	0.561

Table A.13 Natural frequencies, $\left[\text{rad/sec}\right]$, for free beam

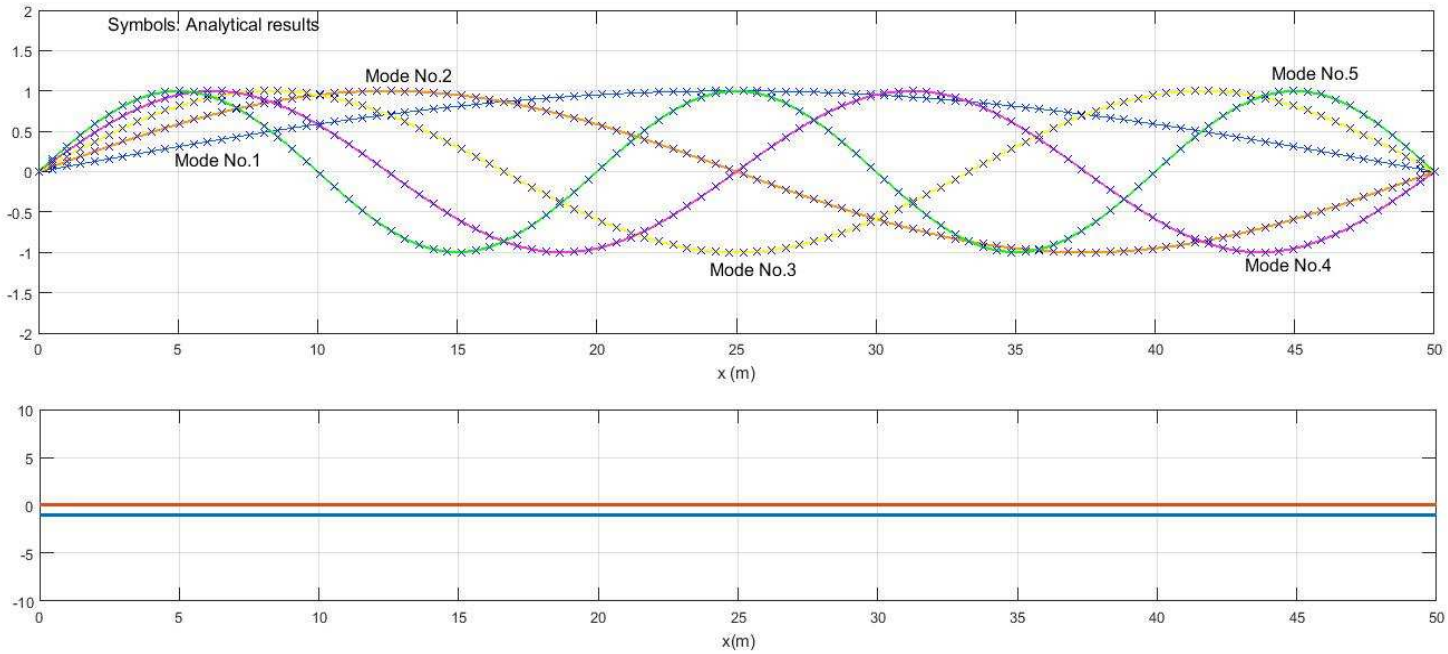

Fig. A.14 Normalized eigenfunctions for homogeneous pinned beam, M=100 points, factor $\sqrt{\frac{2}{L}}$ to scale the modes

Mode	**Analytic Method Frequencies**	**Numerical Method Frequencies (M=100)**	**Error (%)**
1	5.894	5.890	0.079
2	23.578	23.571	0.030
3	53.050	53.017	0.063
4	94.311	94.212	0.106
5	147.361	147.125	0.161
6	212.201	211.709	0.232
7	288.828	287.923	0.313

Table A.14 Natural frequencies, $[\text{rad/sec}]$, for pinned beam

Results for an inhomogeneous beam

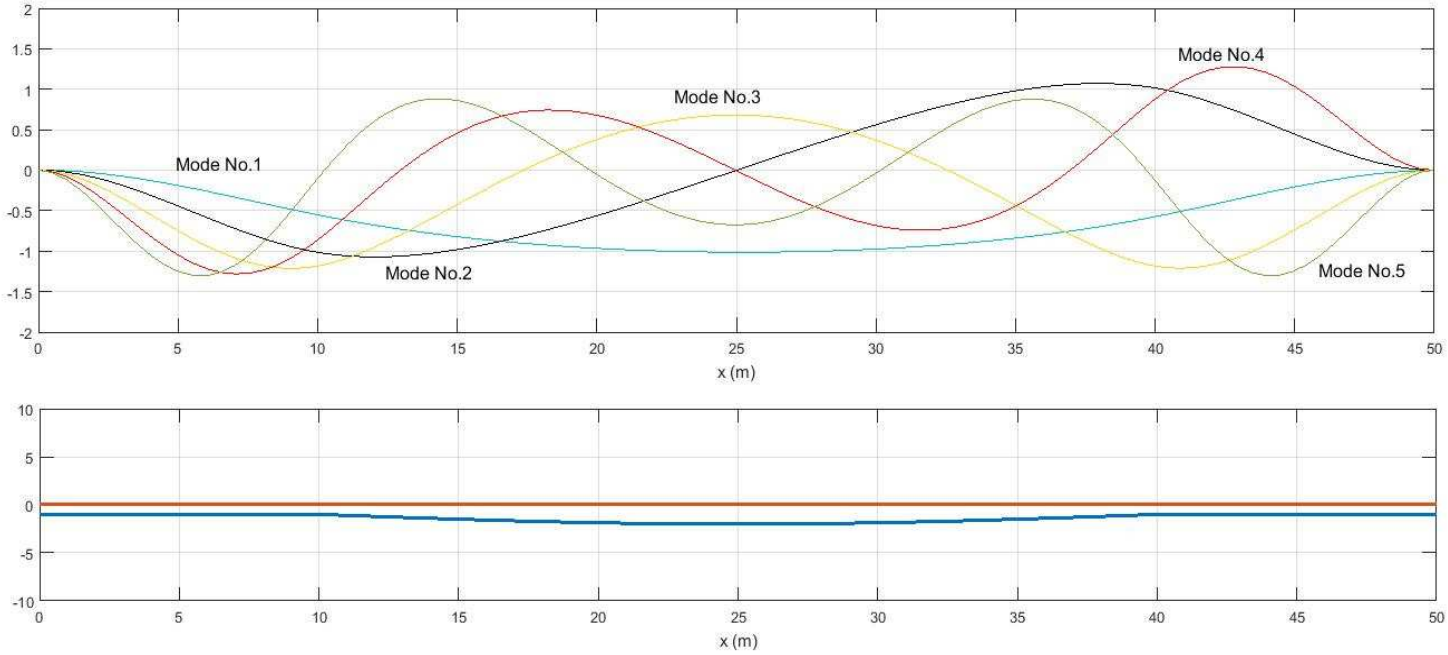

Fig. A.15 Normalized eigenfunctions for inhomogeneous clamped beam, M=100 points, factor $\sqrt{\frac{2}{L}}$ to scale the modes

Mode	**Numerical Method Frequencies (M=100)**
1	15.661
2	43.569
3	96.269
4	160.327
5	236.918
6	327.360
7	434.215

Table A.15 Natural frequencies, $\left[\text{rad/sec}\right]$, for clamped beam

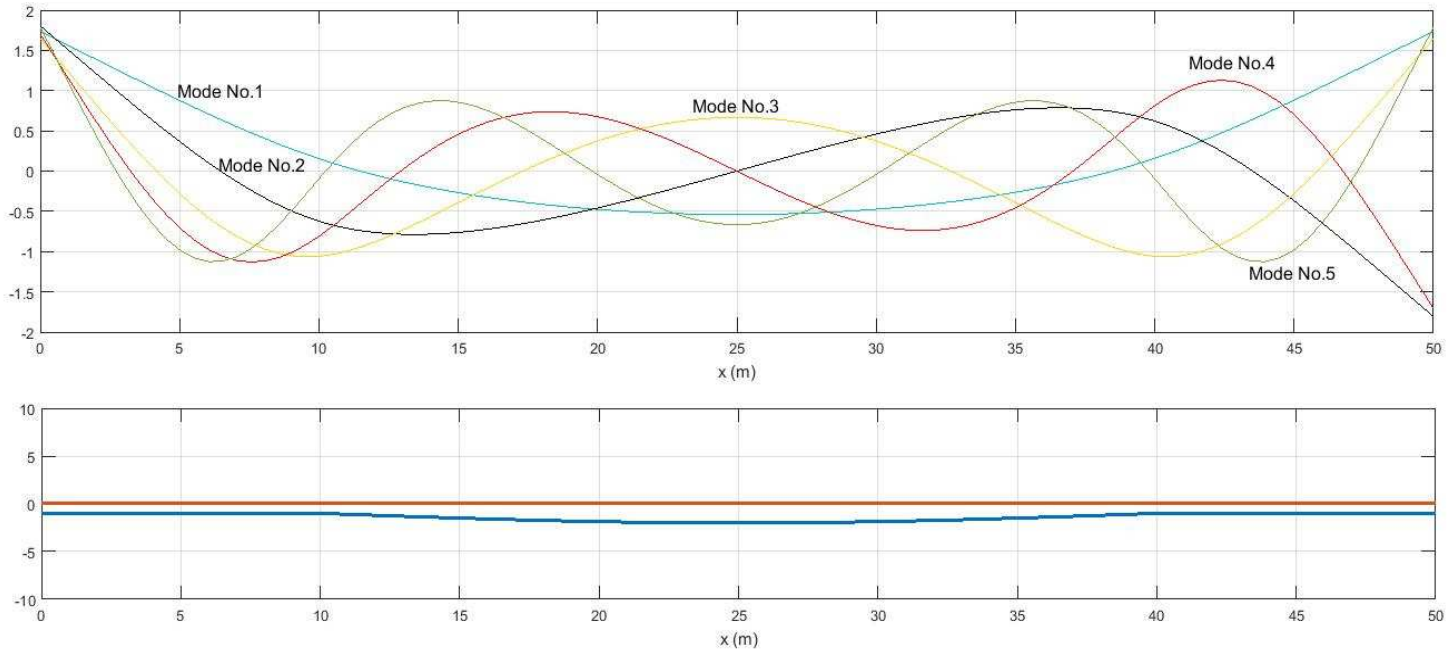

Fig. A.16 Normalized eigenfunctions for inhomogeneous free beam, M=100 points, factor $\sqrt{\frac{2}{L}}$ to scale the modes

Mode	**Numerical Method Frequencies (M=100)**
1	24.456
2	48.486
3	96.408
4	160.050
5	237.749
6	329.646
7	438.093

Table A.16 Natural frequencies, $\left[\text{rad/sec}\right]$, for free beam

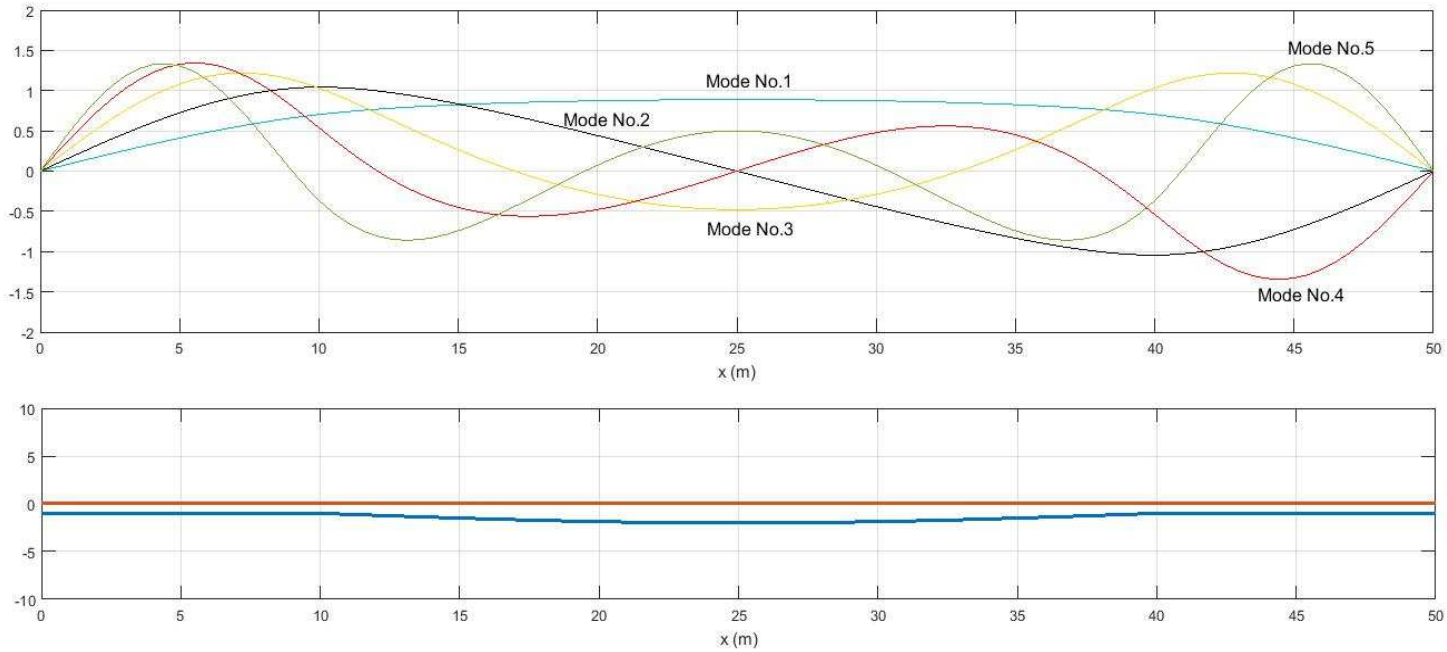

Fig. A.17 Normalized eigenfunctions for inhomogeneous pinned beam, M=100 points, factor $\sqrt{\frac{2}{L}}$ to scale the modes

Mode	**Numerical Method Frequencies (M=100)**
1	8.251
2	27.503
3	72.793
4	126.809
5	194.329
6	277.707
7	378.260

Table A.17 Natural frequencies, $[\text{rad/sec}]$, for pinned beam

Comparative results of natural frequencies concerning a beam and a rod cross section

In the following tables we present the way the natural frequencies change depending the shape of its cross sectional areas. Thus, we compare and contrast all the possible combinations concerning the given boundary conditions.

Mode	NATURAL FREQUENCIES		
1	23.176	23.176	10.206
2	63.956	63.956	40.826
3	125.486	125.486	91.833
4	207.595	207.595	163.185
5	310.305	310.305	254.826
6	433.620	433.620	366.693
7	577.504	577.504	498.698

Table A.18 Homogeneous rod , Clamped (left) , Free (center), Pinned (right)

Mode	NATURAL FREQUENCIES		
1	23.625	47.170	12.683
2	69.538	82.696	44.469
3	174.939	174.731	135.604
4	286.087	284.771	224.661
5	414.479	415.310	338.718
6	570.986	574.726	486.431
7	759.211	765.928	663.437

Table A.19 Inhomogeneous rod , Clamped (left) , Free (center), Pinned (right)

Mode	NATURAL FREQUENCIES		
1	13.364	13.380	5.890
2	36.858	36.925	23.571
3	72.251	72.448	53.017
4	119.414	119.855	94.212
5	178.321	179.152	147.125
6	248.931	250.349	211.709
7	331.180	333.424	287.923

Table A.20 Homogeneous beam, Clamped (left) , Free (center), Pinned (right)

Mode	NATURAL FREQUENCIES		
1	15.661	24.456	8.251
2	43.569	48.486	27.503
3	96.269	96.408	72.793
4	160.327	160.050	126.809
5	236.918	237.749	194.329
6	327.360	329.646	277.707
7	434.215	438.093	378.260

Table A.21 Inhomogeneous beam, Clamped (left) , Free (center), Pinned (right)

Regarding the homogeneous scenario, it is clearly depicted in the Tables (18), (20), that the clamped and free types of boundary conditions have the same values for the natural frequencies. The latter is associated with the roots of the characteristic polynomial which apparently is the same for both the cases; see, eq. (1.2.15). In addition, the first two columns of the inhomogeneous Tables (19), (21) are slightly different concerning the mode No.1 and mode No.2. The presented results are obtained exclusively through numerical analysis. Therefore, such small differences are attainable due to approximation errors.

Mode	EIGENFREQUENCIES	
1	13.364	23.176
2	36.858	63.956
3	72.251	125.486
4	119.414	207.595
5	178.321	310.305
6	248.931	433.620
7	331.180	577.504

Table A.22 Homogeneous beam (left) , homogeneous rod (right),given clamped type of edges

Mode	EIGENFREQUENCIES	
1	15.661	23.625
2	43.569	69.538
3	96.269	174.939
4	160.327	286.087
5	236.918	414.479
6	327.360	570.986
7	434.215	759.211

Table A.23 Inhomogeneous beam (left), inhomogeneous rod (right), given clamped type of edges

We presented the case of the simple beam and rod (homogeneous and inhomogeneous), to investigate the differences as we move from a square cross section area to a circular one. We observe that circular sections are associated with higher frequency excitations compared to the square sections and so do the same for the rest of the boundary conditions, i.e. free and pinned.

Timoshenko beam model

Homogeneous rod

The main characteristics of the rod are: (i) Length: $L = 50\,[\mathrm{m}]$ [m], (ii) Young's modulus: $E = 210\,10^9\,[\mathrm{Pa}]$, (iii) Shear modulus $G = 80\,10^9\,[\mathrm{Pa}]$ (iv) Mass density: $\rho = 7850\,[\mathrm{kg/m^3}]$, (v) Thickness: $t = 1\,[\mathrm{m}]$, (vi) Moment of inertia: $I = \pi t^4/4 = 0.7854\,[\mathrm{kg\,m^2}]$, (vii) Cross section area: $A = \pi t^2 = 3.1416\,[m^2]$

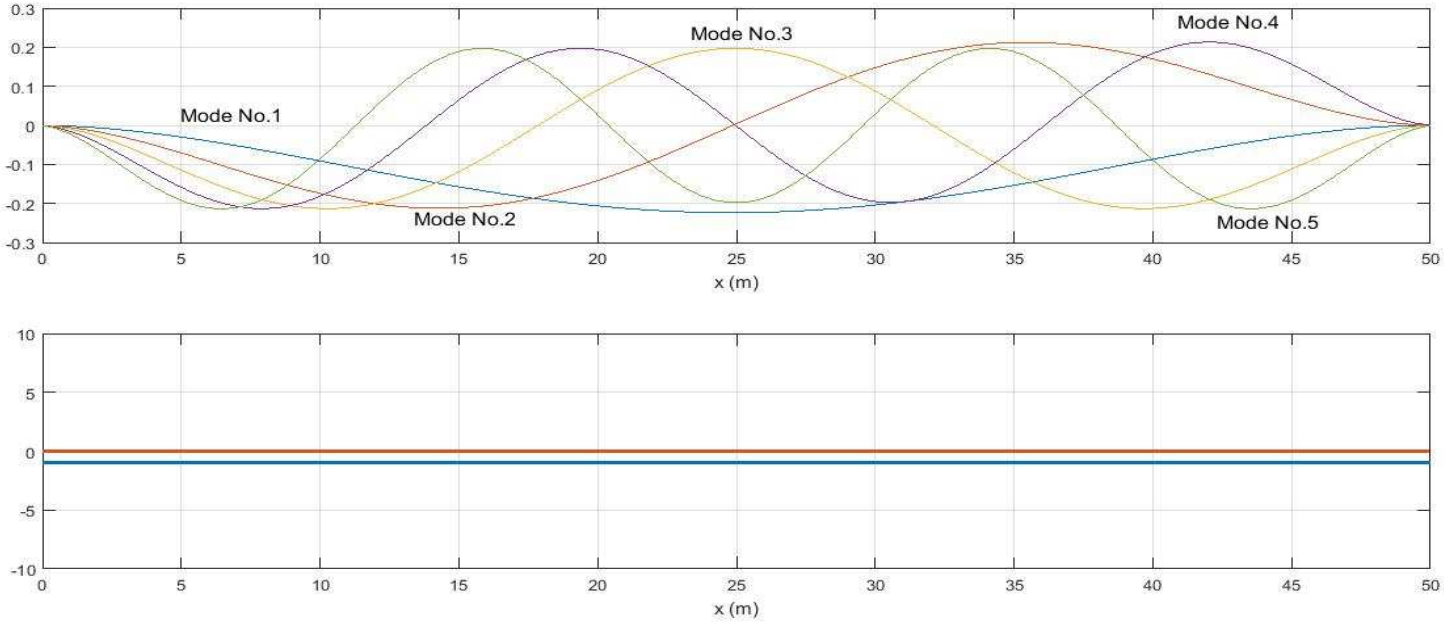

Fig. A.18 Normalized eigenfunctions for homogeneous clamped rod, M=100 points, $K = 0.8571$

Mode	Numerical Method Frequencies (M=100)
1	23.580
2	64.481
3	125.485
4	203.820
5	298.793
6	408.324
7	530.333

Table A.24 Natural frequencies, [rad/sec], for clamped rod

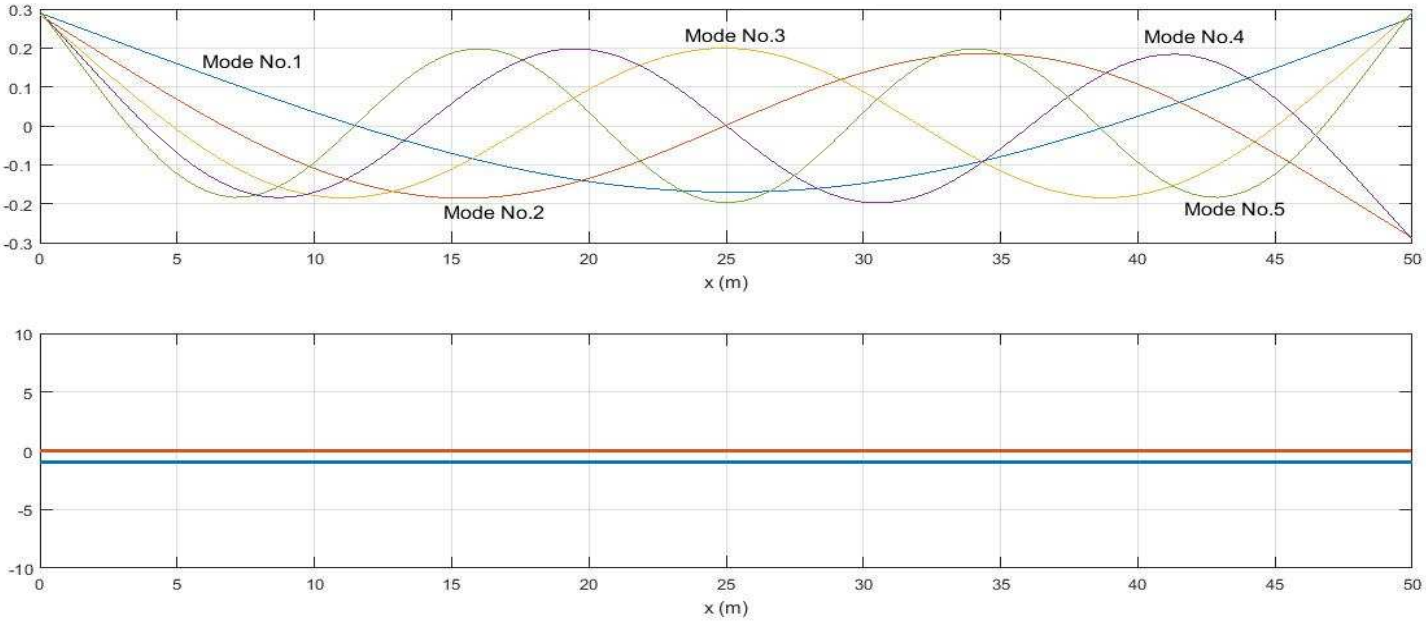

Fig. A.19 Normalized eigenfunctions for homogeneous free rod, M=100 points, $K = 0.8571$

Mode	**Numerical Method Frequencies (M=100)**
1	24.273
2	66.560
3	128.951
4	210.753
5	309.192
6	422.882
7	549.743

Table A.25 Natural frequencies, $\left[\text{rad/sec}\right]$, for free rod

As we see from the obtained results in the Timoshenko model the normal modes, concerning a circular sectional area, differ from the corresponding ones obtained from the Euler – Bernoulli model.

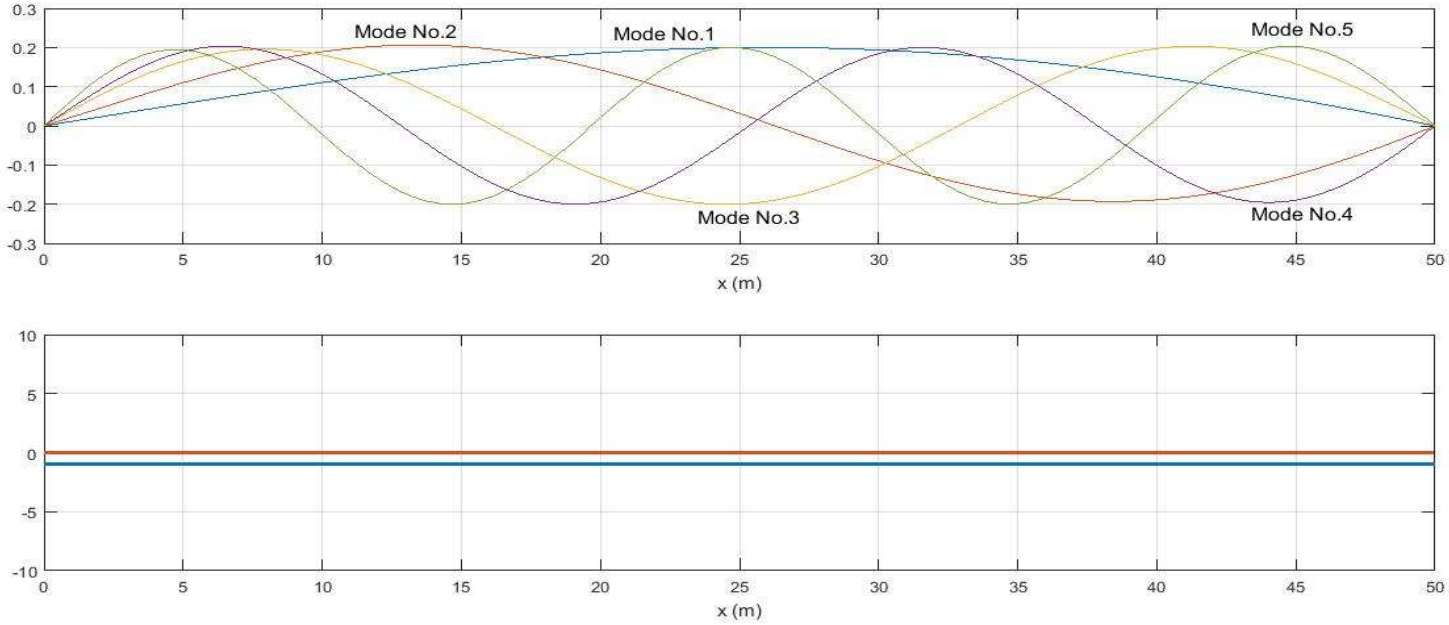

Fig. A.20 Normalized eigenfunctions for homogeneous pinned rod, using 100 points, $K = 0.8571$

Mode	**Numerical Method Frequencies (M=100)**
1	10.409
2	41.604
3	93.596
4	164.306
5	252.347
6	357.025
7	475.567

Table A.26 Natural frequencies, $[\text{rad/sec}]$, for pinned rod

It is now obvious, that the calculations according to the Timoshenko theory lead to higher natural frequencies compared to the ones derived from the Euler – Bernoulli model. The difference regarding the two methods is that the former involves the shear deformations of the beam. Furthermore, we use various discretization steps to demonstrate the progressive convergence of the method as we dense the grid over the beam. The results, concerning a clamped rod, are depicted in the following figures:

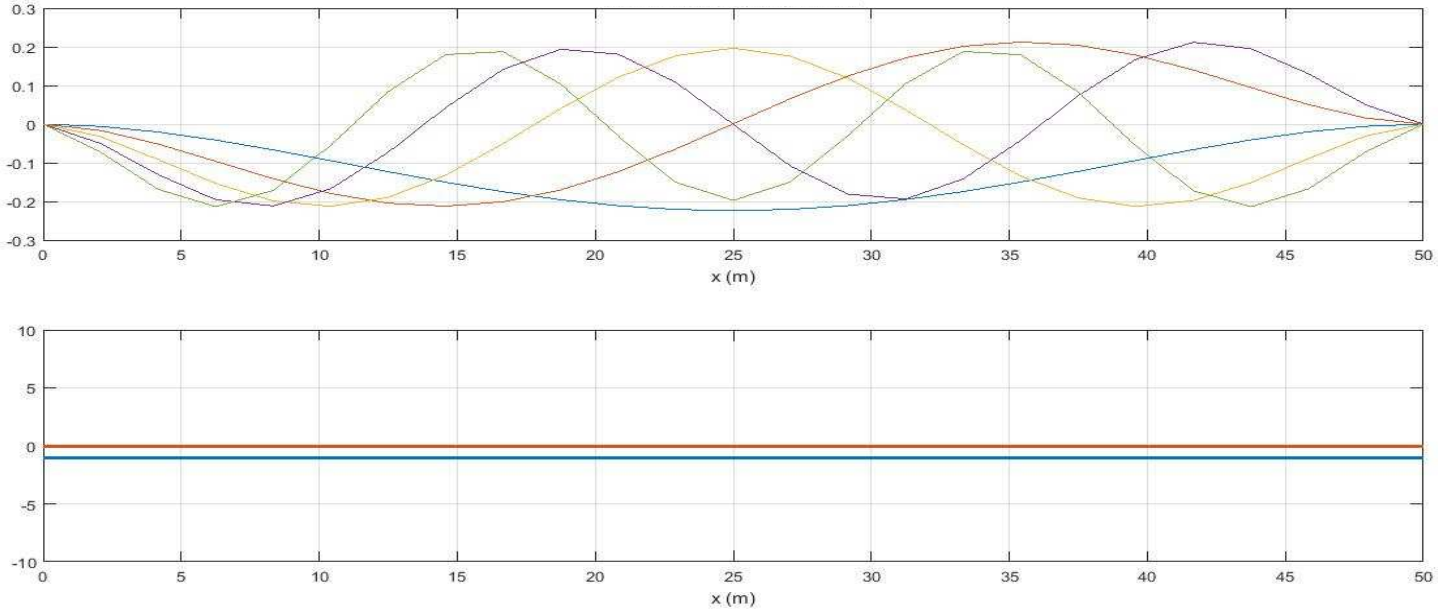

Fig. A.21 Clamped edged homogeneous rod, M=25 points, $K = 0.8571$

Mode	**Numerical Method Frequencies (M=25)**
1	35.365
2	95.676
3	183.023
4	294.634
5	425.655
6	573.313
7	733.450

Table A.27 Natural frequencies

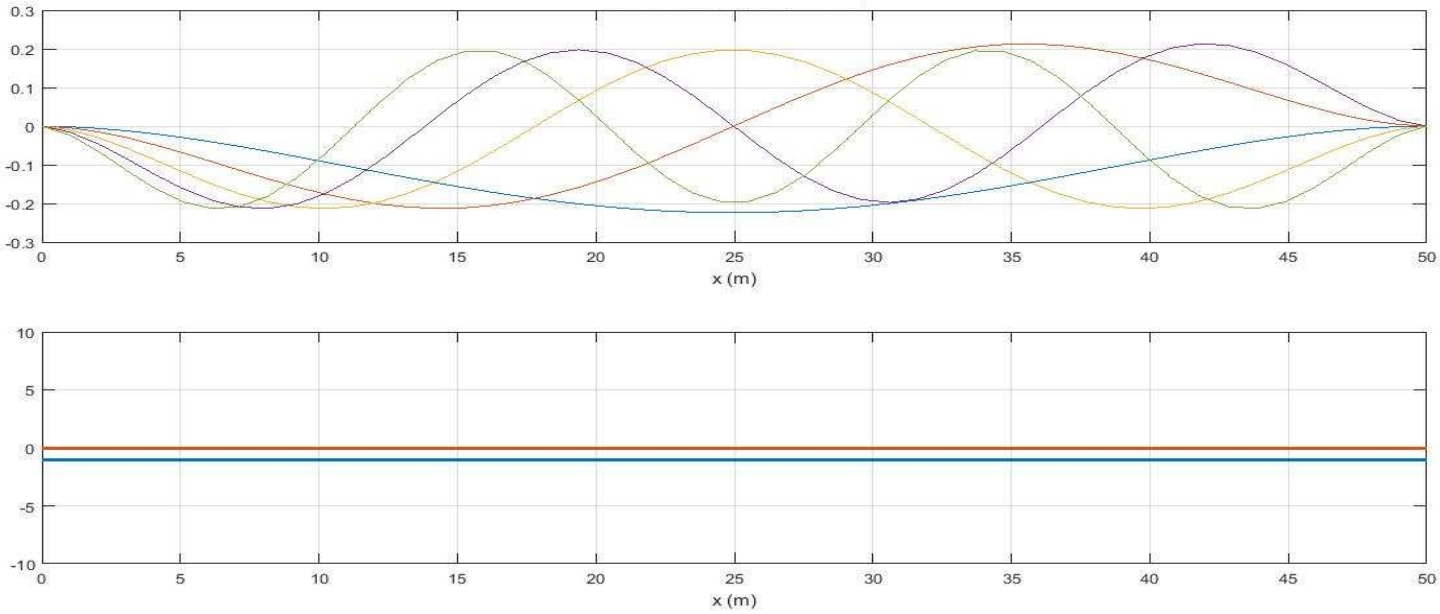

Fig. A.22 Clamped edged homogeneous rod, M=50 points, $K = 0.8571$

Mode	**Numerical Method Frequencies (M=50)**
1	26.353
2	72.106
3	138.656
4	225.311
5	329.295
6	448.531
7	580.939

Table A.28 Natural frequencies

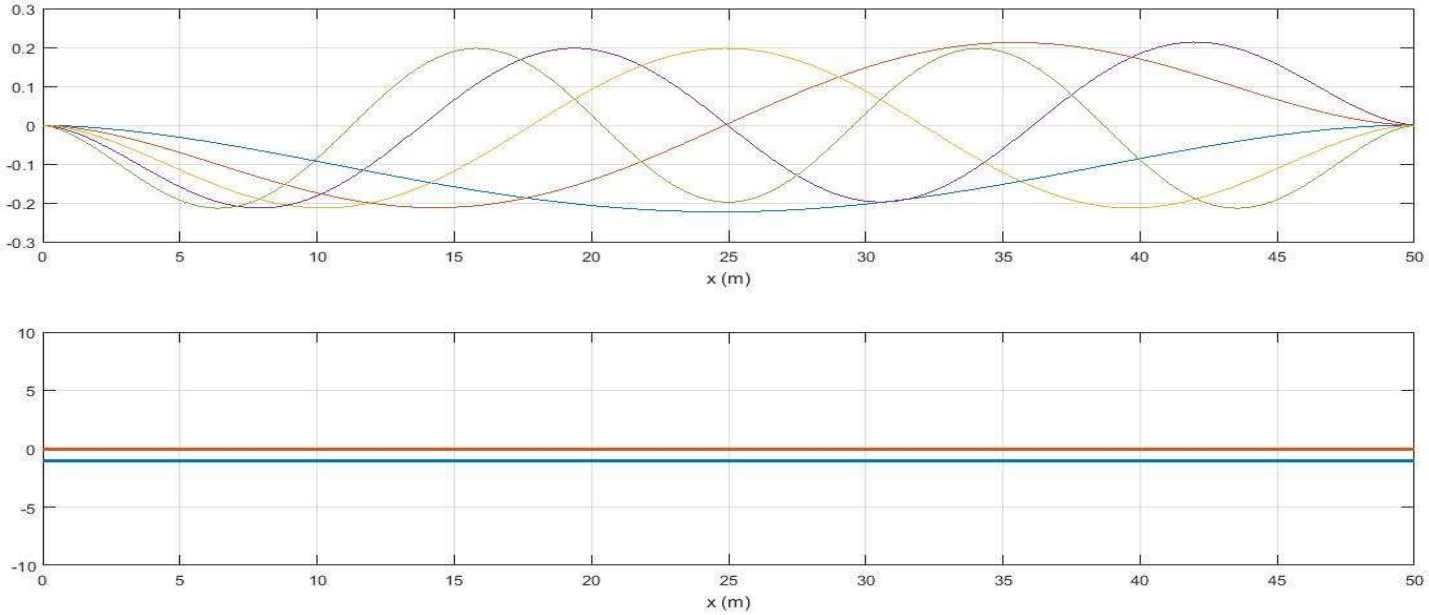

Fig. A.23 Clamped homogeneous rod, M=150 points, $K = 0.8571$

Mode	**Numerical Method Frequencies (M=150)**
1	22.887
2	63.094
3	122.712
4	199.661
5	292.554
6	400.005
7	519.934

Table A.29 Natural frequencies

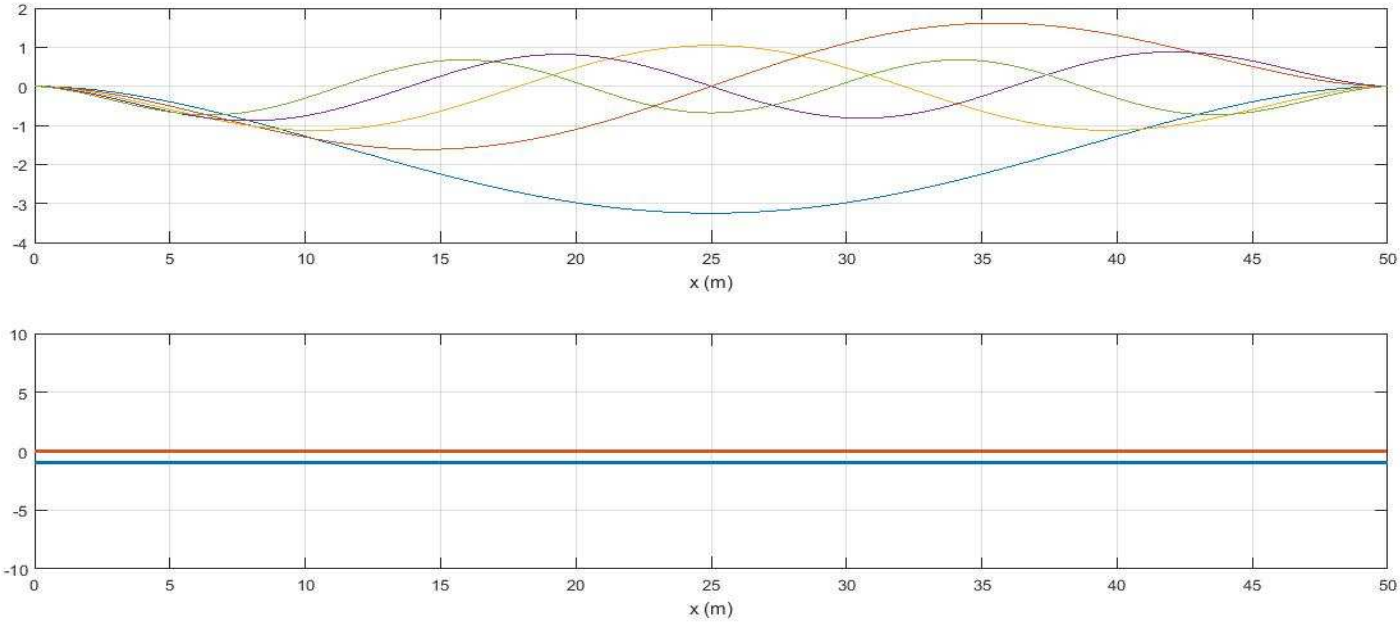

Fig. A.24 Clamped homogeneous rod, M=200 points, $K = 0.8571$

Mode	**Numerical Method Frequencies (M=200)**
1	22.887
2	63.094
3	122.019
4	198.274
5	290.474
6	397.232
7	516.468

Table A.30 Natural frequencies

Points / Mode	**25**	**50**	**100**	**150**	**200**
1	35.365	26.353	23.580	22.887	23.144
2	95.676	72.106	64.481	63.094	63.317
3	183.023	138.656	125.485	122.712	122.744
4	294.634	225.311	203.820	199.661	200.111
5	425.655	329.295	298.793	292.554	294.032
6	573.313	448.531	408.324	400.005	403.122
7	733.450	580.939	530.333	519.934	525.787

Table A.31 Focusing results for the converge of the natural frequencies

Results for an inhomogeneous rod

We use the same function to describe the change of the thickness of the beam. From, $b=1$ [m], concerning the domain, $x \leq 10$ and $x \geq 40$, to $b=2$ [m] in the domain , $10 < x < 40$ with its maximum thickness to be in the middle of the beam.

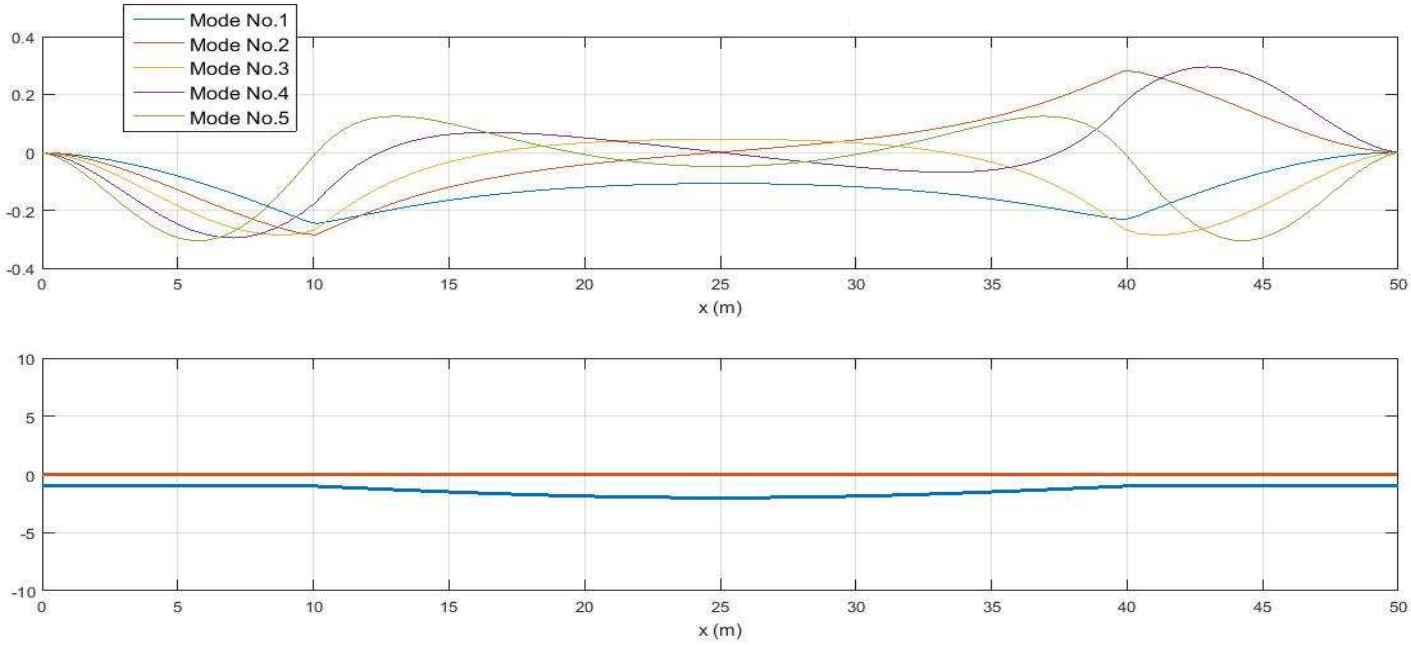

Fig. A.25 Normalized modes for inhomogeneous clamped rod, M=100 points, $K=0.8571$

Mode	Numerical Method Frequencies
1	23.580
2	82.505
3	158.760
4	252.347
5	366.037
6	497.751
7	641.943

Table A.32 Natural frequencies, $[\text{rad/sec}]$, clamped rod

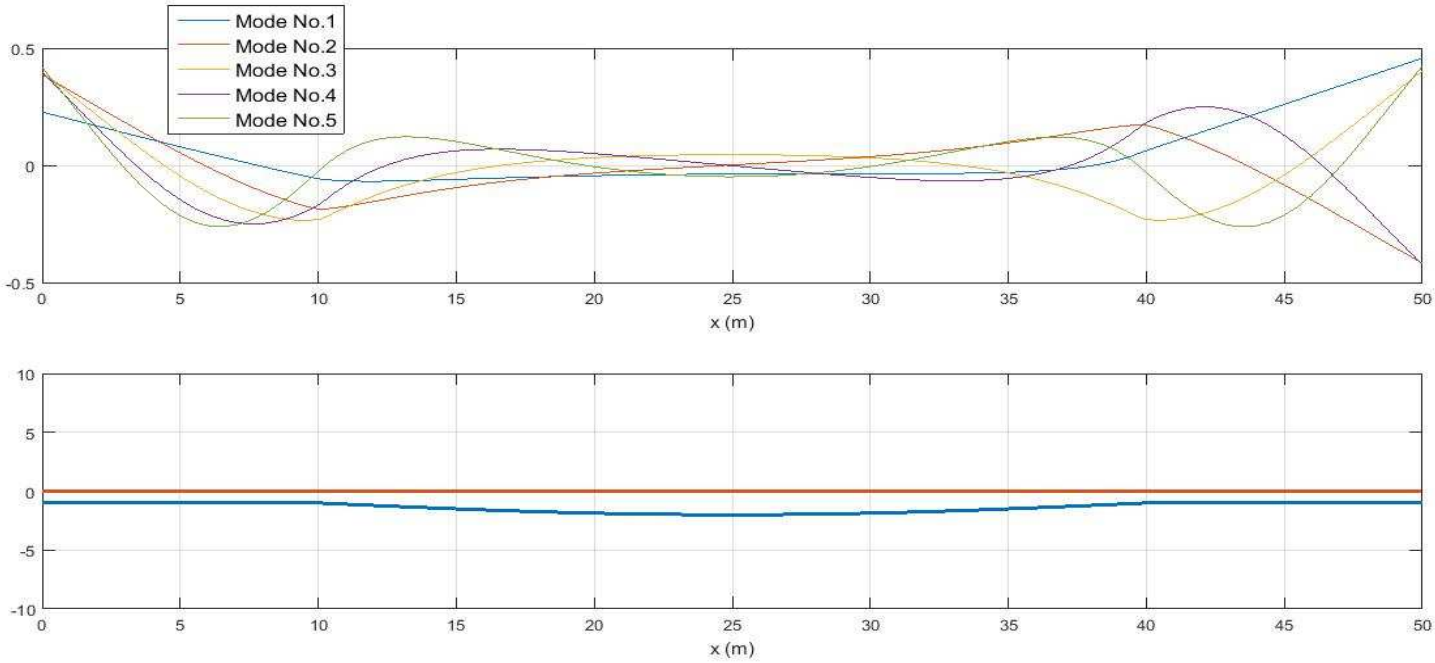

Fig. A.26 Normalized inhomogeneous free rod, M=100 points, $K = 0.8571$

Mode	**Numerical Method Frequencies**
1	21.500
2	84.584
3	164.306
4	262.745
5	379.901
6	517.161
7	667.593

Table A.33 Natural frequencies, $[\text{rad/sec}]$, for free rod

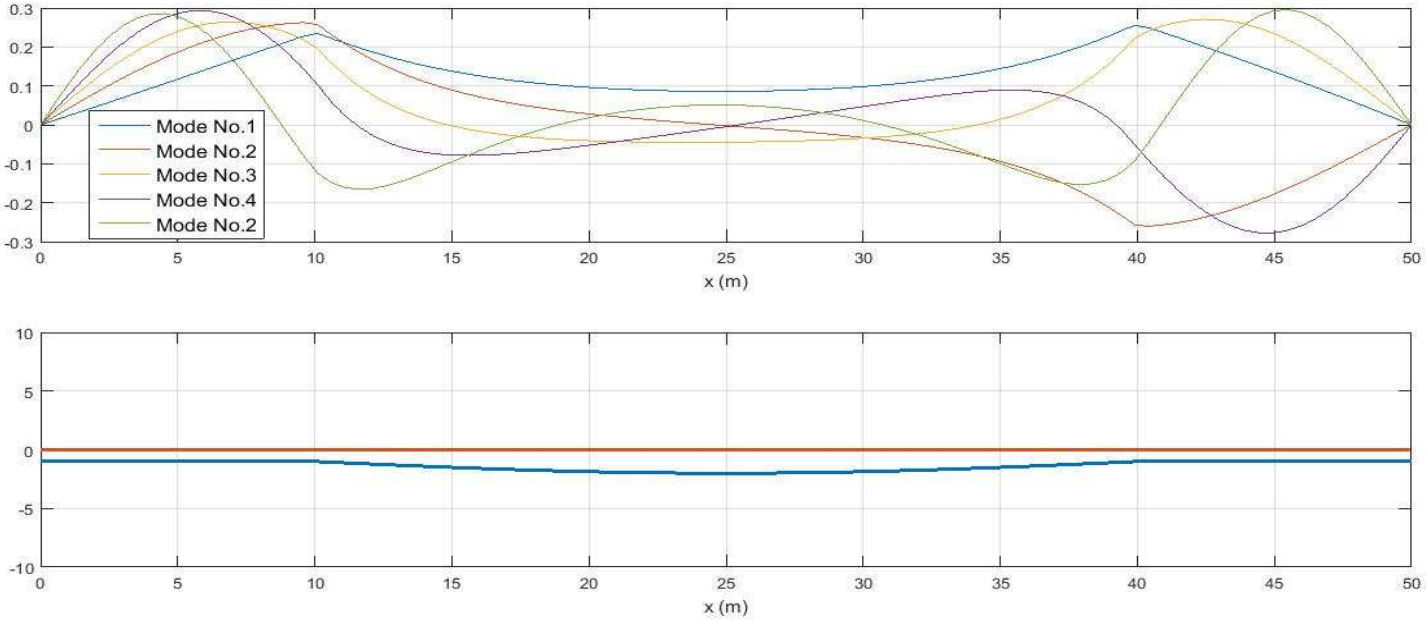

Fig. A.27 Normalized inhomogeneous pinned rod, M=100 points, $K = 0.8571$

Mode	Numerical Method Frequencies
1	6.2491
2	55.4686
3	117.1662
4	202.4338
5	311.9645
6	440.2125
7	580.2454

Table A.34 Natural frequencies, $\left[\text{rad/sec}\right]$, for pinned rod

Results for a homogeneous beam

The main characteristics of the beam are: (i) Length: $L = 50\,\left[\text{m}\right]$ [m], (ii) Young's modulus: $E = 5\,10^6\,\left[\text{Pa}\right]$, shear modulus $G = 80\,10^9\,\left[\text{Pa}\right]$ (ii) Mass density: $\rho = 923\,\left[\text{kg/m}^3\right]$, (iv) Thickness: $t = 1\,\left[\text{m}\right]$, (v) Moment of inertia: $I = \pi t^3 / 12 = 0.0833\,\left[\text{kg m}^2\right]$,(vi) Cross section area: $A = t^2 = 1\,\left[m^2\right]$.

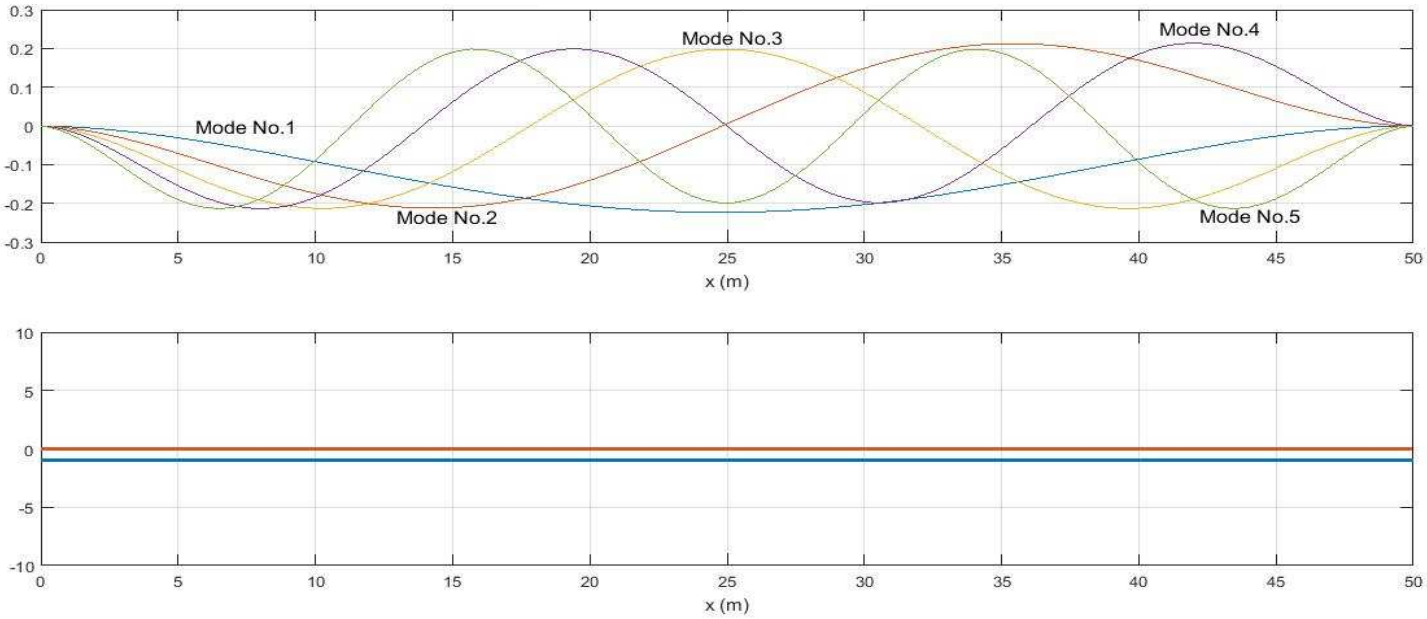

Fig.A.28 Normal modes for homogeneous clamped beam, M=100 points, $K = 0.8333$

Mode	Numerical Method Frequencies
1	14.568
2	40.218
3	79.039
4	130.338
5	192.729
6	266.904
7	352.172

Table A.35 Natural frequencies, $[\text{rad/sec}]$, for clamped beam

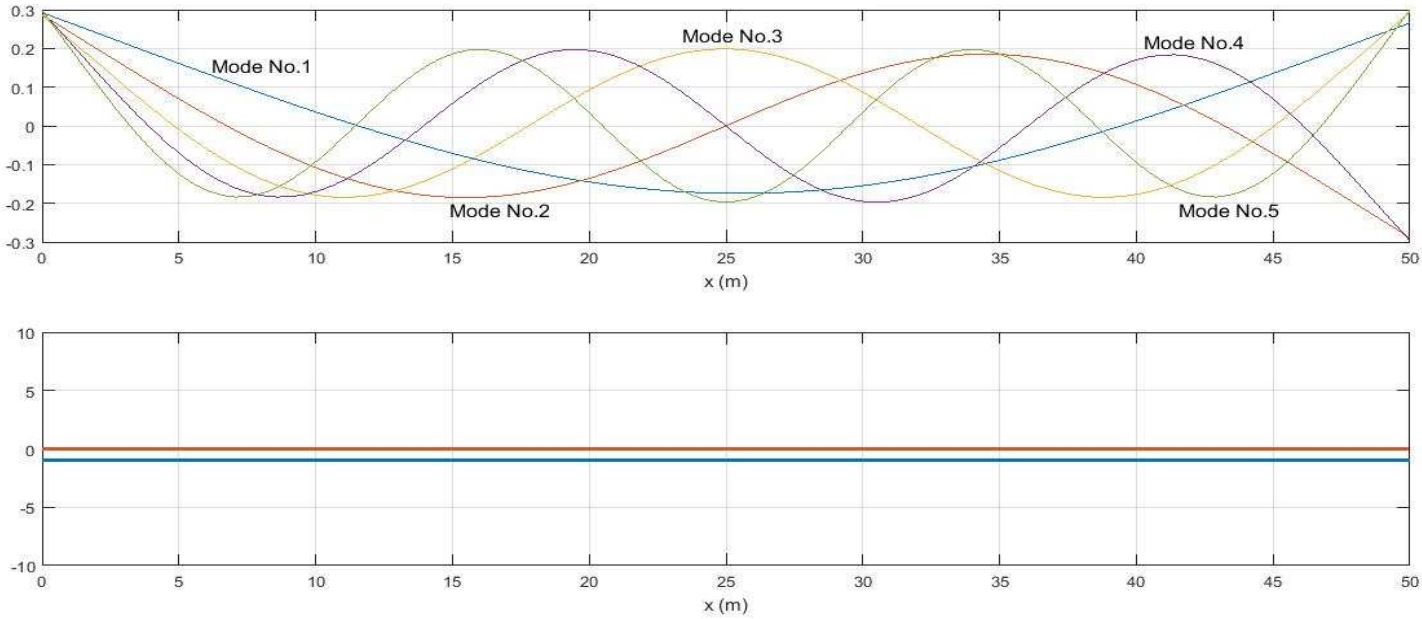

Fig. A.29 Normalized eigenfunctions for homogeneous free beam, M=100 points, $K = 0.8333$

Mode	Numerical Method Frequencies
1	14.568
2	41.604
3	81.118
4	133.804
5	198.274
6	274.530
7	361.877

Table A.36 Natural frequencies, $\left[\text{rad/sec}\right]$, for free beam

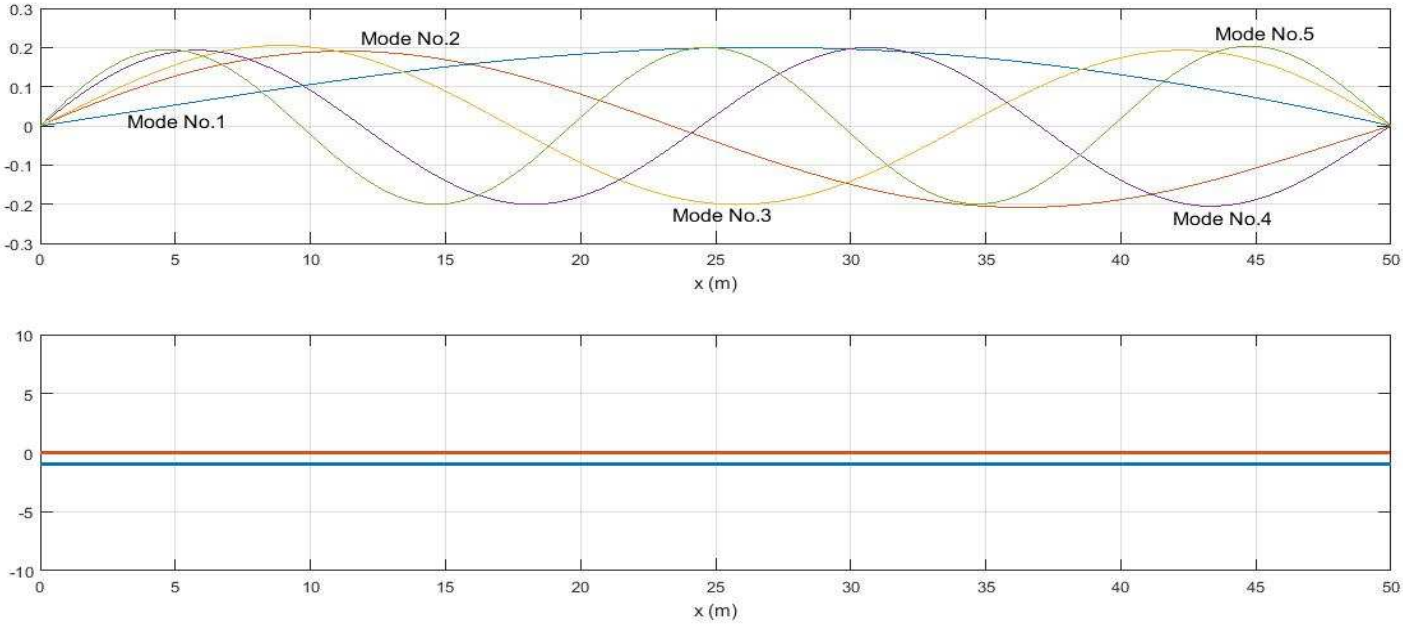

Fig. A.30 Normalized eigenfunctions for homogeneous pinned beam, M= 100 points, $K = 0.8333$

Mode	Numerical Method Frequencies
1	6.249
2	25.660
3	58.242
4	103.302
5	160.840
6	230.163
7	310.578

Table A.37 Natural frequencies, $[\text{rad/sec}]$, for pinned beam

Results for an inhomogeneous beam

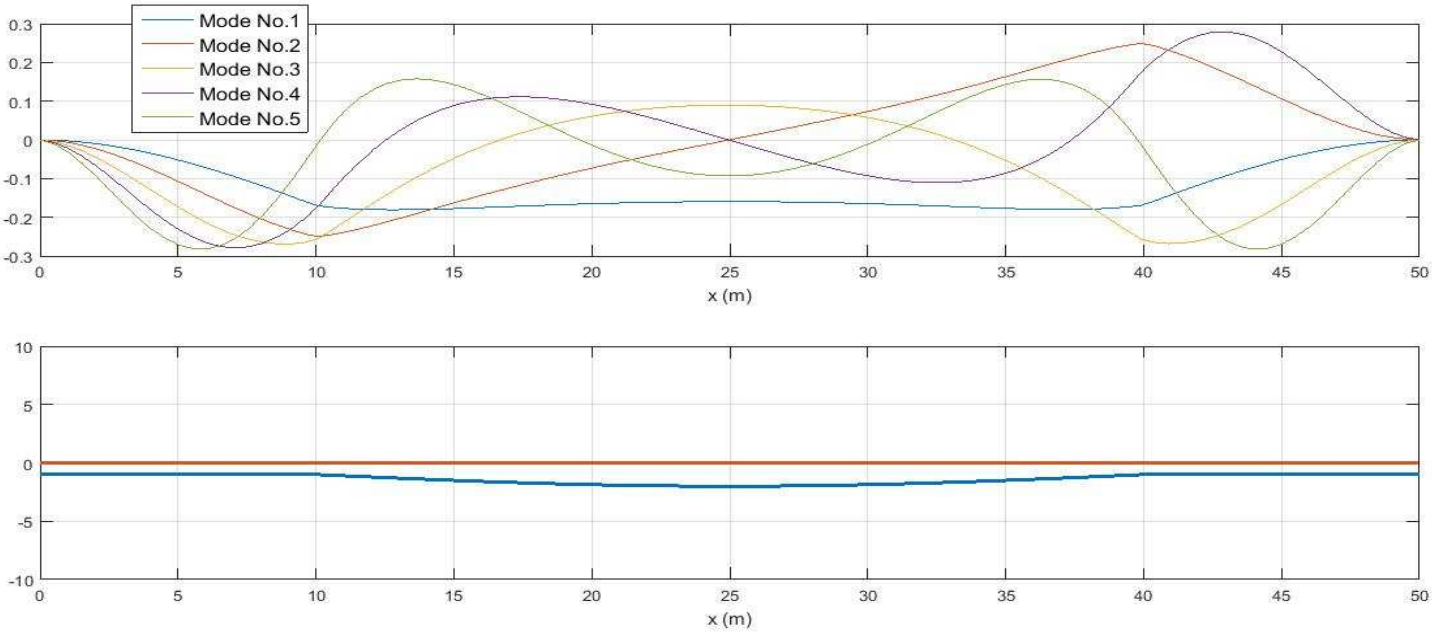

Fig. A.31 Normal modes for inhomogeneous clamped beam, M=100 points, $K = 0.8333$

Mode	Analytic Method Frequencies
1	15.261
2	51.309
3	99.142
4	160.840
5	237.095
6	329.295
7	432.587

Table A.38 Natural frequencies, $[\text{rad/sec}]$, for clamped inhomogeneous beam

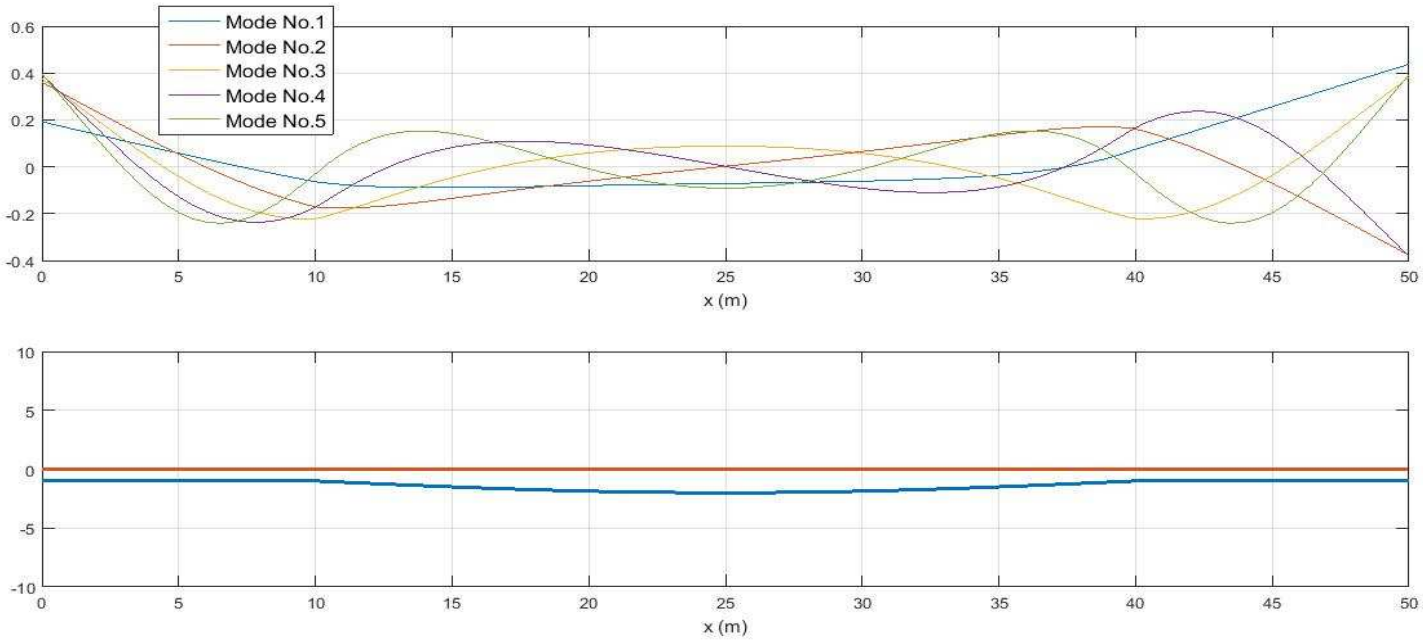

Fig. A.32 Normalized eigenfunctions for inhomogeneous free beam, M=100 points, $K = 0.8333$

Mode	Analytic Method Frequencies
1	13.875
2	52.002
3	102.608
4	165.693
5	244.721
6	339.001
7	446.452

Table A.39 Natural frequencies, $[\text{rad/sec}]$, for free inhomogeneous beam

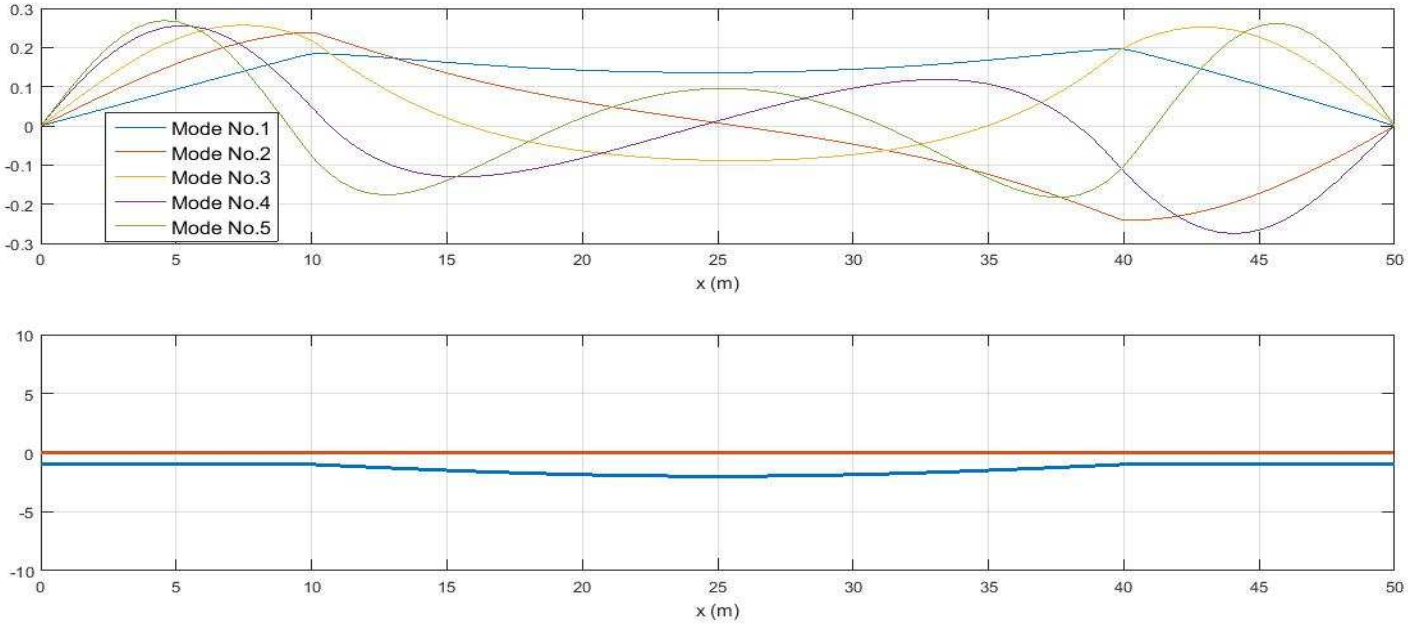

Fig.A.33 Normalized eigenfunctions for inhomogeneous pinned beam, M=100 points

Mode	Analytic Method Frequencies
1	4.863
2	33.978
3	72.799
4	126.872
5	198.968
6	285.622
7	383.367

Table A.40 Natural frequencies, $[\text{rad/sec}]$, for pinned inhomogeneous beam

Comparative results of natural frequencies concerning a beam and a rod cross section area

In the following tables we present the way the natural frequencies change depending on the shape of the cross sectional area. Thus, we compare and contrast all the possible combinations of the geometrical shapes.

Mode	NATURAL FREQUENCIES		
1	23.580	24.273	10.409
2	64.481	66.560	41.604
3	125.485	128.951	93.596
4	203.820	210.753	164.306
5	298.793	309.192	252.347
6	408.324	422.882	357.025
7	530.333	549.743	475.567

Table A.41 Homogeneous rod , Clamped (left) , Free (center), Pinned (right)

Mode	NATURAL FREQUENCIES		
1	23.580	21.500	6.2491
2	82.505	84.584	55.4686
3	158.760	164.306	117.1662
4	252.347	262.745	202.4338
5	366.037	379.901	311.9645
6	497.751	517.161	440.2125
7	641.943	667.593	580.2454

Table A.42 Inhomogeneous rod , Clamped (left) , Free (center), Pinned (right)

Mode	NATURAL FREQUENCIES		
1	14.568	14.568	6.249
2	40.218	41.604	25.660
3	79.039	81.118	58.242
4	130.338	133.804	103.302
5	192.729	198.274	160.840
6	266.904	274.530	230.163
7	352.172	361.877	310.578

Table A.43 Homogeneous beam, Clamped (left) , Free (center), Pinned (right)

Mode	NATURAL FREQUENCIES		
1	15.261	13.875	4.863
2	51.309	52.002	33.978
3	99.142	102.608	72.799
4	160.840	165.693	126.872
5	237.095	244.721	198.968
6	329.295	339.001	285.622
7	432.587	446.452	383.367

Table A.44 Inhomogeneous beam, Clamped (left) , Free (center), Pinned (right)

Mode	EIGENFREQUENCIES	
1	14.568	23.580
2	40.218	64.481
3	79.039	125.485
4	130.338	203.820
5	192.729	298.793
6	266.904	408.324
7	352.172	530.333

Table A.45 Homogeneous beam (left) , homogeneous rod (right),given clamped type of edges

Mode	EIGENFREQUENCIES	
1	15.261	23.580
2	51.309	82.505
3	99.142	158.760
4	160.840	252.347
5	237.095	366.037
6	329.295	497.751
7	432.587	641.943

Table A.46 Inhomogeneous beam (left), inhomogeneous rod (right), given clamped type of edges

We note that in this case too circular sections are excited from higher frequencies compared to the square corresponding ones.

Comparative results for the Timoshenko and Euler – Bernoulli models

In order to understand how shear deformations shape the range of the natural frequencies we demonstrate comparative results for both the TBT and EBT.

Mode	EIGENFREQUENCIES	
1	23.176	23.580
2	63.956	64.481
3	125.486	125.485
4	207.595	203.820
5	310.305	298.793
6	433.620	408.324
7	577.504	530.333

Table A.47 Homogeneous clamped rod, EBT (left), TBT (right)

Mode	EIGENFREQUENCIES	
1	23.176	24.273
2	63.956	66.560
3	125.486	128.951
4	207.595	210.753
5	310.305	309.192
6	433.620	422.882
7	577.504	549.743

Table A.48 Homogeneous free rod, EBT (left), TBT (right)

Mode	EIGENFREQUENCIES	
1	10.206	10.409
2	40.826	41.604
3	91.833	93.596
4	163.185	164.306
5	254.826	252.347
6	366.693	357.025
7	498.698	475.567

Table A.49 Homogeneous pinned rod, EBT (left), TBT (right)

Mode	EIGENFREQUENCIES	
1	23.625	23.580
2	69.538	82.505
3	174.939	158.760
4	286.087	252.347
5	414.479	366.037
6	570.986	497.751
7	759.211	641.943

Table A.50 Inhomogeneous clamped rod, EBT (left), TBT (right)

Mode	EIGENFREQUENCIES	
1	47.170	21.500
2	82.696	84.584
3	174.731	164.306
4	284.771	262.745
5	415.310	379.901
6	574.726	517.161
7	765.928	667.593

Table A.51 Inhomogeneous free rod, EBT (left), TBT (right)

Mode	EIGENFREQUENCIES	
1	12.683	6.2491
2	44.469	55.4686
3	135.604	117.1662
4	224.661	202.4338
5	338.718	311.9645
6	486.431	440.2125
7	663.437	580.2454

Table A.52 Inhomogeneous pinned rod, EBT (left), TBT (right)

Mode	EIGENFREQUENCIES	
1	13.364	14.568
2	36.858	40.218
3	72.251	79.039
4	119.414	130.338
5	178.321	192.729
6	248.931	266.904
7	331.180	352.172

Table A.53 Homogeneous clamped beam, EBT (left), TBT (right)

Mode	EIGENFREQUENCIES	
1	13.380	14.568
2	36.925	41.604
3	72.448	81.118
4	119.855	133.804
5	179.152	198.274
6	250.349	274.530
7	333.424	361.877

Table A.54 Homogeneous free beam, EBT (left), TBT (right)

Mode	EIGENFREQUENCIES	
1	13.380	14.568
2	36.925	41.604
3	72.448	81.118
4	119.855	133.804
5	179.152	198.274
6	250.349	274.530
7	333.424	361.877

Table A.55 Homogeneous pinned beam, EBT (left), TBT (right)

Mode	EIGENFREQUENCIES	
1	15.661	15.261
2	43.569	51.309
3	96.269	99.142
4	160.327	160.840
5	236.918	237.095
6	327.360	329.295
7	434.215	432.587

Table A.56 Inhomogeneous clamped beam, EBT (left), TBT (right)

Mode	EIGENFREQUENCIES	
1	24.456	13.875
2	48.486	52.002
3	96.408	102.608
4	160.050	165.693
5	237.749	244.721
6	329.646	339.001
7	438.093	446.452

Table A.57 Inhomogeneous free beam, EBT (left), TBT (right)

Mode	EIGENFREQUENCIES	
1	8.251	4.863
2	27.503	33.978
3	72.793	72.799
4	126.809	126.872
5	194.329	198.968
6	277.707	285.622
7	378.260	383.367

Table A.58 Inhomogeneous pinned beam, EBT (left), TBT (right)

The above results clearly depict the effect of the shear modulus, G, and of the rotary inertia , J,on the normal frequencies and the normal modes either we refer to a circular cross section or to a square section area.

Appendix B

Calculation of the radiation potentials

For the calculation of the sectional hydrodynamic coefficients $\varpi_{i\ell}(x_1) = \int_{C(x_1)} N_\ell \phi_i ds$, where x_1 denotes the position alongships, the 2D potentials, $\phi_i(x_1)$, $i = 2,3,4$, on the vertical $x_2 - x_3$ plane are required. The latter are obtained by solving boundary value problems consisted of the Laplace equation in deep water

$$\frac{\partial^2 \phi_\ell}{\partial x_2^2} + \frac{\partial^2 \phi_\ell}{\partial x_3^2} = 0 \ , \quad \ell = 2,3,4 \ , \tag{1}$$

the free surface boundary condition

$$-\omega^2 \phi_\ell + g \frac{\partial \phi_\ell}{\partial x_3} = 0 \ , \quad \ell = 2,3,4 \ , \text{ on } x_3 = 0 \ , \tag{2}$$

boundary condition on the wet surface of each section

$$\frac{\partial \phi_\ell}{\partial N} = N_\ell \ , \quad \ell = 2,3,4 \ , \text{ on } \partial D_B(x_1), \tag{3}$$

and finally the condition at infinity expressing the fact that the waves are outgoing at infinity

$$\frac{\partial \phi_\ell}{\partial x_2} \pm \frac{i\omega^2}{g} \phi_\ell = 0 \tag{4}$$

Several methods are available for the solution of (1) with boundary conditions (2)-(4),

- the domain discretization methods using finite difference or finite element methods and boundary element methods (see, e.g. Ohkusu 1996),
- analytic function methods in conjunction with conformal mapping techniques, Ursell (1949), Lewis (1986)
- integral equation methods exploiting the Green function of the Laplace equation (method of potentials, methods based on Green's theorem, Frank 1967).

In this work a Boundary Element Method (BEM) will be developed and used for the solution of the sectional problems, based on source-sink distributions, in conjunction with an absorbing layer technique, permitting to truncate the computational domain at

some distance from the body where the solution is absorbed with minimal reflections, and thus, minimum contamination of the numerical solution.

First we consider a 2D section of the ship with local beam, B, and draft, T, as shown in Fig. A.1. The section is symmetric with respect to x_3-axis. We also assume that the body is even keel; therefore, the center of gravity and the center of buoyancy are collinear.

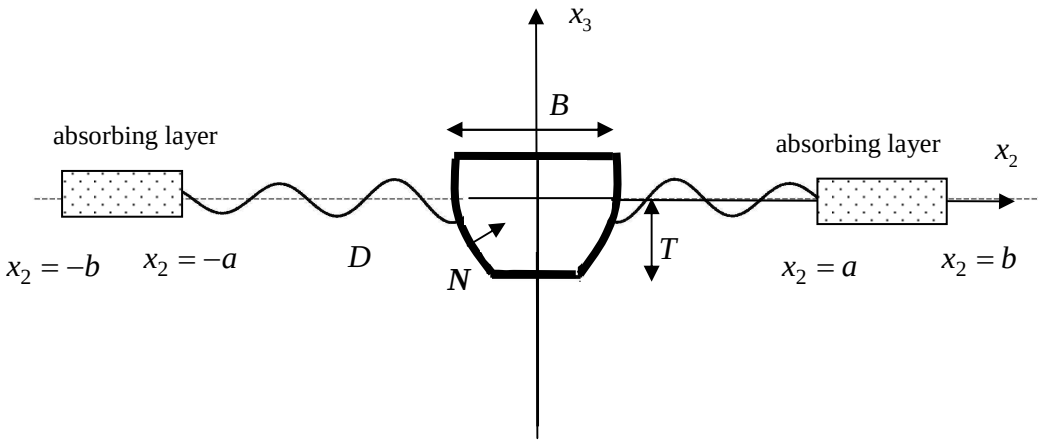

Fig. B.1 Section of the ship

The potential at a point, $\boldsymbol{x}$, $\phi_i(\boldsymbol{x})$ based on surface source-sink distribution $\sigma_i(\boldsymbol{x})$ over the boundary is used,

$$\phi_i(\boldsymbol{x}) = \int_{\partial D_B \bigcup \partial D_F} \sigma_i(\boldsymbol{x}) Q(\boldsymbol{x} \mid \boldsymbol{x_s}) dS \quad i = 2,3,4 \ , \tag{5}$$

where $Q(\boldsymbol{x} \mid \boldsymbol{x_s})$ is the fundamental solution of the 2D Laplace equation, i.e. ,

$$Q(\boldsymbol{x} \mid \boldsymbol{x_s}) = -\frac{1}{2\pi} \ln\left(\left|\boldsymbol{x} - \boldsymbol{x_s}\right|\right) \tag{6}$$

with $\boldsymbol{x} = (x_2, x_3)$ denoting the field point in the domain and $\boldsymbol{x}_s = (x_{2s}, x_{3s})$ denoting the source point on the boundary of the domain $\partial D_F \bigcup \partial D_B$, which consists of two parts the free surface (left and right to the body) ∂D_F and the wetted part of the body ∂D_B.

The derivative of the potential ϕ_i with respect to $\boldsymbol{x}$ at a point in the domain is

$$u_i(\boldsymbol{x}) = \nabla_{\boldsymbol{x}}\phi_i(\boldsymbol{x}) = \int_{\partial D^I} \sigma_i(\boldsymbol{x}) \nabla_{\boldsymbol{x}} Q(\boldsymbol{x} \mid \boldsymbol{x}_s) dS \ , \qquad i = 2,3,4 \ , \tag{7}$$

where

$$\nabla_{\boldsymbol{x}} Q(\boldsymbol{x} \mid \boldsymbol{x}_s) = -\frac{\boldsymbol{x} - \boldsymbol{x}_s}{2\pi |\boldsymbol{x} - \boldsymbol{x}_s|^2} \ . \tag{8}$$

On the boundary $\boldsymbol{x} \in \partial D_B \bigcup \partial D_F$ the derivative of the potential see e.g., Gunter 1967, Kress 1989) , is expressed as follows

$$u_i(\boldsymbol{x}) = \frac{\sigma_i(\boldsymbol{x}) \boldsymbol{N}(\boldsymbol{x})}{2} + \int_{\partial D^I} \sigma_i(\boldsymbol{x}) \nabla_{\boldsymbol{x}} Q(\boldsymbol{x} \mid \boldsymbol{x}_s) dS \, , \quad \boldsymbol{x} \in \partial D_B \bigcup \partial D_F \ , \quad i = 2,3,4$$

(8)

where $\boldsymbol{N} = (N_2, N_3)$ is the normal vector. Accordingly, the normal velocity on the boundary is

$$\frac{\partial \phi_i}{\partial n} = \frac{\sigma_i(\boldsymbol{x})}{2} + \boldsymbol{N}(\boldsymbol{x}) \int_{\partial D^I} \sigma_i(\boldsymbol{x}) \nabla_{\boldsymbol{x}} Q(\boldsymbol{x} \mid \boldsymbol{x}_s) dS \, , \quad \boldsymbol{x} \in \partial D_B \bigcup \partial D_F \ , \quad i = 2,3,4 \, . \tag{9}$$

where $n(\boldsymbol{x}) = (N_2, N_3)$, is the normal vector pointing into the exterior of the domain D, and thus, into the interior of the body on ∂D_B .

The boundary condition on the surface of the body takes the form

$$\frac{\sigma_i(\boldsymbol{x})}{2} + \boldsymbol{N}(\boldsymbol{x}) \int_{\partial D^I} \sigma_i(\boldsymbol{x}) \nabla_{\boldsymbol{x}} Q(\boldsymbol{x} \mid \boldsymbol{x}_s) dS = N_i(\boldsymbol{x}) \ , \ i = 2,3,4 \, , \ \boldsymbol{x} \in \partial D_B \ , \tag{10}$$

and the corresponding boundary condition on the (linearized) free surface is

$$\frac{\sigma_i(\boldsymbol{x})}{2} + \boldsymbol{n}(\boldsymbol{x}) \int_{\partial D^I} \sigma_i(\boldsymbol{x}) \nabla_{\boldsymbol{x}} Q(\boldsymbol{x} \mid \boldsymbol{x}_s) dS - \frac{\omega^2}{g} \int_{\partial D^I} \sigma_i(\boldsymbol{x}) Q(\boldsymbol{x} \mid \boldsymbol{x}_s) dS = 0$$

$$i = 2,3,4 \qquad \boldsymbol{x} \in \partial D_F \tag{11}$$

An important task concerning the present scheme deals with the treatment of horizontally infinite domain and the implementation of appropriate radiation-type conditions at infinity. Although in the case of linear waves, conditions at infinity could be treated using the appropriate time-dependent Green function, the present work is based on the truncation of the domain and on the use of Perfectly Matched

Layer (PML) model, as e.g. described by Berenger (1994) and Turkel, Yefet (1998), optimized by Collino, Monk (1998); see also Filippas, Belibassakis (2014)

The latter model permits the numerical absorption of the waves reaching the left, $x=a$, and right, $x=b$, ends of the truncated domain with minimum reflection. This selection is motivated by the fact that PML model supports the efficient extension of the present numerical scheme to treat generation and propagation of non-linear waves excited due to motion(s) of the moving body; see also Filippas, Belibassakis (2014). Following Sclavounos, Borgen (2004) the boundary condition for $\boldsymbol{x}\in\partial D_F$ inside the absorbing layer ($x_2<-a$ and $x_2>a$ and $x_3=0$) is modified as follows

$$\frac{\partial\phi_i}{\partial x_3}-\frac{\left(\omega+j\delta(\omega)\right)^2}{g}\phi_i=0\ ,\ i=2,3,4\ ,\qquad \partial D_f(x_1)\qquad \text{at } x_3=0\ , \tag{12}$$

where the PML-parameter $\delta(\omega)$ is a positive absorption coefficient with support of size $\ell=b-a$ extended over several wavelengths from the artificial end-type boundaries, $x=\pm b$, used in order to truncate the computational domain. In the present work we use optimum PML coefficients, as described by Collino & Monk (1998) and applied by Belibassakis et al (2001) and Belibassakis & Athanassoulis (2011) to water wave problems. In accordance with the previous works the distribution of the absorption coefficient is of the form:

$$\delta(\omega)=\begin{cases}\delta_0(\omega)\left|x+a\right|^p\ , & x<\alpha\\ 0\qquad\ , & -a<x<a\ ,\\ \delta_0(\omega)\left|x-a\right|^p\ , & x>a\end{cases} \tag{13}$$

The performance of the PML model has been examined for PML absorbing layer with various parameters $\ell=\lambda,1.5\lambda,2\lambda$, $p=2,3,4$ and δ_0. It is found that the performance of the PML becomes better as its layer length increases. Based on extensive numerical evidence, we finally conclude that the PML parameters should be $\ell/\lambda\in[1,2]$, $p\in[2,4]$ and $\delta_0(\omega)$ increasing with ω for optimum performance in the studied problem. In the sequel $\ell/\lambda=1$, $p=3$ and $\delta_0(\omega)=\left(\omega/\omega_{\max}\right)^5$ is used.

Boundary Element Method

In this present work, we treat the problem using the Boundary Element Method, see, e.g. Beer & al (2008). Given a 2D geometry, see, e.g. Fig. A.2,

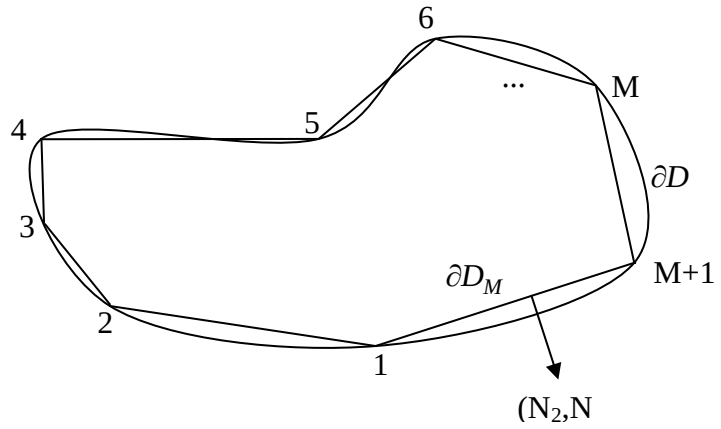

Fig. B.2 Boundary Element approximation

we consider a number M of segments to form a low-order polygonal approximation (polyline) to describe the given geometry, ∂D. The shape of the approximate geometry ∂D_M, is associated with the number of the elements, $i = 1,...,M$, used in the approximation, therefore the bigger number of elements we use, the better we approach the boundary, ∂D. This method is known as ‘’panel method’’ which is based on the property that the geometry approximation becomes more close to the exact geometry as the number of boundary element increases, i.e. $\partial D_M \to \partial D$, as $M \to \infty$. It should be noted that,

- a dense grid is used to minimize the approximation errors,
- specific parts with complicated geometry, e.g. the curvature of the boundary surface, required increased number of the panels,
- and at least 15 elements per wavelength are needed in order to discretize the free-surface part of the boundary, and thus the number of the elements depend on the wavelength and the frequency ω.

Let, $\sigma(\boldsymbol{x})$ be the unknown source-sink distribution over the boundary, ∂D. Concerning the low-order approximation the sink-source distribution, σ_i, is considered partially constant at each panel, $i = 1,...,M$, of the boundary, ∂D_M, see also, Fig. (A.3)

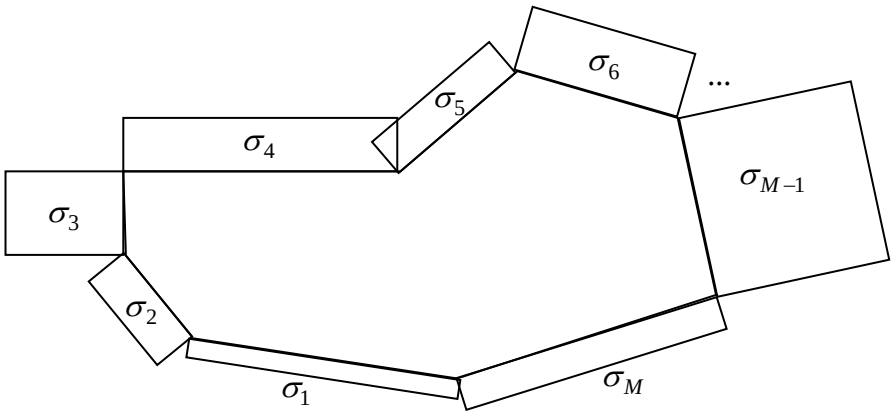

Fig. B.3 Source sink distribution using Boundary Element Method

It is now obvious that the sink-source distribution, σ_i , $i=1,...,M$ approaches the distribution $\sigma(\boldsymbol{x})$ over the real boundary ∂D_B , when,

$\left\|\sigma_i-\sigma(\boldsymbol{x})\right\| \underset{M\to\infty}{\to} 0$.

The integrals associated with the satisfaction of the boundary conditions, (10)-(12) will concern the center of each panel and will be represented by the index $i=1,...,M$. The boundary of the domain consists of the left and right, to the body, free surface and the wetted part of the body ∂D_B. Regarding the panel method, starting from left to right, we set M_1 denoting the number of elements of the free surface to the left of the body, M_2 denoting the wetted part of the body and M_3 denoting the right free surface. The potential $\varphi(\boldsymbol{x})$ based on the action of the sink-source distribution over the element (AB), at some point, $\boldsymbol{x}$, of the domain is given by Eqn. (5), see Fig.(A.4). Also by Eqns. (8), (9) we get the velocity, $u_i(\boldsymbol{x})$ and the normal velocity $\frac{\partial\varphi}{\partial n}$, equivalently produced by the potential, $\varphi(\boldsymbol{x})$.

The above integrals are easily calculated in local ζη- coordinate systems where the ζ-axis is selected to coincide with each panel; see Fig. B4

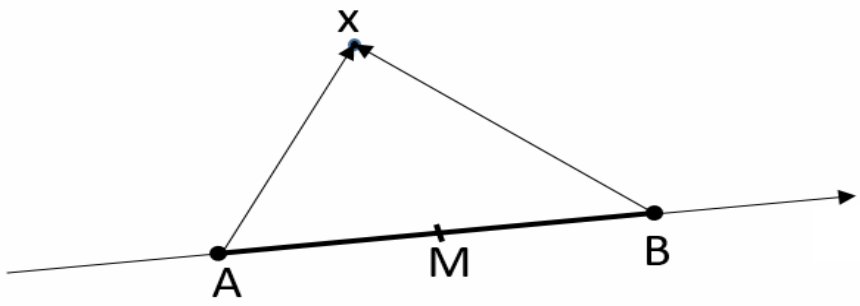

Fig. B.4 Linear segment AB as a low-order panel.

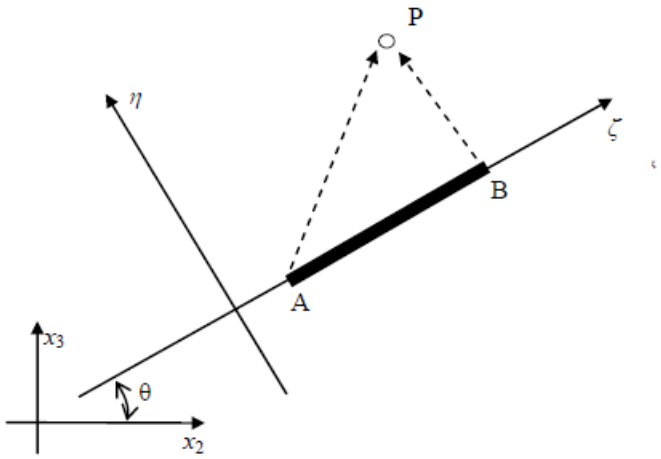

Fig. B.5 Local coordination system for (AB) element

Let (x_2, x_3) be the coordinates of a point P in the global coordinate system and (ζ, η) the coordinates of the same point in the local coordinate system. Let also $\left(x_2^A, x_3^A\right)$, $\left(x_2^B, x_3^B\right)$ denote the coordinates of the panel ends in the global coordinate system , and $(\zeta_A, 0)$, $(\zeta_B, 0)$ be the corresponding coordinates in the local system. The analytical expression of the result of the integral providing the induced potential is as follows

$$\phi(\zeta,\eta) = -\frac{\sigma}{2\pi}\left\{(\zeta-\zeta_A)\,ln\left[(\zeta-\zeta_A)^2+\eta^2\right]-(\zeta-\zeta_B)\,ln\left[(\zeta-\zeta_B)^2+\eta^2\right]+..\right\}$$

$$\left\{..+2\eta\left[\tan^{-1}\left(\frac{\eta}{(\zeta-\zeta_B)}\right)-\tan^{-1}\left(\frac{\eta}{(\zeta-\zeta_A)}\right)\right]\right\} \quad , \qquad (15)$$

and the corresponding velocities (derivatives of the potential) in the local coordinate system are given by

$$u_\eta(\zeta,\eta) = -\frac{\sigma}{2\pi}\left[\tan^{-1}\left(\frac{\eta}{(\zeta-\zeta_B)}\right) - \tan^{-1}\left(\frac{\eta}{(\zeta-\zeta_A)}\right)\right], \tag{16}$$

$$u_\zeta(\zeta,\eta) = -\frac{\sigma}{2\pi}\ln\left[\frac{(\zeta-\zeta_A)^2+\eta^2}{(\zeta-\zeta_B)^2+\eta^2}\right] . \tag{17}$$

As an example the induced potential and flow velocities from a linear element extending from A= (0,0) to B=(1,0) are shown in Fig. B6

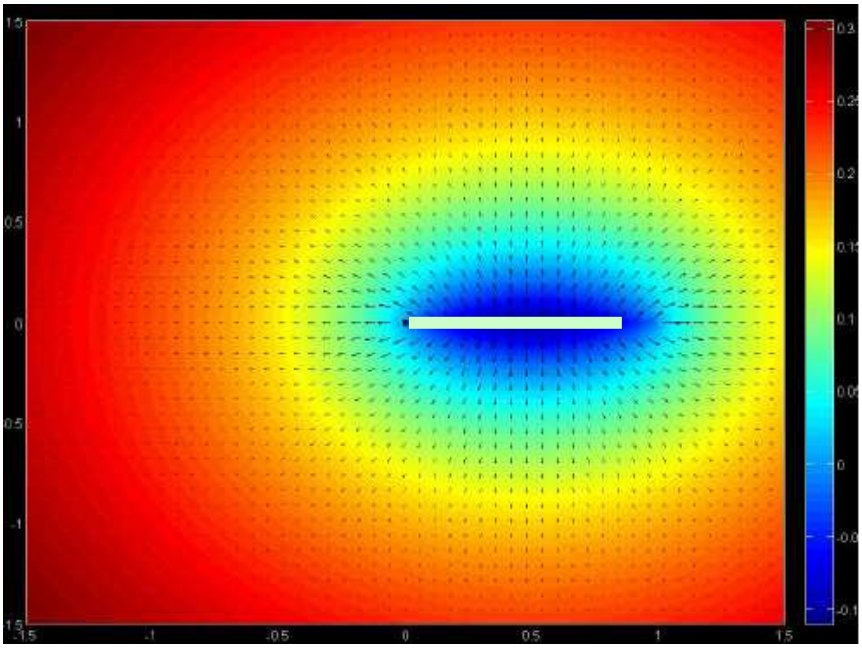

Fig. B.6 Induced potential and flow velocities from a linear element, as calculated using Eqs.(15)-(17). A colorbar is used to indicate the values of the potential.

The induced velocity of the linear source element is given by the integral

$$\boldsymbol{u}_{AB} = -\frac{1}{2\pi}\int_A^B \left(\frac{x_2-x_{2s}}{\sqrt{(x_2-x_{2s})^2+(x_3-x_{3s})^2}}, \frac{x_3-x_{3s}}{\sqrt{(x_2-x_{2s})^2+(x_3-x_{3s})^2}}\right) ds \tag{18}$$

The analytical formulas, for the velocity, in the global coordinate system are then obtained by rotation of the previous result,

$$u_{x_2}(x_2,x_3)=u_\zeta(\zeta,\eta)\cos(\theta)-u_\eta(\zeta,\eta)\sin(\theta)\ , \tag{19}$$

$$u_{x_3}(x_2,x_3)=u_\zeta(\zeta,\eta)\sin(\theta)+u_\eta(\zeta,\eta)\cos(\theta), \tag{20}$$

taking into account that θ is the direction of the boundary element in the global coordinate system, i.e. $\theta=\tan^{-1}\left(\frac{x_3^B-x_3^A}{x_2^B-x_2^A}\right)$.

We proceed with the presentation of the BEM by considering the collocation points $\left(x_2^m,x_3^m\right)$, $m=1,...,M_3$, to be selected the centers of each element, where the boubdary conditions will be satisfied. We denote by the matrix $\phi_{nm}=\phi\left(x_2^n,x_3^n\right)$ the induced potential from the *m*-boundary element to the *n* collocation point, and similarly by $\mathbf{u}_{nm}=u\left(x_2^n,x_3^n\right)$ the induced velocity of the m-element to the center, $\left(x_2^n,x_3^n\right)$, of the n-element , $n=1,..,M_3$. Using the above definitions the boundary conditions of the problem Eqs. (11)-(..) are written in the following discrete form:

$$\frac{\sigma_n}{2}+\sum_{m=1}^{M}\sigma_m\left(\boldsymbol{n}_n\boldsymbol{u}_{\boldsymbol{nm}}-\mu\phi_{nm}\right)=0\ , \qquad n=1,..,M_1\ , \tag{20}$$

$$\frac{\sigma_n}{2}+\sum_{m=1}^{M}\sigma_m\left(\boldsymbol{n}_n\boldsymbol{u}_{\boldsymbol{nm}}\right)=N_i\left(x_2^n,x_3^n\right)\ , \qquad n=M_1+1,..,M_1+M_2\ , \tag{21}$$

$$\frac{\sigma_n}{2}+\sum_{m=1}^{M}\sigma_m\left(\boldsymbol{n}_n\boldsymbol{u}_{\boldsymbol{nm}}-\mu\phi_{nm}\right)=0\,, \qquad n=M_1+M_2+1,..,\sum_{i=1}^{3}M_i\ . \tag{22}$$

The frequency parameter is modified as follows

$$\mu(\omega)=\frac{\left(\omega+j\delta(\omega)\right)^2}{g}\ . \tag{23}$$

in order to model also the absorbing layer .

Based on the previous analysis , the implementation of the code “cresolg.m” in Matlab® solves the linear system (20)-(22), which provides us with the values of $\{\sigma_n\,,n=1,..,M\}$ of the source-sink distribution on each boundary element. The calculated values are used as input to the integral representations (8), (9) which procide the potential and the velocity in the specific domain. Finally, replacing our results into Eq. (2) we the values of the 2D hydrodynamic coefficients are obtained.

Numerical results and demonstration of the present BEM

The application of the panel method is clearly depicted in the following figures, concerning a 2D sectional area, with $B/T=2$, including the free surface at the left and right of the body. The results, derived straight from the implementation of the code ‘’geom.m’’ .

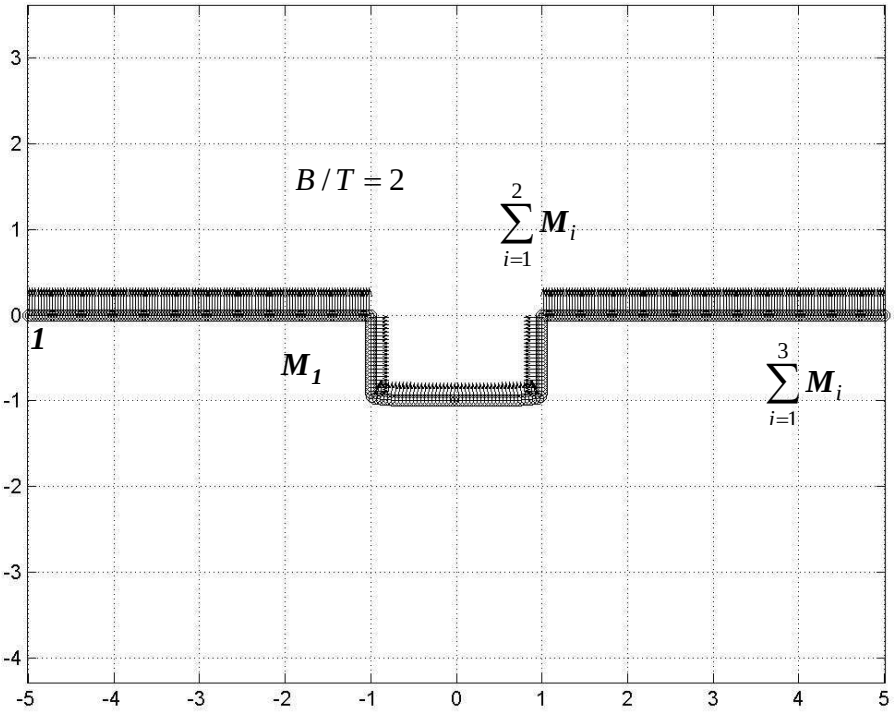

Fig. B.7 BEM discrezization of the boundary of the domain in the case of an orthogonal ship cross section B/T=2.

Using as input the results from ‘’geom.m’’ (sectional area $B/T=2$) , we present the heave and the sway potentials at a low, a medium and a higher angular frequency within the range of investigation $\omega^*\sqrt{B/2g}\in[0,2]$. We recall that the parameters used in the PML model are $\ell/\lambda=1$, $p=3$ and $\delta_0(\omega)=(\omega/\omega_{\max})^5$. The results obtained from the implementation of the code ‘’cresolg.m’’ .

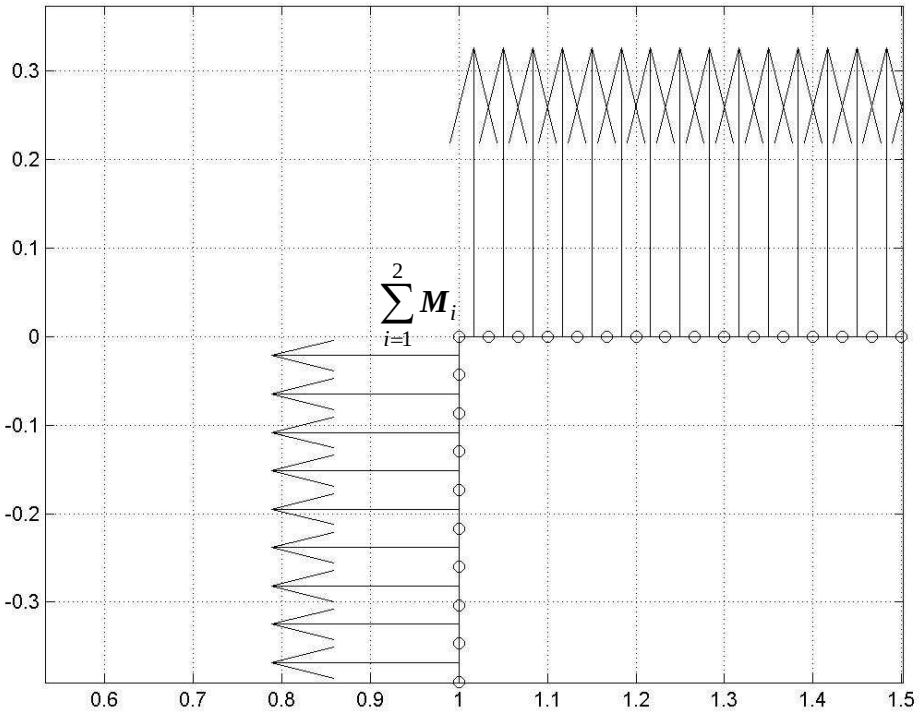

Fig. B.8 BEM discretization near the waterline.

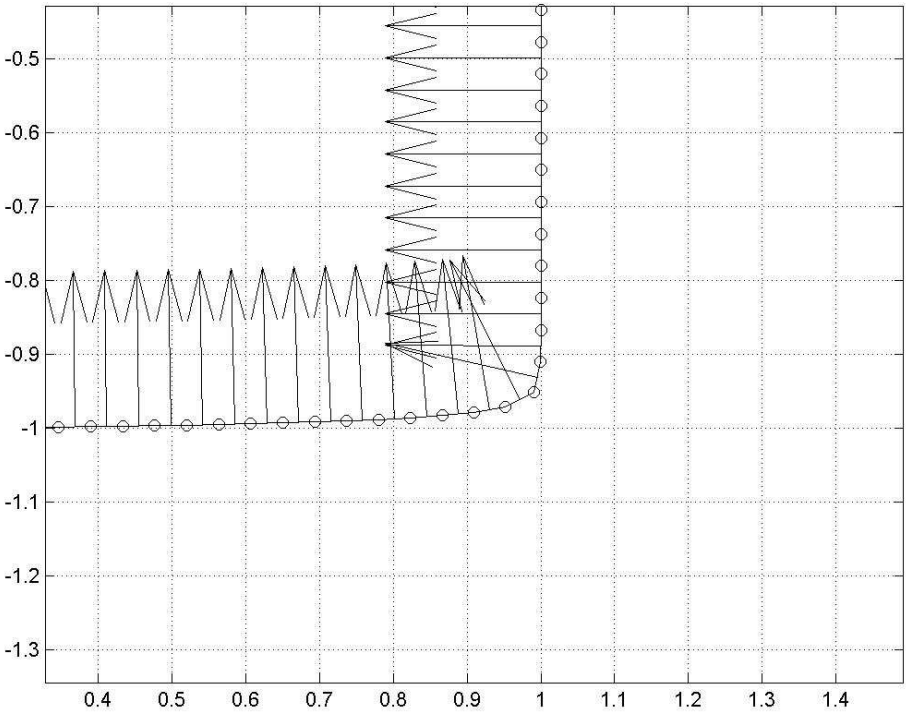

Fig. B.9 BEM discretization near the bilge keel

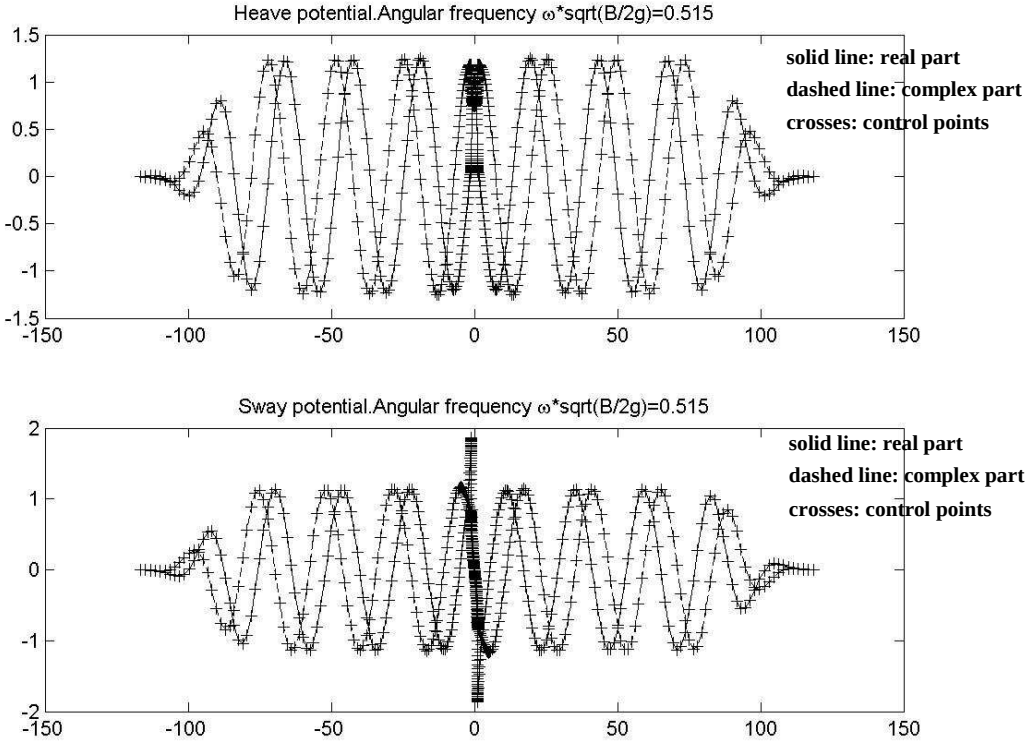

Fig. B.10 Heave & Sway potentials at angular frequency, $\omega^*\sqrt{B/2g}=0.515$

It is now obvious that the PML model used at the ends, $x=\pm a,b$ of the truncated domain allows the absorption of the wave energy with zero reflections. The use of the aforementioned PML coefficients is associated with the angular range frequency and produces a specific number of wavelength which is by approximation 5, see, Fig.A10. We also notice that the energy derived from the motions of the body, is sustained during the propagation of approximately 3.5 wavelengths whereas close to the absorption layers the energy is rapidly absorbed. Therefore, we note that the amplitude of the waves remains the same for almost 3.5λ while approaching the waves close to the edges, the amplitude is decreased to zero as seen in the Fig. A9. We proceed with the presentation of two more cases.

The previous cases provide us with some interesting results regarding the use of the PML model. We observe that both in heave and sway potentials, the produced waves are shorter, in length, as we move to higher frequencies. More specifically, running through the given frequency range the model is developed to adjust the edges of the propagation domain, see Sclavounos, Borgen (2004), according to the boundary conditions inside the absorbing layer , see Eqn. (12).

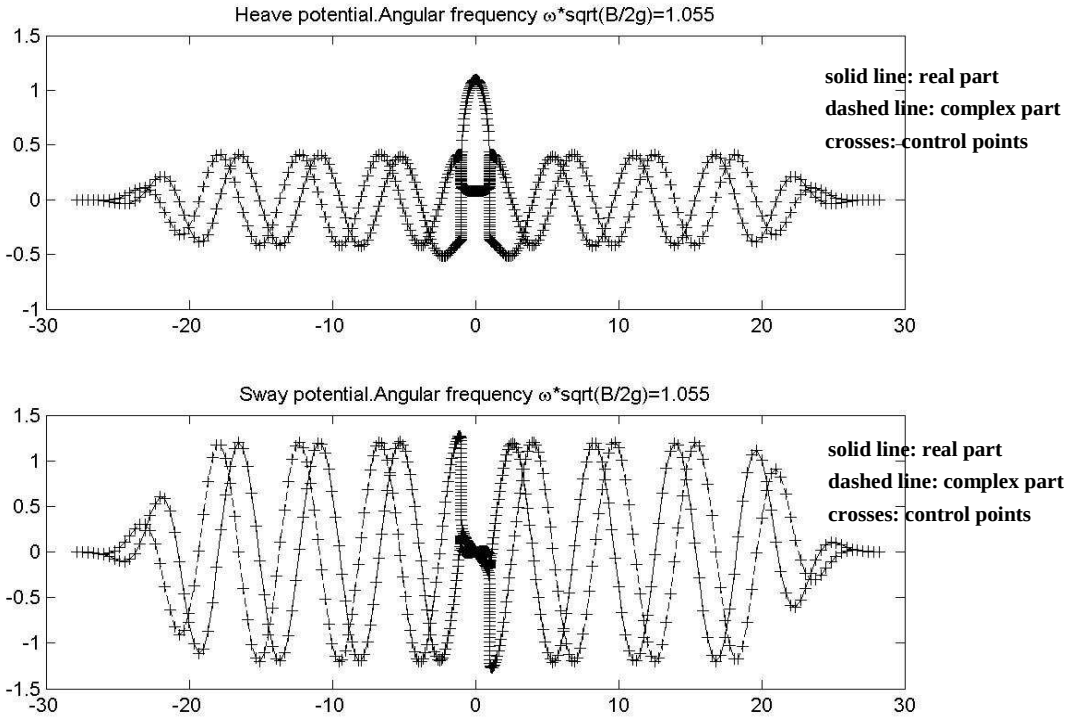

Fig.B.11 Heave & Sway potentials at angular frequency, $\omega^*\sqrt{B/2g}=1.055$

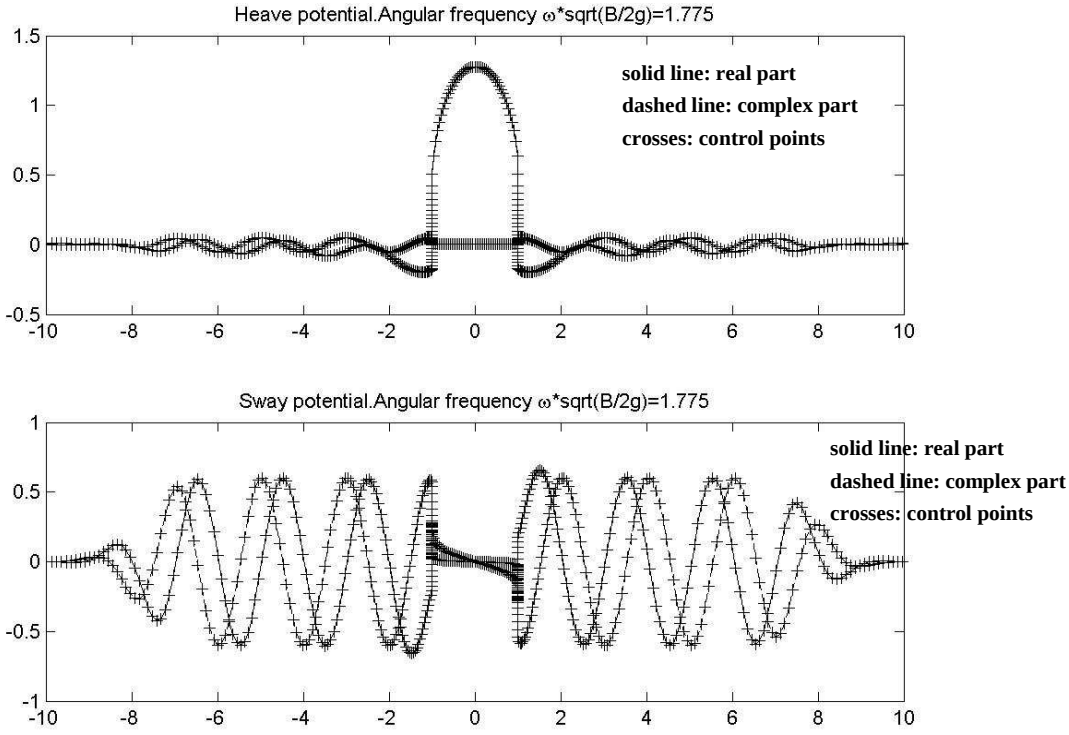

Fig. B.12 Heave & Sway potentials at angular frequency, $\omega^*\sqrt{B/2g}=1.775$

Moreover, following the PML the number of the produced waves has to remain the same given specific parameters ℓ/λ , p , $\delta_0(\omega)$ and B/T see Figs. A10 – A12. In addition, higher frequency excitations, lead to smaller wave amplitudes. For instance, as seen in Figs. A10, A11 as frequency increases the amplitude of the waves, due to the heave motion becomes smaller, while the amplitude of the waves, due to sway motion, is almost the same. As we proceed to higher excitations, see Fig. A12, the sway motion produces waves of distinctively smaller amplitude, while heave produces even smaller ones.

Finally, we proceed with the calculation of the hydrodynamic coefficients $a_{i\ell}$, $b_{i\ell}$, $i,\ell = 2,3,4$ and by extension the calculation of the hydrodynamic forces F_2 , F_3 and F_4. The results are depicted in the following figure

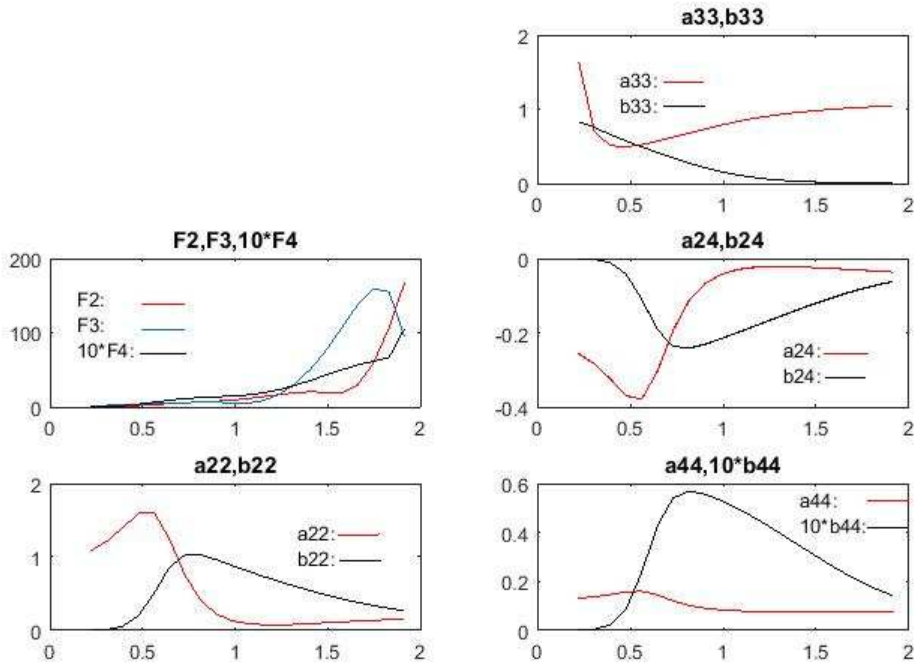

Fig. B.13 Hydrodynamic Forces and coefficients

In order to evaluate the correctness of the present numerical method, we compare our numerically calculated hydrodynamic coefficients $a_{i\ell}$, $\beta_{i\ell}$, with experimentally measured ones, concerning sectional areas of various dimensions B , T . The measurements are included in Vughts (1968) through digitization. In addition, we demonstrate the calculation of the hydrodynamic forces associated with the motions of the different sectional areas. In the following figures, we have the solid line representing the present numerical method and the bullets depicturing the experimental measurements.

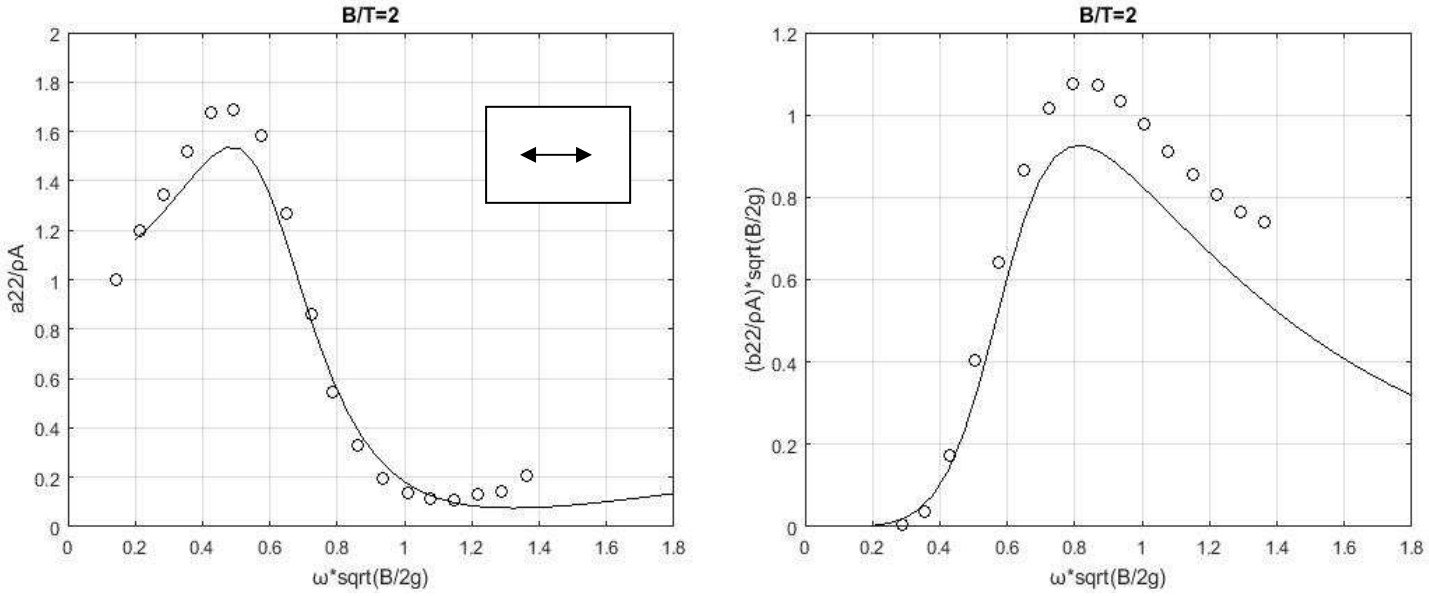

Fig. B.14 Numerical and experimental hydrodynamic coefficients a_{22} , b_{22} for $B/T = 2$

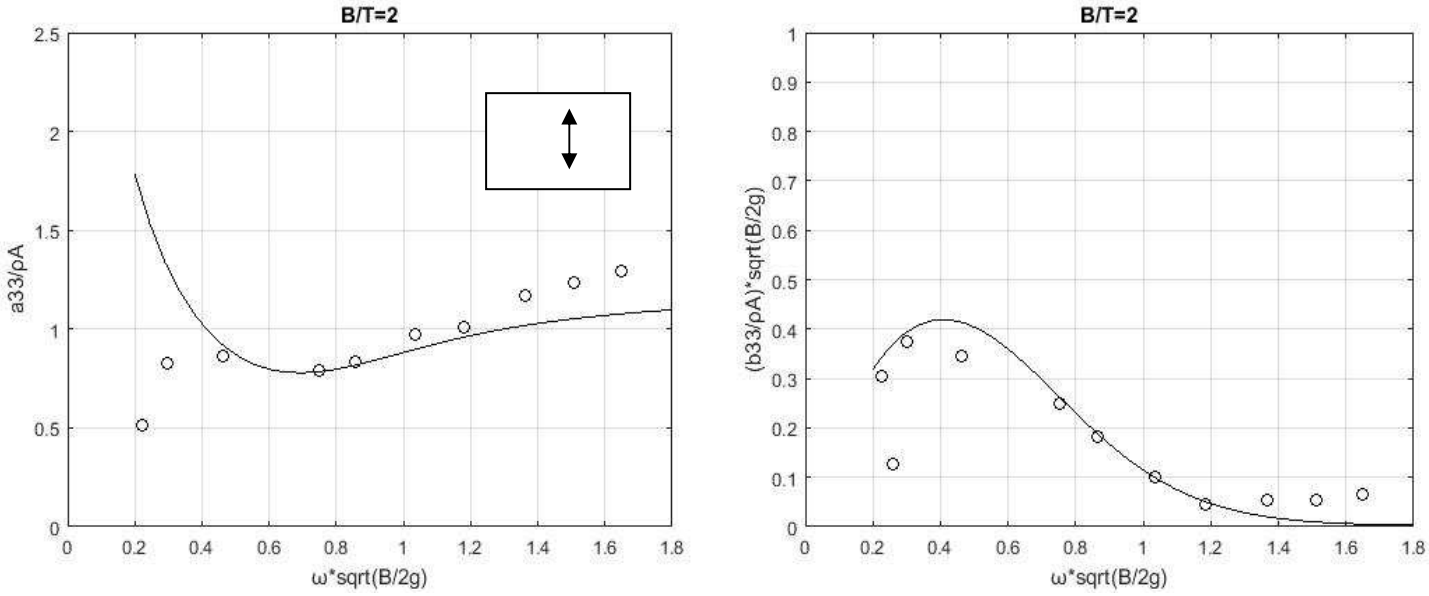

Figure B15 Numerical and experimental hydrodynamic coefficients a_{33} , b_{33} for $B/T = 2$

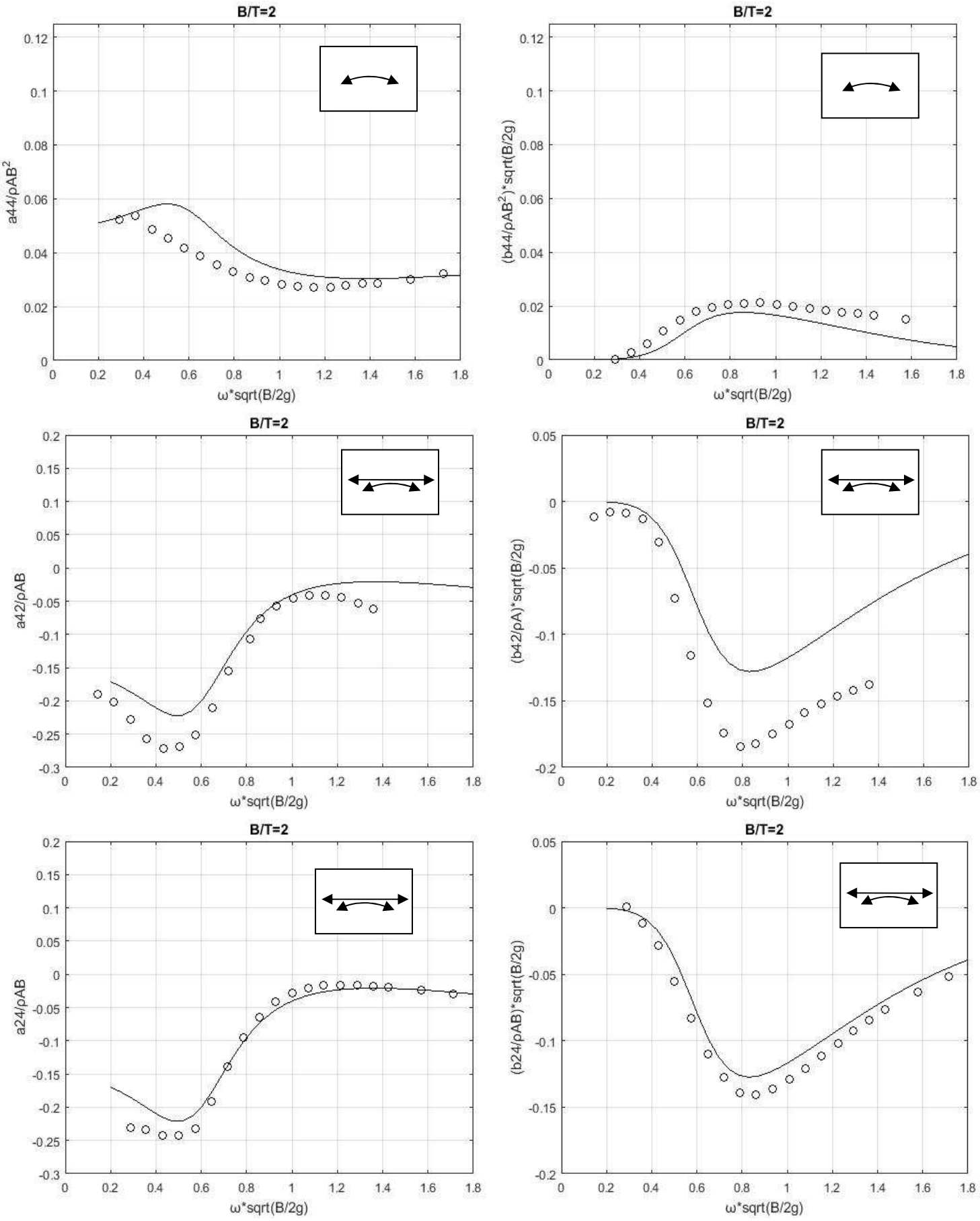

Fig. B.16 Numerical and experimental hydrodynamic coefficients (a_{44}, b_{44}), (a_{42}, b_{42}), (a_{24}, b_{24}), for $B/T = 2$

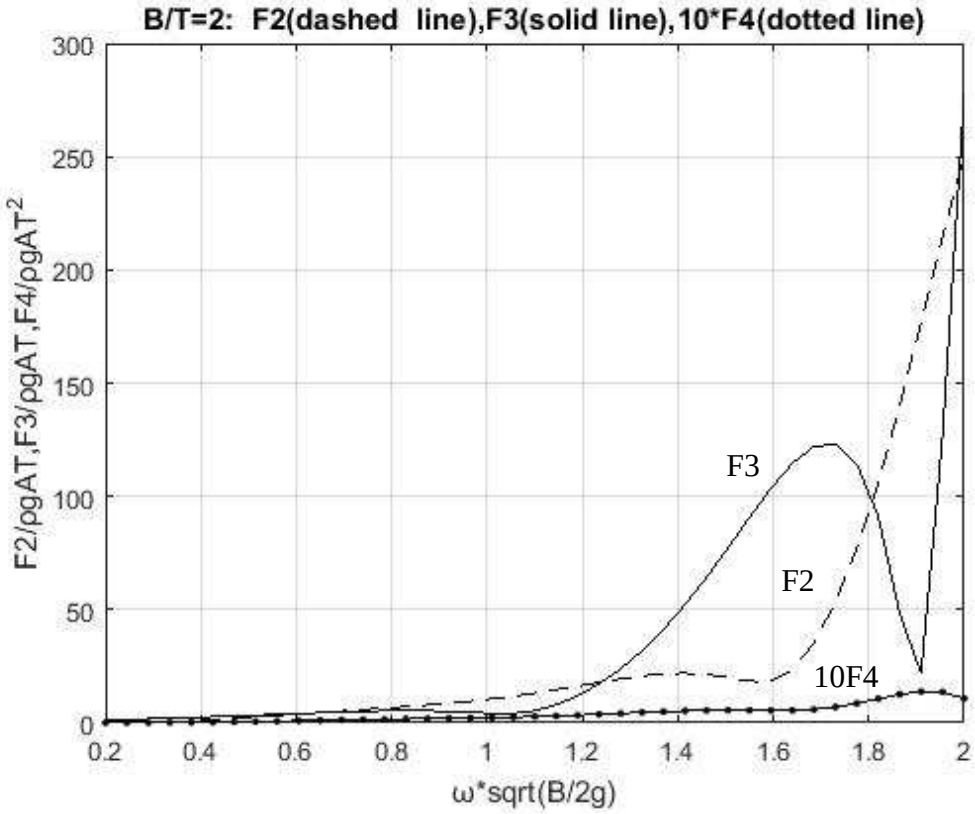

Fig. B.17 Numerical hydrodynamic forces F_2 , F_3 ,$10F_4$ for $B/T = 2$

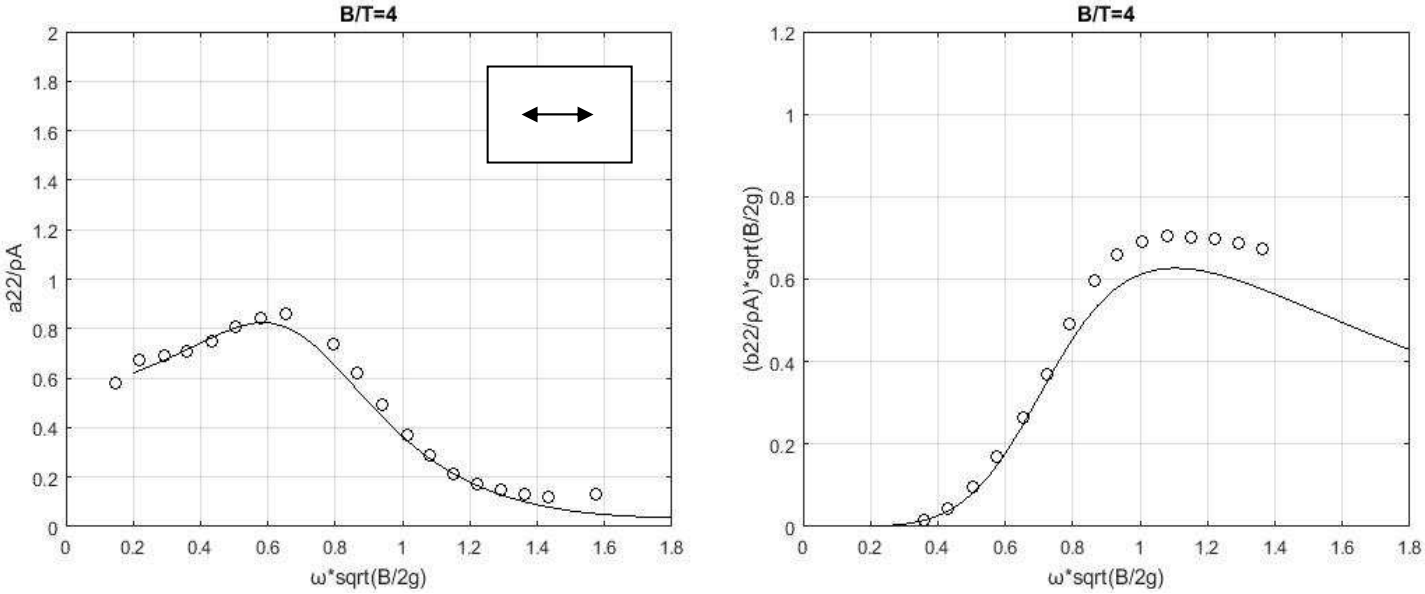

Fig. B.18 Numerical and experimental hydrodynamic coefficients a_{22} , b_{22} for $B/T=4$

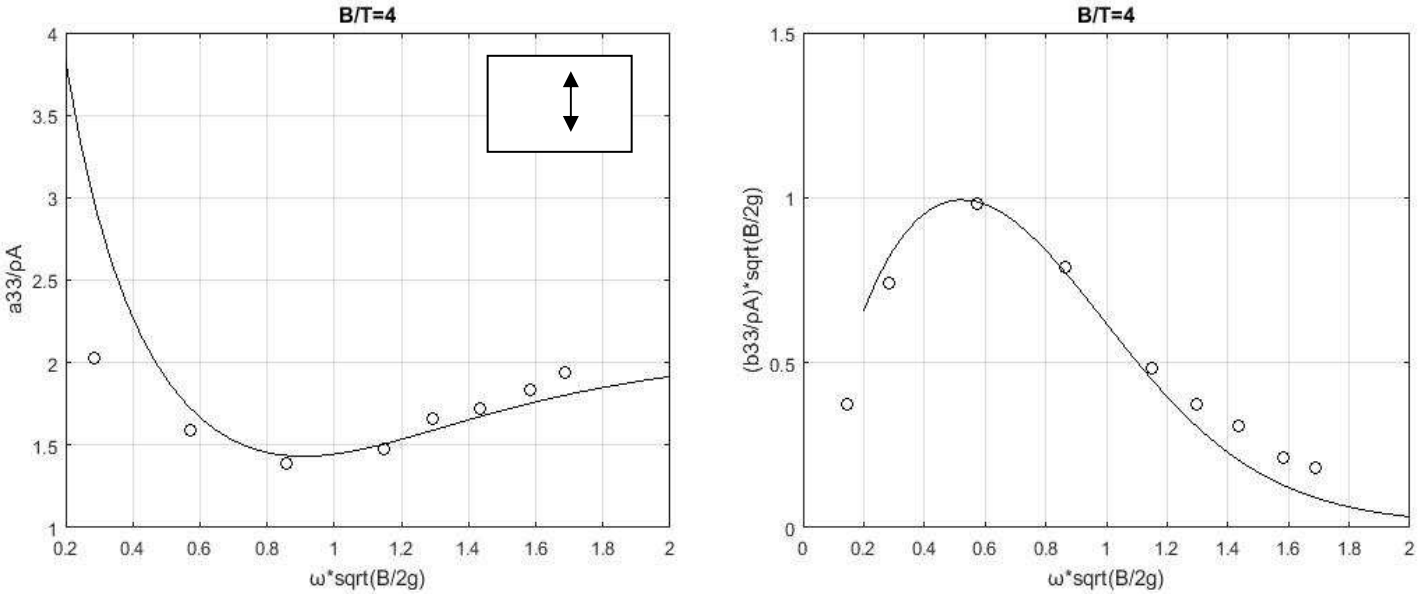

Fig. B.19 Numerical and experimental hydrodynamic coefficients a_{33} , b_{33} for $B/T=4$

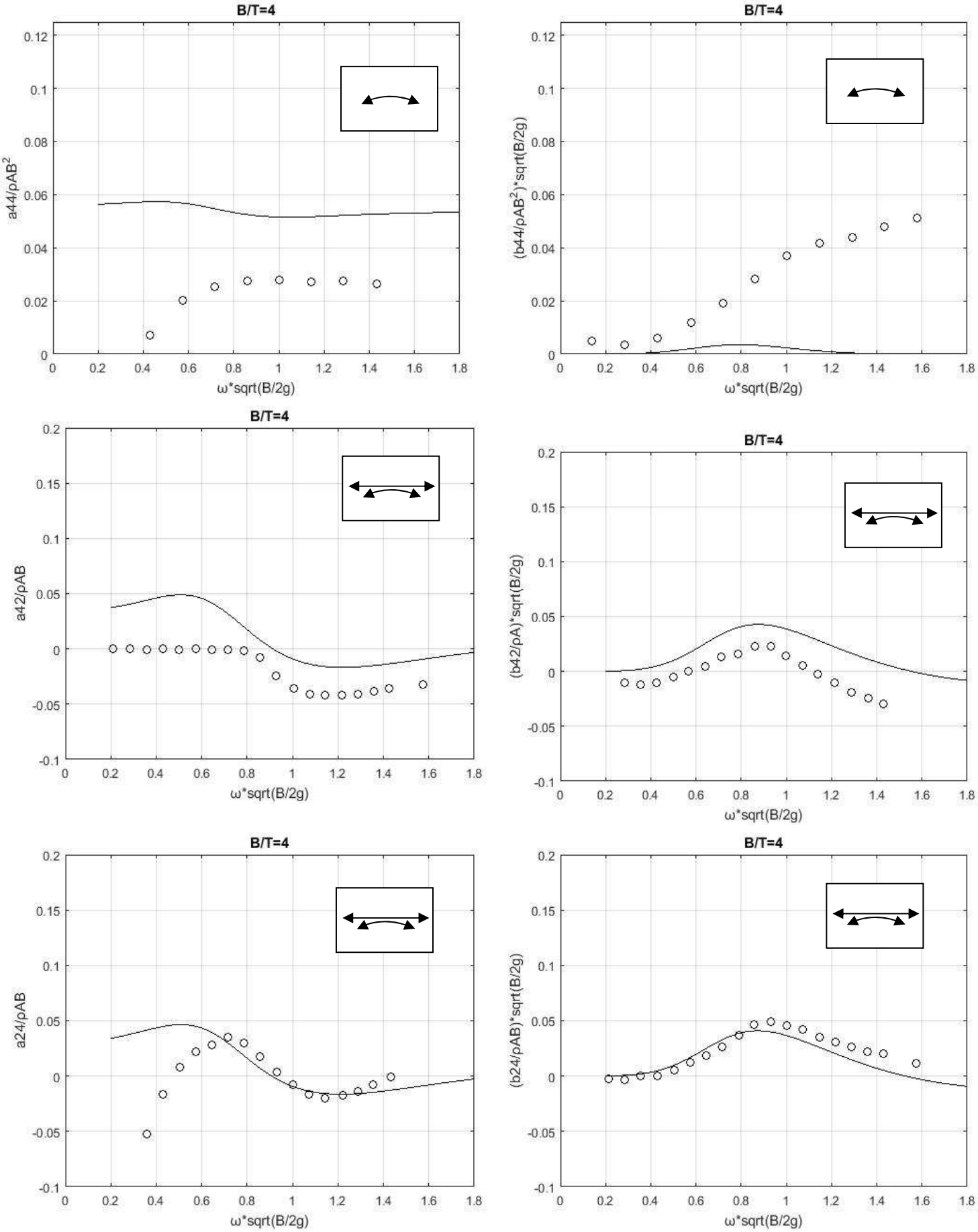

Figure B20 Numerical and experimental hydrodynamic coefficients (a_{44}, b_{44}), (a_{42}, b_{42}), (a_{24}, b_{24}), for $B/T = 4$

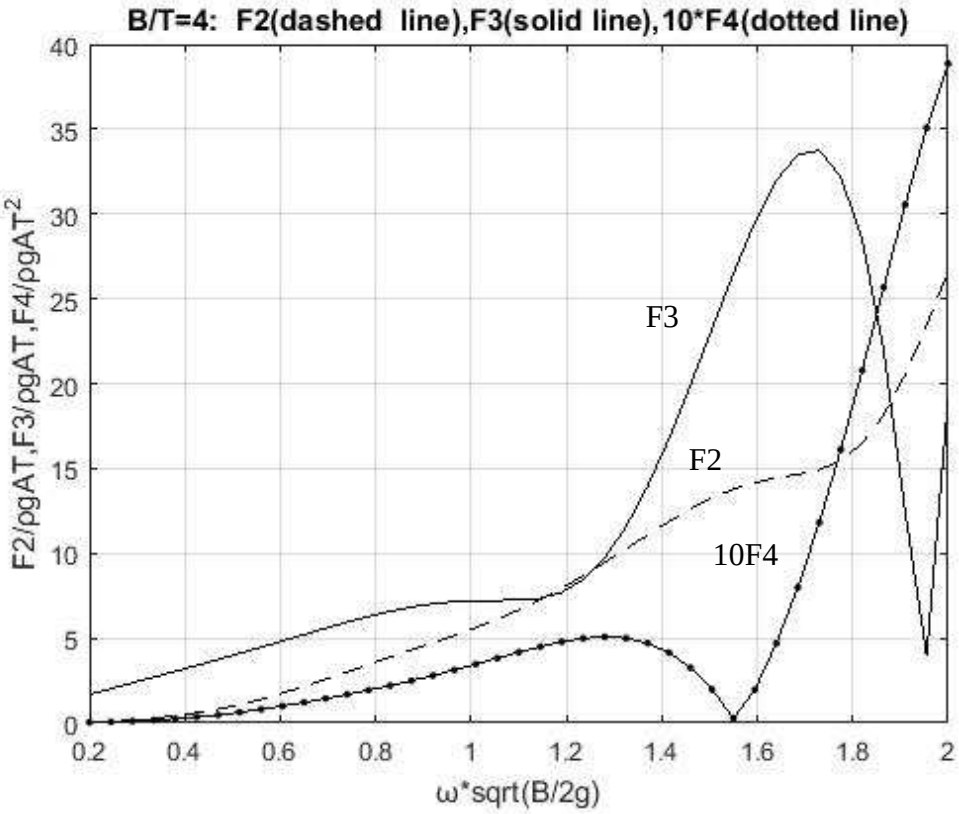

Fig. B.21 Numerical hydrodynamic forces F_2 , F_3 ,$10F_4$ for $B/T = 4$

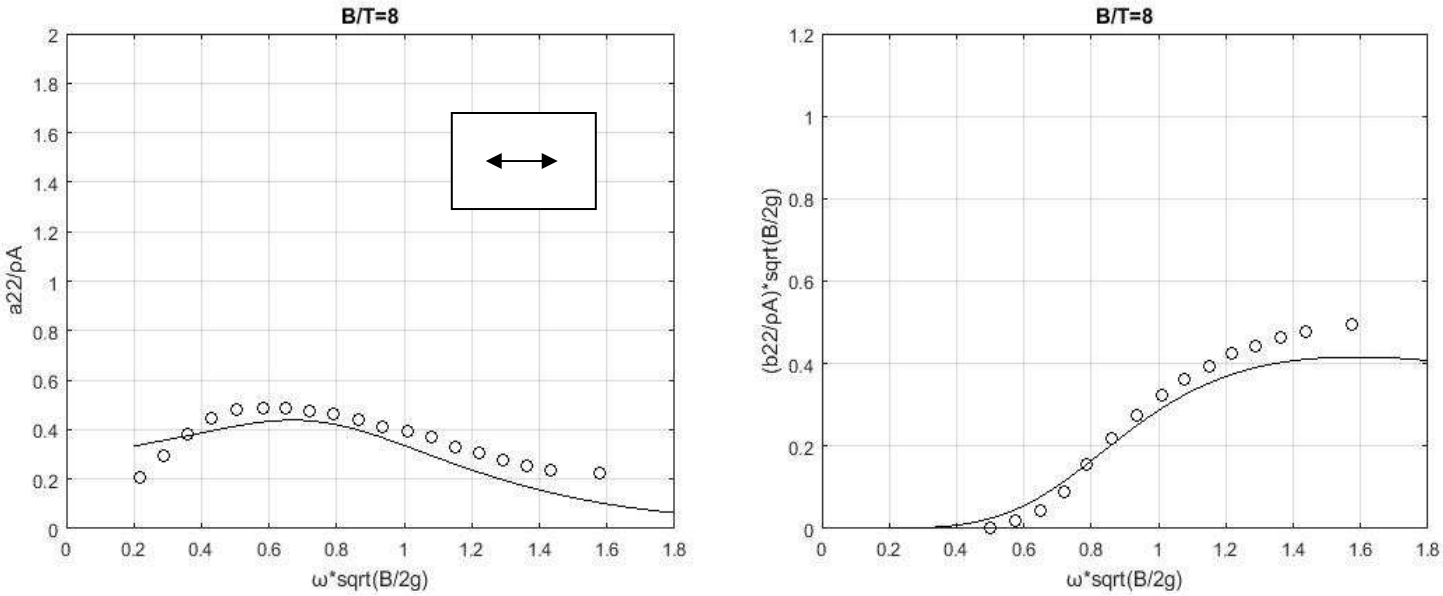

Fig. B.22 Numerical and experimental hydrodynamic coefficients a_{22} , b_{22} for $B/T = 4$

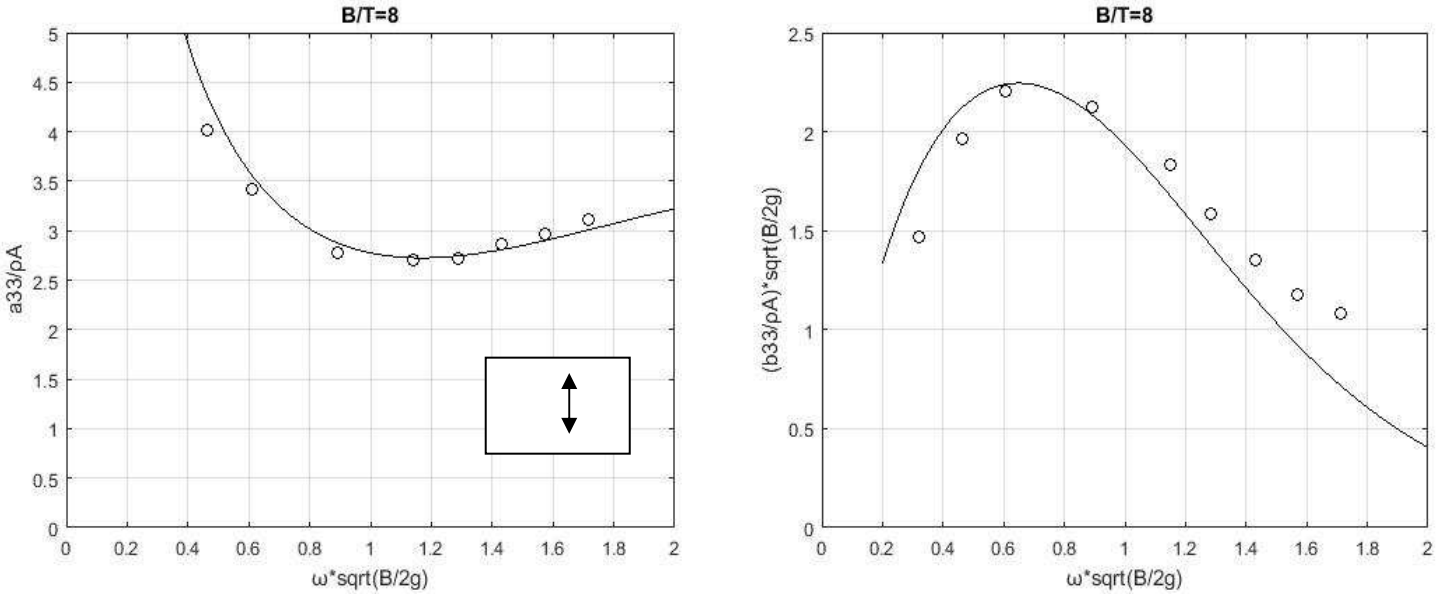

Fig. B.23 Numerical and experimental hydrodynamic coefficients a_{33} , b_{33} for $B/T = 4$

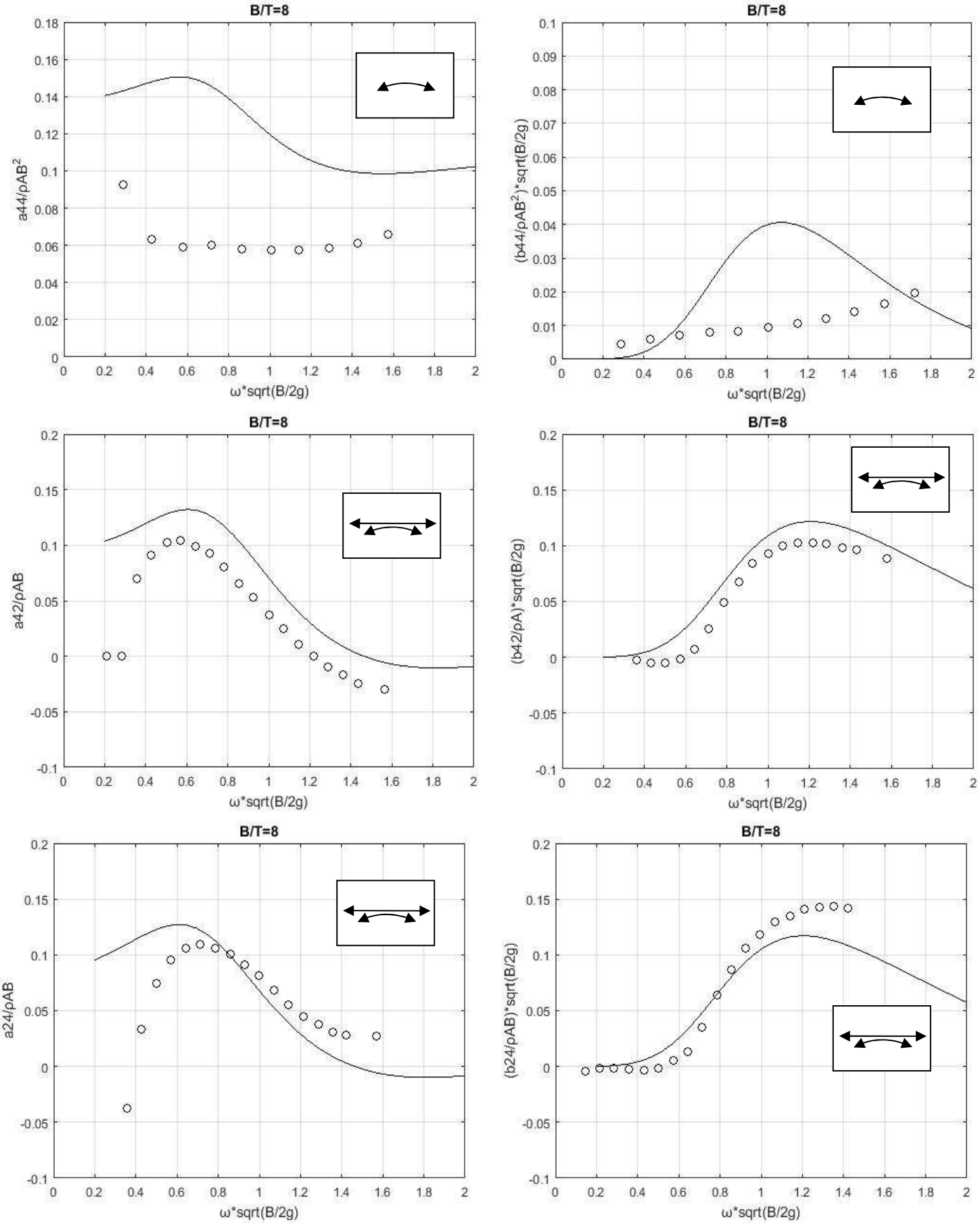

Fig. B.24 Numerical and experimental hydrodynamic coefficients (a_{44}, b_{44}), (a_{42}, b_{42}), (a_{24}, b_{24}), for $B/T = 4$

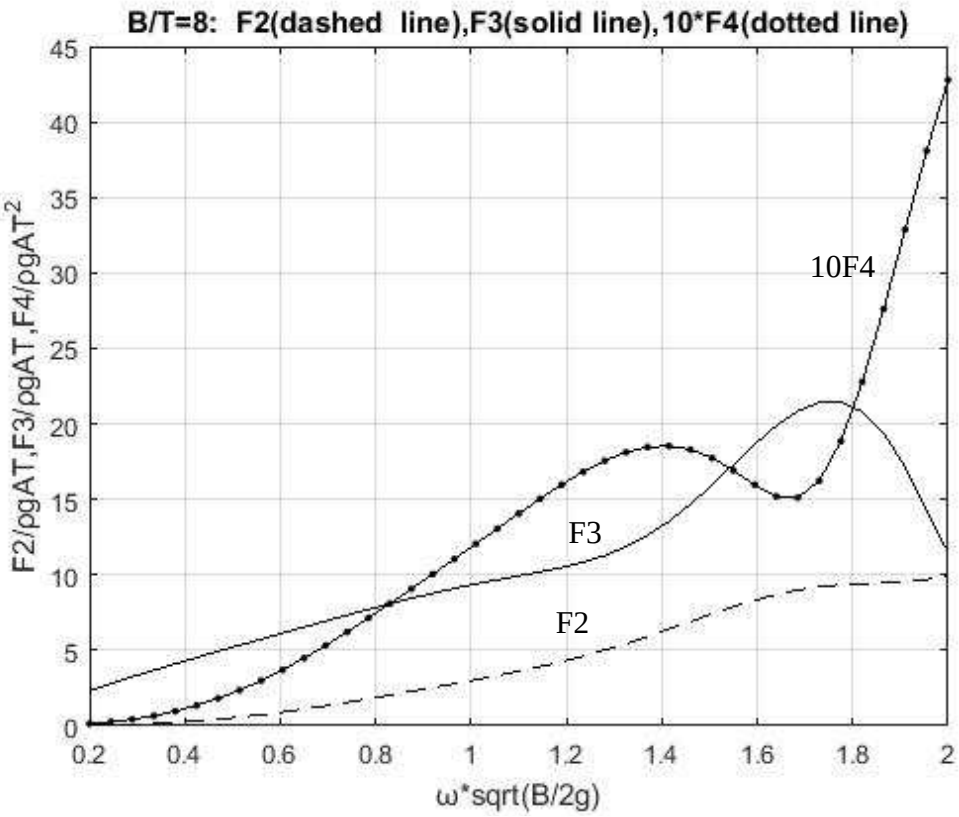

Fig. B.25 Numerical hydrodynamic forces F_2 , F_3 ,$10F_4$ for $B/T=4$

We also examine the case of a cross section with $B/T=6$. Because we lack of experimental measures for such a case we compare the produced results with the previously presented results for $B/T=2$, $B/T=4$ and $B/T=8$.

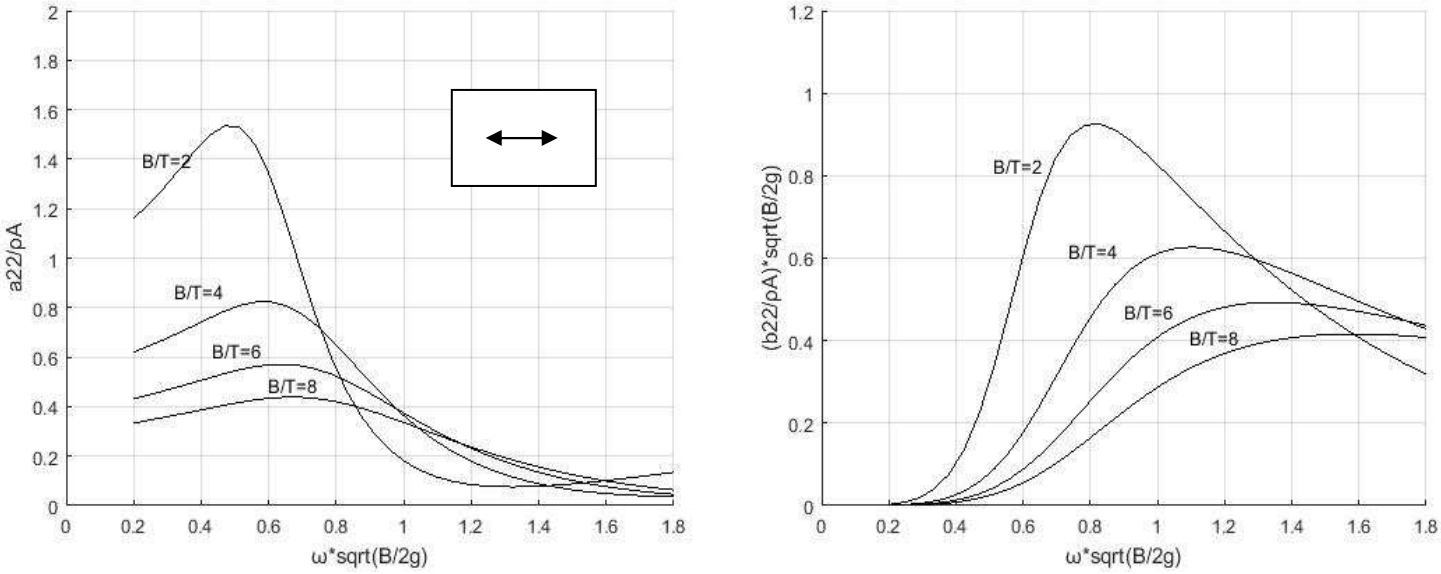

Fig. B.26 Numerical and experimental hydrodynamic coefficients a_{22} , b_{22} for $B/T = 6$

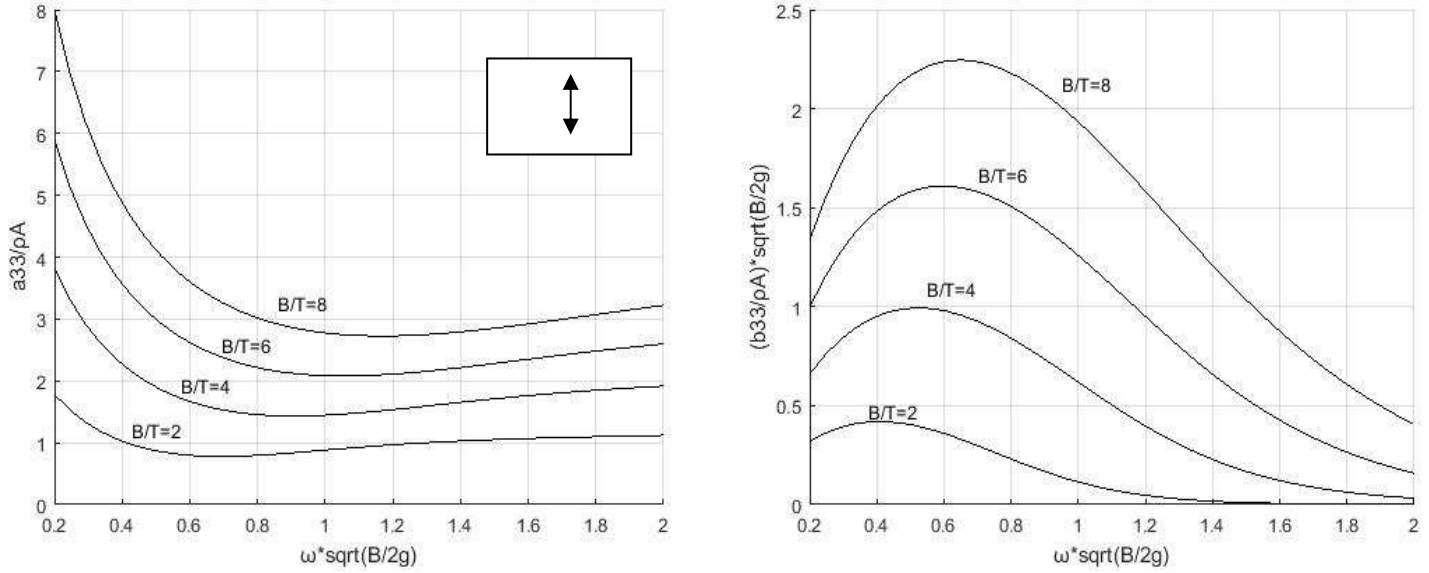

Fig. B.27 Numerical and experimental hydrodynamic coefficients a_{33} , b_{33} for $B/T = 6$

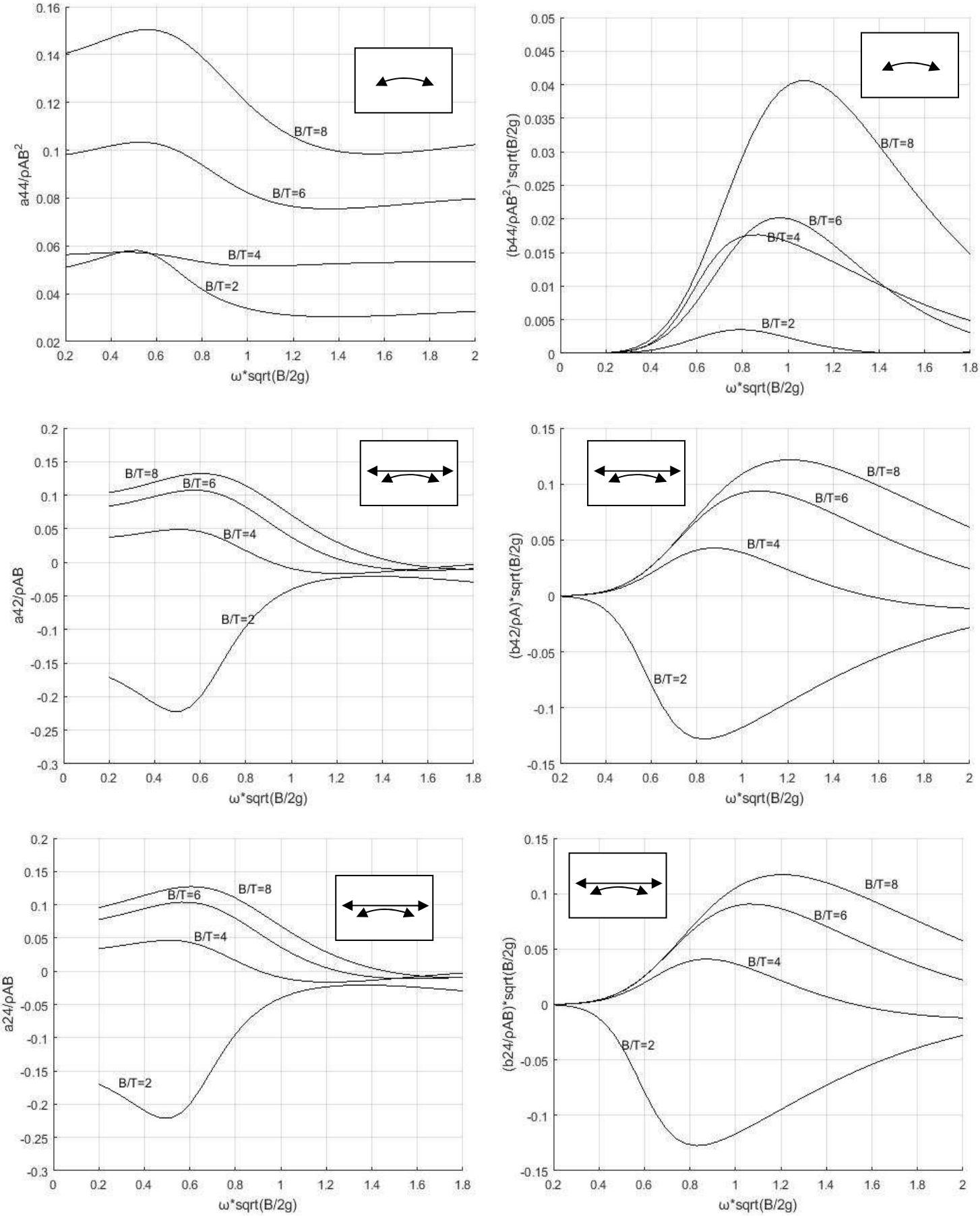

Figure B28 Numerical and experimental hydrodynamic coefficients (a_{44}, b_{44}), (a_{42}, b_{42}), (a_{24}, b_{24}), for $B/T = 6$

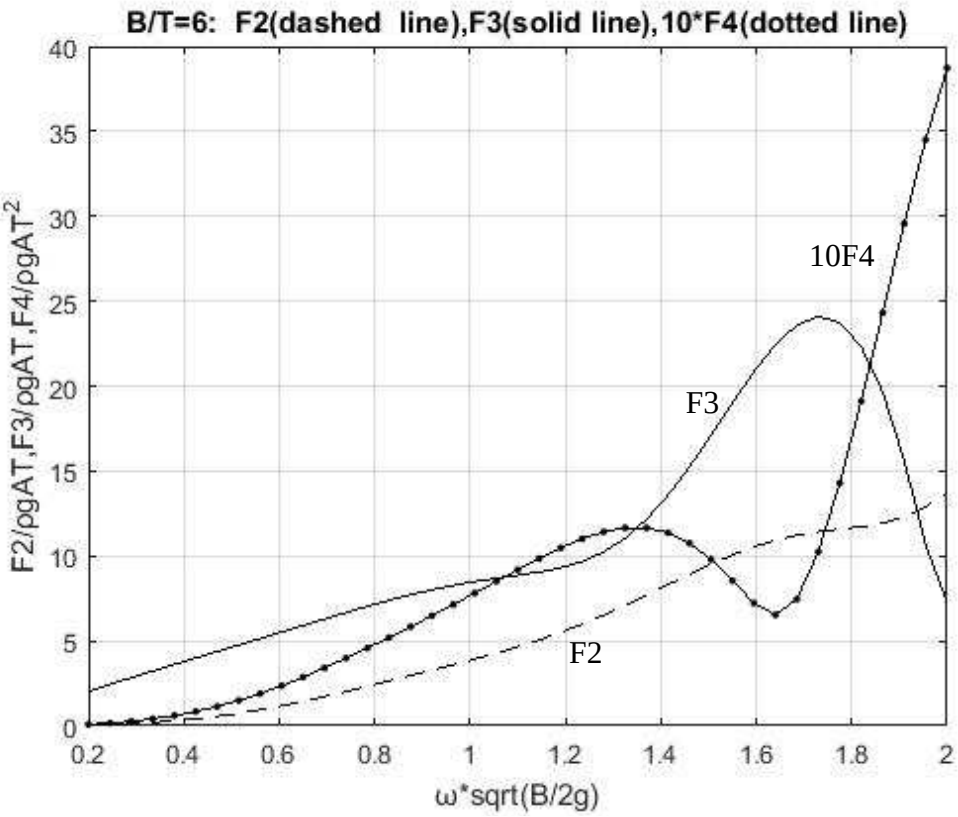

Fig. B.29 Numerical hydrodynamic forces F_2 , F_3 ,$10F_4$ for $B/T = 6$